

UNCLASSIFIED

AD NUMBER

AD892382

LIMITATION CHANGES

TO:

Approved for public release; distribution is unlimited.

FROM:

Distribution authorized to U.S. Gov't. agencies only; Test and Evaluation; MAR 1972. Other requests shall be referred to Air Force Rocket Propulsion Laboratory, Attn: STINFO/DOZ, Edwards, CA 93523.

AUTHORITY

AFRPL ltr, 15 May 1986

THIS PAGE IS UNCLASSIFIED

AD892382

AFRPL-TR-72-19

EXTENSION OF A THRUST CHAMBER  
COMPATIBILITY MODEL

Authors

W. S. Hines  
M. D. Schuman  
W. M. Ford  
K. D. Fertig

Rocketdyne  
A Division of North American Rockwell Corporation  
Canoga Park, California

FINAL REPORT AFRPL-TR-72-19

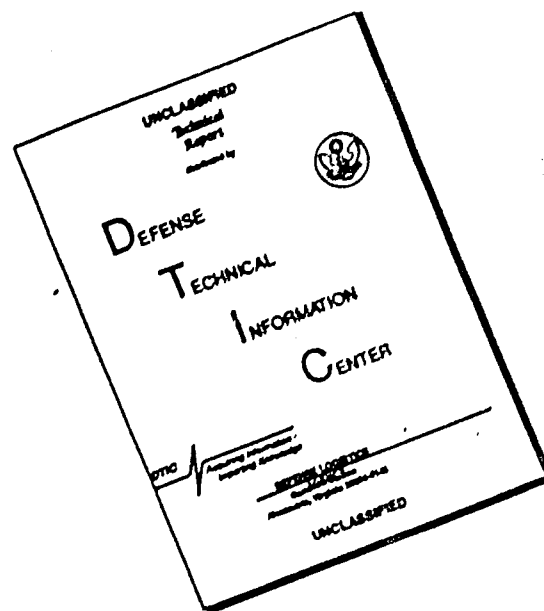
March 1972

Distribution limited to U.S. Government Agencies only; test and evaluation; March 1972. All other requests for this document must be referred to AFRPL (STINFO/DOZ) Edwards, CA 93523.

Air Force Rocket Propulsion Laboratory  
Director of Laboratories  
Air Force Systems Command  
United States Air Force  
Edwards, California

When U. S. Government drawings, specifications, or other data are used for any purpose other than a definitely related Government procurement operation, the Government thereby incurs no responsibility nor any obligation whatsoever, and the fact that the Government may have formulated, furnished, or in any way supplied the said drawings, specifications, or other data, is not to be regarded by implication or otherwise, or in any manner licensing the holder or any other person or corporation, or conveying any rights or permission to manufacture, use, or sell any patented invention that may in any way be related thereto.

# DISCLAIMER NOTICE



THIS DOCUMENT IS BEST QUALITY AVAILABLE. THE COPY FURNISHED TO DTIC CONTAINED A SIGNIFICANT NUMBER OF PAGES WHICH DO NOT REPRODUCE LEGIBLY.

AFRPL-TR-72-19

EXTENSION OF A THRUST CHAMBER  
COMPATIBILITY MODEL

Authors

W. S. Hines  
M. D. Schuman  
W. M. Ford  
K. D. Fertig

Rocketdyne  
A Division of North American Rockwell Corporation  
Canoga Park, California

Final Report AFRPL-TR-72-19

March 1972

Distribution limited to U.S. Government Agencies only; test and evaluation; March 1972. All other requests for this document must be referred to AFRPL (STINFO/DOZ) Edwards, CA 93523.

Air Force Rocket Propulsion Laboratory  
Director of Laboratories  
Air Force Systems Command  
United States Air Force  
Edwards, California

## FOREWORD

This report, prepared by the Advanced Programs Department of Rocketdyne, a division of North American Rockwell Corporation, 6633 Canoga Avenue, Canoga Park, California, summarizes the work performed under Air Force Contract F04611-70-C-0056, Thrust Chamber Compatibility Model, during the period June 1970 to August 1971. The Air Force Project Officer was Capt. Wayne Pritz (USAF); Mr. T. A. Coultas was the Rocketdyne Program Manager.

This report has been assigned the Rocketdyne identification number R-8745.

Wayne L. Pritz, Captain, (USAF)  
Project Engineer, AFRPL (RTSC)

# TABLE OF CONTENTS

Foreword . . . . .	iii
Nomenclature . . . . .	xv
Introduction and Summary . . . . .	1
<u>Model for Thrust Chamber Compatibility and Performance Analysis</u> . . . . .	5
Chamber Flow Field . . . . .	5
Injection Atomization Region . . . . .	11
LISP Computer Program . . . . .	11
Injector Heat Transfer Model . . . . .	20
Combustion Models . . . . .	23
3D COMBUST Computer Program . . . . .	23
Stream Tube Computer Program (STRMTB) . . . . .	27
Boundary Layer Analysis . . . . .	33
3D-COMBUST Region . . . . .	34
STRMTB Region . . . . .	36
Gas Temperature . . . . .	37
<u>Analytical Developments</u> . . . . .	39
Phase 1: Improvement of the LISP Analysis . . . . .	39
Unlike-Douplet Spray Correlations . . . . .	40
Triplet Spray Correlations . . . . .	49
Like-Douplet-Pair Spray Correlations . . . . .	56
HYPERTHIN Like Doublets . . . . .	62
Gas/Liquid Coaxial Elements . . . . .	65
Drop Size Definitions . . . . .	82
Initial Vaporization Definitions . . . . .	83
Initial Performance Predictions . . . . .	87
Phase 2: Development of Injector Face Heat Transfer Analysis . . . . .	93
Analytical Model . . . . .	93
Correlation of Experimental Data With the Analytical Model . . . . .	99
Resume of the IHIM Computer Program . . . . .	109
Development of the 3D-COMBUST Analysis . . . . .	115
Droplet Collisions . . . . .	114
Variable Axial Gas Velocity . . . . .	120
Variable Droplet Evaporation Rates . . . . .	122

Initialization of Gas Flow Field . . . . .	123
Resume of the 3D-COMBUST Program . . . . .	126
Changes in the BLEAT Program . . . . .	133
STRMTB Region Heat Transfer . . . . .	133
3D-COMBUST Region Heat Transfer . . . . .	136
Heat Flux . . . . .	142
Computer Program . . . . .	142
<u>Experimental Studies</u> . . . . .	147
Introduction and Summary . . . . .	147
Cold Flow Experiments . . . . .	149
Test Facility . . . . .	149
Cold Flow Hardware . . . . .	156
Test Program and Results . . . . .	161
HIPERTHIN-Like Doublet . . . . .	165
Motor Firing Experiments . . . . .	167
Facility . . . . .	167
Injectors . . . . .	167
Thrust Chamber Hardware . . . . .	171
Instrumentation . . . . .	177
Test Program and Results . . . . .	188
Spray Heat Transfer Experiments . . . . .	203
Experimental Apparatus . . . . .	203
Experimental Procedure and Results . . . . .	204
Discussion of Experimental Results . . . . .	205
<u>Demonstration Analyses of Motor Firing Experiments</u> . . . . .	209
Introduction and Summary . . . . .	209
Analysis of Demonstration Case TCC-1 . . . . .	211
Analysis of Case TCC-2 . . . . .	227
Analysis of Case TCC-3 . . . . .	235
Analysis of Case TCC-4 . . . . .	245
Conclusions and Recommendations . . . . .	251
Conclusions. . . . .	251
Recommendations. . . . .	252
References . . . . .	253



## LIST OF ILLUSTRATIONS

1.	Separation of Combustion Chamber into Zones for Analysis . . . . .	6
2.	Recirculation Pattern Between Spray Jets in the Pre-reaction Zone . . . . .	6
3.	Example of Injector Face Pattern to Show Use of Symmetry Considerations in Defining Thrust Chamber Mesh Systems . . . . .	9
4.	Slice of Thrust Chamber for Analysis as Determined From Symmetry Considerations . . . . .	9
5.	Network of Mesh Points for Finite Difference Solution of Conservation Equations by 3D-COMBUST Program . . . . .	10
6.	Conversion of Three-Dimensional Combustion Region Mesh System to Stream Tube Network . . . . .	10
7.	Single Like Doublet Element Coordinate System . . . . .	13
8a.	Mass Flux Contours for Doublet With Equal Diameters and Equal Stream Momenta . . . . .	15
8b.	Mass Flux Contours for Doublet With Unequal Diameters and Equal Overall Stream Momenta . . . . .	15
9.	Geometric Factors Affecting the Propellant Distribution of Like-Doublet-Pair Injector Elements . . . . .	15
10a.	Spray Mass Flux From Single Triplet Injector Element . . . . .	16
10b.	Spray Flux Pattern for Four-on-One Element at Moderate and High Momentum Ratios . . . . .	16
11a.	Interelement Recirculation Pattern . . . . .	22
11b.	Interjet Recirculation Pattern . . . . .	22
12.	Coordinate System for Unlike Doublet Element . . . . .	42
13.	Variation of b Coefficient With $R_M$ and $R_D$ for Smaller Orifice of Unlike Doublet . . . . .	47
14.	Variation of b Coefficient With $R_M$ and $R_D$ for Larger Orifice of Unlike Doublet . . . . .	47
15.	Variation of Outer Orifice Spray Coefficient $a_1$ With Momentum Ratio . . . . .	51
16.	Variation of Outer Orifice Spray Coefficient $b_1$ With Momentum Ratio . . . . .	52
17.	Variation of Inner Orifice Spray Coefficient $a_2$ With Momentum Ratio . . . . .	53
18.	Variation of Inner Orifice Spray Coefficient $b_2$ With Momentum Ratio . . . . .	54
19.	Variation of Inner Orifice Spray Coefficient $C_4$ With Momentum Ratio . . . . .	55

20.	General Configuration of Like-Doublet Pair Element and Associated Coordinate System . . . . .	57
21.	Variation of a Coefficient on Same Side of Center With Element Spacing for Fan Impingement Angles of 40 Degrees . . . . .	59
22.	Variation of a Coefficient on Opposite Side of Center With Element Spacing for Fan Impingement Angles of 40 Degrees . . . . .	59
23.	Variation of a Coefficient on Same Side of Center With Element Spacing for Fan Impingement Angles of 0 and 20 Degrees . . . . .	60
24.	Variation of a Coefficient on Opposite Side of Center With Element Spacing for Fan Impingement Angles of 0 and 20 Degrees . . . . .	60
25.	Variation of b Coefficient With Element Spacing for Fan Impingement Angle of 40 Degrees . . . . .	61
26.	Variation of b Coefficient With Element Spacing for 0 and 20 Degrees Fan Impingement Angles . . . . .	61
27.	Mass Distribution Along X-axis of Hyperthin Like Doublet at a Collection Distance of 1.0 Inch . . . . .	64
28.	Schematic Representation of Coaxial Element Geometry . . . . .	68
29.	Typical Mass Flux Profiles for Gas/Liquid Coaxial Elements as Measured by R. J. Burick . . . . .	69
30a.	Variation of $\bar{R}_L/\bar{R}_{L,0}z$ Parameter With Momentum Ratio. . . . .	74
30b.	Variation of $\bar{R}_L/\bar{R}_{L,0}z$ Parameter With Momentum Ratio . . . . .	74
31a.	Variation of $\bar{R}_{L,0}\delta_L$ Parameter With Momentum Ratio . . . . .	75
31b.	Variation of $\bar{R}_{G,0}\delta_G$ Parameter With Momentum Ratio . . . . .	75
32.	Spray Flux at 0.0 Inch From Injector . . . . .	76
33.	Spray Flux at 5.0 Inches From Injector . . . . .	76
34.	Variation of Fractional Propellant Vaporization With Distance From the Injector for ICC2A . . . . .	88
35.	Logic Map for LISP Computer Program . . . . .	89
36.	Coordinate System for Location of Liquid Jet . . . . .	95
37.	Energy Control Volume for the IHM Program . . . . .	98
38.	Heat Flux Distribution on Face of Unlike Doublet Injector ICC2A at a Chamber Pressure of 200 psia . . . . .	101
39.	Heat Flux Distribution on Face of Triplet Injector ICC6 at a Chamber Pressure of 171 psia . . . . .	102

40. Heat Flux Distribution on Face of Triplet Injector ICC6 at a Chamber Pressure of 342 psia . . . . .	103
41. Heat Flux Measured at Transducer 11 on Face of Injector ICC6 . . . . .	104
42. Heat Flux Measured at Transducer 12 on Face of Injector ICC6 . . . . .	105
43. Heat Flux Measured at Transducer 15 on Face of Injector ICC6 . . . . .	106
44. Heat Fluxes Measured on Face of Injector ICC2A Correlated to Analytical Model . . . . .	108
45. IHTM Flow Chart . . . . .	110
46. Coordinate System for Propellant Droplet Collision Model . . . . .	115
47. Transformed Coordinate System for Droplet Collisions . . . . .	115
48. Effect of Droplet Collisions on Gas Mixture Ratio at Chamber Wall of Like Doublet Injector . . . . .	119
49. Effect of Droplet Collisions on Spray Mixture Ratio at Chamber Wall of Like Doublet Injector . . . . .	119
50. The Effect of a Variable Evaporation Coefficient Upon Calculation of a Local Mixture Ratio for a Like Doublet Injector . . . . .	124
51. Logic Map of 3D-COMBUST Computer Program . . . . .	127
52. Logic Diagram for BLEAT Computer Program . . . . .	143
53. Cold Flow Test Facility (Flow System) . . . . .	150
54. Cold Flow Mass Distribution Facility . . . . .	151
55. Radial Spray Flux Sampling Tray . . . . .	153
56. Radial Spray Collector Tray . . . . .	154
57. Cold Flow Test Stand Modified for Radial Spray Sampling Equipment . . . . .	155
58. Workhorse Single Element Cold Flow Injector Arranged as a Triplet . . . . .	157
59. Single Element Workhorse Injector During Triplet Cold Flow Experiment . . . . .	159
60. Single Element HIPERTHIN Cold Flow Model . . . . .	160
61. Pad 3B Test Stand for Storable Propellant Motor Firing Experiments. . . . .	168
62. Test Stand and Hardware . . . . .	169
63. High Pressure Propellant Tanks at Pad 3B . . . . .	169
64. Eight Element Unlike Doublet Injector ICC2A . . . . .	170
65. Backwall View of Injector ICC2A With Heat Transfer Instrumentation . . . . .	172

66.	Twelve Element Triplet Injector ICC6 . . . . .	173
67.	Backwall View of Triplet Injector ICC6 . . . . .	174
68.	Low Contraction Ratio Copper Heat Sink Nozzle . . . . .	175
69.	High Contraction Ratio Copper Heat Sink Nozzle . . . . .	176
70.	Difference Thermocouple Heat Flux Probe . . . . .	178
71.	Electroformed Heat Flux Transducer--Model One . . . . .	179
72.	Electroformed Heat Flux Transducer--Model Two . . . . .	180
73.	Heat Flux Transducer Ready for Installation . . . . .	181
74.	Schematic of Heat Flux Transducer Calibration Apparatus . . . . .	183
75.	Calibration Curves for Heat Flux Transducers . . . . .	184
76.	Location of Heat Transfer Instrumentation on Injector ICC2A . . . . .	191
77.	Location of Heat Transfer Instrumentation on Injector ICC6 . . . . .	195
78.	Transient Temperature Response of the Backwall of Heated Strip Exposed to Burning $N_2O_4/50\%N_2H_4$ -50% UDMH . . . . .	208
79.	Face Pattern of Flintstone Injector Analyzed to Evaluate Injector Heat Transfer Model . . . . .	213
80a.	Layout of Injector Elements In and Around Flintstone Injector Segment Extending From R = 2.19 Inch to R = 3.00 Inch . . . . .	214
80b.	Layout of Injector Elements In and Around Flintstone Injector Segment Extending From R = 1.75 Inch to R = 2.19 Inch . . . . .	214
81.	Layout of Injector Elements In and Around Innermost Slice of Flintstone Injector Analyzed for Heat Transfer . . . . .	215
82a.	Layout of Injector Elements In and Around Flintstone Injector Segment Extending From R = 1.312 Inch to R = 1.75 Inch . . . . .	216
82b.	Layout of Injector Elements In and Around Flintstone Injector Segment Extending From R = .875 Inch to R = 1.312 Inch . . . . .	216
83.	Layout of Fuel Orifice Feed Passages Supplying Regenerative Cooling to Flintstone Injector Face . . . . .	218
84.	Face Heat Flux for a Surface Temperature of 3000 R Along 0-Degree Ray Corresponding to Fuel Orifices . . . . .	220
85.	Face Heat Flux for a Surface Temperature of 3000 R Along 5-Degree Ray Corresponding to Oxidizer Orifices . . . . .	220

86. Erosion of Flintstone Injector After Motor Firing at Chamber Pressure of 500 psia . . . . .	222
87. Face Heat Flux (Along 0 Degree Ray) for a Revised Surface Temperature of 2500 R . . . . .	224
88. Face Heat Flux (Along 5 Degree Ray) for a Revised Surface Temperature of 2500 R . . . . .	224
89. Face Pattern of Like-Douplet-Pair Injector LD-1 Showing Elements In and Around 22.5-Degree Chamber Slice Used in Analysis of FLOX/LPG Motor Firing Test No. 8 . . . . .	231
90. Comparison of Calculated Axial Heat Flux Profile for FLOX/LPG Motor Firing Test No. 8 With Circumferentially Averaged Experimental Results . . . . .	235
91. Variation of Launder Acceleration Parameter With Distance From Injector During FLOX/LPG Test No. 8 . . . . .	235
92. Comparison of Experimental Heat Flux Profile for FLOX/LPG Motor Firing Test No. 8 With Calculated Axial Profile Using Additional Allowance for Acceleration and With Simplified Bartz Correlation . . . . .	234
93. Face Pattern of Nineteen Element Triplet/Quadlet Injector Showing 30-Degree Slice Used to Analyze IRFNA/HYDYNE Motor Firing in an Ablative and Refractory Lined Regeneratively Cooled Thrust Chamber . . . . .	236
94. Thrust Chamber Wall Geometry for IRFNA/HYDYNE Motor Firing With Triplet/Quadlet Injector . . . . .	237
95. Variation of Wall Mixture Ratio and Adiabatic Wall Temperature With Angular Coordinate as Defined in Fig. 93 at the Nozzle Throat. . . . .	240
96. Variation of Wall Mixture Ratio and Adiabatic Wall Temperature With Angular Coordinate 3.96-Inch From Injector . . . . .	240
97. Erosion of Phenolic Refrasil Combustion Chamber During Motor Firing With IRFNA/HYDYNE Propellant Combination and Triplet Injector . . . . .	243
98. Face Pattern of Gas/Liquid Coaxial Element Injector Showing 15-Degree Slice Analyzed in $\text{GH}_2/\text{LO}_2$ Motor Firing . . . . .	246
99. Spray Mass Distribution Along the Boundary Rays of the 15-Degree Slice of Fig. 98 Used to Analyze Gas/Liquid Coaxial Injector . . . . .	249

# LIST OF TABLES

1.	Rocketdyne Cold-Flow Spray Distribution Data for the Unlike Doublet Element . . . . .	41
2.	Available Triplet Cold-Flow Spray Distribution Data for the Single Element Triplet . . . . .	49
3.	Like-Doublet-Pair Cold Flow Spray Distribution Data . . . . .	56
4.	Spray Coefficients for Rectangular Orifice Hiperthin Like Doublets Based Upon Cold-Flow Experiments . . . . .	65
5.	Summary of Single-Element Cold-Flow Data for Gas/Liquid Coaxial Elements . . . . .	72
6.	Summary of Correlated Mass Flow Parameters for Gas/Liquid Coaxial Elements . . . . .	72
7.	Summary of Single Element Cold Flow Experiments Performed to Determine Mass Distribution Characteristics . . . . .	162
8.	Results of Radial Spray Sampling Experiments With Multi-Element Injectors . . . . .	164
9.	Chamber Pressure Measurement Locations . . . . .	187
10.	Summary of Injector Face Heat Fluxes Measured With Unlike Doublet Injector ICC2A . . . . .	189
11.	Summary of Injector Face Heat Fluxes Measured With Triplet Injector ICC6 (Runs 34-86) . . . . .	192
12.	Summary of Local Static Pressure Distributions Measured With Unlike Doublet Injector ICC2A . . . . .	199
13.	Summary of Local Static Pressure Distributions Measured With Triplet Injector ICC6 (Runs 34-86) . . . . .	200
14.	Chamber Wall Heat Flux ( $\text{Btu/in}^2\text{sec}$ ) Obtained with Injector LD-1 . . . . .	228

# NOMENCLATURE

$a$	spray coefficient, sound velocity
$A$	area
$\bar{A}$	specific cross sectional area
$A^*$	throat area
$b$	spray coefficient
$B$	secondary breakup term
$c$	mixture ratio
$C^*$	characteristic exhaust velocity
$C_1, C_2, \dots, C_6$	spray coefficients
$C_1, C_{u_i}$	gas profile coefficients
$C_D$	drag coefficient
$C_p$	specific heat
$C_{KP}$	initial evaporation coefficient
$C_{PR}$	property correction factor
$C_{u_r}$	coefficient describing radial velocity effect on $h_g$
$D$	diameter, drag component
$\bar{D}$	mean drop diameter
$\vec{D}$	drag force vector
$E$	expected value
$E_m$	Rupe mixing efficiency index
$F$	collision force
$F_B$	fraction burned
$g_c$	conversion factor
$h$	heat transfer coefficient

H	enthalpy
$\Delta H_v$	latent heat of vaporization
$J_A$	hydraulic drop size conversion factor
$K_L$	Laundry acceleration parameter
k	thermal conductivity
$k'$	evaporation coefficient
L	chamber length
$\dot{m}$	droplet evaporation rate
M	Mach number
$M_E$	injected momentum of element E
$M_w$	molecular weight
N	droplet number concentration
$\dot{N}$	droplet number change
$N_{EL}$	number of elements
Nu	Nusselt number
p	pressure
P	pressure, point of contact, probability, perimeter
$P_o$	stagnation pressure
$PB_2$	percent vaporization of propellant 2
Pr	Prandtl number
q/A	heat flux
r	radial coordinate
R	universal gas constant, ratio of parameters
Re	Reynolds number
$\bar{R}$	radial momentum arm, rotation matrix
S	flow rate



St	Stanton number
T	temperature
u	velocity component (of gas if not otherwise specified), velocity component of particle in x direction
$\vec{u}$	vector velocity
$\bar{u}$	average velocity
U, $U_{inj}$	injection velocity
v	particle velocity component in y direction
V	injection velocity of coaxial element
w	weight flux, particle velocity component in z direction
$w_{001}$	normalization factor equivalent to weight flux at (x = 0, y = 0, z = 1)
W	collected mass
$w_{RED}$	weight flux reduced by vaporization
$w_{COLD FLOW}$	weight flux in cold flow experiment
We	Weber number
x	coordinate usually along fan of injector element spray pattern
X	element spacing in like-doublet pair
$X_{RD,RM}$	penetration factor for unlike doublet
$\bar{X}$	moment arm of collected mass in x direction
y	coordinate usually normal to fan of injector element spray pattern
$y_M$	resultant momentum line
$\bar{y}$	moment arm of spray flux in y direction
$\bar{Y}$	moment arm of collected mass in y direction

$Y$	$y$ component of injected propellant stream, fan spacing of like-doublet-pair
$z$	axial coordinate
$z'$	axial coordinate based upon pseudo impingement point
$\beta$	gas profile coefficient
$\gamma$	specific heat ratio, impingement angle
$\gamma_F$	fan cant angle for like-doublet-pair
$\delta$	coordinate displacement
$\epsilon$	eddy diffusivity
$\epsilon_C$	contraction ratio
$\eta_{C*}$	characteristic exhaust velocity (chamber pressure) efficiency
$\eta_{Mix}$	mixing limited efficiency
$\eta_{Vap}$	vaporization limited efficiency, fraction vaporized
$\theta$	angular coordinate, momentum thickness, rotation angle
$\mu$	viscosity, gas mixture ratio profile coefficient, particle mass
$\rho$	density
$\phi$	velocity potential, rotation angle
$\phi_T$	energy thickness
$\zeta$	shear stress
$\sigma$	surface tension
$\psi$	accommodation coefficient for vaporization

# SUBSCRIPTS

A	analytical, attachment point
AW	adiabatic wall
bulk	at the average mixture ratio
c	chamber, collection plane
$c_j$	center line of jet j
centerline	along the y axis
cup	in the cup of gas/liquid element
D, d	droplet
E	exit plane, experimental
F, fuel	fuel
g	gas
G	injected gas
H	heat
HG	hot gas
HW	based upon hot wax data
i	injector element i
is	theoretical for stream tube
j	mesh point j, drop group j, jet j
l, $\ell$	liquid
L	liquid of gas/liquid element
MST	multiple stream tube basis
o	reference, orifice, starting point
opposite	opposite side of like-doublet-pair fan

oxid	oxidizer
r	reference
s	stream tube
S	orifice
SAT	saturation
SST	single stream tube basis
same side	same side of like-doublet-pair fan
t	throat
ts	total of stream tube
W	wall
vap	vaporized
x	in the x direction
y	in the y direction
z	in the z direction
1, 2	orifices 1 and 2, thermocouple leads 1 and 2

#### SUPERSCRIPT

i	before collision
f	after collision
n	orifice index

## INTRODUCTION AND SUMMARY

In June 1970, Rocketdyne began a combined analytical and experimental project under Air Force Contract No. FO4611-70-C-0056 to extend and improve a previously developed computerized analysis of the effects of injector configuration upon thrust chamber wall compatibility and upon performance. The project was a continuation of an earlier effort under Air Force Contract FO4611-68-C-0043 (Ref. 1), during which this computerized analysis was developed. The original analysis was done with seven computer programs (LISP, PØT, 3D-CØMBUST, STRMTB, BLEAT, 3D-DEAP, and 2D-ABLATE) which calculated the spray patterns and gas flow field in a thrust chamber and, subsequently, the resultant heat transfer, charring, and erosion of ablative or refractory chamber walls. The objectives of the follow-on program were (1) to increase the range of injector element configurations over which liquid/liquid propellant systems could be adequately described by the analysis, (2) to develop an additional analysis for injector-face heat transfer, and (3) to extend the overall analysis to include gas/liquid injectors and other cooling methods.

The first phase of the project was directed toward the improvement of the LISP computer program which predicts the spray-mass and mixture-ratio distribution downstream of conventional impinging-stream injectors through the use of cold-flow-based empirical correlations. The spray distribution coefficients for unlike doublet, triplet, and like-doublet-pair single elements were obtained and correlated over a wider and more useful range. Correlations were also developed for the HIPERTHIN\* like doublet and the gas/liquid coaxial element from cold-flow data. A subsequent mass distribution model for the gas/liquid coaxial element, which included combustion effects, was also developed when the cold-flow model proved inapplicable to thrust chamber flow field calculations.

An injector-face convective heat-transfer model was developed based upon assumed forms of the velocity and mixture ratio profiles in the recirculating gas flow fields around the spray jets from arrays of injector elements. Necessary empirical coefficients were fitted from experimental data.

---

\*Aerojet-General trademark for a micro-orifice injector

Empirical coefficients in the model were evaluated from experimental data obtained during the project with doublet and triplet elements. The analysis was subsequently converted into a computer program (IHTM) for prediction of local injector-face heat transfer.

Three improvements were incorporated into the previous 3D-COMBUST computer program which calculates transverse spray migration and the three-dimensional gas flow field in the rapid combustion region a few inches downstream of the injector. These changes were: calculation of the effects of collisions between unlike propellant droplets upon mixture ratio, calculation of a nonuniform axial velocity distribution based upon a one-dimensional pressure field, and use of a variable  $k'$  spray evaporation model based upon local mixture ratio in the chamber.

Based upon the results of burning spray heat transfer experiments, the calculation of heat transfer at thrust chamber walls due to propellant spray impingement was simplified in the BLEAT computer program. Near injector film coefficients are now calculated on the basis of an injection Reynolds number; the unburnt spray at the wall is assumed to effect only the adiabatic wall temperature. The calculation of convective heat transfer further downstream was modified to make use of the Elliott-Bartz-Silver model based upon the buildup of the energy boundary layer thickness.

The analytical modeling and computer program development efforts were supported by cold-flow and model motor firing experimental programs.

Three series of cold-flow experiments were performed. During the first series, measurements were made of the spray distribution patterns produced by single-element unlike doublets, triplets, and HIPERTHIN like doublets. These measurements were made to allow development of correlations of spray coefficients for the LISP program. In the second series of cold-flow experiments, the overall spray distributions from multielement injectors were measured and, in particular, the amount of propellant spray impinging upon the chamber walls within 0.75 inch downstream of the injector. Results from these experiments indicated that backwash of spray near the injector face is minimal. The third series of experiments

was performed to measure recirculation gas velocities near the injector face which were predicted in the analytical model due to the aspiration effects of discrete spray jets. Although only a limited number of successful measurements were made during this test series, reverse gas velocities up to 65 ft/sec were measured.

A total of 86 model motor firings was made with two injectors (an 8-element unlike doublet and a 12-element triplet injector) and with the  $N_2O_4/50\% N_2H_4$ -50% UDMH propellant combination. These firings were made to measure injector-face heat transfer and, in addition, axial variation of static pressure. Tests were made over a mixture ratio range from 0.91 to 1.84 and a chamber pressure range from 46.6 to 472 psia. Chamber dimensions corresponded to contraction ratios of 1.04, 2.15, and 4.3, and chamber lengths of 8 and 16 inches. Local heat fluxes, varying from 0.75 to 7.2 Btu/in.<sup>2</sup>-sec, were measured on the injector face with electroformed heat flux transducers developed particularly for the program. Unfortunately, a large fraction of the transducers failed to function satisfactorily after manufacture so that only a limited number of usable transducers was obtained. Because of this, successful local heat flux measurements were made at only three locations on each injector face, which was insufficient to allow adequate demonstration of the analytical model for injector-face heat transfer.

A final series of experiments was performed to evaluate the heat transfer from an electrically heated metal strip to the impinging spray from a single doublet. Both water and the burning propellant combination  $N_2O_4/50\% N_2H_4$ -50% UDMH were tested in the open air to minimize gaseous convection.

Four demonstration analyses were performed with the system of computer programs to evaluate their usefulness as design tools. These analyses were: (1) the prediction of face heat transfer to a 338-element, like-doublet injector using the propellant combination  $ClF_3/M-20$  Fuel<sup>†</sup>; (2) prediction of performance and chamber wall heat transfer in a model motor test employing a 112-element, like-doublet-pair injector and the FLOX/55% methane-45% ethane fuel blend at a nominal mixture ratio of 3.75 and a nominal chamber pressure of 104 psia; (3) prediction of <sup>†</sup>80% hydrazine-20% monomethylhydrazine

conditions existing during a classified motor firing; and (4) prediction of wall heat transfer and performance for a 40-element gas/liquid coaxial-element injector employing the propellant combination  $\text{CH}_2/\text{LO}_2$  at a nominal mixture ratio of 6.0 and a nominal chamber pressure of 500 psia.

This report is subdivided into four major sections which respectively present:

- A brief review of the analytical model and the system of computer programs in their present form
- A description of the analytical studies made to extend the capabilities of the analytical model
- A description of the experimental studies done in support of the analytical effort
- The results from the four motor firing analyses made to demonstrate the computer programs



## MODEL FOR THRUST CHAMBER COMPATIBILITY AND PERFORMANCE ANALYSIS

The following brief review is presented to acquaint the new user with the basis of the various computer programs and to establish the background for the subsequent Analytical Studies section. A more detailed description of the model, as originally developed, is provided in Ref. 1.

### CHAMBER FLOW FIELD

As formulated previously (Ref. 1), the theoretical model to describe the combustion and flow processes in a liquid rocket thrust chamber is structured with the combustor and divided into the following three zones (shown in Fig. 1):

1. An injection/atomization zone in which the liquid propellants are atomized into spray, with the propellants being mainly confined to relatively discrete jets along the momentum vectors of the individual elements
2. A rapid combustion zone in which most of the liquid propellants are vaporized and reacted, and the resultant gases are distributed across the chamber by a transverse velocity field
3. An expansion region in which burning is completed under essentially "stream tube" flow conditions, and the gas is expanded to sonic, then supersonic velocities

The three zones represent regions in which different physical mechanisms (surface tension, interphase drag, inertia, gas-phase turbulence, etc.) are dominant. Therefore, different terms in the various differential and algebraic conservation and state equations which describe the flow field may be neglected when analyzing each region. Between the three-dimensional combustion gas flow field of Fig. 1 and the chamber walls is a thin boundary layer. Gradients in velocity, temperature, and composition in the boundary layer are functions of the local free stream conditions and the wall cooling method. These gradients, in turn, control the heat transfer, char rate, and erosion of the walls.

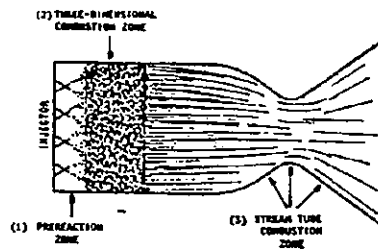


Figure 1. Separation of Combustion Chamber Into Zones for Analysis

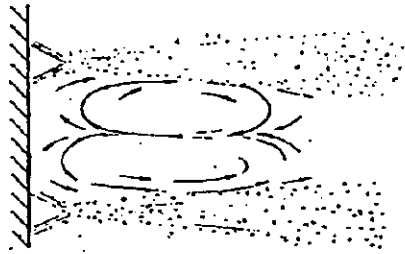


Figure 2. Recirculation Pattern Between Spray Jets in the Pre-reaction Zone

Therefore, the response of the walls is determined by the combustion processes in the three zones of the main flow field.

The injection/atomization zone immediately adjacent to the injector is least amenable to analytical description because of the large gradients with respect to propellant mass distribution which exist in all directions, as well as incomplete droplet atomization and (most probably) deviations from thermodynamic equilibrium for initially cold propellants. Nonetheless, at least a simplified model of the flow field in this region is necessary for prediction of injector face heat transfer. Therefore, a model was formulated for the gas flow field near the injector based on the assumed recirculation patterns shown in Fig. 2. These recirculation patterns in regions of low spray concentration are assumed to be driven by the aspiration effects of spray drag upon the combustion gas in regions of high drop concentration along with the global continuity requirements for low degrees of vaporization.

A description of the main gas flow field is obtained from the finite-difference (numerical) solution of a set of nonlinear differential and algebraic equations originally formulated by Sutton (Ref. 2). These relations represent the conservation of mass and momentum for the spray and gas phases as well as the state equation for the combustion gas at its local mixture ratio and appropriate expressions for the drag coefficients and evaporation rates of single droplets. The numerical calculations follow (in a marching fashion) the injected spray from the injector to the nozzle throat.

Employing the finite difference procedure, the chamber volume is divided into a sufficient number of nodes or mesh points so that the differences are representative of the gradients in temperature, flow, phase, and species concentration within the chamber. However, to be useful, the array of mesh points and associated variables must not require excessive computer core storage space or machine time in the calculations. To achieve a satisfactory compromise, the overall chamber volume as shown in Fig. 1 is usually subdivided into typical slices between planes of symmetry exhibited by the injector element pattern. For example, the solution

of a flow field downstream of the 45-degree chamber segment shown between rays OA and OC of Fig. 3, i.e., of the chamber slice shown in Fig. 4 is all that is required to completely describe the flow field downstream of the 36-element injector of Fig. 3 because all other 45-degree segments will be equivalent as mirror images of the first. It should be noted in Fig. 3 that additional injector elements outside the slice AOC should be considered in determining the spray concentration within the slice; however, the 13 elements inside the broken lines represent only one-third of the total injector elements and mesh points must be assigned to only one-eighth of the chamber cross section.

The mesh network employed in the 3D-COMBUST computer program, which performs the finite difference calculations describing the rapid combustion zone as shown in Fig. 4, is defined in terms of a cylindrical coordinate system  $(r, \theta, z)$  with the thrust chamber axis coinciding with the  $z$  axis. Either the injector face or the plane of the injection element impingement points is ordinarily chosen as  $z = 0$ , with the positive sense of  $z$  being in the direction of the bulk gas flow. The angular coordinate  $\theta$  is ordinarily referenced to the right hand boundary of the chamber slice being investigated, e.g., OC of Fig. 3 and 4 is chosen as  $\theta = 0$ .

The present version of the 3D-COMBUST program has computer storage space allotted for up to 105 mesh points in any  $z$ -plane. For simplicity in programming, the mesh points are defined for equal  $\Delta r$  and  $\Delta \theta$  intervals between adjacent mesh points. An example of a typical  $r, \theta$  mesh network for a given  $z$  plane in the rapid combustion zone is shown in Fig. 5.

In the stream tube combustion zone shown in Fig. 4, the flow is described by the STRMTB computer program with the flow in each stream tube being considered one-dimensional, i.e., no interchange of mass or energy is allowed between stream tubes. In this region, the conditions in only the stream tubes next to the wall directly affect the wall response. Therefore, it is convenient and sufficiently accurate to combine interior mesh points from the three-dimensional region, as typified by Fig. 5, into a limited number of large stream tubes while maintaining small stream tubes near the wall. Figure 6 shows an example of the combining or lumping of the mesh system of Fig. 5 into a useful stream-tube array. The STRMTB program is dimensioned to employ up to 40 stream tubes in a given calculation.

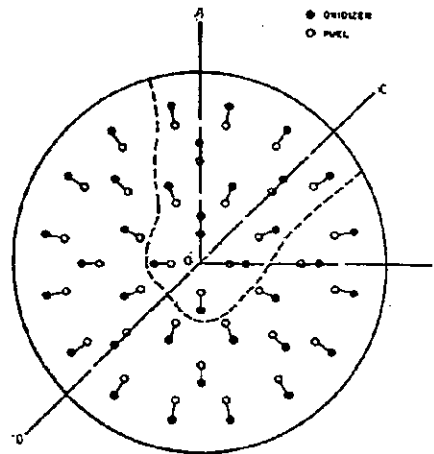


Figure 3 . Example of Injector Face Pattern to Show Use of Symmetry Considerations in Defining Thrust Chamber Mesh System

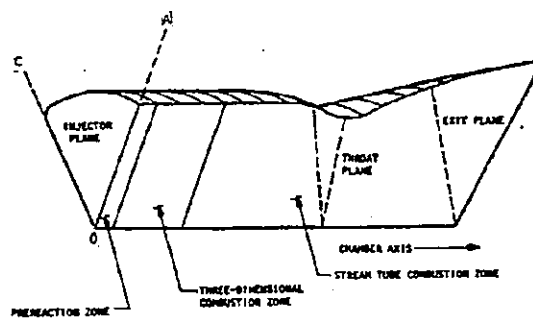


Figure 4. Slice of Thrust Chamber for Analysis as Determined From Symmetry Considerations

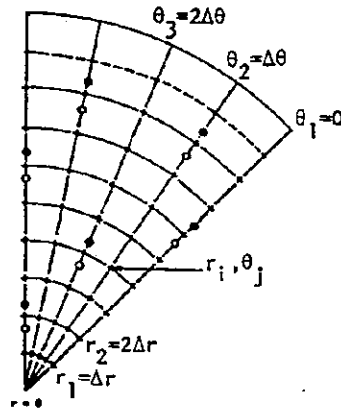


Figure 5. Network of Mesh Points for Finite Difference Solution of Conservation Equations by 3D-COMBUST Program

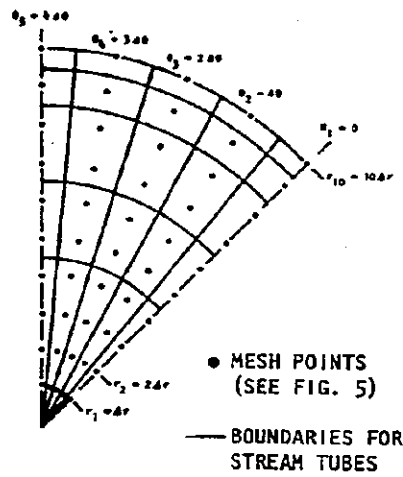


Figure 6. Conversion of Three-Dimensional Combustion Region Mesh System to Stream Tube Network

## INJECTION ATOMIZATION REGION

The injection atomization zone shown in Fig. 1 is described by two computer programs: Liquid Injector Spray Patterns (LISP) and Injector Heat Transfer Model (IHTM). The LISP program calculates the spray mass and mixture ratio distributions at the plane, downstream of the injector, chosen to start the marching combustion calculations. The IHTM program calculates the velocity, temperature, and mixture ratio distributions for the gas between the spray jets and then defines the local heat transfer coefficient distribution on the injector face.

### LISP COMPUTER PROGRAM

The LISP computer program calculates spray mass fluxes ( $\text{lbm/in.}^2 \text{ sec}$ ) at mesh points in the chosen plane ( $r, \theta, z_0$ ) by the straightforward summation of the mass fluxes from individual injector elements

$$w(r, \theta, z_0) = \sum_{i=1}^{N_{EL}} w_i(r, \theta, z_0) \quad (1)$$

a technique first used by Rupe (Ref. 3) to analyze the spray distributions in the Corporal engine. The method is considered to be effective when: (1) the individual injector elements have predictable spray flux patterns which can be measured and correlated; (2) the individual spray patterns of the various elements are not destroyed between the element impingement points and the plane  $z_0$  by collisions between neighboring fans; and (3) there is limited vaporization of injected spray mass between the element impingement points and plane  $z_0$  such that the uncertainty in vaporized spray mass is 10 percent or less of the total injected spray mass. These requirements are usually met when the liquid jets are fully turbulent, i.e., the element orifices have sufficient length/diameter ratio and surface roughness to provide fully developed turbulent velocity profiles in the impinging liquid streams, and, in addition, the plane  $z_0$  is on the order of 1 to 2 inches downstream of the injector.

The use of Eq. 1 to calculate the total spray flux at a position  $(r, \theta, z)$  requires relationships for the spray flux  $w_i$  from each individual element. Based upon the general shape of the mass flux distributions observed in single element cold-flow experiments with doublets, triplets, and four-on-one (pentad) elements, the following expression with several constants to be empirically determined has been chosen to describe  $w_i$

$$w_i(x, y, z) = \frac{w_{001}}{z^2} \left\{ \left[ 1 + C_1 \left(\frac{y}{z}\right) + C_2 \left(\frac{y}{z}\right)^2 \right] + \left[ C_3 \left(\frac{x}{z}\right) + C_4 \left(\frac{x}{z}\right)^2 \right] \right. \\ \left. \left[ 1 + C_5 \left(\frac{y}{z}\right) + C_6 \left(\frac{y}{z}\right)^2 \right] \right\} e^{-a \left(\frac{x}{z}\right)^2 - b \left(\frac{y}{z}\right)^2} \quad (2)$$

Equation 2 is applied separately to each propellant from an element. The  $(x, y, z)$  coordinate system used in Eq. 2 is referenced to the impingement point of the element. The empirical coefficients  $a, b, w_{001}$  and  $C_1$  through  $C_6$  are functions of such parameters as element type (doublet, triplet, etc.) impingement angle, orifice diameter, impinging stream momenta, orifice length, and manifold effects. The form of Eq. 2 was chosen because it satisfies continuity, predicts the observed inverse square relationship between mass flux and distance from the impingement point, and because closed form integrals of Eq. 2 and its  $x$  and  $y$  moments over the  $x, y$  plane allow straightforward evaluation of the empirical coefficients from experimental cold-flow data.

Although, this spray correlation equation with its nine coefficients is unwieldy to use even in a computerized calculation, the expression usually may be simplified so that the form of Eq. 2 generally serves only to provide the total computer core allocation. For the usual injector element types (doublet, triplet, etc.), requirements for fan symmetry and a spray mass flux that must be positive for  $z$  greater than zero specifies that many of the coefficients must be either zero or related to other coefficients. For example, with the like doublet the coordinate system shown in Fig. 7 leads to a much simpler expression,

$$w(x, y, z) = \frac{w_{001}}{z^2} \left[ 1 + C_4 \left(\frac{y}{z}\right)^2 \right] e^{-a \left(\frac{y}{z}\right)^2 - b \left(\frac{y}{z}\right)^2} \quad (3)$$



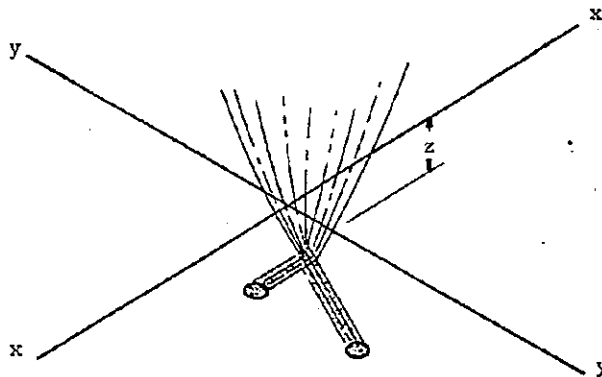


Figure 7. Single Like Doublet Element Coordinate System

Because at least one of the coefficients (ordinarily  $w_{001}$ ) can be eliminated by the requirement for global continuity of the total flowrate from the element (lbm/sec), only three spray coefficients,  $a$ ,  $b$ , and  $C_4$ , are actually required to describe the distribution of flow from a like doublet\*.

In its present form, the LISP model considers that conventional injector elements can be classified in terms of nine types:

1. Unlike doublet
2. Like doublet
3. Like-doublet-pair
4. Triplet
5. Four-on-one (Pentad)
6. Gas/liquid coaxial element
7. Showerhead
8. Special callout by general spray flux equation
9. Gas transpiration cooled injector face

---

\*The expression for mass flux from a like doublet is actually even simpler because in correlating experimental cold-flow data, coefficient  $C_4$  is set equal to  $a$ .

The general shape of the spray mass flux distributions and the coordinate reference frames (x,y,z) defined in LISP for the unlike doublet, the like-doublet-pair, the triplet, and the four-on-one element are shown in Fig. 8 through Fig. 10 . The mass flux distributions for the Type 6 gas/liquid coaxial element and the Type 7 showerhead element are naturally axisymmetric about the element axis. Employing symmetry, the generalized correlation presented by Eq. 2 reduces to the following expressions for the Type 1 through Type 7 elements:

Unlike Doublet (same equation form for either orifice)

$$w = \frac{w_{001}}{z^2} \left\{ \left[ 1 + C_1 \left(\frac{y}{z}\right) + \frac{C_1^2}{4} \left(\frac{y}{z}\right)^2 \right] + C_4 \left(\frac{x}{z}\right)^2 \left[ 1 + C_5 \left(\frac{y}{z}\right) + \frac{C_5^2}{4} \left(\frac{y}{z}\right)^2 \right] \right\} e^{-a \left(\frac{x}{z}\right)^2 - b \left(\frac{y}{z}\right)^2} \quad (4)$$

Triplet (outer orifice, 1)

$$w = \frac{w_{001}}{z^2} e^{-a \left(\frac{x}{z}\right)^2 - b \left(\frac{y}{z}\right)^2} \quad (5a)$$

Triplet (inner orifice, 2)

$$w = \frac{w_{001}}{z^2} \left[ 1 + C_4 \left(\frac{x}{z}\right)^2 \right] e^{-a \left(\frac{x}{z}\right)^2 - b \left(\frac{y}{z}\right)^2} \quad (5b)$$

Four-on-One (same relation for both orifices)

$$w = \frac{w_{001}}{z^2} \left[ 1 + C_4 \left(\frac{y}{z}\right)^2 \right] \left[ 1 + C_4 \left(\frac{x}{z}\right)^2 \right] e^{-a \left[ \left(\frac{x}{z}\right)^2 + \left(\frac{y}{z}\right)^2 \right]} \quad (6)$$

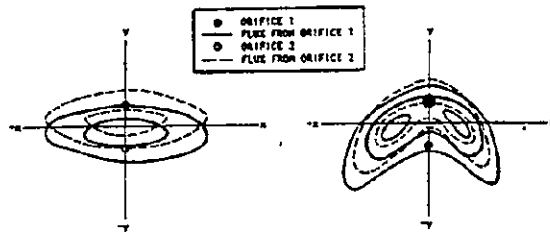


Figure 8a. Mass Flux Contours for Doublet With Equal Diameters and Equal Stream Momenta

Figure 8b. Mass Flux Contours for Doublet With Unequal Diameters and Equal Overall Stream Momenta

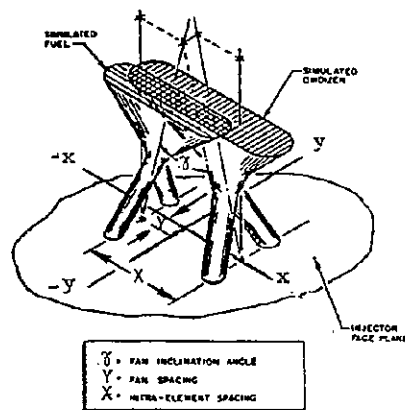


Figure 9. Geometric Factors Affecting the Propellant Distribution for Like-Doublet-Pair Injector Elements

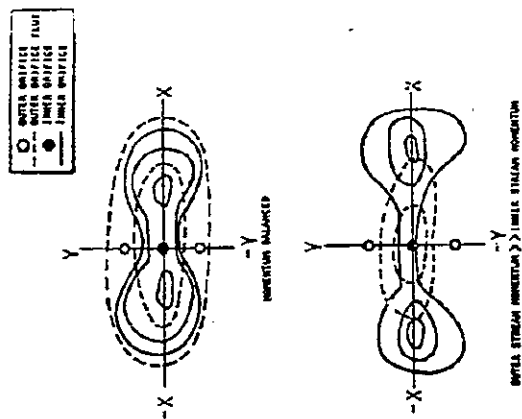


Figure 10a Spray Mass Flux From Single Triplet Injector Element

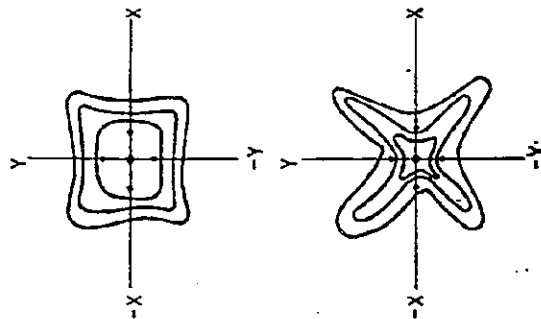


Figure 10b Spray Flux Pattern for Four-on-One Element at Moderate and High Momentum Ratios

Like-Doublet-Pair (same relation for both orifices)

$$w = w_{001} e^{-a \left(\frac{x}{z}\right)^2 - b \left(\frac{y}{z}\right)^2} \quad 0 < x \quad (7a)$$

$$w = w_{001} e^{-a \left(\frac{x}{z}\right)^2 - b \left(\frac{y}{z}\right)^2} \quad x < 0 \quad (7b)$$

Gas/Liquid Coaxial (same relation for both orifices, cold-flow basis)

$$w = \frac{w_{001}}{z^2} \left\{ 1 + C_4 \left[ \left(\frac{x}{z}\right)^2 + \left(\frac{y}{z}\right)^2 \right] \right\} e^{-a \left[ \left(\frac{x}{z}\right)^2 + \left(\frac{y}{z}\right)^2 \right]} \quad (8)$$

Gas/Liquid Coaxial (annular gas orifice, hot-fire basis)

$$w = \frac{w_{001}}{z^2} e^{-a \left[ \left(\frac{x}{z}\right)^2 + \left(\frac{y}{z}\right)^2 \right]} \quad (5a)$$

Showerhead

$$w = \frac{w_{001}}{z^2} e^{-a \left[ \left(\frac{x}{z}\right)^2 + \left(\frac{y}{z}\right)^2 \right]} \quad (5a)$$

The actual methods used to evaluate the spray coefficients in the simplified distribution equations are discussed in the Analytical Studies section of this report. Correlated values of the spray coefficients for Type 1 through Type 6 elements in terms of their controlling parameters (orifice diameters and diameter ratios, impinging stream momentum ratios, jet impingement angles, etc.) are stored in the subroutines of the LISP computer program, the stored values being restricted to the range of these parameters for which cold data are available. The Type 7 showerhead element was found to exhibit such a narrow mass distribution

profile around its element centerline that it was impractical to develop correlations for it to be used in finite difference calculations. The Type 8 and Type 9 elements represent special cases. The Type 8 element is provided to give the user the maximum flexibility in setting up a problem. The total flow from the element is calculated as if the element were a doublet with equivalent orifice diameters, and the mass flux distribution is calculated by means of Eq. 2. However, spray coefficients for the Type 8 element are supplied directly as input data rather than being supplied by subprograms within LISP. This feature permits the designer to develop a cold-flow characterization of the element (or elements) to be incorporated into a prospective injector and then employ the correlated experimental spray coefficients directly in LISP. This procedure is useful not only when spray coefficients are not available in LISP, but also when such factors as short L/D and manifold crossflows are important because such effects may be included in the supplemental single-element experiments. Mass flux from the Type 9 (rigimesh transpiration cooling) element is not calculated in LISP by means of Eq. 2, but is treated as being uniformly distributed over the injector face and the cross section of the chamber under consideration.

Because the burning rate calculations of the 3D-COMBUST and STRMTB combustion programs require specification of drop diameters, an option is included in the LISP program to calculate a mean drop diameter for Type 1 through Type 5 elements. The volume mean diameter  $D_{30}$  is calculated from Dickerson's correlations (Ref. 4) which have the general form

$$D_{30} = C \prod_n D_{o_n}^{2n} U_D^{m_n} \quad (9)$$

and is based on drop size measurements in hot wax experiments.

The drop diameter required for use in the combustion calculations must be modified from the hot wax average diameter because of secondary breakup from gas/drop shear and interfan droplet collisions. The combustion drop diameter used in the combustion calculations is obtained from Falk's method (Ref. 5), i.e.,

$$\bar{D} = \frac{1}{J_A/D_{30} + B} \quad (10)$$

where B is the secondary breakup term which is about a linear function

of the relative velocity between the gas and liquid ( $\Delta V$ ) and, thus, primarily of the contraction ratio. The relations currently used in the LISP program are tabulated later in the report. The drop diameters defined by Eq. 9 and 10 apply to the flow from individual elements. The average drop diameters at the various  $(r, \theta)$  mesh points in plane  $z_0$  used in the calculations are the mass-flux weighted means of the drops from all elements whose spray impinges upon point  $(r, \theta, z_0)$ .

Mass-weighted drop velocity vectors are calculated at each  $(r, \theta, z)$  mesh point based upon the assumptions that (1) the injection kinetic energies of the drops are conserved and (2) the drops travel along rays (straight lines) from the element impingement points. With these assumptions, the velocity component  $u_{Dx}$  for drops from element  $i$  at  $(x, y, z)$  in the coordinate system of element  $i$  is given by

$$u_{Dx} = \frac{x}{\sqrt{x^2 + y^2 + z^2}} u_D$$

with analogous expressions for  $u_{Dy}$  and  $u_{Dz}$ .

In addition to calculating mass fluxes and drop sizes on a cold-flow basis, a "combustion-reduced" mass flux is calculated on the basis of the simplified droplet burning relation

$$W_{RED} = W_{COLD FLOW} \left[ 1 - \frac{0.0833 C_{KP} \Delta z}{D_D^2 u_{Dz} \rho} \right]^{3/2} \quad (11)$$

which was obtained by integration over  $\Delta z$  of a simplified version of the  $k'$  evaporation model. Corresponding reduced droplet diameter is calculated from the following:

$$\frac{D_{RED}}{D_{COLD FLOW}} = \left( \frac{W_{RED}}{W_{COLD FLOW}} \right)^{1/3}$$

The accumulation of spray on chamber walls and baffle surfaces is accounted for by introducing (folding in) spray from additional mesh lines defined outside the actual chamber slice boundaries. Spray calculated to impinge on such "extra" mesh lines in a plane  $z_i$  is, in the real chamber, physically stopped by chamber walls upstream of  $z_i$  and flows along the wall to the  $z_i$ -plane wall mesh points. Assuming that angular spray velocities are unaffected by the wall, these folding calculations should be physically correct.

A logic diagram for the LISP computer program, lists of subroutines, and input and output data are presented in the Analytical Developments Section.

#### INJECTOR HEAT TRANSFER MODEL

The Injector Heat Transfer Model (IHTM) was formulated to analytically describe the local heat transfer rate to the injector face. A description of the combustion and gas circulation in the near-injector region where the spray exists as relatively discrete jets is required. This region extends, presumably, from the injector face to a distance somewhere between 0.5 and 1.5 inches downstream of the injector, the distance depending upon such factors as orifice diameter, element type, jet impingement distance, injection velocity, and chamber contraction ratio. Analysis of this gas flow field has been structured in the same general fashion as the LISP program for the spray distribution.

This approach, namely a linear summation of contributions from each injector element, represents a simplification of the actual physical system but, nonetheless, provides a systematic method by which empirical data for single elements or simple arrays of elements can be used for a general computerized analysis. Such an approach is similar to that used for the overall injector chamber compatibility analytical model, and it provides a flexible framework for utilizing the separate results from basic experimental studies of the various combustion processes in a simple manner which is theoretically consistent to the degree that a partially "linearized" treatment of a nonlinear problem can be. It is expected that a later improvement of the Injector Heat Transfer Model will be possible after experience in its application is obtained along with additional experimental data.



The physical model for the region close to the injector considers the gas flow to be driven by the pumping action of the injected liquid streams. Two types of such recirculating gas flows are considered. The first is inter-element recirculation pattern as shown in Fig. 11a and the second is inter-jet recirculation within a single element as shown in Fig. 11b. A combination of both types is naturally also possible; in fact, the real flow in the injector region is probably comprised of both. The effect of the inter-jet recirculation is probably not important in the case of like doublets, but may contribute substantially to injector erosion problems when unlike doublets are employed or when one of the propellant vapors is unusually reactive with the injector surface.

Numerical solution of the continuity, momentum and energy relationships for the gas flow field and the injector heat transfer was not considered appropriate due to the complexity of the three-dimensional, two-phase flow equations. Instead, a version of the integral boundary layer technique was used to obtain the velocity and concentration profiles in the near-injector region. With the integral boundary layer technique, functional relationships containing undetermined constants are assumed for the axial gas velocity distribution and the concentration distribution. Some of the constants in these relationships are determined from requirements for continuity of mass and from boundary conditions. The remaining constants in the relationships have been determined from experimental data.

The injector face heat flux is calculated from

$$\frac{q}{A} = k \left. \frac{\partial T}{\partial z} \right|_{z=0} \quad (12)$$

where the normal temperature gradient is obtained from the energy equation. At the present time, the IHTM computer program uses the one-dimensional energy equation

$$\frac{\partial}{\partial z} \left[ (k + \epsilon \rho C_p) \frac{\partial T}{\partial z} \right] = \rho C_p u_z \frac{\partial}{\partial z} (T - T_E) \quad (13)$$

to calculate the temperature profile near the injector face.

Further details of the analytical model are developed in the Analytical Studies section.

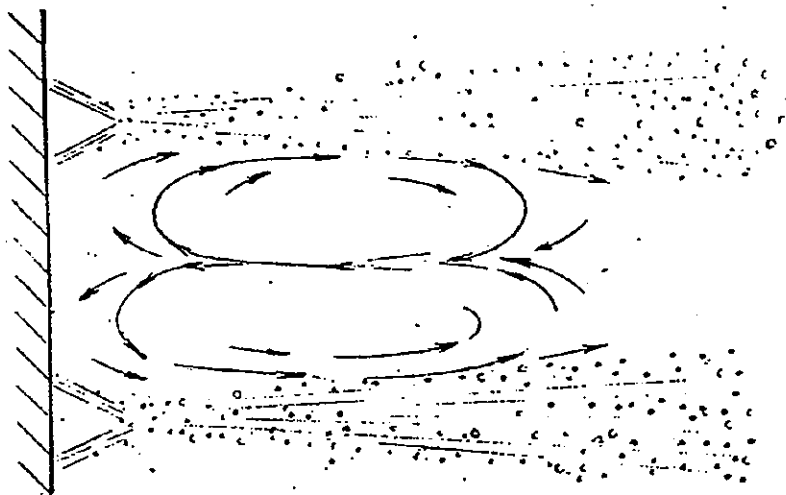


Figure 11a Interelement Recirculation Pattern

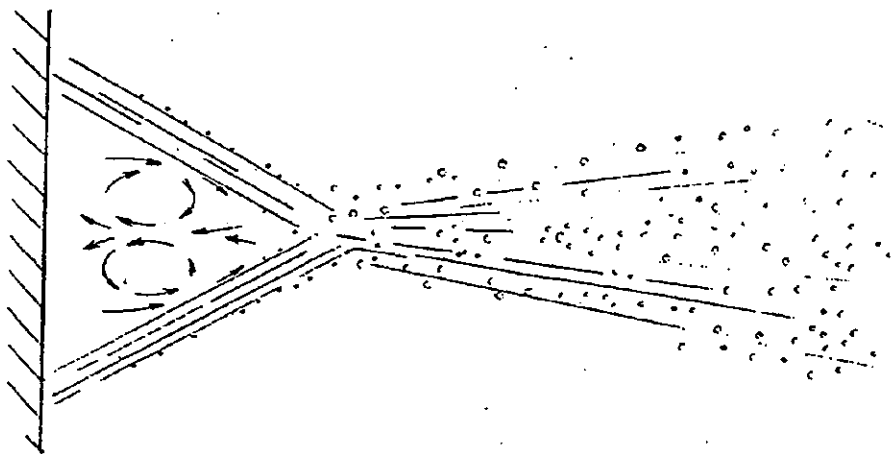


Figure 11b Interjet Recirculation Pattern

## COMBUSTION MODELS

### 3D COMBUST COMPUTER PROGRAM

The theoretical model for the rapid combustion and mixing zone as shown in Fig. 1 is based upon the specialization to a cylindrical coordinate system of a general analytical formulation for multiphase reacting flows developed under another Air Force contract (Ref. 2). The combustion model consists of two sets of algebraic and partial differential equations describing the conservation of mass and (to the greatest degree possible) of momentum and energy for the gas and liquid spray phases. The two sets of equations are linked by drag and evaporation coupling terms.

For the gas phase, the theoretical model employs an overall mass continuity relation,

$$\frac{\partial}{\partial r} (r \rho u_r) + \frac{\partial}{\partial \theta} (\rho u_\theta) + \frac{\partial}{\partial z} (r \rho u_z) = \frac{r}{12} \sum_{n,j} \dot{m}_j^n \quad (14)$$

A mixture ratio (species) continuity relation,

$$\frac{\partial}{\partial r} (r \rho c u_r) + \frac{\partial}{\partial \theta} (\rho c u_\theta) + \frac{\partial}{\partial z} (r \rho c u_z) = \frac{r}{12} \left[ (2c+1) \sum_n \dot{m}_{\text{oxid}}^n - c^2 \sum_n \dot{m}_{\text{fuel}}^n \right] \quad (15)$$

and the axial momentum equation

$$\begin{aligned} \frac{\partial}{\partial z} (r \rho u_z^2) + \frac{\partial}{\partial r} (r \rho u_r u_z) + \frac{\partial}{\partial \theta} (\rho u_\theta u_z) = \frac{r}{12} \left[ -g_c \left( \frac{\partial p}{\partial z} + \sum_{j,n} \vec{D}_{zj}^n \right) + \right. \\ \left. \sum_{j,n} \dot{m}_j^n u_{dzj}^n \right] + F_{j,j_2} + \frac{\mu}{144} \left[ \frac{\partial}{\partial r} \left( r \frac{\partial u_z}{\partial r} \right) \right] + \frac{\mu}{144} \left[ \frac{1}{r} \frac{\partial^2 u_z}{\partial \theta^2} \right] \quad (16) \end{aligned}$$

along with the state and the adiabatic energy relations

$$T = T_o \left[ 1 - \frac{Y-1}{2} M_o^2 \right] \quad (17)$$

$$p = \frac{12\rho RT}{M_w} \quad (18)$$

These equations are used to define local values of the six variables  $u_z$ ,  $u_r$ ,  $u_\theta$ ,  $c$ ,  $p$ , and  $T$ . Because there are only five relations available to define the six desired unknowns, the overall continuity relation expressed by Eq. 14 is actually modified to

$$\frac{\partial}{\partial r} \left( r \rho \frac{\partial \phi}{\partial r} \right) + \frac{\partial}{\partial \theta} \left( \frac{\rho}{r} \frac{\partial \phi}{\partial \theta} \right) + \frac{\partial}{\partial z} (r \rho u_z) = \frac{r}{12} \sum_{n,j} \dot{m}_j^n$$

$$u_\theta = \frac{1}{r} \frac{\partial \phi}{\partial \theta}, \quad u_r = \frac{\partial \phi}{\partial r}$$

which implies that a velocity potential is assumed to exist for the transverse velocities due to the unequal local generation of gas by evaporation of nonuniformly distributed spray. The use of this velocity potential for transverse velocities is, therefore, equivalent to the assumption made in the usual stream tube analysis that flow distributes itself over a given cross section of the flow field so as to satisfy axial momentum relations and global continuity.

The theoretical model considers drops of each propellant and different size groups of the same propellant to be distinguishable (separate) phases. Descriptive equations for each droplet phase (denoted by the subscript  $j$ ) include:

Conservation of spray mass

$$\frac{\partial}{\partial r} \left( r \rho_{d,j}^n u_{d,r,j}^n \right) + \frac{\partial}{\partial \theta} \left( \rho_{d,j}^n u_{d,\theta,j}^n \right) + \frac{\partial}{\partial z} \left( \rho_{d,j}^n u_{d,z,j}^n \right) = - \frac{r}{12} \dot{m}_j^n \quad (19)$$

Continuity of droplet numbers

$$\frac{\partial}{\partial r} \left( r u_{d,r,j}^n N_{d,j}^n \right) + \frac{\partial}{\partial \theta} \left( u_{d,\theta,j}^n N_{d,j}^n \right) + \frac{\partial}{\partial z} \left( u_{d,z,j}^n N_{d,j}^n \right) = 0 \quad (20)$$

and momentum conservation equations in the z, r, and  $\theta$  directions as typified by the z-momentum relation

$$\begin{aligned} \frac{\partial}{\partial z} \left[ \rho_{d_j}^n \left( u_{dz_j}^n \right)^2 \right] + \frac{\partial}{\partial r} \left[ r \rho_{d_j}^n u_{dr_j}^n u_{dz_j}^n \right] + \\ \frac{\partial}{\partial \theta} \left[ \rho_{d_j}^n u_{d\theta_j}^n u_{dz_j}^n \right] = \frac{r}{12} \left[ g_c \overrightarrow{D}_{z_j}^n - \dot{m}_j^n u_{dz_j}^n \right] \end{aligned} \quad (21)$$

Droplet mass and number concentrations are related by

$$\rho_{d_j}^n = N_{d_j}^n \frac{\pi}{6} \left( d_{d_j}^n \right)^3 \rho_{\ell_j}$$

while the spray and gas phases are coupled through the drag and evaporation relations:

$$\overrightarrow{D}_j^n = \left( \overrightarrow{u} - \overrightarrow{u}_{d_j}^n \right) \left[ \left( \frac{12}{g_c} \right) \left( \frac{\pi}{8} \right) N_{d_j}^n \rho \left( d_{d_j}^n \right)^2 C_{D_j}^n \left| \overrightarrow{u} - \overrightarrow{u}_{d_j}^n \right| \right] \quad (22)$$

$$\dot{m}_j^n = N_{d_j}^n \left( \frac{\pi}{8} \right) \rho_{\ell_j} d_{d_j}^n \left( Nu \right)_j^n \left( k'_g \right)_j^n \quad (23)$$

where the  $k'$  evaporation coefficient is given by

$$k'_g = \frac{8}{\rho_{\ell}} \int_{T' = T_{\ell}}^T \frac{k_g(T')}{\left[ \Delta H_v + \int_{T''=T_{\ell}}^T C_{p_v}(T'') dt'' \right]} dT' \quad (24)$$

This system of partial differential equations is solved by a finite difference technique in a marching fashion from a starting plane  $z_0$  where conditions are defined by the LISP computer program to a final plane,  $z_{ST}$ , where the calculation is transferred to STRMTB, stream tube combustion program. In a mesh system of regular  $\Delta r$  and  $\Delta \theta$  spacings (Fig. 5), central finite difference approximations are used around the point  $r, \theta$ , e.g.,

$$\frac{\partial U}{\partial r} = \frac{U_{r+\Delta r} - U_{r-\Delta r}}{2\Delta r}$$

$$\frac{\partial U}{\partial \theta} = \frac{U_{\theta+\Delta \theta} - U_{\theta-\Delta \theta}}{2\Delta \theta}$$

and backward difference partial approximations are used in the z direction at plane  $z_2$  and r,  $\theta$ , e.g.

$$\left. \frac{\partial U}{\partial z} \right|_{r,\theta,2} = \frac{U_{r,\theta,2} - U_{r,\theta,1}}{z_2 - z_1}$$

Predictor/corrector techniques are used at each z plane in the marching calculations. In the predictor cycle the phase-coupling terms and the coefficients for the various derivatives are defined at the previously calculated points  $(r,\theta,z = z_1)$  and in the corrector these are updated to the current values at  $(r,\theta, z = z_2)$ . The system of  $(m \times n)$  linear difference (algebraic) equations in m unknowns and n mesh points is solved through use of matrix methods which take advantage of the fact that the coefficient matrix for the system of equations is tridiagonal in form, i.e., the non-zero elements lie essentially on the three main diagonals. Three matrix routines, BAND, ABAND, and TRIDI are employed to solve the gas-phase continuity, gas-phase axial momentum, or gas-phase mixture ratio and spray-phase equations, respectively.

As discussed later in the Analytical Developments section of this report, the chamber pressure is assumed to be only a function of the z coordinate and spray migration is assumed to be a function not only of interphase drag, but also of droplet collisions.

A logic diagram for the 3D-COMBUST program together with a list of subroutines and the input and output data are presented in the Analytical Developments Section.

#### STREAM TUBE COMPUTER PROGRAM (STRMTB)

Analysis with the preceding three-dimensional combustion model is moderately expensive, particularly if multiple drop size groups are defined for each propellant. Therefore, the overall combustion analysis is structured for use of the three-dimensional model over as short a portion of the combustor length as possible and subsequent use of a simpler model for analysis of continued combustion further downstream. This model maintains differences in local mass and mixture ratio existing at the end of the 3D-COMBUST region, but utilizes the simplifying assumptions of one-dimensional flow in the stream tubes formed by lumping mesh points of the 3D-COMBUST region as depicted in Fig. 6 .

As implied by the name "stream tubes," propellant flows (both sprays and combustion gases) which initially enter a stream tube are, thereafter, constrained to flow in that tube; no provisions are made for exchange of mass, momentum, or energy among neighboring stream tubes. Flow within each stream tube is treated as one-dimensional by further specialization of the three-dimensional model equations to a single dimension. The model formulation, therefore, parallels the three-dimensional formulation; the same nomenclature is used except that directional subscripts ( $r$ ,  $\theta$ ,  $z$ ) are dropped and a subscript ( $s$ ) has been added to denote stream tube indexing. The stream tube equations, being one-dimensional, are ordinary differential equations. When converted to finite difference form, they are similar to the system of equations programmed in earlier one-dimensional liquid spray combustion models; hence, the computer programming was structured along lines paralleling those existing programs.

In the one-dimensional conservation equations, cross-sectional flow area,  $A_s(z)$ , appears as an explicit variable. Most prior one-dimensional combustion models have been based on this being a known, independent variable (chamber area or some proportionate function of it). In the multiple stream tube formulation,  $A_s(z)$  appears as a dependent variable for which a solution must be found. Individual stream tube areas can vary, however, only under the constraint that the sum over all stream tubes must equal the local chamber cross-sectional area. This constraint couples the stream tube solutions together. A second constraint (assumed in order to close the problem) is that pressure is constant across any  $z$ -plane cross section.

The stream tube conservation relations for total mass and z-momentum of the respective gas and spray phases corresponding to relations in Eq.14, 16, 19, and 21 are:

1. Gas Phase Continuity

$$\frac{d}{dz} (\rho_s u_s A_s) = \frac{A_s}{12} \sum_{n,j} (\dot{m}_j^n)_s$$

2. Gas Phase Momentum

$$\frac{d}{dz} (\rho_s u_s^2 A_s) = \frac{A_s}{12} \left[ -g_c \left( \frac{dp}{dz} \right) + \sum_{j,n} (\overline{D}_j^n)_s + \sum_{j,n} (\dot{m}_j^n)_s (u_{dj}^n)_s \right]$$

3. Spray Phase Continuity (for a particular drop group)

$$\frac{d}{dz} \left[ (\rho_{dj}^n)_s (u_{dj}^n)_s A_s \right] = - \frac{A_s}{12} (\dot{m}_j^n)_s$$

4. Spray Phase Momentum (for a particular drop group)

$$\frac{d}{dz} \left[ (\rho_{dj}^n)_s (u_{dj}^n)_s^2 A_s \right] = \frac{A_s}{12} \left[ g_c (\overline{D}_j^n)_s - (\dot{m}_j^n)_s (u_{dj}^n)_s \right]$$

The relations for temperature and pressure are the same as Eq. 17 and 18 and, as in the 3D-COMBUST program, such properties as stagnation temperature, molecular weight, viscosity, and specific heat ratio are considered to be single-valued functions of mixture ratio, i.e., no Mach number corrections are applied to properties evaluated at stagnation conditions. In addition, the relations for inter-phase drag and droplet evaporation rate are equivalent to Eq. 22 through 24 of the 3D-COMBUST formulation.

The stream tube and three-dimensional models differ in the formulation of the mixture ratio continuity equations which, in the case of the stream tube program, is simply



$$\dot{m}_{js}(z) = \dot{m}_{js}(z_0) + \int_{z'=z_0}^z \sum_n \left( \dot{m}_j^n \right)_s dz'$$

in place of three dimensional Eq. 15 . In addition, the area continuity relationship is introduced, i.e.,

$$\sum_s A_s = A_c$$

The most significant difference between models, however, occurs in the equations for droplet number continuity. If a polydisperse spray is included (more than one drop size group for each propellant, the total number of drops in each stream tube are conserved by the relation

$$\left( \dot{N}_{dj}^n \right)_s = 12 \left( N_{dj}^n \right)_s \left( u_{dj}^n \right)_s A_s = \text{constant}$$

which is analogous to Eq. 20 in the 3D-COMBUST model.

However, an alternative formulation, used if monodisperse sprays are input, has droplet diameters held constant,  $\left( d_{dj}^n \right)_s = \text{constant}$ , and the spray droplet number flowrates are reduced to account for gasification:

$$\frac{d}{dz} \left[ \left( \dot{N}_j^n \right)_s \right] = - \frac{A_s \left( \dot{m}_j^n \right)_s}{\left( \frac{\pi}{6} \right) \rho_{lj} \left( d_{dj}^n \right)_s^3}$$

The stream tube model, like any rocket combustion model, must satisfy a downstream boundary condition in the form of sonic surface near the nozzle throat. With one-dimensional models, this is customarily considered to be a planar surface at the throat. The throat boundary condition is not imposed during the numerical solution of the equations, but is invoked by comparing the calculated gas velocity at the

throat to calculated local static sound speed there. Rather than require precise equality, an acceptable error,  $\epsilon$ , is defined. If  $|u_t - a_t| > \epsilon$ , inconsistent initial plane conditions have been used, so an adjustment is made in either initial propellant flowrates or chamber pressure and the entire model calculations are repeated until  $|u_t - a_t| < \epsilon$ .

There is nothing in the formulation of the stream tube model, to prevent one or more stream tubes from flowing sonic while others are still subsonic; consequently, matching the nozzle throat boundary condition is somewhat nebulous. Two features appear in the model to ensure a close approximation. The first requires that if any stream tube that goes sonic upstream of the geometric nozzle throat the flow is subsequently constrained to continue at its local sound speed to the throat. If these gas velocities are not constrained, these streams go supersonic, but the pressure is too high so, according to continuity of mass, their areas decrease. This leaves more flow area for the subsonic flows so that they are under-accelerated and the pressure remains high, leading to computational instabilities. The second feature is the use of an averaged, single stream tube analysis, with iterations for adjusting the initial plane conditions to satisfy, on a one-dimensional basis, the throat sonic flow condition, prior to performing any multiple stream tube calculations. A further refinement is a multiple stream tube starting pressure defined by

$$\left[ p(z_0) \right]_{MST} = \left[ p(z_0) \right]_{SST} \left[ \frac{\sum_s c_{is}^* \dot{w}_{ts}}{c_i^* \sum_s \dot{w}_{ts}} \right]$$

where  $\dot{w}_{ts}$  is a stream tube total propellant flowrate,  $c_{is}^*$  is its theoretical characteristic velocity determined simply from its injection mixture ratio,  $c_{is}$ :

$$c_{is}^* = c^*(c_{is})$$

and  $c_i^*$  is similarly the theoretical  $c^*$  evaluated at overall engine injection mixture ratio. The bracketed term is just a mixing inefficiency corresponding to complete spray gasification and reaction. Its use gives throat velocities that

are typically 0 to 10 percent below sound speeds. From this same rationale, a characteristic exhaust velocity efficiency,  $\eta_{c^*}$ , is calculated for nozzle throat conditions from:

$$\eta_{c^*} = \frac{\sum_{j,s} c^*_{js} \dot{W}_{js}}{c^*_{i} \sum_s \dot{W}_{ts}}$$

The present STRMTB computer program permits the definition of up to 40 stream tubes and 12 drop group sizes in a combustion analysis. In addition to calculating the usual combustion gas parameters for performance calculations, it also calculates several useful parameters for use in heat transfer calculations from the stream tubes located adjacent to the chamber walls. A logic diagram for the STRMTB program along with a detailed description of the marching calculational procedure and the program input and output data are presented in Ref. 1 .

The development effort on the STRMTB computer program during the current project was confined to a few minor coding changes. However, an advanced version, linked to sophisticated models for the nozzle expansion of chemically reacting flows is currently under development as part of the DER (Distributed Energy Release) Analysis (Ref. 6 ).

## BOUNDARY LAYER ANALYSIS

The BLEAT computer program calculates the parameters which control local thrust chamber wall compatibility on the basis of the combustion gas flow field defined by the 3D-COMBUST and STRMTB programs. The parameters of interest are the adiabatic wall temperature,  $T_{AW}$ , the heat transfer film coefficient,  $h_g$ , and the concentrations of any corrosive species in the near-wall combustion gas. For ablative thrust chambers, temperature and chemical composition are more important than the film coefficient. With regenerative and/or film cooling,  $T_{AW}$  and  $h_g$  are of approximately equal importance and chemical composition plays a minor role. Wall compatibility parameters are calculated in a separate computer program, BLEAT, rather than in the 3D-COMBUST and STRMTB programs, themselves, primarily to simplify modifications to the analytical models of physical processes in the boundary layers which are presently poorly understood.

The BLEAT analytical model divides the chamber wall boundary layer into two "free stream" regions defined by the 3D-COMBUST and STRMTB models. In portions of the region bordering the 3D-COMBUST zone, appreciable amounts of unburned spray may impinge upon the chamber walls and the transverse gas velocity,  $u_r$ , may be comparable to the axial gas velocity  $u_z$ . In the second region, corresponding to the STRMTB (stream tube) zone of the main flow field, the liquid spray impingement is low (none is defined by the STRMTB model) and the axial gas velocity is high relative to transverse components. For the second region, a highly simplified version of the Elliot-Bartz-Silver analysis (Ref. 7) was originally programmed for use with ablative chambers, and provisions were made in both the STRMTB punch card output and the BLEAT punch card input data formats for expansion of the model to handle the highly cooled boundary layers associated with regenerative cooling. In the first (or upstream) region bounding the 3D-COMBUST zone, the original analysis was based upon a model proposed earlier by Rowley at the Jet Propulsion Laboratory (Ref. 8).

### 3D-COMBUST REGION

In the upstream region, the net heat flux and the equilibrium surface temperature were assumed to represent a competition between periodic heating by the gas and spray cooling by liquid drops. This model is expressed by a relation

$$h(T_{AW} - T_W) = h_g(T_g - T_W) - q/A|_{\text{Spray}} \quad (25)$$

net heat
heat flux
heat removed  
flux
from gas
by spray

based upon Rowley's formulation (Ref. 8). Use of Eq. 25 required definition of the time averaged heat transfer coefficients  $h_g$  and  $h$ . Very little pertinent work in this regard was found in the literature other than the exploratory studies of Rowley (Ref. 8,9,10). A theoretical analysis of the transient heating and vaporization of a flattened single drop upon a surface formed the basis for a model which defined

$$q/A|_{\text{Spray}} = \dot{m}_F \left( \frac{T_W - T_{\text{Sat},F}}{T_g - T_{\text{Sat},F}} \right) \Delta H + \frac{C_{pF}}{2} (T_W - T_{\text{Sat},F})$$

(26)

$$+ \dot{m}_{\text{ox}} \left( \frac{T_W - T_{\text{Sat,ox}}}{T_g - T_{\text{Sat,ox}}} \right) \Delta H + \frac{C_{pox}}{2} (T_W - T_{\text{Sat,ox}})$$

where  $\dot{m}_F$  and  $\dot{m}_{\text{ox}}$  are the masses of fuel and oxidizer evaporating at a given location  $(\theta, x)$  on the wall. The model assumed that liquid droplets reach their saturation temperature before contact with the wall and also assumed no mixing and chemical reaction of the propellant vapors at the wall. Use of Eq. 26 requires definition of  $\dot{m}_F$  and  $\dot{m}_{\text{ox}}$ . For lack of a better specification, the assumption was made in Ref. 1 that the evaporation rate on the wall is equal to the evaporation rate of an equal amount of drops in the adjacent gas stream as calculated by the 3D-COMBUST program. For convenience in calculations with ablative chambers, the bracketed  $\Delta T$  ratios in Eq. 26 were modified to

$$\frac{T_W - T_{Sat,F}}{T_g - T_{Sat,F}} = \frac{T_{AW} - T_{Sat,F}}{T_g - T_{Sat,F}}$$

(27)

$$\frac{T_W - T_{Sat,ox}}{T_g - T_{Sat,ox}} = \frac{T_{AW} - T_{Sat,ox}}{T_g - T_{Sat,ox}}$$

because the surface temperature of an ablative chamber quickly approaches the adiabatic wall temperature except at very low chamber pressures. Similarly the net heat flux quickly approaches zero; therefore Eq. 25 was approximated by

$$h_g (T_g - T_W) - q/A|_{\text{Spray}} = 0$$

which permits the adiabatic wall temperature to be calculated by means of the quadratic formula. The approximate  $T_{AW}$  is used in the substitution defined by Eq. 27 either for subsequent heat transfer calculations by means of Eq. 26 or as a definition supplied to ablative response computer programs.

The hot gas heat transfer coefficient in the upstream region was defined through the assumption that a kernel defined by the usual Dittus Boelter equation

$$St = 0.023 Re^{-0.2} Pr^{-.67}$$

should be modified by a factor

$$\left(1 + C_{u_r}\right) \left(\frac{u_r}{u_z}\right)$$

to account for the fact that gas velocity component into the wall should enhance the gas-to-wall heat transfer.

In Ref. 1, the value of  $C_{uT}$  was theoretically estimated to be approximately 13.0 by numerical integration of the forced convection energy equation over an overall turbulent boundary layer thickness chosen equal to one  $\Delta r$  increment of the 3D-COMBUST program mesh system. This calculation was made under the assumption that both the axial velocity profile and the eddy diffusivities for heat and momentum could be represented by the same relations as apply for ordinary pipe flow or for the flat plate without a pressure gradient. The calculated powerful effect of radial velocity was considered to be reasonable in terms of the known high heat transfer rates at the stagnation point of cylinders or bluff bodies in cross flow.

#### STRMTE REGION

Calculations of heat transfer coefficient in the downstream portion of the chamber were based upon the assumptions that physical property variation across the boundary layer was not important (for ablative chambers) and that the Stanton number would be approximately equal to that for a flat plate with its leading edge at the injector face exposed to a free stream with a temperature, velocity, and mixture ratio equal to that of the stream tubes at the wall. The Stanton number was defined as

$$St = .024 \left( \frac{T_g}{T_r} \right) Re_{\phi_T}^{-.25} Pr^{-.67}$$

with the Reynolds number and energy thickness defined as

$$Re_{\phi_T} = \frac{\rho_{g_j} u_{z_j} \phi_T}{\mu_{g_j}}$$

$$\phi_T = .055 \left( \frac{\rho_{g_j} u_{z_j}^2}{\mu_{g_j}} \right)^{-.2} \quad (28)$$

The relations employed above differ from the usual Elliot-Bartz-Silver analytical procedure primarily in that no allowance was made for variation in the energy thickness due to acceleration of the combustion gas either by vaporization or nozzle convergence.

### GAS TEMPERATURE

The use of the equilibrium thermodynamic temperature of the gas at its local mixture ratio as the definition of  $T_g$  in the heat transfer relations of the BLEAT program was found to give predictions of  $T_{AW}$  which were considerably higher than the experimental values measured in a model motor firing program conducted concurrently with the development of the ICC system of computer programs (Ref. 1). An empirical expression

$$T_g = T_A + (T_E - T_A) \left[ 1 - e^{-(u_z/u_c)^2} \right] \quad (29a)$$

In Eq. 29a,  $T_A$  represents some minimum gas temperature,  $T_E$  is the equilibrium thermodynamic gas temperature at the local mixture ratio, and  $u_c$  is the axial gas velocity corresponding to complete burning of the propellant at the mixture ratio and contraction ratio of the problem. The ratio  $(u_z/u_c)$  is therefore seen to be equivalent to the local percent burn.

A simple method of accounting for the effects of residual spray cooling in the stream tube region was developed by simply assuming that the local effective gas temperature for heat transfer was equal to the local combustion gas temperature in the stream tube times the local fraction burned. This amounts to assuming that the spray-gas two-phase flow is equivalent to a gas flow whose enthalpy potential is equal to the mean enthalpy of the two phase mixture.\*

In the downstream region of the thrust chamber, the Mach number effects require a correction for kinetic enthalpy; therefore, the general definition for adiabatic wall temperature in the stream tube region is used

$$T_{AW} = T_g F_B + Pr^{0.3} \left( \frac{u_z^2}{2J C_p} \right) \quad (29b)$$

\* The enthalpy of the liquid is effectively zero in comparison to the enthalpy of the combusted gas at the local mixture ratio.



## ANALYTICAL DEVELOPMENTS

The analytical efforts during the program were directed toward the general improvement of the entire previously developed Injector/Chamber Compatibility Analysis by broadening the range of applicability, improving the accuracy of the calculations, and reducing the amount of engineering labor required in processing the computer analysis of a problem. The first phase was directed toward improvement of the LISP program. A second phase was directed toward development of a model for the combustion gas flow field close to the injector and the resultant heat transfer to the injector face. A third phase was directed toward improvement of the calculations made by the 3D-COMBUST and BLEAT programs.

### PHASE 1: IMPROVEMENT OF THE LISP ANALYSIS

Upon completion of the initial development of the Injector/Chamber Compatibility Analysis (Ref. 1), the LISP computer program was recognized to be deficient in several areas. First, the correlations of the spray coefficients, required for prediction of single element mass and mixture ratio profiles, had been included for only a very limited range of controlling parameters, such as orifice diameter, impingement angle, impinging stream momentum ratio, etc., even for common elements, such as the doublet and triplet. Second, the definition of mean drop size for the spray from the various elements was unsatisfactory\*. Third, the required punched-card input data were so extensive that it made the processing of multi-element injector calculations excessively time-consuming for the designer. Finally, because much of the advanced technology in liquid rocket engines was shifting toward gas/liquid and gas/gas injection schemes, it was important to determine whether the LISP concept of adding single element contributions to produce an overall injector flow field was also applicable to the gaseous injection schemes. Improvement of LISP in all areas was beyond the scope of this project; therefore several were

\*The lack of effective mean drop size correlations actually reflects the state of the art in this area of combustion technology rather than representing a shortcoming of the LISP program.

selected for further development and were incorporated into the analysis. These were:

1. Correlation of spray coefficients over a more useful range was accomplished for the unlike doublet, the triplet, and the like-doublet-pair elements and added to LISP subroutines.
2. The program input requirements and format were restructured to reduce programming labor; also, the output was restructured for more convenient use in subsequent 3D-COMBUST calculations.
3. A tentative analytical model for gas/liquid coaxial elements was incorporated into the program.

A description of these developments is presented in the following paragraphs.

#### UNLIKE-DOUBLET SPRAY CORRELATIONS

The initial spray-coefficient correlations for unlike doublets presented in Ref. 1 were based upon the cold-flow data provided by Rupe from the investigation reported in Ref. 11. Because of a characteristic of Rupe's experimental apparatus, correlations were based almost completely upon mass collected along the x and y axes as defined in Fig. 8. These correlations were considered to be directly applicable only for the case of equal impinging stream momenta. This made the correlations useful for like doublets\*, but not for unlike doublets, which satisfy the Rupe criterion for optimum performance.

$$\rho_1 U_1^2 D_1 = \rho_2 U_2^2 D_2 \quad (30)$$

The Rupe criterion for most propellant combinations at their optimum mixture ratio corresponds to unlike doublets with unequal orifice diameters and unequal stream momenta. Spray coefficient correlations applicable for injection conditions approximately satisfying the Rupe criterion were developed from three sets of data obtained

\*The assumption was made that a like doublet is equivalent to an unlike doublet with equal orifice diameters and the same propellant flowing from each orifice.

from Rocketdyne experiments at the conditions shown in Table 1 and, in addition, re-correlation of data from a number of Rupe's cold-flow experiments to permit the correlation curves to be extrapolated to equal diameter and equal momentum conditions as limiting cases. Data obtained with the Rocketdyne cold-flow sampling apparatus (see the description in the Experimental Studies section of this report) were particularly useful for this purpose because the 29x29 equal increment sampling matrix permitted efficient mapping of spray flux over the x-y plane as defined in Fig.8 without requiring geometric transformations before application to Eq. 2 .

Table 1 Rocketdyne Cold-Flow Spray Distribution Data for the Unlike Doublet Element\*

Water Orifice Diameter, inch	Trichloroethylene Orifice Diameter, inch	Diameter Ratio	Mixture Ratio	Momentum Ratio
0.028	0.038	1.36	1.73 to 2.03	1.1 to 1.52
0.028	0.0465	1.66	2.30 to 2.59	1.3 to 1.67
0.085	0.130	1.53	1.65 to 2.93	0.78 to 2.51

\*Obtained with water/trichloroethylene propellant simulants and with an impingement angle of 60 degrees

The development of unlike doublet correlation coefficients was done with the revised single element coordinate system shown in Fig. 12 . This revised coordinate system is chosen with the resultant spray momentum vector as the  $z_E$  axis rather than the originally used perpendicular bisector of the element impingement angle  $\gamma_E$ . The change in coordinate definition corresponds essentially to a translation of the  $y = 0$  location by an amount

$$\Delta y = \left( \frac{\dot{w}_1 U_1 - \dot{w}_2 U_2}{\dot{w}_1 U_1 + \dot{w}_2 U_2} \right) \tan \left( \frac{\gamma_E}{2} \right) z_c \quad (31)$$

where  $\dot{w}$  and  $U$  are injection weight flow and injection velocity from orifices 1 and 2 and  $z_c$  is the  $z$  plane at which the spray mass is being collected.

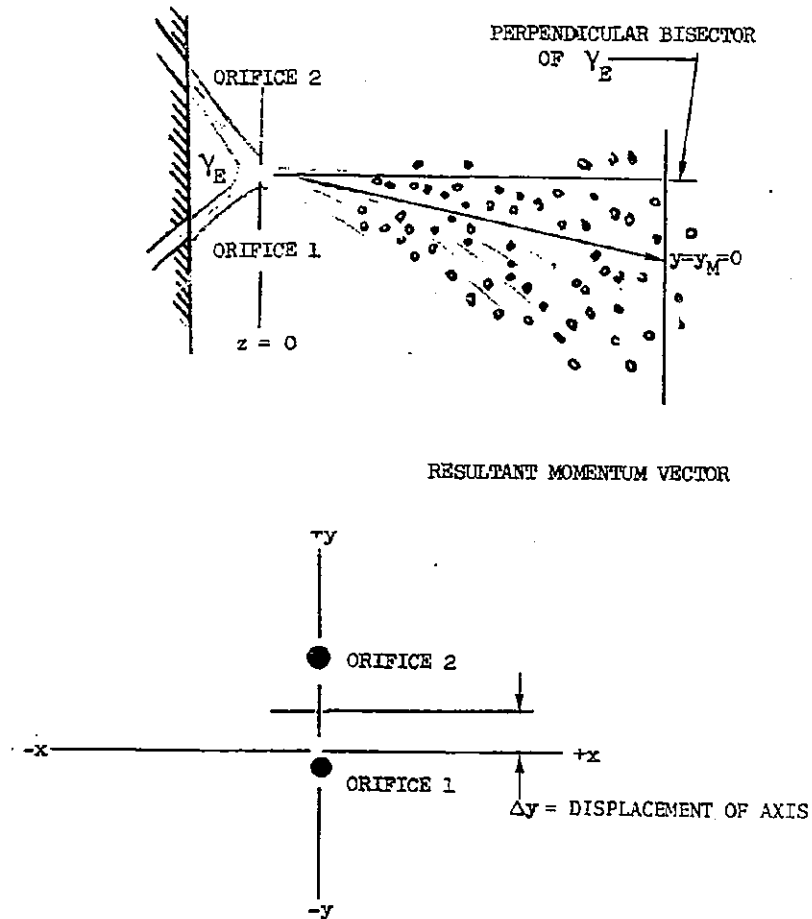


Figure 12 Coordinate System for Unlike Doublet Element

The change in selected coordinate system was made because the spray pattern of the unlike doublet has been found to be distributed about the resultant momentum line in such a fashion that the spray coefficients ( $b$ ,  $C_1$ , and  $C_5$ ) can be correlated in a more consistent fashion with the new coordinate system than was possible when the perpendicular bisector was used for the  $z_E$  axis.

The technique used for evaluation of the various spray coefficients was to equate the experimental values of suitable  $x$  or  $y$  momentum arms of the mass flux distribution to the corresponding analytical expressions obtained by integration of Eq. 4 over the  $x, y$  plane. For example, the first  $y$  moment arm of the collected mass of a given propellant in the Rocketdyne 29 x 29 element spray collection matrix is

$$\bar{Y}_E^1 = \frac{\sum_{I=1,29} \sum_{J=1,29} y_{I,J} w_{I,J}}{\sum_{I=1,29} \sum_{J=1,29} w_{I,J}} \quad (\text{in the collection plane } z_c)$$

The corresponding analytical expression is

$$\bar{Y}_A^1 = \frac{\int_{-\infty}^{\infty} \int_{-\infty}^{\infty} y w(x, y, z_c) dx dy}{\int_{-\infty}^{\infty} \int_{-\infty}^{\infty} w(x, y, z_c) dx dy} \quad (\text{in the collection plane } z_c) \quad (32)$$

If Eq. 4 is substituted for  $w(x, y, z_c)$  the closed form integral of Eq. 32 becomes

$$\bar{Y}_E^1 = \bar{Y}_A^1 = \frac{z_c}{2b} \cdot \frac{\left[ C_1 + \frac{C_4 C_5}{2a} \right]}{\left[ \left( 1 + \frac{C_1^2}{8b} \right) + \frac{C_4}{2a} \left( 1 + \frac{C_5^2}{8b} \right) \right]}$$

It is clear that an equal number of equations and unknown coefficients can be obtained which may be solved, in principle, for the spray coefficients. However, because the momentum arm integrals are not linear in the spray coefficients and, further, because the accuracy in determination of momentum arms higher than  $\bar{Y}_E^2$

or  $\bar{X}_E^2$  was not satisfactory, evaluation of the spray coefficients required some exploration to develop a satisfactory technique. To evaluate the spray coefficient b, it was useful to define a modified doublet correlation

$$w(x,y,z) = \frac{w_{001}}{z^2} \left\{ \left[ 1 + C_1' \left(\frac{y}{z}\right) + \frac{C_1'^2}{4} \left(\frac{y}{z}\right)^2 \right] \left[ 1 + C_4' \left(\frac{x}{z}\right)^2 \right] e^{-a\left(\frac{x}{z}\right)^2 - b\left(\frac{y}{z}\right)^2} \right\}$$

From Eq. 32,  $\bar{Y}_A^1$  becomes

$$\bar{Y}_A^1 = \frac{z_c C_1'}{2b} \left[ \frac{1}{1 + \frac{C_1'^2}{8b}} \right] \quad (33)$$

A second expression in b and  $C_1'$  is obtained by defining the ratios

$$\frac{S}{S_0} \Big|_A = \frac{\int_{-\infty}^{\infty} \int_{-\infty}^{\infty} w(x,y,z_c) dx dy}{\int_{-\infty}^{\infty} w(x,0,z_c) dx} \quad (34)$$

$$\frac{S}{S_0} \Big|_E = \frac{\sum_{I=1,29} \sum_{J=1,29} W_{I,J}}{\frac{1}{\Delta} \sum_{I=1,29} W_{I,J=J_0}}$$

where  $J_0$  is the row of the spray collection device corresponding to the resultant momentum vector of the doublet and  $\Delta$  is the width of the row.

Integration of Eq. 34. gives

$$\frac{S}{S_0} \Big|_A = \frac{S}{S_0} \Big|_E = \sqrt{\frac{\pi}{b}} \left[ 1 + \frac{C_1'^2}{8b} \right] \quad (35)$$

Equation 33 and 35 provide two expressions which may be solved for the coefficients  $b$  and  $C_1'$  in terms of the measured parameters  $\bar{Y}_E$  and  $S/S_o|_E$ . The value of  $b$  obtained is assumed to also apply for Eq. 4, the "working" expression for the unlike doublet. The value of  $C_1'$ , an intermediate coefficient, is then discarded after obtaining the coefficient  $b$ .

The coefficient  $b$  was found to be a function of both momentum ratio and diameter ratio. The correlations assigned to coefficient  $b$  in terms of these parameters after smoothing the experimental data are shown in Fig. 13 and 14, respectively, for both the smaller and larger orifices of the doublet. These values should be used in place of the values presented in Fig. 11 of Ref. 1.

Procedures similar to that described for coefficient  $b$  were employed to briefly re-examine spray coefficients  $a$  and  $C_4$ . The correlations reported previously in Ref. 1 were found adequate and no changes were made.

The spray coefficients  $C_1$  and  $C_5$  are employed to describe the displacement of the center of mass of either propellant from the resultant momentum line of the element. Calculation is based on the observation that, in the cold flow data analyzed, the overall center of mass of the propellant from each orifice, defined by

$$\bar{y}_1 = \frac{\int_{-\infty}^{\infty} y w_1(x,y) dx dy}{\int_{-\infty}^{\infty} w_1(x,y) dx dy} \quad (36a)$$

$$\bar{y}_2 = \frac{\int_{-\infty}^{\infty} y w_2(x,y) dx dy}{\int_{-\infty}^{\infty} w_2(x,y) dx dy} \quad (36b)$$

could be correlated satisfactorily in terms of  $y_M$ , the resultant momentum line coordinate and the initial trajectory coordinates  $Y_1$  and  $Y_2$  defined by

\*Eq. 36a is equivalent to Eq. 36b except that in the later derivation the symbols are subscripted to distinguish between the flow from orifices 1 and 2.

$$Y_1 = z_c \tan \left( \frac{Y_E}{2} \right)$$

$$Y_2 = z_c \tan \left( \frac{Y_E}{2} \right)$$

The relations found to apply were

$$\bar{Y}_1 = Y_1 - 0.96 (Y_1 - Y_M) \quad (37a)$$

$$\bar{Y}_2 = Y_2 - 0.96 (Y_2 - Y_M) \quad (37b)$$

where the coefficient 0.96 represents an average for a range of coefficient values from 0.93 and 0.98 depending upon the approach to the Rupe criterion in Eq. 30 and the diameter ratio.

In a similar fashion, the centers of mass for the spray along the plane of symmetry of the element,

$$\bar{Y}_{1,o} = \frac{\int_{-\infty}^{\infty} y w_1(x=0,y) dy}{\int_{-\infty}^{\infty} w_1(x=0,y) dy} \quad (38a)$$

$$\bar{Y}_{2,o} = \frac{\int_{-\infty}^{\infty} y w_2(x=0,y) dy}{\int_{-\infty}^{\infty} w_2(x=0,y) dy} \quad (38b)$$

could be located in terms of  $Y_1$ ,  $Y_2$  and the centerline resultant momentum line  $Y_{M,0}$  defined by

$$Y_{\text{centerline}} = \left( \frac{\frac{w_1 U_1}{D_1} - \frac{w_2 U_2}{D_2}}{\frac{w_1 U_1}{D_1} + \frac{w_2 U_2}{D_2}} \right) \tan \left( \frac{Y_E}{2} \right) z_c$$



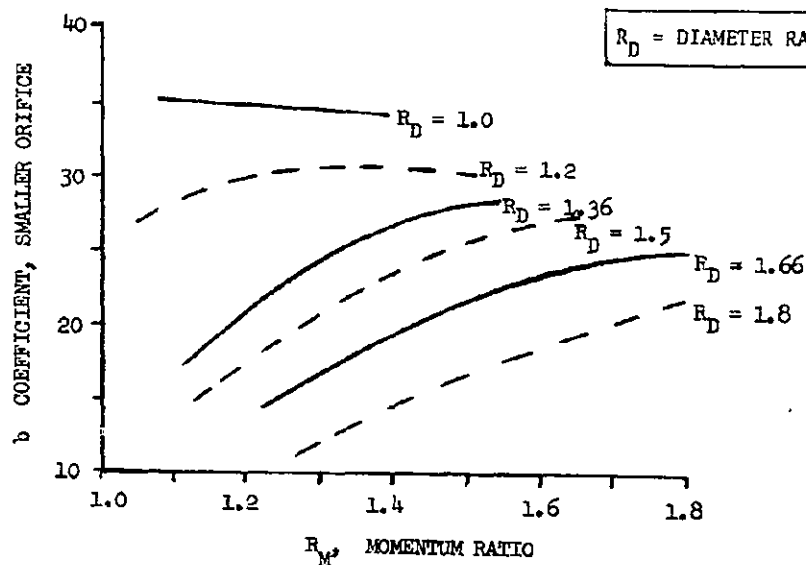


Figure 13 Variation of  $b$  Coefficient With  $R_M$  and  $R_D$  for Smaller Orifice of Unlike Doublet

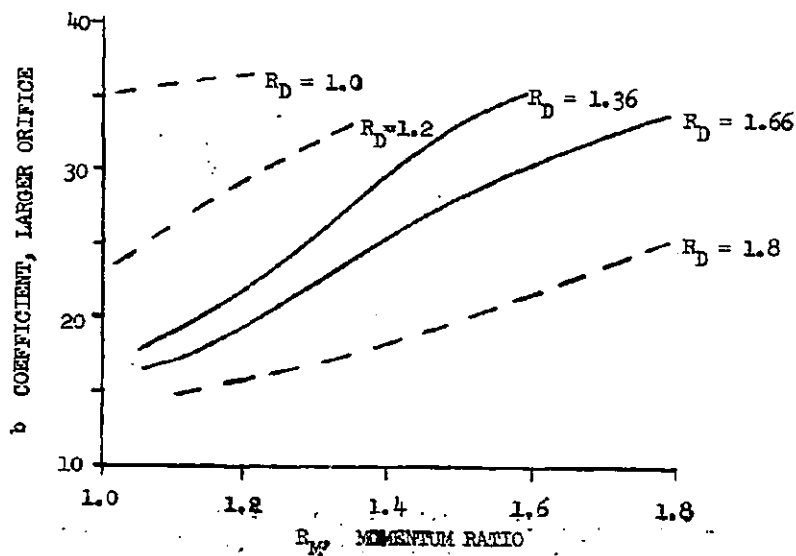


Figure 14 Variation of  $b$  Coefficient With  $R_M$  and  $R_D$  for Larger Orifice of Unlike Doublet

The expressions chosen to describe the relationship are

$$\bar{y}_{1,o} = Y_1 - X_{R_D, R_M} (Y_1 - Y_{M,o})$$

$$\bar{y}_{2,o} = Y_2 - X_{R_D, R_M} (Y_2 - Y_{M,o})$$

The factor  $X_{R_D, R_M}$  for either orifice varies from approximately 0.9 to 1.02, depending upon which orifice is smaller, upon the diameter ratio  $R_D$  and upon the total momentum ratio  $R_M$ .

Equations 37a and 37b define  $\bar{y}_1$  or  $\bar{y}_2$  and  $\bar{y}_{1,o}$  and  $\bar{y}_{2,o}$  are defined by

$$\bar{y}_{o,i} = \frac{z}{2b_i} \frac{C_{1,i}}{\left[1 + \frac{C_{1,i}^2}{8b_i^2}\right]} \quad i = 1 \text{ or } 2$$

which was obtained by integration of Eq. 4 with  $x = 0$ . With coefficient  $b$  defined by Eq. 33 and 35, and with  $y_M$  defined as  $y = 0$ , the coefficient  $C_{1,o}$  is calculated from

$$C_{1,1} = \frac{1.0 - \sqrt{1.0 - 2b_1 \bar{y}_{1,o}^2}}{0.5 \bar{y}_{1,o}}$$

$$C_{1,2} = \frac{1.0 - \sqrt{1.0 - 2b_2 \bar{y}_{2,o}^2}}{0.5 \bar{y}_{2,o}}$$

at plane  $z_E = 1.0$

A similar relation defines  $C_5$  after  $C_1$  has been calculated. The new relationships for the unlike doublet coefficients have been incorporated into the spray coefficient library routines in the revised LISP program along with those previously defined for  $a$  and  $C_4$ .

### TRIPLET SPRAY CORRELATIONS

Calculation of the spray patterns for the triplet element has been done with Eq. 5a and 5b as shown in the Analytical Model section with empirically determined values of  $a_1$ ,  $b_1$ ,  $a_2$ ,  $b_2$ , and  $C_{4,2}$  of outer orifice pair 1 and inner orifice 2, respectively.

Only one set of cold flow data, obtained with one single element geometry, was available during the original Injector/Chamber Compatibility project for determination of spray coefficients and, consequently, the general applicability of the correlations was questionable. During the current program, additional data were obtained with the Rocketdyne cold-flow collection matrix and with a triplet of different orifice sizes. As reported in the Experimental Program section of this report, a total of eight new cold-flow experiments were performed; however, the data from the first three were only of limited usefulness because of difficulties in obtaining proper stream impingement. These data and the earlier data from Ref. 1 provide the overall parametric matrix shown in Table 2.

Table 2 Available Triplet Cold-Flow Spray Distribution Data for the Single Element Triplet\*

Water Orifice Diameter, inch	Trichloroethylene Orifice Diameter, inch	Diameter Ratio	Mixture Ratio	Impingement Angle, degrees
0.043	0.067	1.55	0.41 to 6.7	70
0.085	0.130	1.53	0.49 to 2.64	70

\*Using water/trichloroethylene propellant simulants.

These combined data show variation of spray distribution with momentum ratio (by variation of mixture ratio) at two ranges of single element size.

Spray coefficients were obtained and correlated by procedures equivalent to those employed for the unlike doublet. However, because of the simpler spray distribution relations applicable to the triplet, the spray flux moment arm expressions

were correspondingly simpler. From Eq. 5a and 32, the first y moment arm of the flux is given by

$$\frac{\int_0^{\infty} \int_0^{\infty} y w \, dx dy}{\int_0^{\infty} \int_0^{\infty} w \, dx dy} = \frac{z}{\sqrt{\pi b}} \quad (39)$$

so that  $b = \frac{z^2}{\pi} [\bar{Y}_E]^{-2}$

The corresponding expression for  $a_1$ , applying to the outer orifice pair is

$$a = \frac{z^2}{\pi} [\bar{X}_E]^{-2}$$

Note that the moment arms are evaluated by an integration from 0 to  $\infty$  rather than from  $-\infty$  to  $+\infty$ . To evaluate the  $a_2$  and  $C_{4,2}$  coefficients applicable to the inner single orifice of the triplet, the following expressions were solved simultaneously:

$$\frac{\int_0^{\infty} \int_0^{\infty} x w \, dx dy}{\int_0^{\infty} \int_0^{\infty} w \, dx dy} = \frac{z}{\sqrt{\pi a}} \left[ \frac{1 + (C_4/a)}{1 + (C_4/2a)} \right] \quad (40)$$

and

$$\frac{\int_{-\infty}^{\infty} \int_{-\infty}^{\infty} w \, dx dy}{\int_{-\infty}^{\infty} w \, dy \big|_{x=0}} = z \sqrt{\frac{\pi}{a}} \left[ 1 + \left( \frac{C_4}{2a} \right) \right] \quad (41)$$

The new correlations for the triplet are shown in Fig. 15 through 19 .

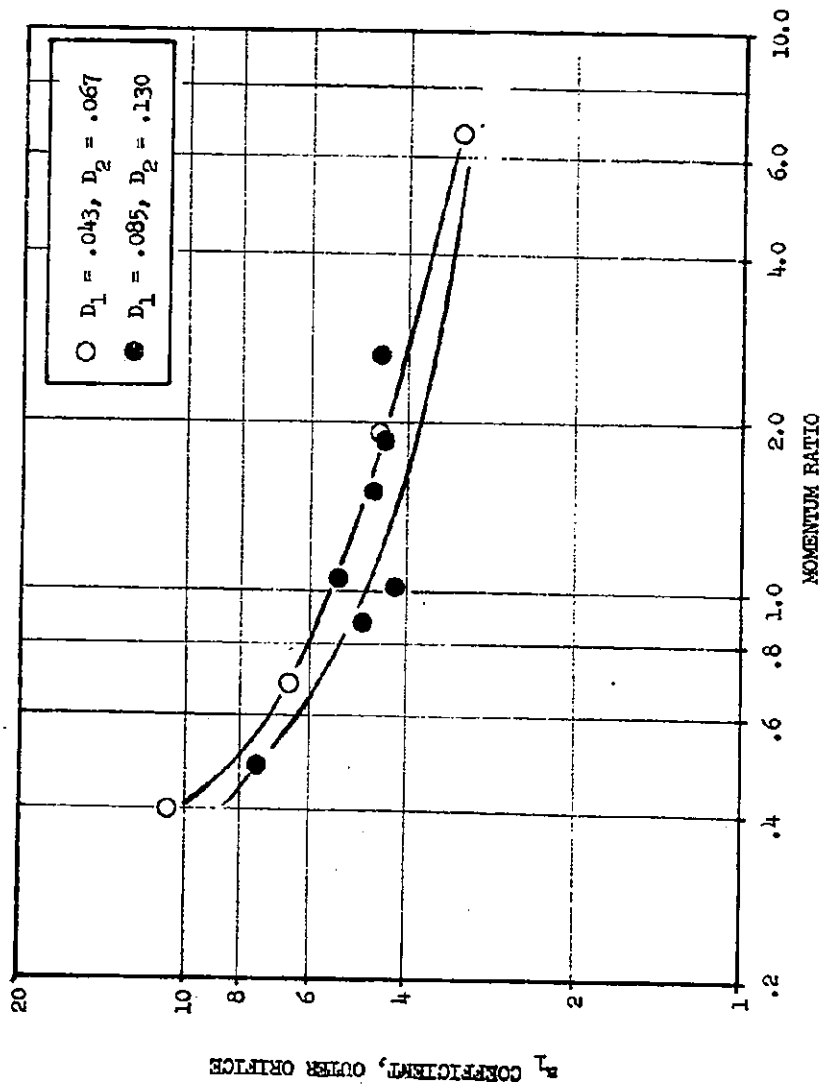


Figure 15 Variation of Outer Orifice Spray Coefficient  $a_1$  With Momentum Ratio

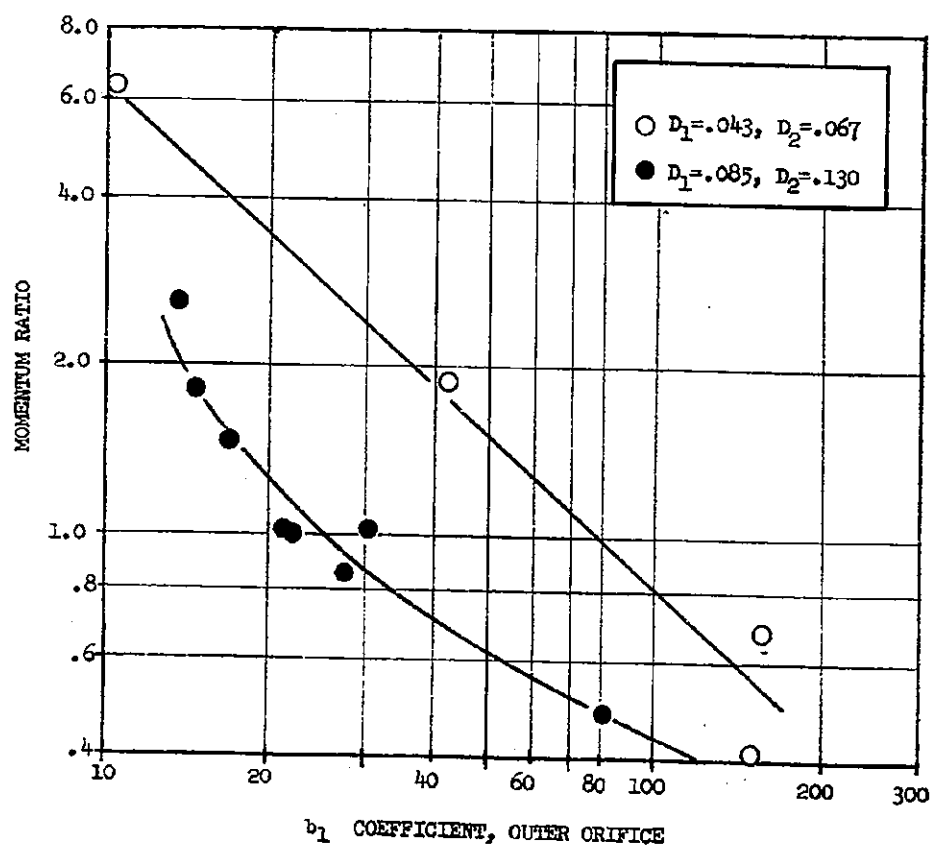


Figure 16 Variation of Outer Orifice Spray Coefficient  $b_1$  With Momentum Ratio

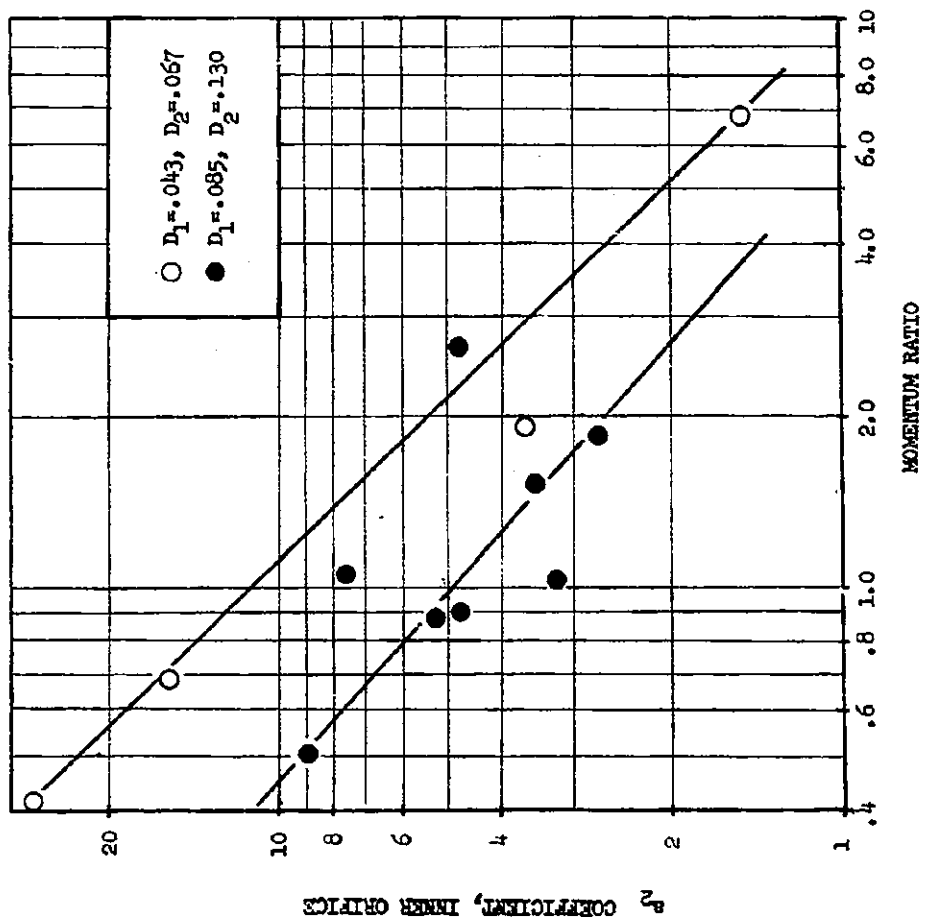


Figure 17 Variation of Inner Orifice Spray Coefficient  $a_2$  With Momentum Ratio

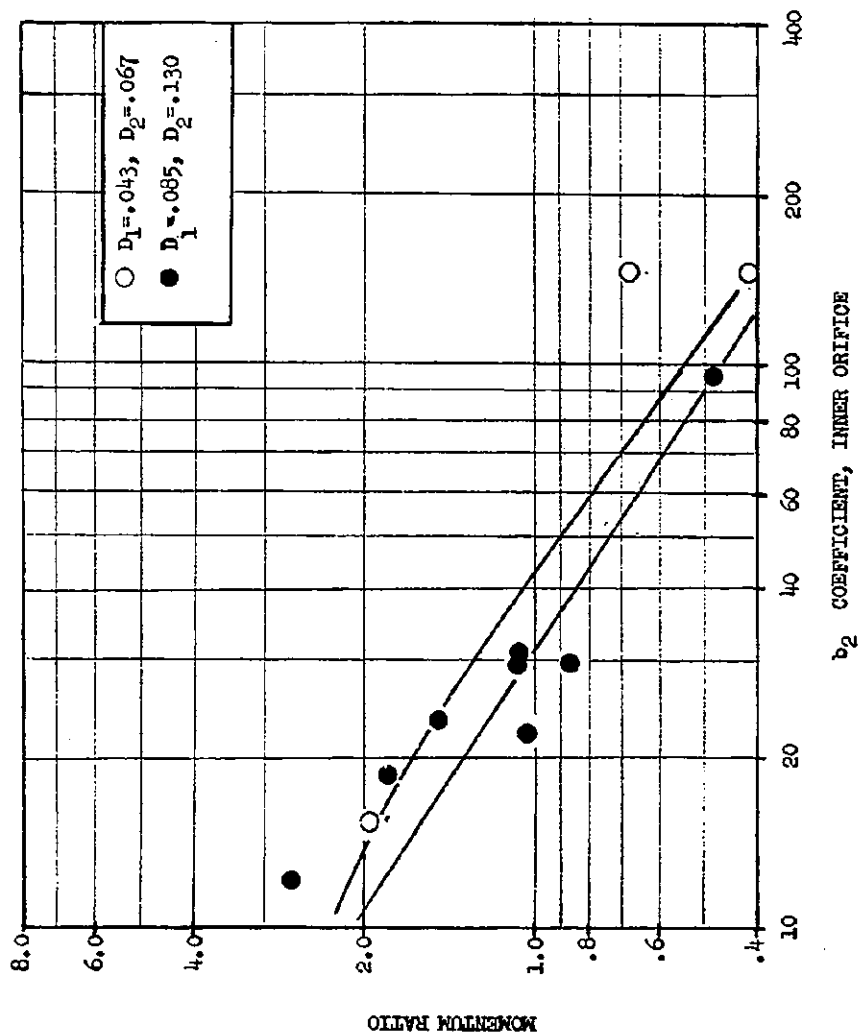


Figure 18 Variation of Inner Orifice Spray Coefficient  $b_2$  With Momentum Ratio



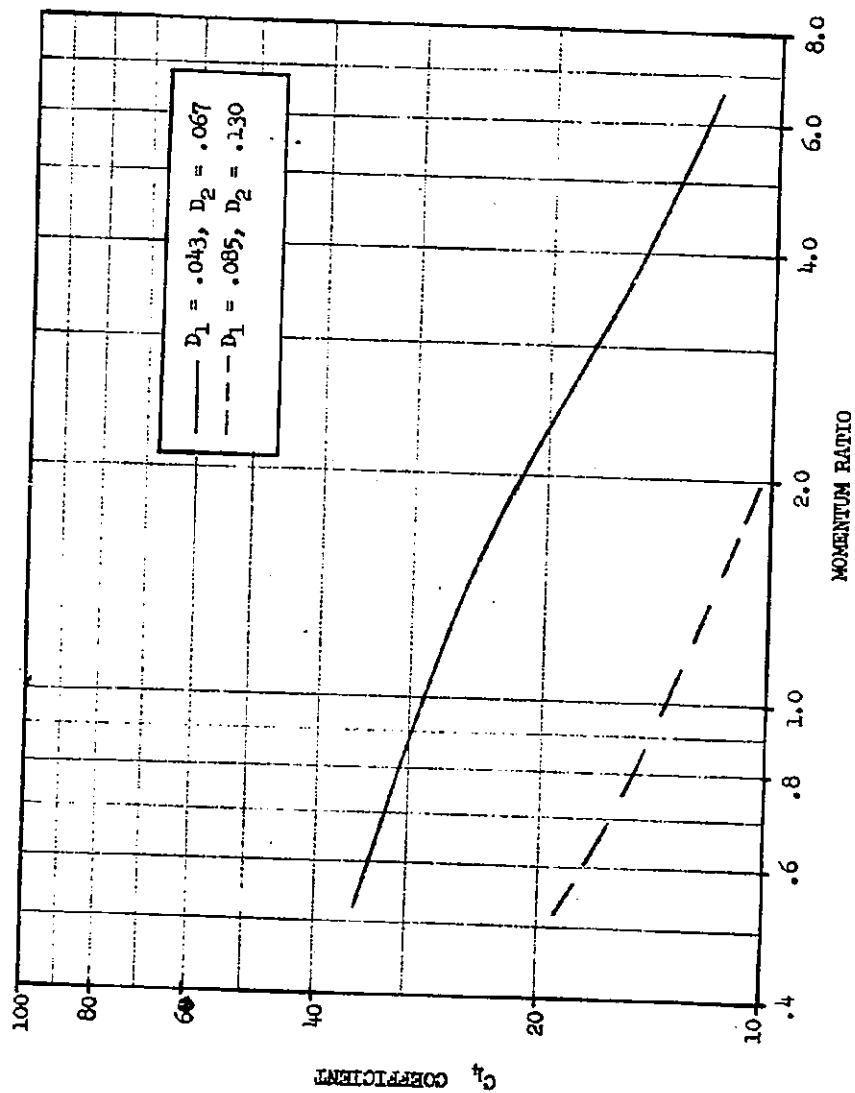


Figure 19 Variation of Inner Orifice Spray Coefficient  $C_4$  With Momentum Ratio

profiles did not resemble the experimental distributions even when the calculated and experimental mass moment arms were equal. The correlation procedure was therefore modified for use of separate correlations on each side of the like-doublet-pair center,  $x = 0$ , as given by Eq. 7a and 7b in the model for thrust chamber compatibility and performance analysis section. On this basis, the coefficients reduced to  $a_{(+),1}$ ,  $a_{(-),1}$ , and  $b$ . These coefficients were evaluated by means of Eq. 34 and 36.

The correlations developed for the like-doublet-pair coefficients are shown in Fig. 21 through Fig. 26. The "a" coefficients are presented as  $a_{\text{opposite}}$  and  $a_{\text{same side}}$  for both the smaller and the larger diameter orifices. For orifice(s) 1,  $a_{+}$  is equal to  $a_{\text{opposite}}$  and  $a_{-}$  is equal to  $a_{\text{same side}}$ ; the converse is true for orifice(s) 2. The  $b$  coefficients shown in Fig. 25 and 26 are differentiated only according to larger and smaller sizes.

An extensive evaluation of what is at first glance an almost meaningless scatter of data points was required to draw the correlation curves shown in Fig. 21 through 26. Where data points deviated markedly from the correlation line, examination of the raw cold-flow data usually indicated that the assumed geometric center for the like doublet pair had not been adequately defined\*. The correlation was, therefore, drawn on the basis of a judgement of what the geometry had actually been and what a normal trend in mass distribution should have been.

It is notable that the  $b$  coefficient of the larger orifice always tended to be substantially less than would be the case for the single like doublet element (see Fig. 14). For the smaller orifice, this was only true for fan impingement angles of 20 degrees or higher. This effect is probably due to the drops from the smaller (inner) orifice doublet splitting the fan of the larger (outer) orifice doublet in much the same fashion as the smaller orifice of the unlike doublet splits the jet of the larger orifice at the practical design momentum ratios. At larger fan impingement angles, the secondary droplet collisions in the intersecting fans spread the y-direction dimensions of both fans (i.e., they reduce the  $b$  coefficient).

\*The cold flow data were not originally intended for use in the LISP program, but rather for calculation of  $E_m$ . As a consequence, the geometric location was usually not adequately documented.

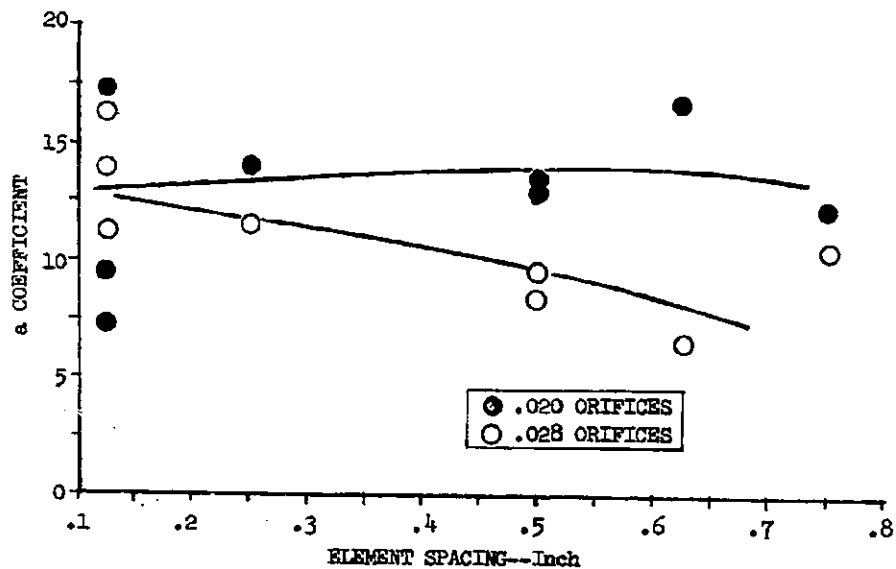


Figure 21 Variation of a Coefficient on Same Side of Center With Element Spacing for Fan Impingement Angles of 40 Degrees

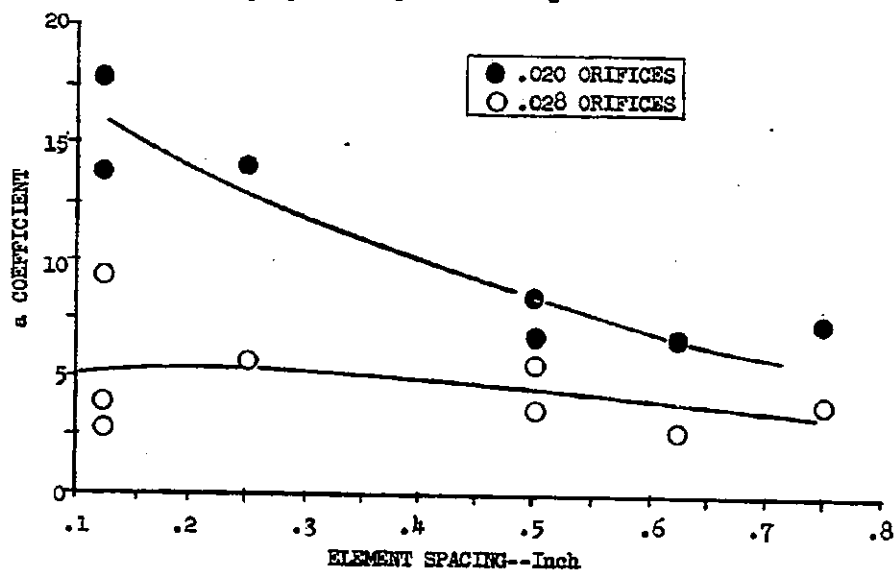


Figure 22 Variation of a Coefficient on Opposite Side of Center With Element Spacing for Fan Impingement Angles of 40 Degrees

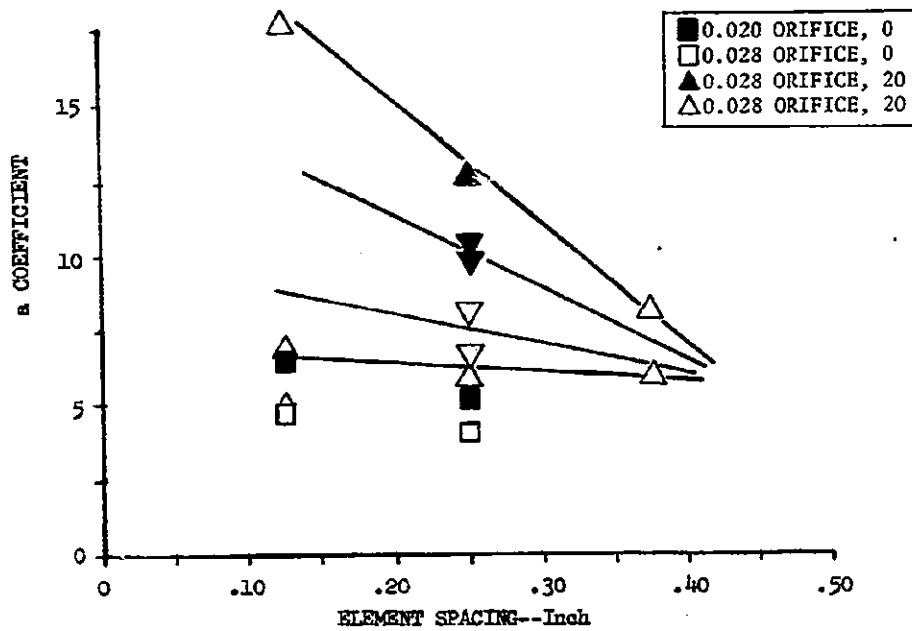


Figure 23 Variation of a Coefficient on Same Side of Center With Element Spacing for Fan Impingement Angles of 0 and 20 Degrees

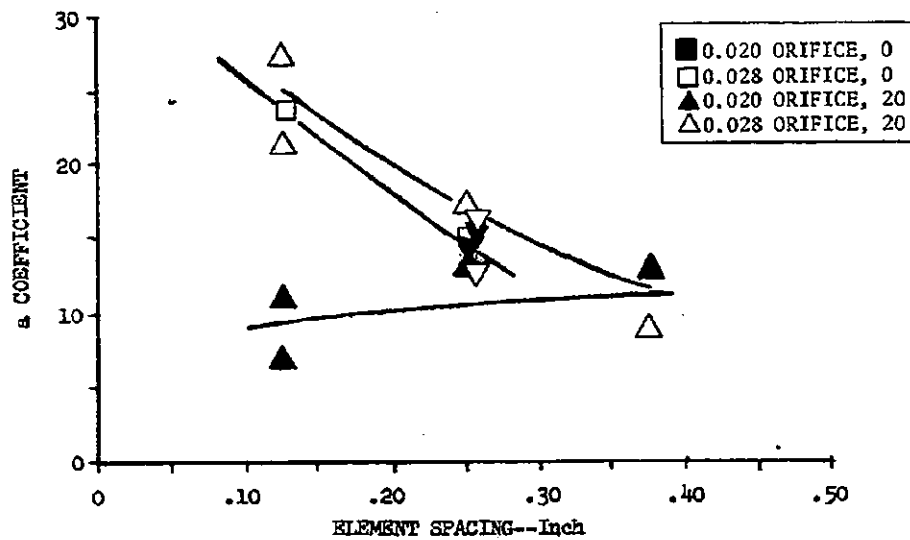


Figure 24 Variation of a Coefficient on Opposite Side of Center With Element Spacing for Fan Impingement Angles of 0 and 20 Degrees

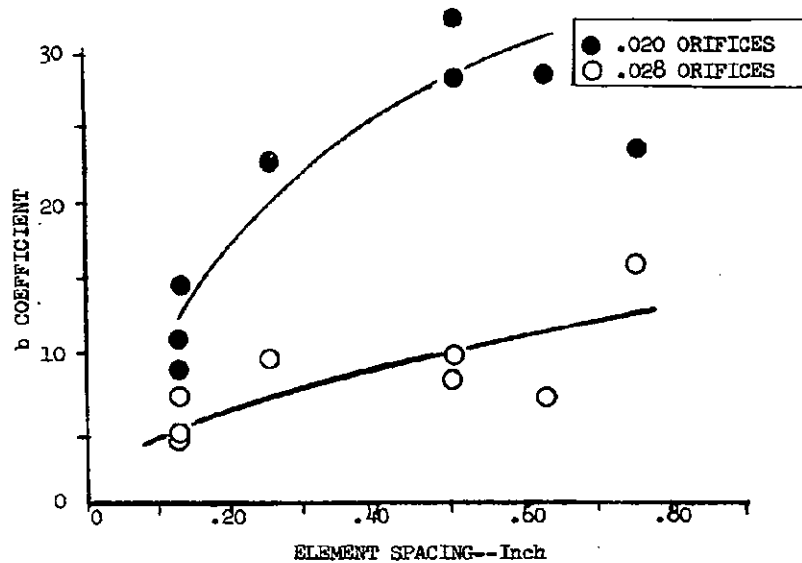


Figure 25 Variation of b Coefficient With Element Spacing for Fan Impingement Angle of 40 Degrees

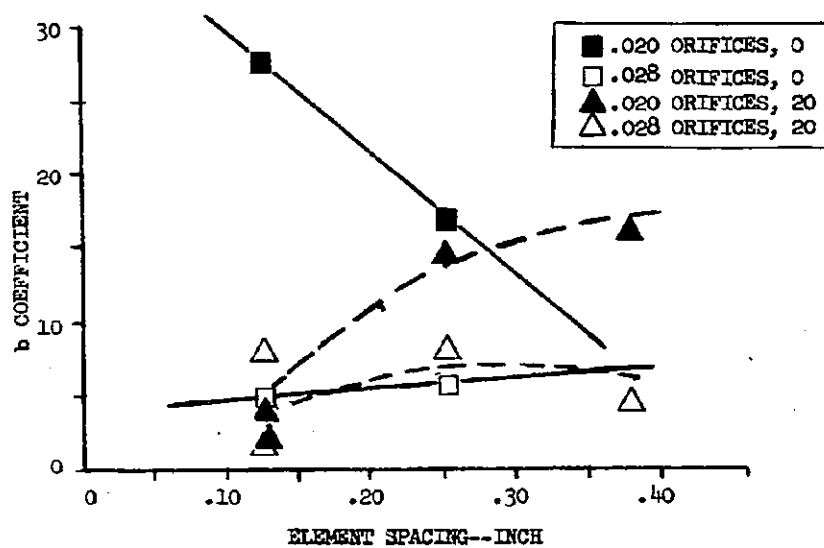


Figure 26 Variation of b Coefficient With Element Spacing for 0 and 20 Degrees Fan Impingement Angles

## HIPERTHIN LIKE DOUBLETS

The HIPERTHIN\* injector concept was developed by the Aerojet General Corporation (Ref. 12). It involves use of injectors containing thousands of very small, closely spaced orifices of rectangular cross section. The orifices may be oriented to produce either impinging or showerhead streams. In concept, the small drops and intimate mixing resulting from injection through these orifices should produce very high combustion efficiencies.

The objectives of the analytical and experimental studies of this project were to measure the size and shape of the spray fans produced by two separate HIPERTHIN elements whose configuration was specified by the AFRPL project engineer and then determine whether the spray pattern was amenable to analysis by LISP and the other computer programs of the Injector/Chamber Compatibility Model. As described in more detail in the Experimental Program section of this report, cold flow mass distribution experiments were performed with two HIPERTHIN like doublets, each consisting of two orifices of rectangular cross section with an impingement angle of 60 degrees along a plane parallel to the long side of the orifices (edge-wise impingement). The orifice dimensions of the two elements were 0.004 x 0.0185-inch and 0.008 x 0.0185-inch, respectively. Over most of the injection velocity range employed in the experiments (34 to 72 ft/sec), the deionized water used as propellant simulant formed a fan that is best described as a continuous sheet at right angles to the impinging streams of the element rather than the expected droplet spray fan. This fan began to disintegrate at a distance approximately 0.75-inch downstream of the impingement point. Visually, the fan breakup appeared to be accomplished more nearly by the liquid drawing up into two diverging jets at right angles to the original impinging streams than by the formation of drops. This observation was corroborated by the distribution of the collected mass, which suggests that the overall atomization of the injected liquid is not as effective as would be expected for the small orifice size.

\*HIPERTHIN is an Aerojet trademark

The spray correlations for the HIPERTHIN spray flux distribution were based on the shape of the histograms of the collected mass distribution, examples of which are shown in Fig. 27 . The distribution of the mass along the usual x axis was definitely non-Gaussian and resembled more closely the mass flux distributions for the inner orifice of the triplet element shown in Fig. 10 . Therefore, the triplet version of the general LISP equation was used, i.e.,

$$w = \frac{w_{001}}{z^2} \left[ 1 + C_4 \left( \frac{x}{z} \right)^2 \right] e^{-a \left( \frac{x}{z} \right)^2 - b \left( \frac{y}{z} \right)^2}$$

The coefficients a and  $C_4$  were evaluated with the data from the six individual cold flow experiments performed by employing the same relations that were used with the triplet, i.e. Eq. 40 and 41. However, as discussed in the Experimental Studies section, the spray fan of the HIPERTHIN element was so thin in the y-direction (defined by Fig. 7 ) that essentially all of the mass was collected in a single row of the cold-flow collection apparatus (Fig. 54 ), and only an estimate could be made of the minimum value of coefficient b according to Eq. 39 . The spray coefficients a, b, and  $C_4$  as determined by this analysis are presented in Table 4. These coefficients exhibit unusual character in that they appear to be a fairly strong function of the element injection velocity. Such a dependence was not observed for larger diameter circular orifices. It appears possible from the data that the a and  $C_4$  coefficients may approach limiting values at sufficiently high injection velocities and that the thin sheet fans produced by the lower injection velocities break up completely at high injection velocities into the droplet spray fans usually achieved with circular orifice elements.

Examination of the configuration of reported prototype HIPERTHIN injectors shows that they are ordinarily arranged in rectangular arrays such that the planes of symmetry which define essentially independent chamber slices for analysis (see the first portion of the Theoretical Model section of this report) occur at 90 degrees or 180 degrees. The hundreds or even thousands of individual elements located within such a segment exceed the LISP computer program limit of 50 elements by an order of magnitude. Similarly, the fine spray which should presumably occur (if the observations discussed previously are ignored) should produce a very high degree

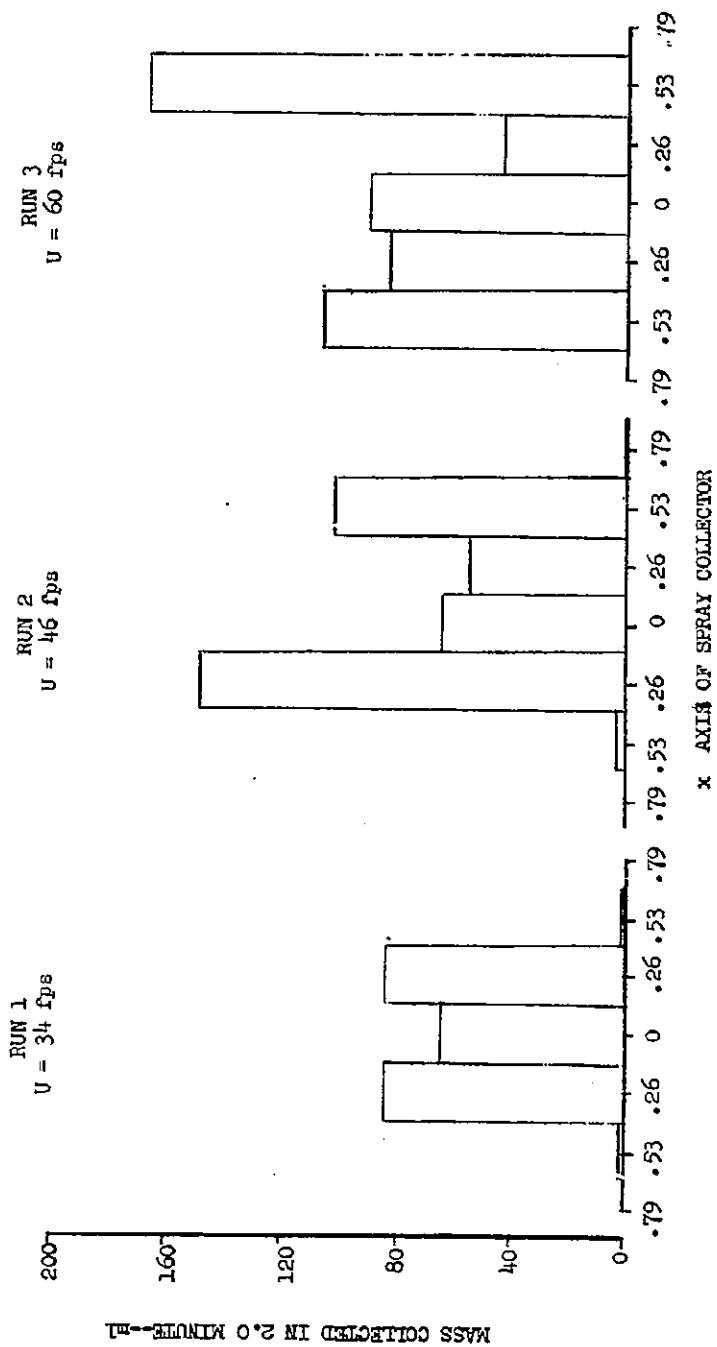


Figure 27. Mass Distribution Along X-axis of Hyperthin Like Doublet at a Collection Distance of 1.0 Inch



Table 4 Spray Coefficients for Rectangular Orifice Hiperthin Like Doublets Based Upon Cold-Flow Experiments

Test Number	Orifice Height, inch	Orifice Width, inch	Injection Velocity, ft/sec	Coefficients		
				a	b	C <sub>4</sub>
1	0.0185	0.004	34	17.0	500	42
2		0.004	46	8.8	500	27
3		0.004	60	4.4	500	6.2
11		0.008	44.0	7.3	300	16
12		0.008	55.5	4.0	250	4.5
13		0.008	72.0	4.1	230	8.0

of vaporization between the injector and the LISP calculation plane. As a consequence the HIPERTHIN injector does not lend itself to routine calculations by the Injector/Chamber Compatibility Model. Therefore, the spray coefficient correlations presented in Table 4 were not incorporated into the subroutines of the LISP program. Calculations can still be performed by representing individual HIPERTHIN elements or groups of these elements as Type 8 elements with spray coefficients and drop sizes supplied as special data by the designer.

#### GAS/LIQUID COAXIAL ELEMENTS

Analysis of the performance of injectors which use gas/liquid elements has been aided significantly by the use of cold flow mass distribution studies. Recent data (Ref. 13) indicate that effective correlation exists between the mixing efficiency and drop sizes measured in single element cold flows and the motor firing performance of multi-element injectors. However, if single element gas/liquid cold flow data are used to define the spatial distribution of the gas and liquid flow field near the injector rather than the mixing distribution, and this spatial distribution is used in a combustion calculation, a number of complications are introduced:

1. The single element cold flow data are limited.
2. Although Eq. 1 must apply (from continuity), the weight flux of a continuous medium such as a gas from a given element to a given location ( $r, \theta, z$ ) is not as independent of the flow from neighboring elements as is the case with liquid/liquid injection.
3. More liquid evaporation occurs close to the injector than with liquid/liquid injection producing additional gas generation.

4. In many of the propellant combinations employed in gas/liquid injectors, the chamber pressure is near or above the critical pressure of the liquid propellant, i.e., the  $k'$  evaporation model employed in the 3D-COMBUST and STRMTB calculations is not as applicable as with storable propellants and lower chamber pressure.

Because of the above complications, the incorporation of gas/liquid elements into the LISP computer program was undertaken on an exploratory basis. Analytical studies were limited to the gas/liquid coaxial element for which both promising cold-flow experimental data and a useful near-injector combustion analysis were available. In addition, it was assumed that the analysis would be confined to chamber pressures below the critical pressure of the liquid propellant so that the  $k'$  evaporation model is at least reasonable. The first analytical approach tried, which was unsuccessful, was to assume that the single-element mass-flux distribution under combustion conditions could be defined in terms of the cold-flow distribution with a correction for the near injector evaporation process made in essentially the same fashion as the liquid/liquid injection spray patterns are calculated. The evaporated liquid propellant would be assumed to be either distributed uniformly across the chamber cross section or to follow its cold-flow injection path; choice between these over-simplified distributions was to be based upon the results of initial calculations. Evaporated liquid propellant would be assumed to be mixed with and in chemical equilibrium with the gas phase at the local mixture ratio. Finally, local gas velocities would be calculated from the the local gas mass fluxes and the local density based upon chamber pressure and local mixture ratio.

With this approach, the primary analytical effort required was the correlation of gas/liquid cold-flow mass flux profiles as described in the following paragraphs. However, when the resultant version of LISP was employed to analyze an AFRPL model motor firing, made with a multi-element coaxial injector and  $\text{GH}_2/\text{LO}_2$  propellants, a serious complication arose because of the high degree of liquid propellant evaporation within the first inch downstream of the injector. A modification in the model for the gas flow was then incorporated into the LISP program which is described in the paragraphs following the cold-flow derivations.

### Correlation of Cold-Flow Distributions

The single-element cold-flow data employed to develop the required correlations for gas/liquid coaxial elements were obtained by R. J. Burick of Rocketdyne as part of the technical effort under NASA contract NASA5-11199 (Ref. 13). Burick's experiments were done with water and gaseous nitrogen as the propellant simulants and measurements were made of gas and liquid mass fluxes at 11 radial and 4 circumferential stations around the element centerline in a collection plane 5.0-inches downstream of the injector face. Experiments were made both with and without post recess. For the correlation, because of the assumed radial symmetry of the ideal coaxial element, the measured circumferential distributions of both propellants were averaged to give distributions which were functions of only the radial coordinate.

The system analyzed is shown schematically in Fig. 28. Because of the radial symmetry, the usual Cartesian coordinate was replaced by a cylindrical  $(r, z)$  coordinate system (Fig. 28). The center of the post exit of the element was chosen as the origin of this coordinate system. The subscript 1 is assigned to the annular orifice while subscript 2 is assigned to the post orifice. The gaseous propellant must flow from orifice 1. The liquid and gas flows are assumed to be emitted from point sources located at an axial location of  $z$  equal to  $-\delta_L$  and  $-\delta_G$ , respectively. Although this represents an approximation of the real physical situation, visual observations of single coaxial element flows indicates that at least the liquid spray trajectories are qualitatively described by this model.

Typical profiles of the gas and spray mass flux ( $\text{lbm/in.}^2 \text{ sec}$ ) measured by Burick at a collection distance of 5.0-inches downstream of a coaxial element are shown in Fig. 29a and 29b. The correlation scheme was developed not only to fit these Gaussian distributions at relatively long distances from the injector, but also to provide a reasonable fit in the region close to the post exit plane where the mass flux profiles must approach the limiting case shown in Fig. 29c.

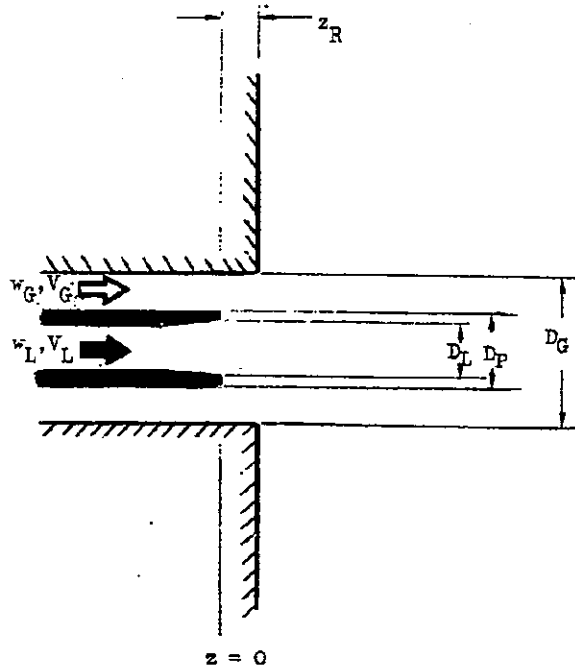


Figure 28 Schematic Representation of Coaxial Element Geometry

Because of the radial symmetry of the coaxial element, the general LISP spray correlation given by Eq. 2 may be simplified to

$$w(x,y,z) = \frac{w_{001}}{z^2} \left[ 1 + C_4' \left( \frac{x}{z} \right)^2 + C_4' \left( \frac{y}{z} \right)^2 \right] e^{-a \left[ \left( \frac{x}{z} \right)^2 + \left( \frac{y}{z} \right)^2 \right]}$$

or

$$w(r_E, z) = \frac{w_{001}}{z^2} \left[ 1 + C_4' \left( \frac{r_E}{z} \right)^2 \right] e^{-a \left( \frac{r_E}{z} \right)^2} \quad (42)$$

for  $z$  measured relative to the pseudo impingement point.

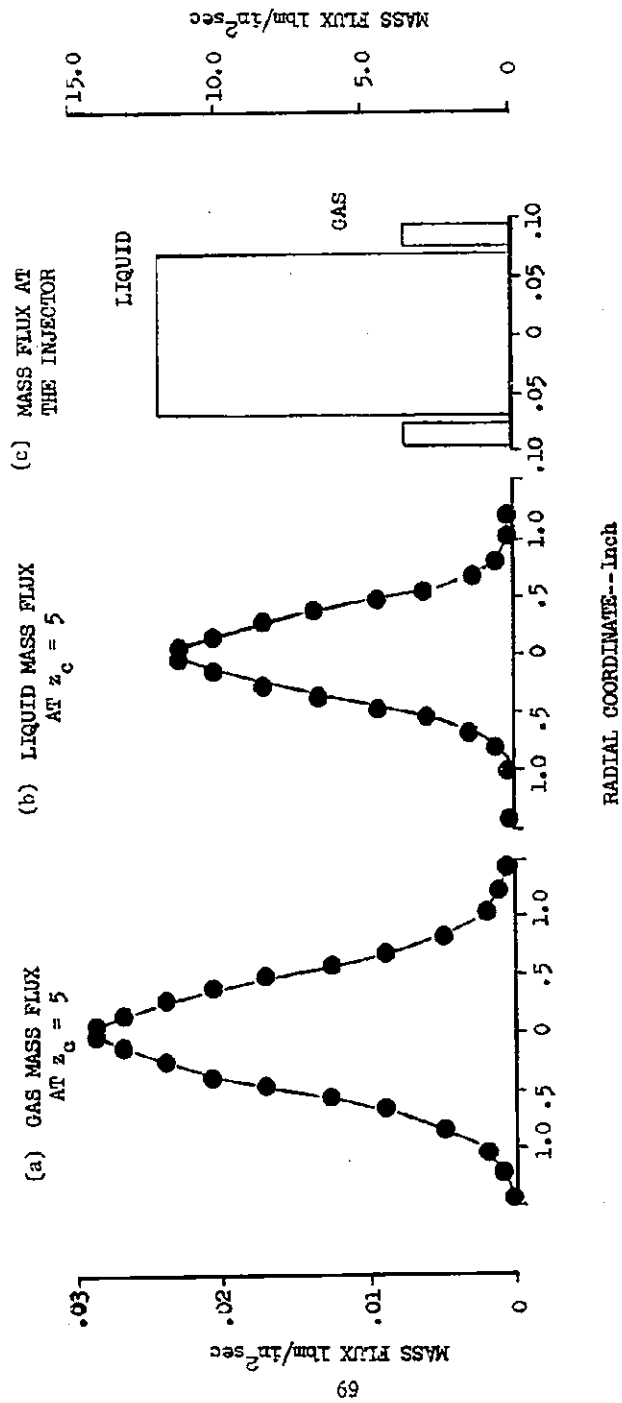


Figure 29 Typical Mass Flux Profiles for Gas/Liquid Coaxial Elements as Measured  
by R. J. Burick (Run 6, Program NAS3-11199)

The coefficient  $C_4'$  is retained in the expression to permit representation of a maximum mass flux at radial locations other than  $r_E = 0$  in the case of the gaseous propellant and to permit a flattening of the mass flux profile near  $r_E = 0$  for the liquid propellant. However, because the mass flux at the downstream collection plane,  $z_c$ , decreases monotonically with radial coordinate,  $r_E$ , coefficient  $C_4'$  must be limited by

$$C_4' \leq a$$

From Eq.42 and this intended purpose for  $C_4'$ , the final form of the coaxial element LISP correlation was chosen as

$$w_2(r, z_2') = \frac{w_{001}}{z_2'^2} \left[ 1 + a_2 \left( \frac{r}{z_2'} \right)^2 \right] e^{-a_2 (r/z_2')^2} \quad (43)$$

$$w_1(r, z_1') = \frac{w_{001}}{z_1'^2} \left[ 1 + a_1 \left( \frac{z_c'}{z_1'} \right) \left( \frac{r}{z_1'} \right)^2 \right] e^{-a_1 (r/z_1')^2} \quad (44)$$

where, with  $z$  measured relative to the post exit,

$$z_2' = z + \delta_L$$

$$z_1' = z + \delta_G$$

Note from Eq. 43 that the definition of the  $C_4'$  coefficient for the gaseous flow from orifice 1 is a function of the ratio  $z_c'/z_2'$  (the ratio of the distances between the pseudo impingement point and the cold-flow collection plane and the LISP calculation plane, respectively). This definition is made in place of a constant  $C_4$  (including  $C_4 = 0$ ) as is the case with other element types.

Calculation of the spray coefficients  $a_1$  and  $a_2$  and the source points  $\delta_L$  and  $\delta_G$  was again done by equating the experimentally determined mass flux moments to the equivalent integral of Eq. 36a and 36b, e.g.,

$$\bar{R}_{z_c} = \frac{\int_0^\infty 2\pi r^2 w(r, z_c) | \frac{dr}{E}}{\int_0^\infty 2\pi r w(r, z_c) | \frac{dr}{E}} = \frac{\int_0^\infty 2\pi r^2 w(r, z) | \frac{dr}{A}}{\int_0^\infty 2\pi r w(r, z) | \frac{dr}{A}} \quad (45)$$

The radial mass flux moment arm,  $\bar{R}_{z_c}$ , is given by

$$\bar{R}_{z_c} = \frac{7}{8} z_2' \frac{\pi}{a_2} \quad (46)$$

Distance  $\delta_L$  is evaluated by noting from Fig. 28 and 29 and the definition of  $\bar{R}$  that

$$\bar{R}_{z=0} = \frac{1}{2} D_L \quad (47)$$

Combining Eq. 46 and 47 gives

$$\frac{z_{z=0}'}{z_{z=z_c}'} = \frac{\delta_L}{z_c + \delta_L} = \frac{D_L}{3\bar{R}_{z_c}} \quad (48)$$

Equation 48 is solved for  $\delta_L$  after which  $a_2$  is evaluated from Eq. 46. A similar procedure is employed for determination of  $\delta_G$  and  $a_1$ .

The mass distribution data, correlated in this manner, were obtained from the nine cold-flow runs listed in Table 5. These tests were made with a single exit liquid orifice diameter (0.136 inch) and, essentially, a single liquid injection velocity together with a limited combination of gas injection velocities and gas annular slot widths. Results of the correlation are shown in Table 6.

Table 5 Summary of Single-Element Cold-Flow Data for Gas/Liquid Coaxial Elements\*

Run No.	$D_L^{**}$ inch	$D_P$ inch	$D_G$ inch	$\dot{W}_L$ lbm/sec	$V_L$ ft/sec	$\dot{W}_G$ lbm/sec	$V_G$ ft/sec
6	0.136	0.146	0.182	0.174	27.6	0.0333	350
12	↓	↓	0.228	0.174	27.6	0.0333	135
13	↓	↓	0.156	0.174	27.6	0.0333	630
7	↓	↓	0.182	0.154	24.5	0.0529	555
22	↓	↓	↓	0.183	29.6	0.0244	256
20	↓	↓	↓	0.154	24.5	0.0522	546
14	↓	↓	↓	0.174	27.6	0.0333	350
21	↓	↓	↓	0.183	29.6	0.0244	256

\*Symbols are defined in Fig. 28 and Nomenclature section

\*\*Liquid diameter is defined at the exit to liquid post for both uniform diameters and shallow chamfers.

Table 6 Summary of Correlated Mass Flow Parameters for Gas/Liquid Coaxial Elements\*

Run No.	$\bar{R}_1^*$ inch	$\bar{R}_2^*$ inch	$a_1$	$a_2$	$\delta_L$	$\delta_G$
6	0.424	0.494	409	428	0.60	1.56
12	0.473	0.713	329	182	0.53	1.18
13	0.419	0.423	418	609	0.61	1.73
7	0.396	0.434	470	596	0.64	1.83
22	0.448	0.533	368	351	0.57	1.43
20	0.507	0.484	302	467	0.50	1.65
14	0.574	0.585	235	291	0.44	1.30
21	0.525	0.628	282	245	0.48	1.20

\*Subscript 2 refers to liquid stream and subscript 1 to gas stream



Effective incorporation of these results into the LISP program requires that the calculated values of  $a$  and  $\delta$  be related to design parameters, such as orifice diameter, injection velocities, etc. Because  $a$  and  $\delta$  are obtained by arbitrary definitions (Eq. 42) from the experimentally determined  $\bar{R}$ , the mass moment arm was correlated with the design parameters rather than the derived terms. When coefficient  $\bar{R}$  was plotted versus gas velocity, gas/liquid velocity difference, gas momentum and gas/liquid momentum ratio, a fair correlation of  $\bar{R}$  with each of these parameters was obtained, but none was clearly superior. Momentum ratio was selected as the correlation parameter primarily to maintain consistency with the procedures employed for other element types. The best correlation was obtained by plotting the parameters  $\bar{R}_{L,Z}/(\bar{R}_{L,0}Z)$ ,  $\delta_L \bar{R}_{L,0}$ ,  $\bar{R}_{G,Z}/(\bar{R}_{G,0}Z)$ , and  $\delta_G \bar{R}_{G,0}$  against momentum ratio; these are shown in Fig. 30 and 31. The correlations presented in these graphs permit the required spray parameters  $a$  and  $\delta$  (and then  $C_d$ ) to be determined from the propellant mass flux moment arm at the coaxial element exit by means of Eq. 46 or the equivalent gaseous relation. Calculation of the spray coefficients for the LISP computer program is then possible directly from the coaxial element geometry and the injected mixture ratio.

An example of the mass profiles thus calculated for both liquid and gas with the above correlations is compared with Burick's experimental data in Fig. 32 and 33. The agreement appears satisfactory at the 5-inch collection plane. No data were available to check the prediction scheme in the region 1 to 2 inches downstream of the injector where the combustion chamber design application must be made.

The liquid velocity is obtained by utilizing the assumption that the overall velocity vector corresponds to conservation of the injection velocity such that

$$u_{z_D}(r, z_1) = \frac{z_1}{\sqrt{z_1^2 + r^2}} V_L$$

$$u_{r_D}(r, z_1) = \frac{r}{\sqrt{z_1^2 + r^2}} V_L$$

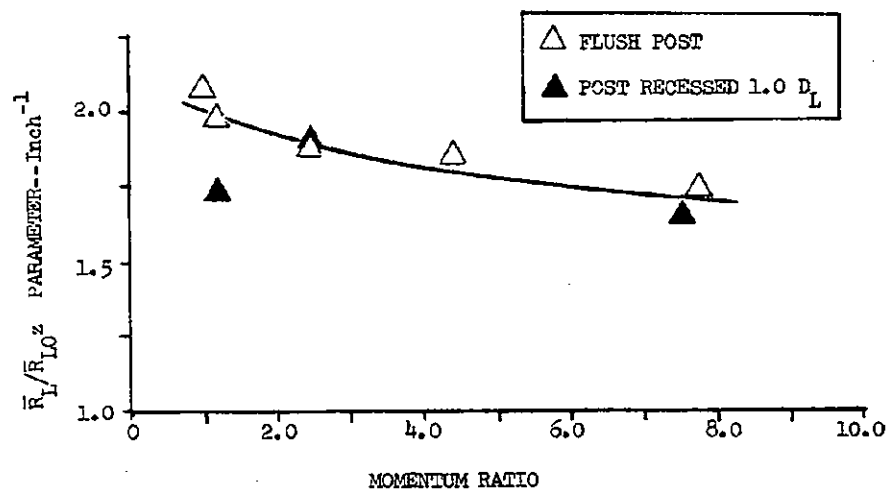


Figure 30a Variation of  $\bar{R}_L/\bar{R}_{L,0}^z$  Parameter With Momentum Ratio

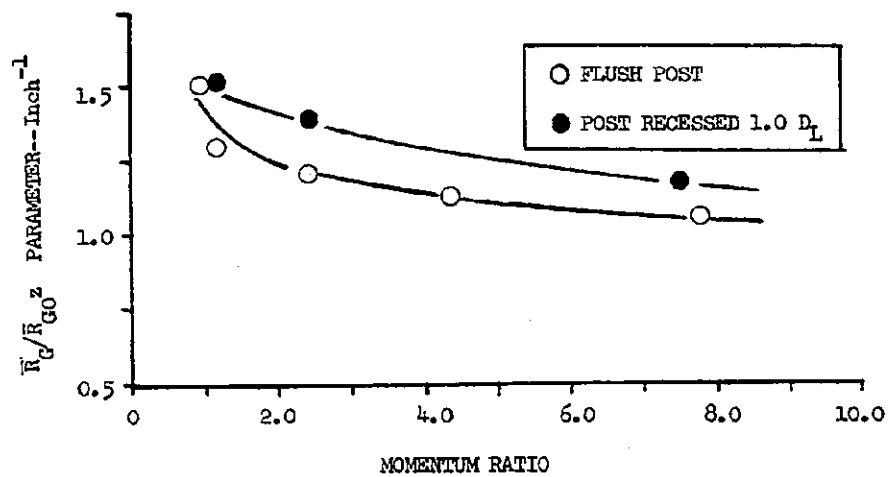


Figure 30b Variation of  $\bar{R}_L/\bar{R}_{L,0}^z$  Parameter With Momentum Ratio

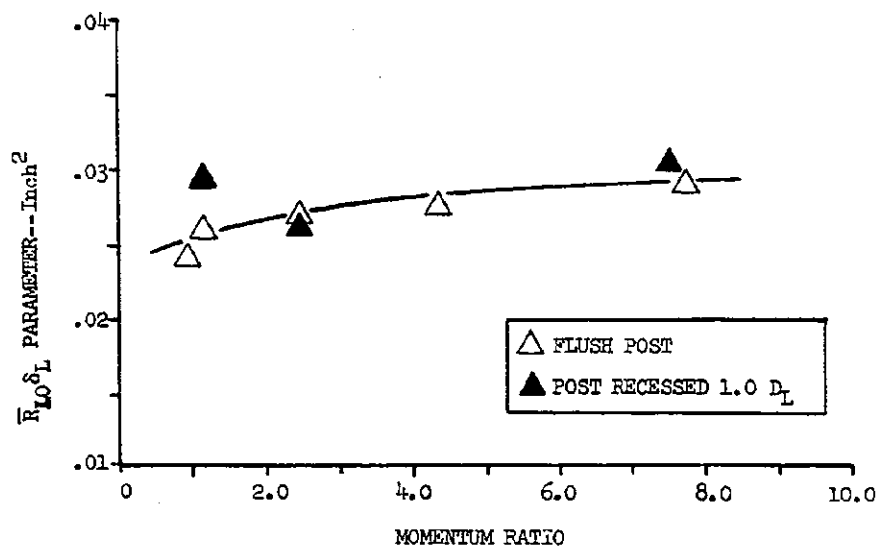


Figure 31a Variation of  $\bar{R}_{L,0}\delta_L$  Parameter With Momentum Ratio

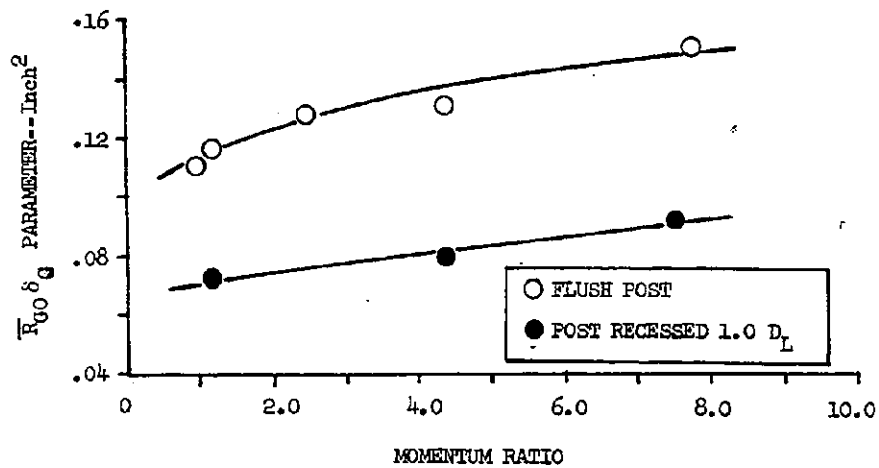


Figure 31b Variation of  $\bar{R}_{G,0}\delta_G$  Parameter With Momentum Ratio

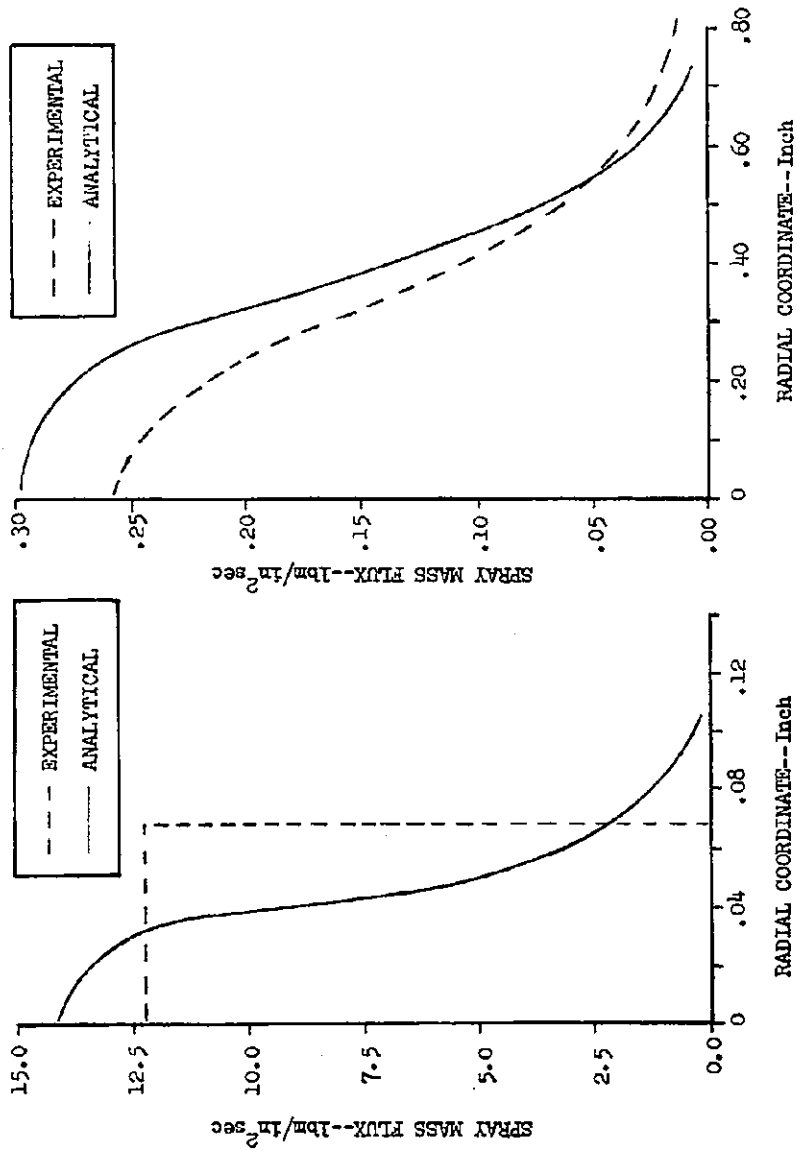


Figure 32 Spray Flux at 0.0 Inch From Injector

Figure 33 Spray Flux at 5.0 Inches From Injector

however, the gas phase is a continuum, therefore

$$w_1(r, z_1') = \rho_1(r, z_2') u_z(r, z_2')$$

or

$$u_z(r, z_2') = \frac{w(r, z_2')}{\rho(r, z_2')} \quad (49)$$

In a combustion chamber, as in cold-flow experiments, the injected gas mixes with surrounding gas, and  $\rho(r, z_2')$  is dependent upon the local mole fraction of the injectant gas which is presently impossible to predict at any distance from the injector. Close to the injector, however, it was initially assumed that the injected gas and the vaporized liquid propellant followed their original trajectories. On this basis the gas velocity is

$$u_z(r, z') = \frac{w_1(r, z') + w_{2 \text{ vap}}(r, z')}{\rho(r, z', c)}$$

where  $w_{2 \text{ vap}}$  is the mass flux of the evaporated liquid if it follows its liquid-phase trajectory and  $c$  is the local gas mixture ratio defined by

$$c(r, z') = \frac{w_{2 \text{ vap}}(r, z')}{w_1(r, z')}$$

#### Initial Vaporization for Coaxial Elements

A correlation for the vaporization of the liquid propellant from orifice 2, between the post exit and the collection plane  $z_c$  at which the LISP computer program calculations are to be made, was developed by assuming that liquid evaporation is controlled by the stripping rate of spray from the liquid jet. The stripping rate ( $\text{lbm/in.}^2 \text{ sec}$ ) was assumed to be proportional to the jet surface area and the velocity difference between the gas and liquid streams, but independent of distance

from the injector. Separate rates were assumed to apply in the recessed cup and the external chamber. Different relations are also needed for low Mach number (cup burning) and high Mach number (nonburning) injection. Consequently the following relation was assumed

$$PB_2 = [\text{Percent Vap}]_2 = \frac{K\rho_1 (V_1 - V_2)z}{\rho_2 V_2 D_2}$$

The coefficient K was evaluated from the calculations of the CSS computer program of Sutton and Schuman (Ref.14 ) for the  $\text{GH}_2/\text{LO}_2$  propellant combination at a chamber pressure of 500 psia under conditions of no cup burning. The results led to

$$PB_2 = [\text{Percent Vap}]_2 = \frac{\rho_1 (V_1 - V_2)}{\rho_2 V_2 D_2} [280 \Delta z_{\text{cup}} + 39 (z_c - \Delta z_{\text{cup}})] \quad (50)$$

This expression was incorporated into the LISP program. Its general effectiveness in the prediction of the initial vaporization of other propellant combinations or for  $\text{GH}_2/\text{LO}_2$  under cup burning conditions has not been evaluated.

#### Gaseous Mass Flux Distribution With Combustion

As discussed above, the experimental cold-flow distributions for the gas/liquid coaxial element could be well correlated with the general LISP formulation. This suggests that mixing-limited  $c^*$  combustion efficiencies can probably be calculated as effectively for gas/liquid elements from cold-flow correlations as can be done with liquid/liquid injection. However, for heat transfer calculations with the Injector/Chamber Compatibility Model, use of the cold-flow distribution of gas was found to be impractical. The difficulty arises primarily because of the high degree of liquid vaporization which occurs close to the injector; during the demonstration analysis made of the AFRPL coaxial element injector discussed later in this report, vaporization of 54 percent of the injected oxygen was calculated in the first inch downstream from the post exit. Because the cold-flow model constrained the hot gas generated from the mixing of the oxygen vapors and injected hydrogen to the cold-flow jet, and because of the continuity requirements imposed

by Eq. 49, the calculated gas velocities in the jets were supersonic, certainly a physically unacceptable prediction for a flow field assumed to have negligible transverse pressure gradients.

Consequently, for calculation of the combustion gas flow field, the calculation of the mass flux distribution was modified by the following assumptions:

1. The gaseous propellant and the vapors from the evaporated liquid propellant from a single element are assumed to mix intimately and react to chemical equilibrium at the local resultant mixture ratio with corresponding gas molecular weight and temperature.
2. Momentum of the jet is assumed to be conserved, i.e., the jet expands with combustion such that the momentum of the resultant hot gas and of the unevaporated liquid are equal to the initial momentum of the injected propellants.
3. The distribution of the unevaporated liquid is assumed to be described by the corresponding cold-flow mass flux distribution.
4. The mass flux distribution of the hot combustion gas from a single element is assumed to be described by

$$w(r,z) = \frac{w_{001}}{z^2} e^{-a_1' \left(\frac{r}{z}\right)^2} \quad (51)$$

where  $w_{001}$  and  $a_1'$  are defined by mass continuity and the momentum continuity of assumption 2 above.

With these assumptions, the momentum of the hot-gas jet,  $M_E$ , is given by

$$M_E = \int w v dA = \int_0^\infty \frac{2\pi r}{\rho_{HG}} \frac{w_{001}^2}{z^4} e^{-2a_1' \left(\frac{r}{z}\right)^2} dr$$

or

$$M_E = \frac{\pi w_{001}^2}{2a_1' \rho z^2}$$

The total mass of the hot gas jet,  $S$ , is

$$S_E = \int_0^{\infty} 2\pi r \frac{w_{001}}{z^2} e^{-a_1' \left(\frac{r}{z}\right)^2} dr = \frac{\pi w_{001}}{a_1}$$

therefore, the specific momentum of the hot gas is:

$$\frac{M_E}{S_E} = \frac{w_{001}}{2az^2}$$

The sum of the hot-gas jet momentum and the unevaporated liquid momentum must equal the initial momentum of the jet, i.e.,

$$\frac{w_{001}}{2az^2} = \frac{M_E}{S_E} = S_1 V_1 + S_2 V_2 \left(1 - \frac{PB_2}{100}\right) \quad (52)$$

Mass continuity requires that

$$\frac{\pi w_{001}}{a_1} = S_E = S_1 + S_2 \cdot \frac{PB_2}{100} \quad (53)$$

Equations 52 and 53 are solved simultaneously for  $a_1'$  and  $w_{001}$  and the resultant values used in Eq. 51 in place of the cold flow values.

The analytical model described in the paragraphs above describes the combustion gas flow field for a single coaxial element in a fashion that conserves both mass and momentum within a single element. In a multi-element injector, however, momentum will be conserved only if the gas velocity profiles do not significantly overlap. If the profiles for adjacent elements do appreciably overlap, then the linear addition of mass contributions from each element according to Eq. 1 is not a physically sound assumption. Because of this complication, the LISP calculation of gas/liquid mass flux profiles has also been set up to make the alternate calculation of a uniform gas velocity and mixture ratio across the entire chamber slice. This velocity is defined such that



$$u_z = \frac{1}{c \frac{A}{g} c} \sum_i \left( s_{1_i} + s_{2_i} \cdot \frac{PB_2}{100} \right) \quad (54)$$

If inspection of the LISP calculated gas velocity distribution defined by adding single element contributions indicates that impossible local velocities are defined\*, then the definition of a uniform gas velocity is to be utilized in the succeeding calculations with 3D-COMBUST or STRMTB. It must be noted, however, that the uniform gas velocity definition will ordinarily result in the conservation of both mass and momentum for only a single value of initial vaporization.

As discussed later in the Program Demonstration portion of this report, a uniform combustion gas velocity was defined in the analysis of an AFRPL multi-element gas/liquid coaxial injector. Problems encountered in the overall analysis of that injector indicate that the simplification involved in the definition of a uniform axial gas velocity will not be an important consideration until required modifications to the 3D-COMBUST computer program are made.

---

\* An extreme example of an impossible calculated velocity distribution is the case where the velocities at (r,  $\theta$ ) locations between the (r,  $\theta$ ) coordinates of the elements are greater than  $w_{001}$ .

## DROP SIZE DEFINITIONS

The LISP predictions of mean droplet diameter have been changed from the values presented in Ref. 1 to include both corrections of initial hydraulically produced  $D_{30}$  as defined in hot wax atomization experiments and (in the case of like doublets and like doublet pairs) of the  $\bar{D}$  resulting from a more detailed definition of secondary atomization. Revised definitions of a hot wax mean drop diameter,  $\bar{D}_{HW}$ , were provided by Dickerson (private communication) whose data (Ref. 4) provided the original definitions of  $\bar{D}_{HW}$  in Ref. 1. Modifications to the calculation of  $\bar{D}$  for like doublets were developed by Combs as part of the DER (Distributed Energy Release) Analysis (Ref. 6). The present correlations of  $\bar{D}_{HW}$  in LISP are:

### Unlike Doublet (Larger Diameter Orifice)

$$\bar{D}_{HW} = 1.27 \frac{D_{opp}^{.38}}{D} \frac{1}{U_D^{1.19} U_{D,opp}^{.86}} \quad (55a)$$

### Unlike Doublet (Smaller Diameter Orifice)

$$\bar{D}_{HW} = 2.29 \frac{D^{.27} D_{opp}^{.023}}{U_D^{.74} U_{D,opp}^{.33}} \quad (55b)$$

### Triplet and 4-on-1 (Center Orifice)

$$\bar{D}_{HW} = 0.85 \frac{D \cdot 1 D_{opp}^{.12}}{U_D^{.74} U_{D,opp}^{.33}} \quad (55c)$$

### Triplet and 4-on-1 (Outer Impinging Streams)

$$\bar{D}_{HW} = 3.82 \frac{D^{.68}}{D_{opp}^{.35} U_D^{.56} U_{D,opp}^{.57}} \quad (55d)$$

For the unlike doublet, triplet, and 4-on-1 elements, no changes have been made in the coefficient  $J_A$  and B which appear in Eq. 10. The currently-used values are therefore:

$$\begin{aligned} J_A &= 0.8, \quad B = 250 && \text{(unlike doublet)} \\ J_A &= 0.03, \quad B = 310 && \text{(triplet, 4-on-1)} \end{aligned}$$

For like doublets and like-doublet-pairs, the correlation developed by Combs for the combined effects of hydraulic and secondary breakup is

$$\bar{D} = 1.524 \left[ 2.54 \sqrt{\frac{u_D}{D}} + \left( \frac{1.075}{C_{PR}} \right) \left( \frac{\epsilon_c - 1}{\epsilon_c + 3} \right) \left| \frac{480}{\epsilon_c} - u_D \right| \right] \quad (55e)$$

where

$\epsilon_c$  is the contraction ratio which defines the gas velocity

$C_{PR}$  is a property correction parameter Ref. (15, 5) equal to

$$\left( \frac{\mu \sigma}{\rho_2 \rho_G} \right)^{0.25}$$

No attempt has been made to incorporate a recommended drop size for gas/liquid coaxial elements. As discussed elsewhere in this report (see Case 4 in the Program Demonstration section of this report), an appreciable amount of work remains to be done before a satisfactory model for the local gas/liquid combustion process is available to replace the  $k'$  droplet evaporation model which has been carried over from the liquid/liquid combustion analyses. Any recommendations for drop size are therefore premature.

#### INITIAL VAPORIZATION DEFINITIONS

A "combustion-reduced" mass flux of spray is calculated in LISP on the basis of a simplified  $k'$  evaporation model. The model is based upon the heat balance around a single drop in a hot gas which is given by

$$\Delta H_v \rho_l u_{D_z} \frac{d}{dz} \left( \frac{\pi}{6} D_D^3 \right) = \pi D_D^2 \left( \frac{k}{D_D} \right) Nu (T_g - T_{SAT}) \quad (56)$$

Re-arranging and integrating Eq. 56 results in Eq. 11 if the definition is made

$$C_{KP} = \frac{4 Nu k}{\rho_l \Delta H_v} (T_g - T_{SAT}) \quad (57)$$

A consistent calculation of the expected degree of vaporization of the liquid spray between the injector and a desired LISP collection plane is therefore possible by use of Eq. 11 together with the combustion gas properties of the propellant combination and the liquid propellant injection conditions. Although the above calculation can be made in a consistent manner, the resultant prediction of initial vaporization is expected to be considerably in error because the conveniently assumed definitions for most of the terms in Eq. 56 and 11 ( $\bar{D}$  for  $D_D$ , the Nusselt number applicable to an isolated drop for  $Nu$ , a bulk mixture ratio definition of gas temperature for  $T_g$ , etc.), can be applied reasonably accurately only at distances more than 1-2 inches downstream of the injector element impingement points. However, it is reasonable to assume that actual experimentally determined spray vaporization close to the injector for conventional doublet and triplet type elements should at least scale with injection parameters and propellant properties according to Eq. 11. In this case, Eq. 57 becomes

$$C_{KP} = 4\psi \frac{Nu k}{\rho_l \Delta H_v} (T_g - T_{SAT})$$

where the accommodation coefficient  $\psi$  should be approximately a constant for a given injector element type and chamber contraction ratio.

To obtain a definition of the accommodation coefficient  $\psi$ , an analysis was made of the pressure profiles obtained during the motor firings made with the 8-element unlike doublet injector ICC 2A and the 12-element triplet injector ICC6. Because of uncertainties in the measurement of both chamber pressure

and propellant flow rate with the triplet element, only the results obtained with ICC2A proved useful for the definition of initial vaporization. The procedure employed for the analysis consisted of the following steps:

- (1) The overall  $\eta_c^*$  combustion efficiency was assumed to be defined by

$$\eta_c^* = \eta_{vap} \eta_{mix}$$

Based upon the results of four cold flow spray sampling experiments with ICC2A over a range of mixture ratios from 1.16 to 1.83 which gave values of  $\eta_{mix}$  ranging from .928 to .952, a value of .95 for  $\eta_{mix}$  was assigned to ICC2A for mixture ratios between 1.3 and 1.7 which covered the motor firings analyzed.

- (2) From the measured overall  $\eta_c^*$  efficiencies and the definition of  $\eta_{mix}$ ,  $\eta_{vap}$  was calculated and defined to be the actual fraction of the propellants vaporized at the throat. In the subsequent discussion, this definition of  $\eta_{vap}$  is extended to mean the fraction of propellant flow vaporized at any given distance from the injector.
- (3) To utilize the axial pressure profile through the combustion chamber to define the axial variation of  $\eta_{vap}$ , it was necessary to establish a baseline definition of the variation of  $\eta_{vap}$  between the nozzle throat (or start of nozzle convergence where applicable) and the axial station of the most downstream of the chamber pressure measurements which was at 6.15-inch from the injector (see Table 9). To accomplish this, performance data obtained with ICC2 during the previous Injector/Chamber Compatibility Project (Ref. 1, Table 9) were analyzed. Data obtained at chamber lengths of 5.0-, 8.0-, and 13.0-inch were cross plotted against chamber length to give the approximate variation of  $\eta_{vap}$  with chamber length assumed to be applicable for distances greater than 6.0-inch downstream from the injector. Based upon the cross plotted data, a change of only 3.1 percent in propellant vaporization was expected between the chamber pressure measurement at 6.15-inch and the nozzle throat at test conditions.

- (4) With a baseline value of  $\eta_{\text{vap}}$  established at a distance of 6.15-inch from the injector, vaporization at distances closer to the injector was calculated from the functional relationship between specific area and pressure for a compressible fluid (Ref. 16 ).

$$\frac{\bar{A}}{A_c} = \sqrt{\left(\frac{\gamma-1}{2}\right) \frac{\left(\frac{2}{\gamma+1}\right)^{\frac{\gamma+1}{\gamma-1}}}{\left[1 - \left(\frac{P}{P_0}\right)^{\frac{\gamma-1}{\gamma}}\right] \left(\frac{P}{P_0}\right)^{2/\gamma}}} \quad (58)$$

where the specific area  $\bar{A}$  is the cross sectional area per unit mass of combustion gas. As combustion proceeds with distance from the injector in a thrust chamber, the specific area decreases even though the geometric area may remain constant.

To utilize Eq. 58 , the assumption is made that the specific area is related to the actual chamber cross sectional area by

$$\frac{\bar{A}(z)}{A_c} = \frac{1}{\eta_{\text{vap}}}$$

or

$$\frac{\eta_{\text{vap}}(z)}{\eta_{\text{vap}}(6.15)} = \frac{\bar{A}(6.15)}{\bar{A}(z)}$$

Area  $\bar{A}$  is obtained from Eq. 58 , the measured local chamber pressure, and the value of  $\eta_{\text{vap}}$  at 6.15-inch (as obtained from the  $c^*$  efficiency together with the 3.1 percent correction factor obtained from step (3) above).

Use of pressure profiles to define the axial variation of  $\eta_{\text{vap}}$  is facilitated by a low contraction ratio which produces a reasonable Mach number (greater than .3) and consequently measurable pressure differences between stations. As a consequence, although injector ICC2A was fired at contraction ratios of 1.04, 2.15, and 4.3, the useful data were obtained at the lowest contraction ratio. In addition, although chamber pressure measurements were obtained at a distance

of 1.0-inch from the injector, the pressure field at this point may be strongly affected by a combination of 3-dimensional effects, spray drag, and Rayleigh heating phenomena; therefore, no significance was attached to measurements in this region.

Analytical results are presented in Fig. 34. At a distance of 1.4-inch from the injector (1.0-inch downstream of the element impingement points),  $\eta_{vap}$  was estimated to be .20 by extrapolation of the measurement at 2.0-inch to zero vaporization at the impingement point for the conditions of the low contraction ratio experiments. At a contraction ratio of 2.15, the data are extrapolated to predict an  $\eta_{vap}$  of .15 at the same location. Because secondary droplet breakup should be more intense at the lower contraction ratio, the trend in initial vaporization is in agreement with droplet combustion theory; however the reliability of the higher contraction is low because of the above mentioned difficulties in accurately measuring the smaller pressure differences. As a consequence, only the low contraction ratio curve for  $\eta_{vap}$  was applied to calculating the accommodation coefficient  $\Psi$ . Based upon the limited data presented in Fig. 34 and use of Eq. 11 and 9, coefficient  $\Psi$  has been assigned a value of 0.102 in LISP. Although the value of this coefficient is strictly speaking applicable only to unlike doublets and very low contraction ratios, it must be assumed to be a constant for all injection conditions until more data become available.

#### INITIAL PERFORMANCE PREDICTIONS

Additional features which have been added to the original LISP program include an estimation of the mixing limited chamber pressure efficiency  $\eta_{mix}$  together with a specification of the gas phase parameters in the LISP collection plane which are subsequently required by the 3D-COMBUST program. The calculation of  $\eta_{mix}$  is based upon the method developed by Wrobel (Ref. 17)

$$\eta_{mix} = \frac{\sum_j w_j c_j^*}{c^*_{bulk} \sum_j w_j}$$

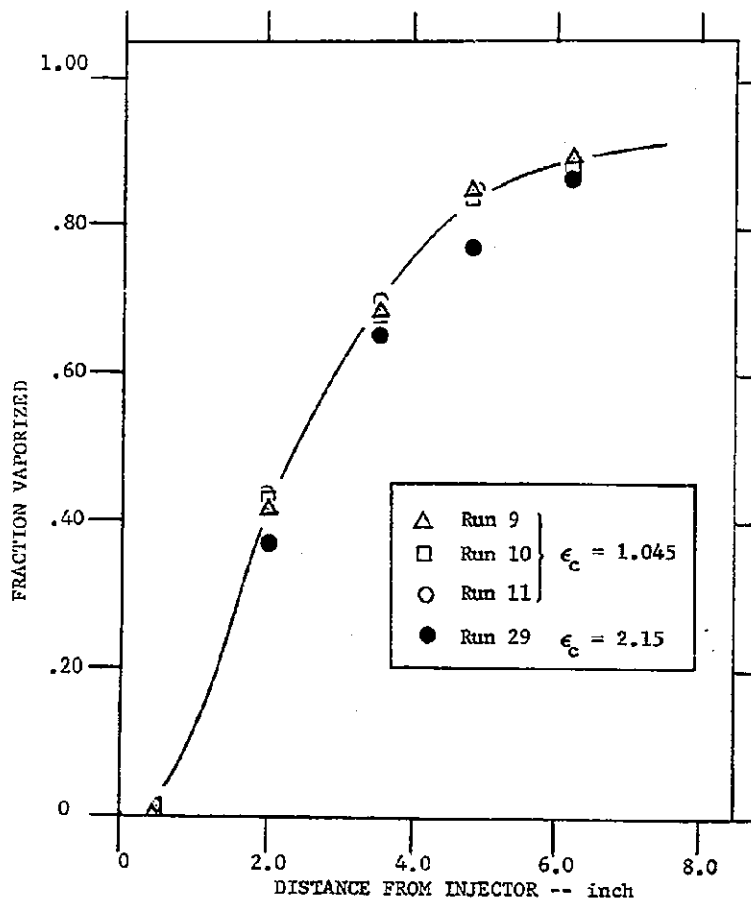


Figure 34 Variation of Fractional Propellant Vaporization With Distance From the Injector for ICC2A



with the summation being made over all the mesh points  $j$  in the LISP collection plane. This preliminary calculation assumes that mixing is completed at the LISP collection plane and that propellant vaporization will be completed upstream of the throat; therefore, it is subject to revision by the subsequent calculations of the 3D-COMBUST and STRMTB combustion programs. With  $\eta_{mix}$  defined, the chamber pressure is then estimated on the basis of

$$P_c = \frac{\eta_{mix} c_{bulk}^*}{A^* g_c} \sum_j w_j \quad (59)$$

Gas phase parameters, calculated on the basis of the mean mixture ratio of the propellants vaporized upstream of the LISP collection plane (see the preceding paragraphs above) and the chamber pressure, include the gas temperature, gas density, and mean gas velocity.

#### RESUME OF CURRENT LISP PROGRAM

The present version of the LISP computer program consists of a main or calling program and a family of subroutines coded into Fortran IV or Fortran IV H language. A logical map of the LISP system which follows the calculations which are or can be performed is shown in Fig. 35. In this chart, the flow of the steps in the main program follow the leftmost column, the calculations in the principal subprograms are shown in the center column, and the operations in the supporting routines (including storage and interpolation of tabular data) are presented in the rightmost column.

#### Input Data

The input data read into the LISP program may be summarized as follows:

- (1) Two punch cards which describe the calculation to be performed (Alphanumeric format)



- (2) General data describing the total number of elements, the number of separate kinds of elements, the number of  $r$  and  $\theta$  mesh lines for the analysis and their spacing, the number of  $z$  locations for the calculations, baffle locations, and injector pressure drops.
- (3) The specifications for the different kinds of elements including element types (doublet, triplet, etc.), orifice diameters and discharge coefficients, droplet diameters (if not to be calculated by subprogram DSIZE),  $z$  coordinate of the impingement point, angular orientation of the element coordinate system to the chamber coordinate system, and spray coefficients (for Type 8 elements). The similar elements are assigned to groups according to the designation LSPEC.
- (4) The particular data for the individual elements including their  $r$  and  $\theta$  coordinates, the cant of the element relative to the chamber, and the group LSPEC in which its other specifications are defined.
- (5) The properties of the liquid propellants and their combustion gases including liquid density, temperature and latent heat of vaporization, and the combustion gas viscosity, temperature, specific heat ratio, molecular weight and characteristic exhaust velocity ( $c^*$ ) as tabular functions of mixture ratio.

#### Output Data

The printed output of the LISP program contains, first of all, a tabulation of the input data. The LISP output calculations are presented in four tables which respectively list:

- (1) The coordinates, propellant flow rates, and drop sizes for each of the injector elements considered in the analysis.
- (2) The cold flow mass fluxes ( $\text{lbm/in}^2\text{sec}$ ), collected mass ( $\text{lbm/sec}$ ), velocity components ( $\text{ft/sec}$ ) in the axial, radial and angular directions, and mean drop diameters at each of the chamber mesh points employed in the analysis. Separate values are listed for fuel and oxidizer spray.

- (3) The weight flux and average drop diameters of each propellant at each chamber mesh point after allowance for vaporization between the injector elements and mesh points together with the percent of each propellant vaporized.
- (4) The weight flux, average drop diameter, gas mixture ratio, gas temperature, and gas velocity at each mesh point for a gas/liquid coaxial injector.

In addition to the four tables described above, the calculated mixing efficiency ( $\bar{E}_m$ ), mixing limited  $c^*$  efficiency ( $\eta_{mix}$ ), chamber pressure, and the mean mixture ratio, temperature, density and axial velocity of the vaporized propellants are also listed.

In addition to the printed output, the required punch card input to the 3D-COMBUST program is provided. This deck includes the spray mass fluxes, velocity vectors, and drop diameters at each of the chamber mesh points to be employed in the subsequent combustion analysis.

PHASE 2: DEVELOPMENT OF INJECTOR FACE  
HEAT TRANSFER ANALYSIS

ANALYTICAL MODEL

The initially developed overall analytical model was purposely formulated to avoid detailed treatment of the near-injector gas-flow field within the injection/atomization zone of Fig. 1. However, to analyze the local heat transfer rate to the injector face an analytical description of gas flows in this region is required.

As indicated in the Analytical Model section of this report, the gas-flow field near the injector was assumed to exhibit recirculatory flows which are driven by the pumping action of the individual element spray jets. This model was developed through analysis of the array of spray jets shown in Fig. 11. Because of the interphase drag the gas velocity ( $u_z$ ) in the dense core of each jet should be roughly equal to the spray velocity or the jet injection velocity. Also because the overall flowrate of gas near the injector face is low, the gas velocity must fall off sharply with distance outside each jet boundary. Finally, the gas boundary layer around each jet must be very thin near the injector face and must become progressively thicker in the downstream direction.

Although a rigorous solution of the gas-flow field could be attempted by the simultaneous solution of the continuity, momentum, and energy relationships, it is impractical. Therefore, because of the complexity of the three-dimensional two-phase flow equations, a version of the integral boundary layer technique was used to calculate the velocity and oxidizer-concentration profiles in the near-injector region. With the integral boundary layer technique, functional relationships containing several unspecified constants are assumed for the axial gas velocity distribution and for the concentration distribution. These constants are then determined from the boundary conditions, requirements for continuity of mass, and from experimental data.

Based on the work of Keagy, Weller, Reed, and Reid (Ref. 18 ), the velocity and concentration profiles around a single liquid jet, or spray fan, were assumed to exhibit similarity at all cross sections. It was further assumed that the profiles could be approximated by error functions. Thus, in the near-injector region, axial gas velocity was represented by a relationship of the form

$$u_z = c_1 + \sum_{\text{elements}} C_{u_i} e^{-\beta_i \left( \frac{r'_i - r_{o_i}}{z} \right)^2}$$

where  $r/z$  is the similarity variable and where the origin of the  $r'_i$  coordinate system was chosen as the center of the  $i^{\text{th}}$  element and  $r_{o_i}$  is the liquid core or spray radius as shown in Fig. 36 . The constants  $\beta_i$  must be determined from experimental data. If all of the elements are the same, then a satisfactory approximation is obtained assuming all of the  $\beta_i$ 's are equal. The boundary conditions for the axial velocity are  $u_z = u_{z_o}$  at  $r = r_{c_j}$  and  $\theta = \theta_{c_j}$  (Fig. 36'). Hence, for any mesh point  $j$

$$u_{z_{c_j}} = c_1 + \sum C_{u_i} e^{-\beta_i \left( \frac{r'_{i_j} - r_{o_i}}{z} \right)^2} \quad i = 1, \text{ number of elements}$$

where

$$r'_{i_j}{}^2 = r_{c_i}^2 + r_{c_j}^2 - 2r_{c_i} r_{c_j} \cos(\theta_{c_i} - \theta_{c_j})$$

Note that  $r_{c_i}$  and  $\theta_{c_j}$  can be functions of  $z$ , so that both interelement and inter-jet calculations can be performed with the same velocity function.

The global continuity equation requires that

$$\bar{u}_z A_c = \iint_{A_c} u_z r dr d\theta \quad (61)$$

where  $A_c$  is the chamber cross-sectional area. Eq. 61 assumes a constant gas density.

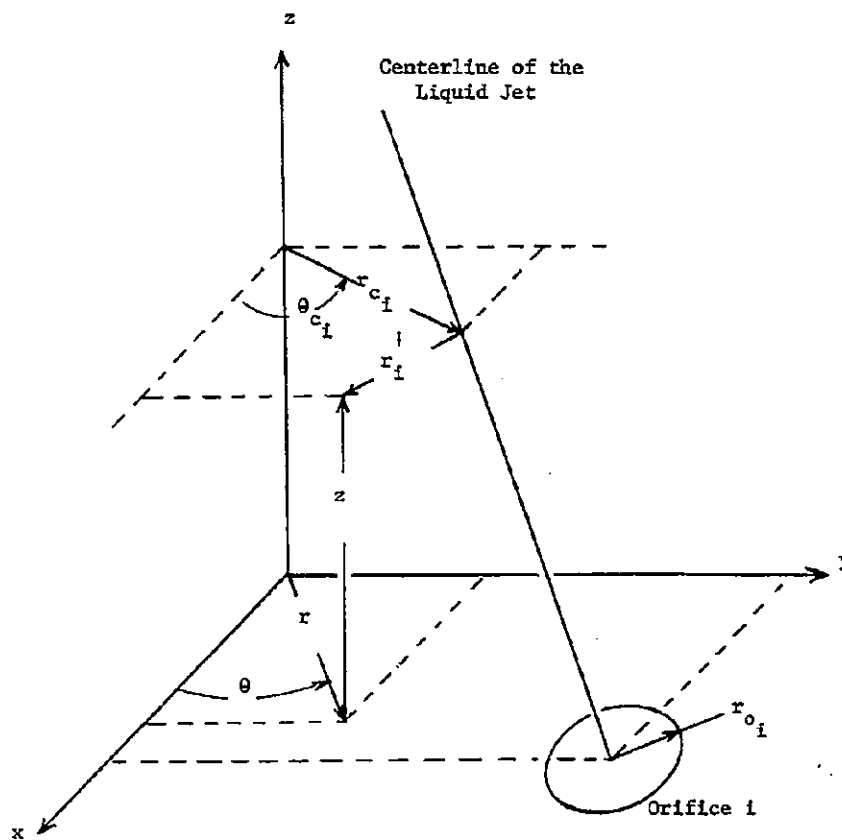


Figure 36 Coordinate System for Location of Liquid Jet

With the assumed velocity distribution equation, the global continuity equation becomes

$$\bar{u}_z A_c = C_1 A_c + \sum_i C_{u_i} \frac{\pi z}{\sqrt{\beta_i}} \left[ \sqrt{\pi} o_i + \frac{z}{\sqrt{\beta_i}} \right] \quad (62)$$

Employing methods for solution of simultaneous linear equations, the variable  $C_1$  and the variables  $C_{u_i}$  ( $i = 1, 2, \dots, n$ ) are calculated from the boundary conditions and from the global continuity equation.

A similar relationship was chosen for the concentration distribution,

$$C_{\text{oxid}} = C_2 + \sum_{\text{elements}} C_{c_i} e^{-\mu_i \beta_i \left( \frac{r_i' - r_{o_i}}{z} \right)^2} \quad (63)$$

where  $\mu_i$  is determined from experimental data. The boundary conditions are

$$C_{\text{oxid}} = C_{\text{oxid } c_j} \text{ at } r = r_{c_j} \text{ and } \theta = \theta_{c_j}$$

Hence,

$$C_{\text{oxid } c_j} = C_2 + \sum_i C_{c_i} e^{-\mu_i \beta_i \left( \frac{r_i' - r_o}{z} \right)^2}$$

The global continuity equation for the oxidizer is

$$\bar{u}_{\text{ox}} A_c = \iint_{A_c} C_{\text{oxid}} u_z r dr d\theta \quad (64)$$

Equation 64 again assumes that the gas density is constant. Combining the relations for gas velocity and mixture ratios gives



$$C_{\text{oxid}} u_z = C_2 u_z + \sum_i C_{u_i} C_{c_i} e^{-\beta_i (1+\mu_i) \left( \frac{r_i^2 - r_{o_i}^2}{z} \right)}$$

Therefore, by integration the global continuity equation becomes

$$\begin{aligned} \bar{u}_{ox} A_c &= \bar{u}_z A_c C_2 \\ &+ \sum_i C_{u_i} C_{c_i} \frac{\pi z}{\sqrt{\beta_i (1+\mu_i)}} \left[ \sqrt{\pi} r_{o_i} + \sqrt{\frac{z}{\beta_i (1+\mu_i)}} \right] \end{aligned} \quad (65)$$

Again solving the simultaneous linear equations, the variable  $C_2$  and the variables  $C_{c_i}$  ( $i = 1, 2, \dots, n$ ) are calculated from the oxidizer boundary conditions and the oxidizer global continuity equation.

This analysis of the flow field near the injector face allows subsequent calculations of the heat transfer to the injector face. Injector face heat flux is defined by

$$q/A = + k \left. \frac{\partial T}{\partial z} \right|_0 \quad (66)$$

With the normal temperature gradient being obtained from the energy equation. At present, it is unreasonable to attempt solution of the three-dimensional energy equation for all locations near the injector face. The near injector temperature profile is calculated, therefore, from a one-dimensional equation based on the control volume shown in Fig. 37, where the convective and conductive energy fluxes are:

Convection into the control volume

$$\rho_{u_z} C_p T + C_p T \frac{\partial}{\partial z} (\rho u_z) \Delta z$$

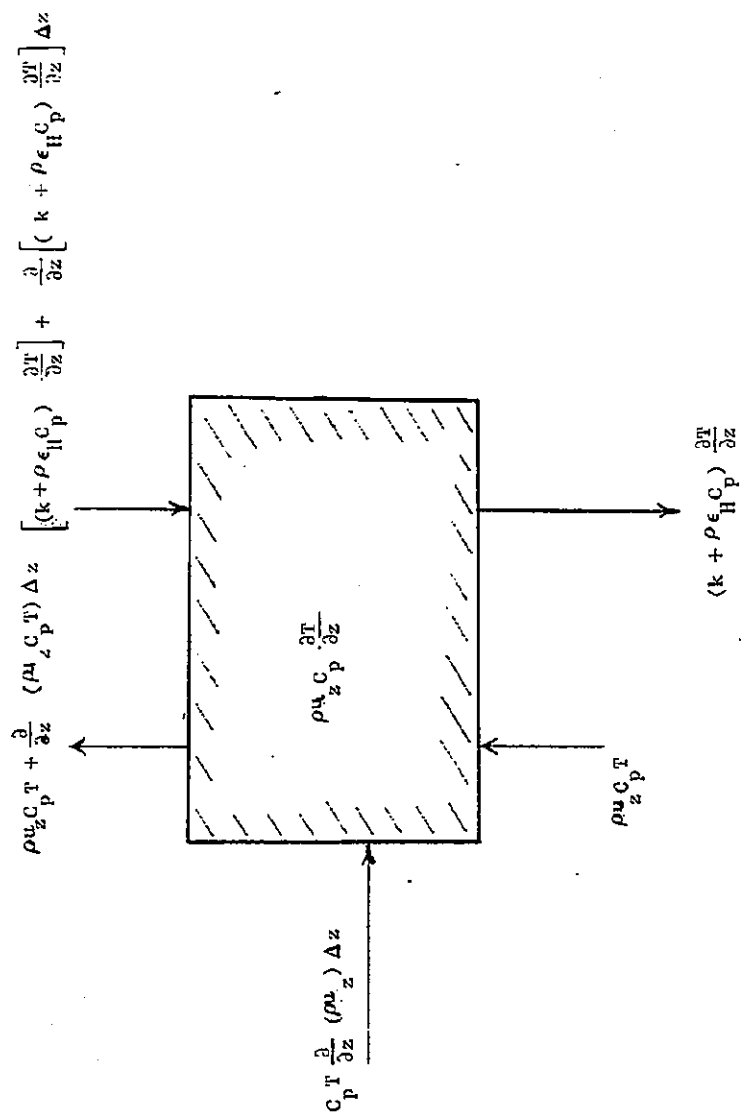


Fig. 37 Energy Control Volume for the IHTM Program

Convection out of the control volume

$$\rho u_z C_p T + \frac{\partial}{\partial z} \left[ \rho u_z C_p T \right] \Delta z$$

Conduction out of the control volume

$$\left[ (k + \rho \epsilon_H C_p) \frac{\partial T}{\partial z} \right]$$

Conduction into the control volume

$$\left[ (k + \rho \epsilon_H C_p) \frac{\partial T}{\partial z} \right] + \frac{\partial}{\partial z} \left[ (k + \rho \epsilon_H C_p) \frac{\partial T}{\partial z} \right] \Delta z$$

Energy generation rate within the control volume

$$\rho u_z C_p \frac{\partial T_E}{\partial z}$$

where  $T_E$  is the local equilibrium temperature based on the local concentration (mixture ratio).

Thus, the energy balance yields the following simplified energy equation

$$\frac{\partial}{\partial z} \left[ (k + \rho \epsilon_H C_p) \frac{\partial T}{\partial z} \right] = C_p u_z \frac{\partial}{\partial z} (T - T_E)$$

The effective eddy thermal conductivity was defined by means of a modified Prandtl mixing length,

$$\epsilon_H = C_\ell z^2 \left| \frac{\partial u_z}{\partial z} \right|$$

where  $C_\ell$  is determined from experimental data.

#### CORRELATION OF EXPERIMENTAL DATA WITH THE ANALYTICAL MODEL

Injector-face heat transfer data from the motor firings described later in this report with the ICC 2 and ICC 6 injectors were used to specify the empirical

velocity decay constants  $\beta_i$  and the effective eddy thermal conductivity  $\epsilon_H$  that appear in the preceding equations of the analytical model. The coefficient for each entire injector (constants  $\beta_i$ ) were set equal to each other; then a value of  $\beta_i = 0.125$  was selected after several trials to get the best simplified correlation between model calculations and experimental data.

Several expressions for the effective eddy thermal conductivity and the coefficient  $C_Q$  were tried including Prandtl's assumption that  $C_Q$  is a constant. However, with a constant value of  $C_Q$ ,  $\beta_i$  was found to be a strong function of injector type and spacing, a requirement which was considered to be unacceptable. Examination of the usual formulation of the mixing length, which involves a shear stress and thence an equivalent length relationship to any pressure gradients (the constant force across a given cross sectional area), indicated that the equivalent length must be related to the spacing between orifices. When  $C_Q$  was interpreted in this fashion, it was possible to correlate

$$C_Q = (\text{distance between orifices})^2 \times (55.6)$$

The concentration decay rate constants ( $\mu_i$ ) are expected to be functions of the propellant system and the relative vaporization rates of the propellants. Because both the ICC 2 and ICC 6 injectors used the same propellant combination, the constants  $\mu_i$  were set equal to each other and a value of 1.0 was assigned to make the concentration profile similar to the velocity profile. The assumptions of similar velocity and concentration profiles are reasonable for a gas if the spray jet has a well-defined radius  $r_o$ .

The shape of the heat flux contours on injectors ICC 2 and ICC 6, as predicted by the analytical model are shown in Fig. 38 through 40. The figures show the face heat flux contour lines within a representative 45-degree sector which, because of symmetry, describes the heat flux to the entire face of the two injectors. Comparisons of model predictions with experimental data from three heat flux transducers in the face of the ICC 6 triplet injector are presented in Fig. 41 through 43. Finally, comparisons between measured and predicted results for two heat flux transducer locations on the face of unlike

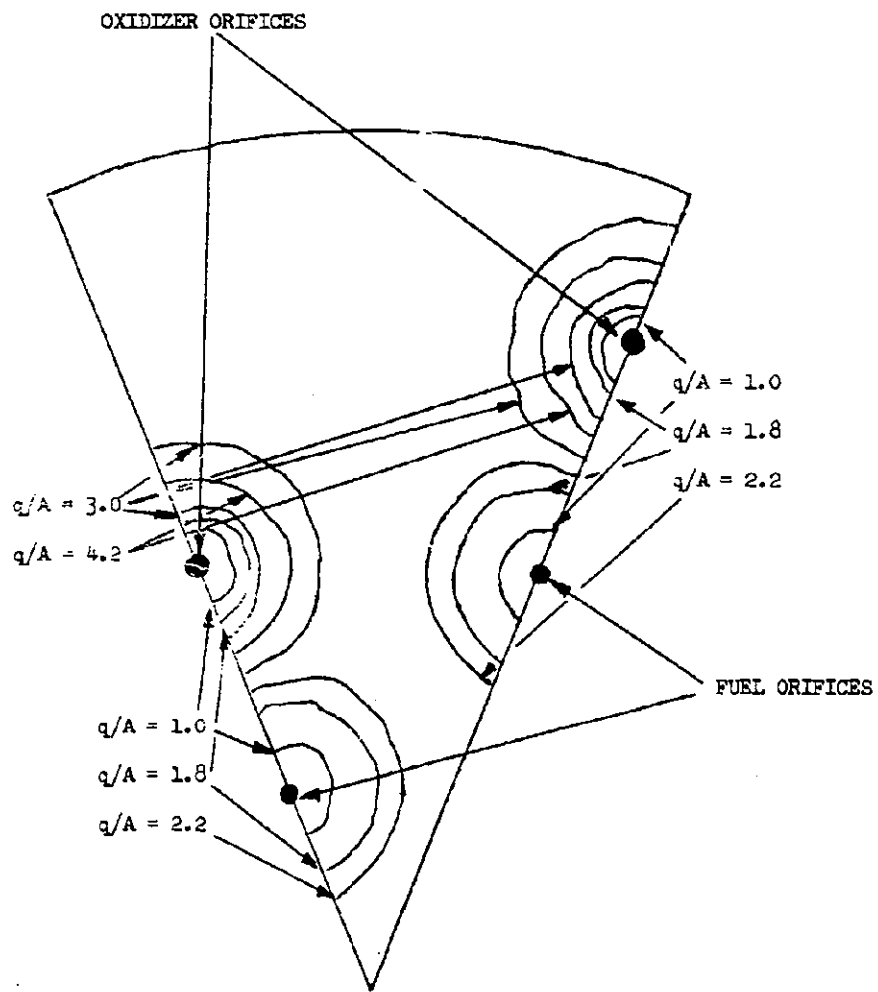


Figure 38 Heat Flux Distribution on Face of Unlike Doublet Injector ICC2A  
at a Chamber Pressure of 200 PSIA

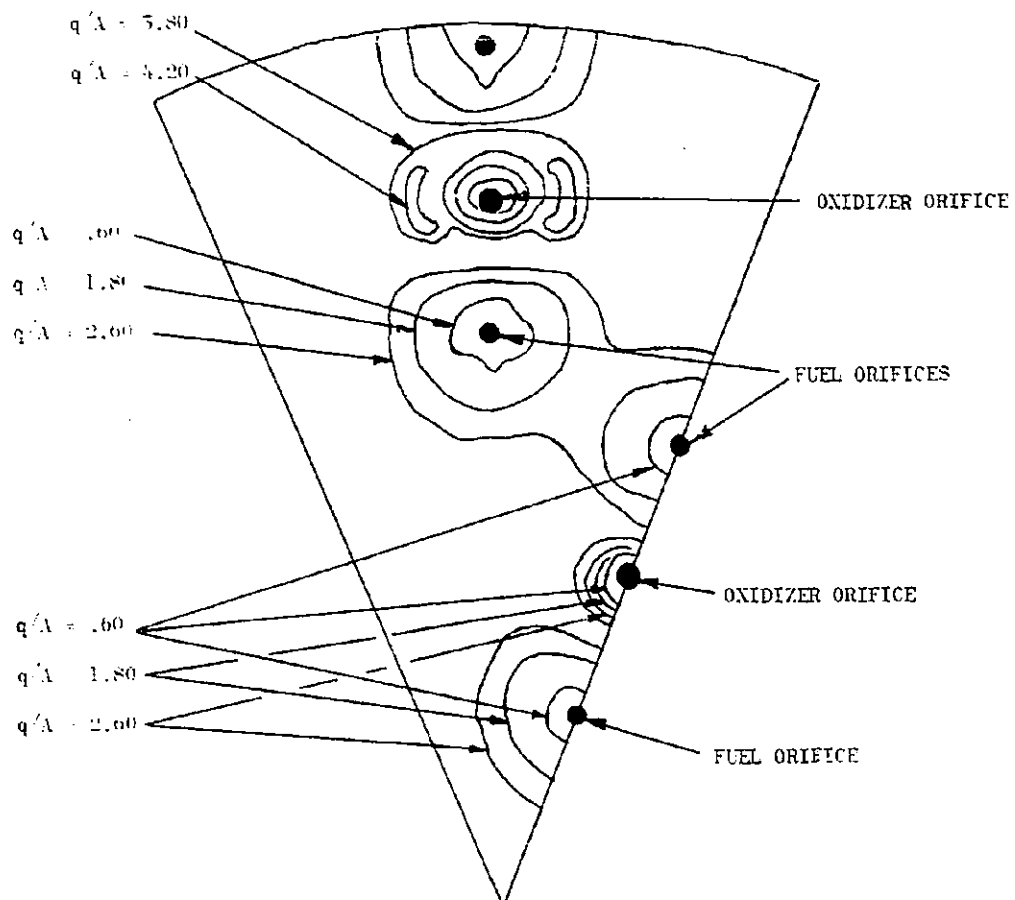


Figure 39 Heat Flux Distribution on Face of Triplet Injector ICC6 at a Chamber Pressure of 171 PSIA

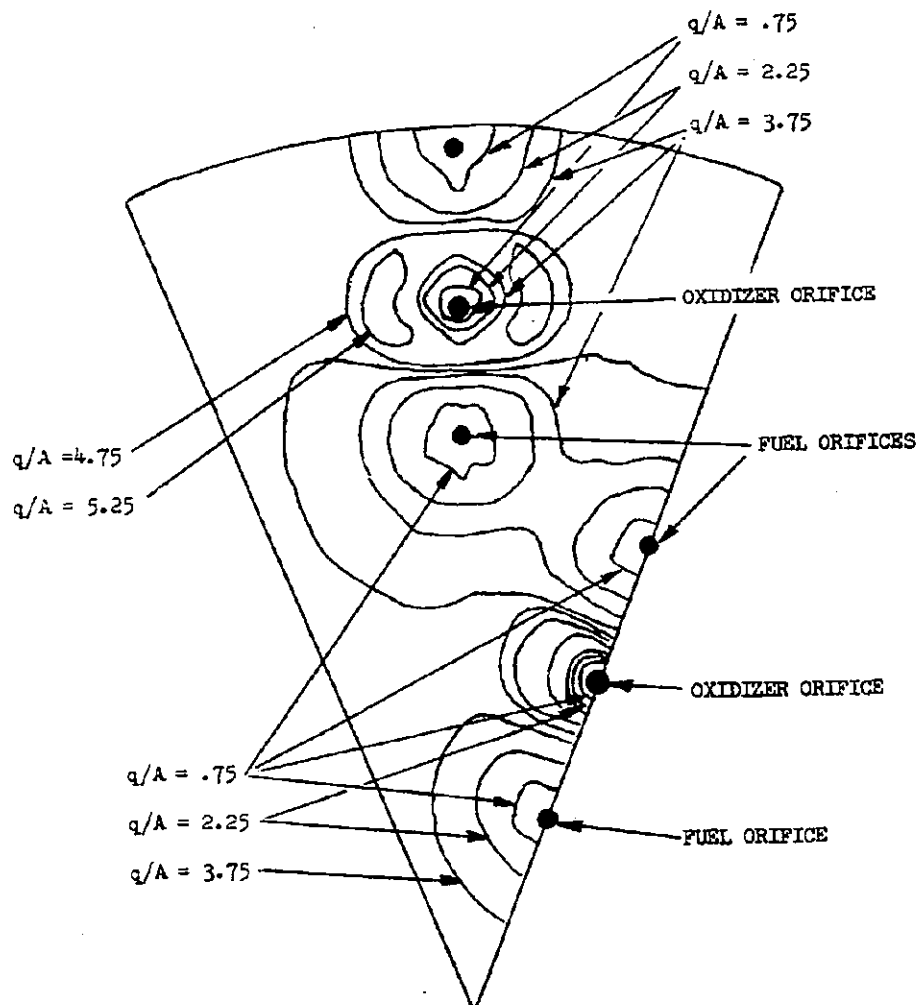


Figure 40 Heat Flux Distribution on Face of Triplet Injector ICC6 at a Chamber Pressure of 342 PSIA

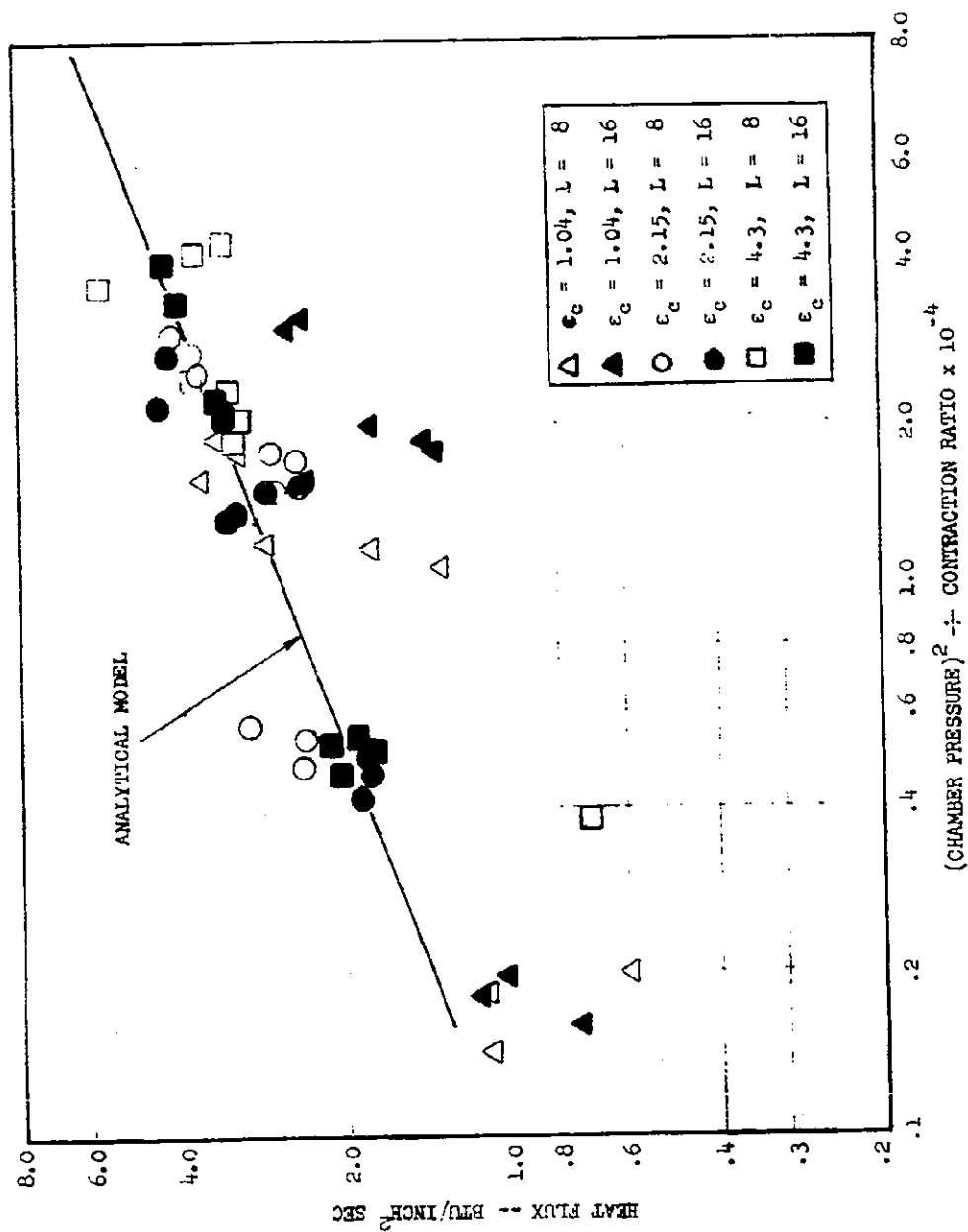


Fig. 41 Heat Flux Measured at Transducer 11 on Face of Injector ICC 6



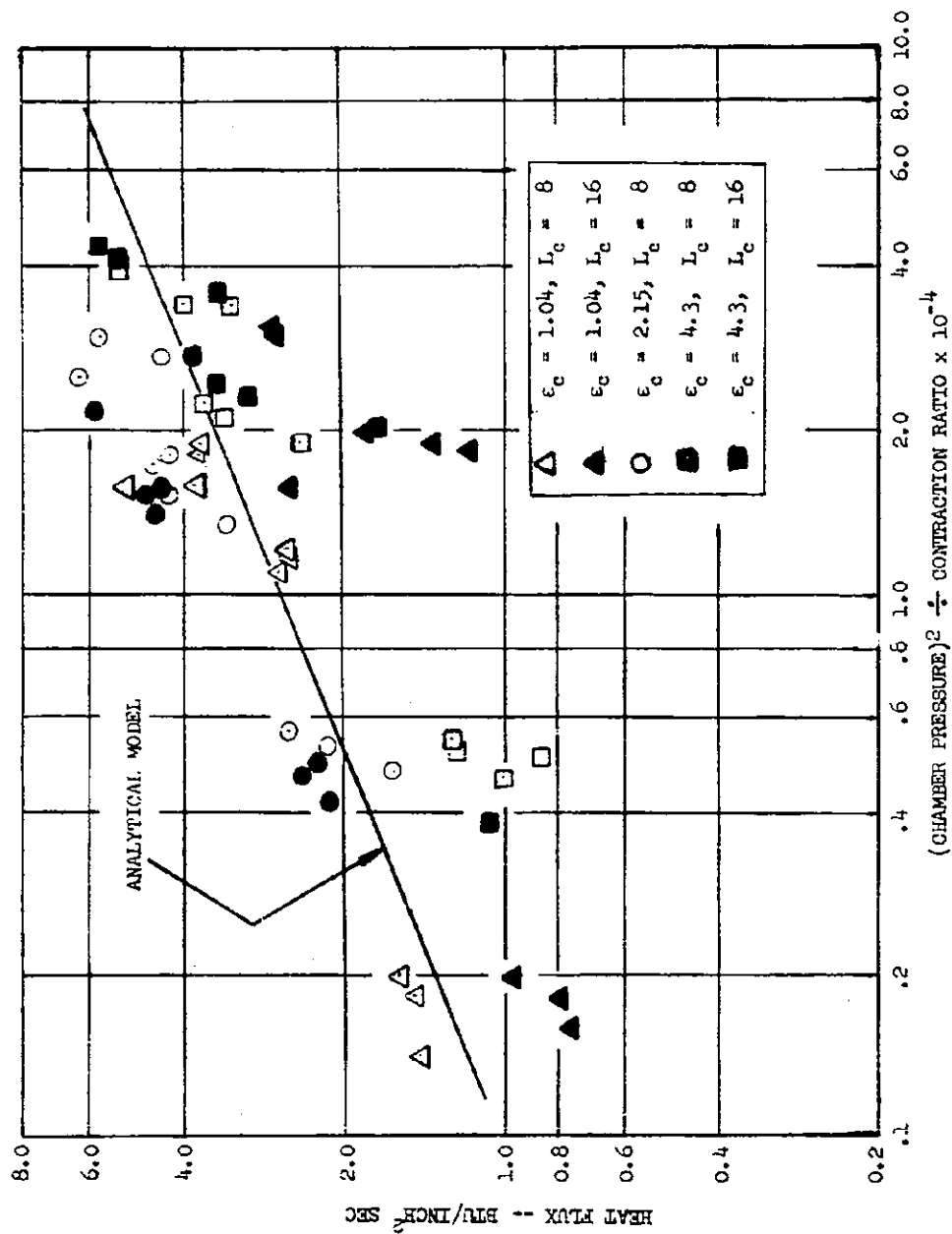


Fig. 42 Heat Flux Measured at Transducer 12 on Face of Injector ICC 6

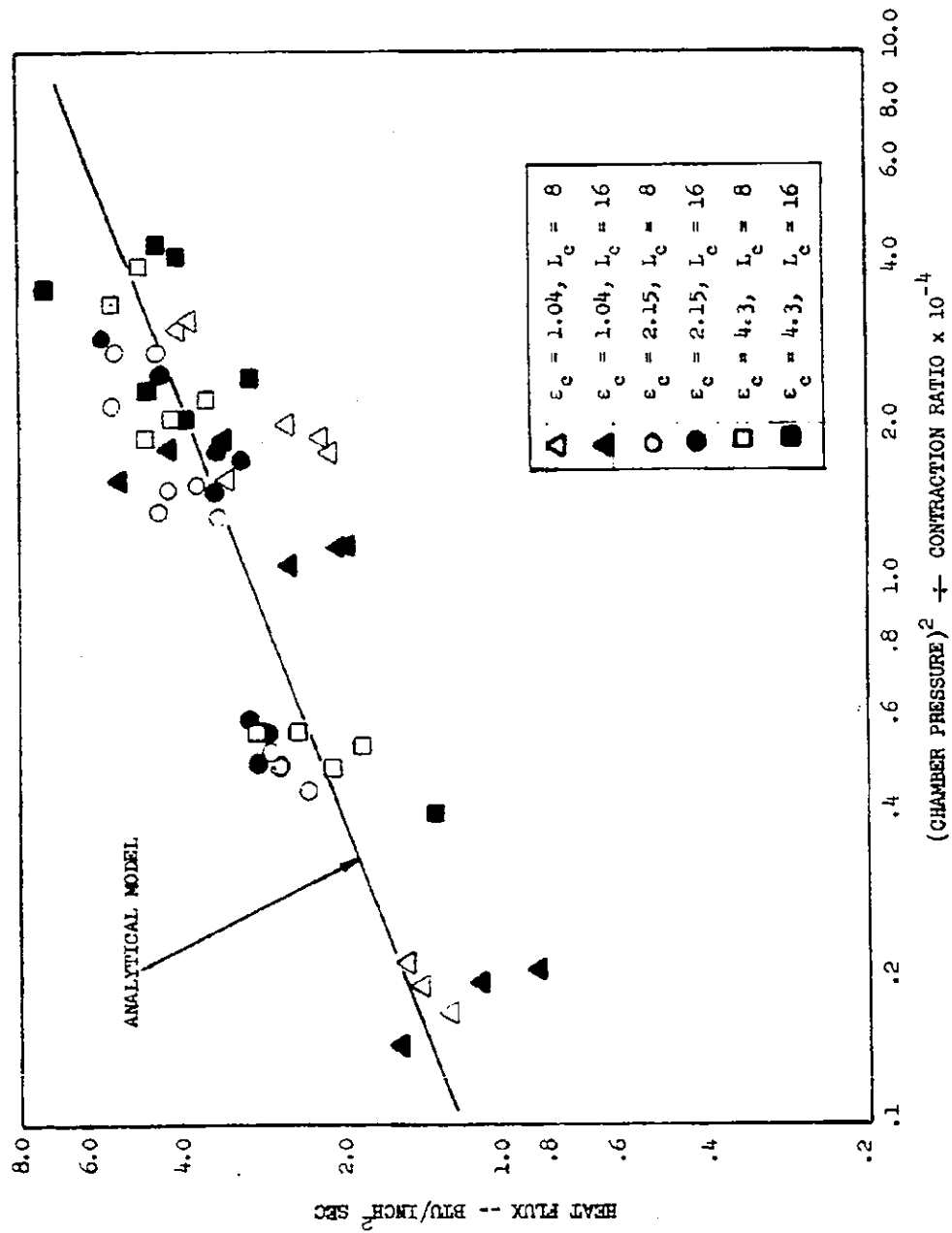


Fig. 43 Heat Flux Measured at Transducer 15 on Face of Injector ICC 6

doubler injector ICC 2A are shown in Fig. 44\*. Note that the analytical model properly predicts the trend exhibited by the experimental data with a parameter defined as the ratio of the chamber pressure squared divided by the contraction ratio.

This correlation parameter was selected on the basis of an expected relationship of the form

$$q/A \sim Nu \sim Re^{\alpha}$$

The proper choice of velocity in the Reynolds number according to the analytical model should be the recirculatory gas velocity. According to both the analytical model and the cold flow recirculation experiments described later in this report, the recirculation velocity is in turn a function of the injection velocity. An appropriate Reynolds number should therefore be of the form

$$Re = \frac{\rho_g U_{inj} L}{\mu_g}$$

Because the gas density is proportional to the chamber pressure and the liquid injection velocity is proportional to the product of the chamber pressure and the nozzle throat area, the heat transfer rate for a constant chamber area should therefore be given approximately by

$$q/A \sim \left[ \frac{p_c^2}{\epsilon_c} \right]^{\alpha}$$

Based upon calculations with the IHTM computer program for the configuration represented by the ICC2A injector, the exponent  $\alpha$  has a value of approximately 0.4 which is substantially in agreement with the experimental data correlation shown in Fig. 41 through 44.

---

\*The correlated data shown in Fig. 44 actually include results from three locations; however, two of these locations (HF1 and HF5) are essentially equivalent.

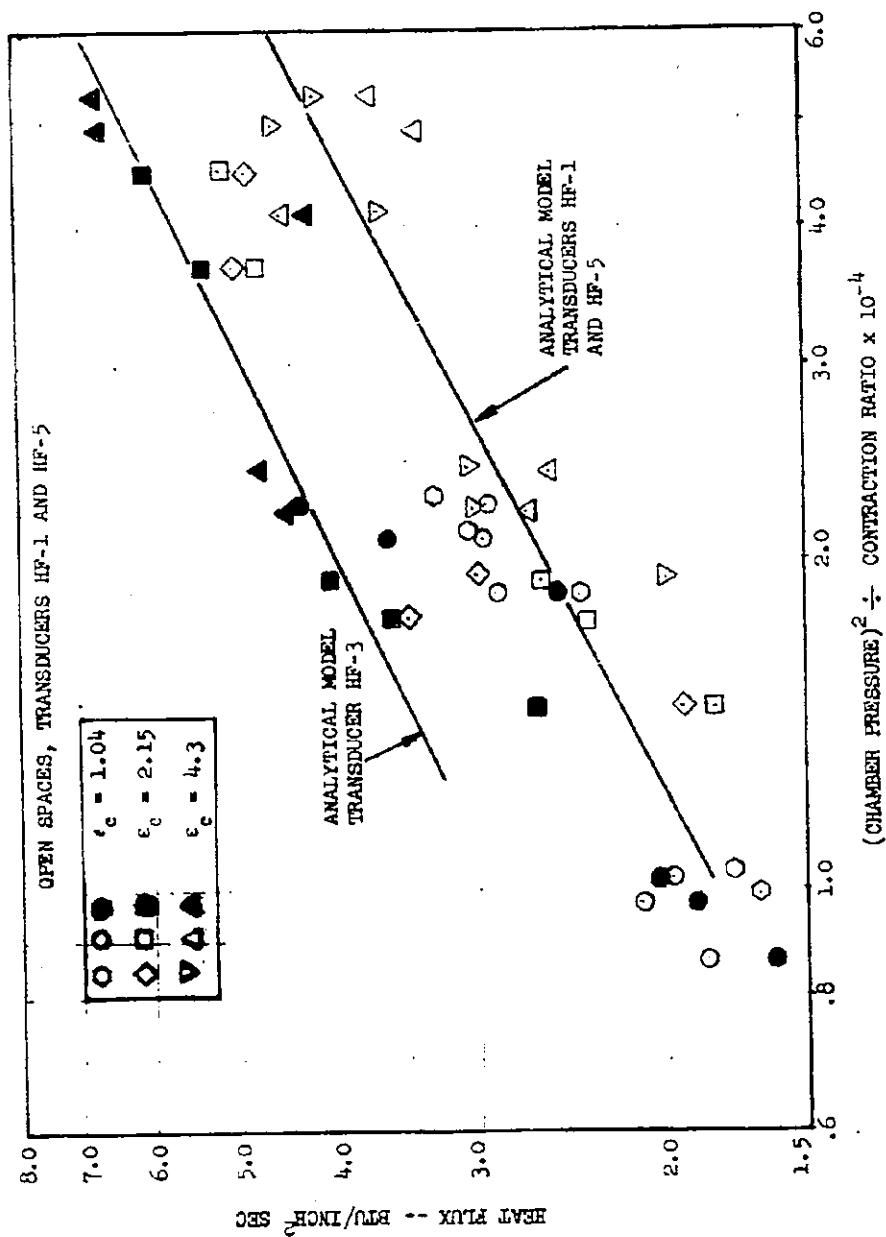


Fig. 44 Heat Fluxes Measured on Face of Injector ICC 2A Correlated to Analytical Model

## RESUME OF THE IHTM COMPUTER PROGRAM

A logical map of the IHTM computer program is shown in Fig. 45.

The method of solution is summarized in the following paragraphs. To make it easier to follow the description, the paragraph numbers are given in circles at the appropriate points on the flow chart.

- 1) Input data required are: (1) tables of combustion gas properties versus mixture ratio; (2) location of the gas flow field and heat transfer areas; (3) complete specification of orifice locations, orifice size, type of orifice (fuel or oxidizer), injection velocity, and liquid jet orientation (4) miscellaneous program control information.

The input data are used in an initialization section to calculate a number of program variables which include the centerline locations of the liquid jets as a function of the distance away from the injector face, the values of  $R$ ,  $\theta$ , and  $z$  for the different mesh points, velocity and concentration decay coefficients, etc. Input and initialized data are printed out before entering the main computational iteration loops.

- 2) For each axial plane, the average velocity and the average oxidizer velocity are calculated based upon droplet vaporization to that plane. At the present time, both are assumed to be zero. Based on the average velocities and the boundary conditions at the center of each liquid jet, the velocity coefficients,  $C_1$  and  $C_{u_i}$ , and the oxidizer coefficients,  $C_2$  and  $C_{c_i}$ , are calculated for each axial plane.
- 3) The main iteration loops performs incrementation of the radial and angular locations. Nested inside the main loops is an iteration loop which performs incrementation to the axial direction. For each  $R$ ,  $\theta$ ,  $Z$  location, the axial velocity and the oxidizer concentration

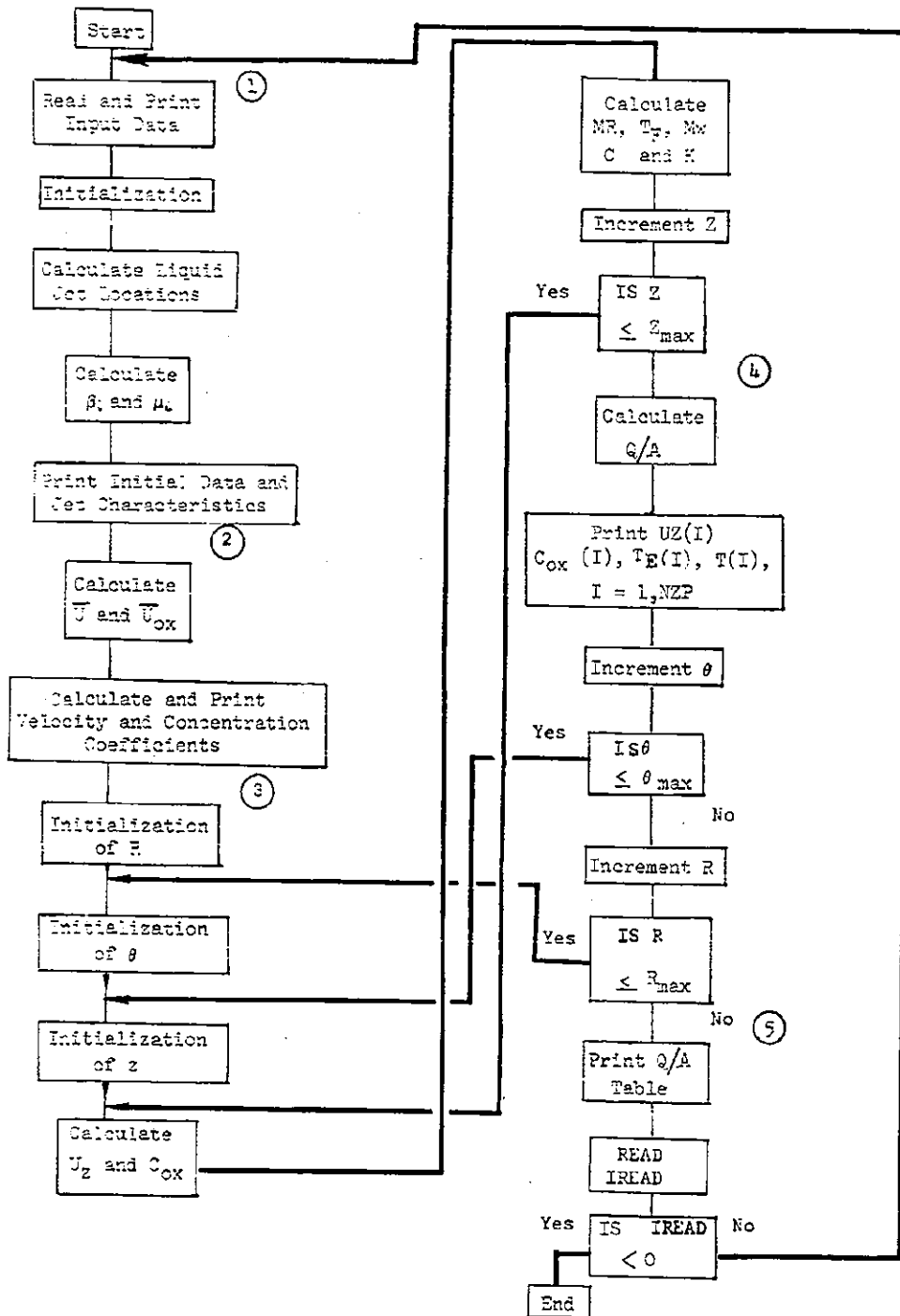


Figure 45 IHTM Flow Chart

are calculated based on the assumed velocity and concentration profiles. From the oxidizer concentration, local mixture ratio, equilibrium and combustion gas temperature and combustion gas properties are calculated.

- 4) For each  $R, \theta$  location, the simplified, one-dimensional, energy equation is used to solve for the temperature profile in the axial direction. Based on this temperature profile, the local injector heat transfer rate is calculated.
- 5) After the injector heat transfer rate for each  $R, \theta$  location has been calculated, a table of heat flux versus  $R, \theta$  is printed out. Depending upon the value of the control variable IREAD, the program may either begin a new case or terminate the calculation.

## DEVELOPMENT OF THE 3D-COMBUST ANALYSIS

The initially developed version of the 3D-COMBUST computer program utilized several simplifying assumptions in describing the physical processes in the rapid combustion zone of Fig. 1. These assumptions were made principally for expediency. During the present investigation, a number of the original simplifications were either removed or replaced by better approximations to improve the accuracy of the model.

One of these changes was the addition of a calculation for the effects of collisions between droplets from differing size groups or unlike propellants. In the original formulation collisions were ignored, i.e., the spray was considered to be dilute such that a given droplet could pass through the cloud of droplets about it without encountering any collisions. Although not intentionally included in the original formulations, because of the nature of the droplet momentum relations (see Eq. 21), and because of their use to define a single mean velocity vector for each individual drop group at each mesh point, a proper accounting was made for the effect of collisions between droplets of the same propellant and size group. However, the effect of collisions between droplets of unlike size and/or propellant groups that can produce significant mixture ratio stratification was ignored, and consequently injector configurations that provide mixture ratio bias were not properly analyzed. In the present investigation, the effect of collisions between unlike droplets has been incorporated into the 3D-COMBUST program through use of the collision model described in succeeding paragraphs. This model treats the spray collisions in the same fashion as inter-molecule collisions are described in the kinetic theory.

With the second change the assumption of a uniform axial gas velocity at any chamber cross section ( $z = z_1$ ) was replaced by a requirement for a uniform pressure gradient ( $\partial p / \partial z$ ) at any chamber cross section. This change allows the axial gas velocity to assume local values ( $r, \theta, z$ ) specified by local spray/gas drag. The change results in somewhat different calculations of heat transfer, burning rate, and transverse gas migration.



The third change involved the substitution of a local value for  $k'$  in place of constant values for each propellant, the calculation of the local  $k'$  evaporation coefficient being made to correspond to the local mixture ratio and flow field.

#### DROPLET COLLISIONS

The analytical model developed to account for the effects of collisions between droplets of different propellant or size groups was derived assuming elastic collision and randomly distributed collision angles as described below.

Consider a drop from Group A with velocity, mass, and diameter of  $\vec{v}$ ,  $\mu_A$ , and  $D_A$ , respectively, colliding with a drop from Group B with a velocity, mass, and diameter of  $\vec{w}$ ,  $\mu_B$ , and  $D_B$ . The analysis is facilitated by considering four separate Cartesian coordinate systems (see Fig. 46 and 47). System zero is the reference frame fixed in the chamber, while system one corresponds to a translation of system zero to the center of drop A at the time of collision. System two corresponds to a rotation of system one such that the  $y_2$  axis is antiparallel to the relative velocity  $\vec{u} = \vec{w} - \vec{v}$ . System three corresponds to a rotation of system two such that the positive  $x_3$  axis goes through the point of contact,  $P = (P_{x2}, P_{y2}, P_{z2})$ .

Assuming elastic collisions, the velocity of drop A after collisions can be calculated immediately, i.e.,

$$v_{x_3}^f = \left( \frac{\mu_A - \mu_B}{\mu_A + \mu_B} \right) v_{x_3}^i + \left( \frac{2\mu_B}{\mu_A + \mu_B} \right) w_{x_3}^i$$

$$v_{y_3}^f = v_{y_3}^i$$

$$v_{z_3}^f = v_{z_3}^i$$

where the superscript  $i$  denotes the velocity before collision and  $f$  denotes the velocity after collision. This result can be written in system two coordinates through the use of the rotation matrix  $R$ .

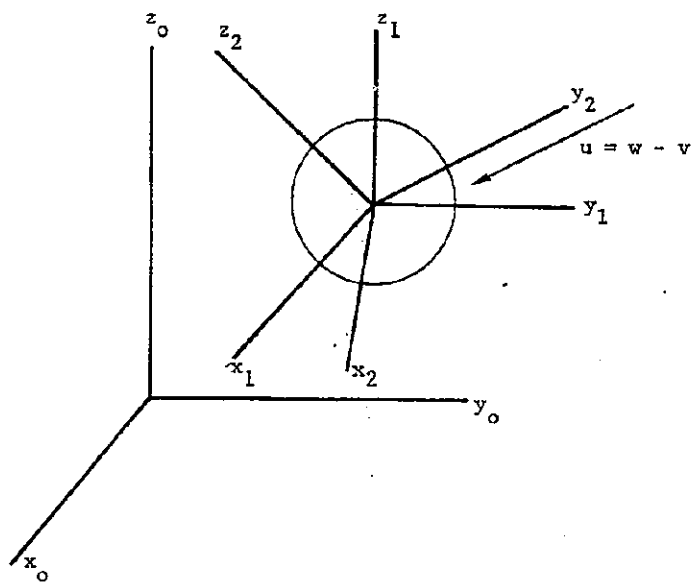


Figure 46. Coordinate System for Propellant Droplet Collision Model

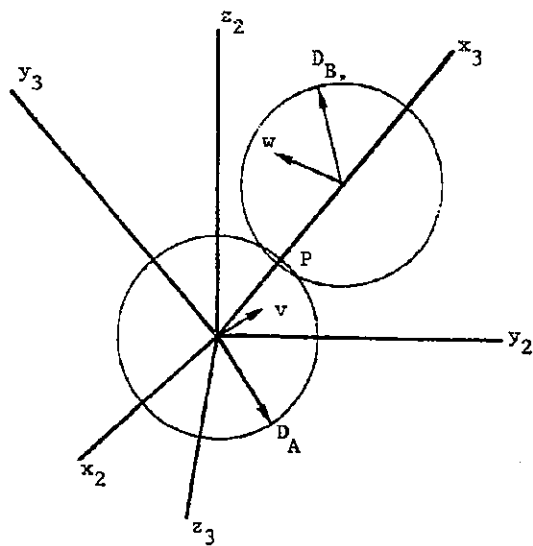


Figure 47. Transformed Coordinate System for Droplet Collisions

$$R = \begin{bmatrix} \sin \phi \cos \theta & \sin \phi \sin \theta & \cos \phi \\ -\sin \theta & \cos \theta & 0 \\ -\cos \theta \cos \phi & -\cos \theta \sin \phi & \sin \phi \end{bmatrix}$$

$$\phi = \cos^{-1} \left( \frac{p_{z_2}}{\sqrt{p_{x_2}^2 + p_{y_2}^2 + p_{z_2}^2}} \right), \quad \theta = \tan^{-1} \left( \frac{p_{y_2}}{p_{x_2}} \right)$$

Let  $\vec{v}_h$  also denote the column vector  $\begin{bmatrix} v_{x_h} \\ v_{y_h} \\ v_{z_h} \end{bmatrix}$  in system h. Thus

$$\vec{v}_3 = R \vec{v}_2 \quad \vec{w}_3 = R \vec{w}_2$$

and

$$\vec{v}_2^f = (R_3^{-1} G R_3) \vec{v}_2^i + (R_3^{-1} H R_3) \vec{w}_2^i$$

where

$$G = \begin{bmatrix} \frac{\mu_A - \mu_B}{\mu_A + \mu_B} & 0 & 0 \\ 0 & 1 & 0 \\ 0 & 0 & 1 \end{bmatrix} \quad H = \begin{bmatrix} \frac{2\mu_B}{\mu_A + \mu_B} & 0 & 0 \\ 0 & 0 & 0 \\ 0 & 0 & 0 \end{bmatrix}$$

The usual assumption that the center of drop B is uniformly distributed over the cross-sectional area presented to it yields the joint probability distribution of the "random" variables  $(p_{x_2}, p_{y_2}, p_{z_2})$ . Requiring  $p_{x_2}^2 + p_{y_2}^2 + p_{z_2}^2 = D^2$  where  $D = D_A + D_B$ , then

$$P(p_{x_2}, p_{z_2}) = \begin{cases} \frac{1}{\pi D^2} & -D \leq p_{x_2} \leq D \\ & \sqrt{D^2 - p_{x_2}^2} \leq p_{z_2} \leq \sqrt{D^2 - p_{x_2}^2} \\ 0 & \text{otherwise} \end{cases}$$

is the joint probability density function of  $p_{x_2}$  and  $p_{z_2}$ .

The expected value of  $\vec{v}_2^f$  can then be defined as

$$E(\vec{v}_2^f) = \iint \vec{v}_2^f P(x, z) dx dz$$

Since  $\vec{v}_2^i$  and  $\vec{w}_2^i$  are independent of the point of contact, then

$$\vec{v}_2^f = E(R_3^{-1} G R_3) \vec{v}_2^i + E(R_3^{-1} H R_3) \vec{w}_2^i$$

After performing the necessary computations and writing the result in system one coordinates using the rotation matrix analogous to  $R$ , the result is

$$E(\vec{v}_1^f) = \vec{v}_1^i + \left( \frac{\mu_A \mu_B}{\mu_A + \mu_B} \right) (\vec{w}_1^i - \vec{v}_1^i)$$

The velocity components in system one are the same as in the reference frame. Hence, it is found that the expected change in momentum of drop A due to a collision with drop B is

$$\Delta \vec{p}_A^B = \left( \frac{\mu_A \mu_B}{\mu_A + \mu_B} \right) (\vec{w} - \vec{v}) \quad (67)$$

where  $\vec{w}$  and  $\vec{v}$  are the original velocities. From Eq. 67, the average momentum change  $\Delta \vec{p}_A^B$  is in the direction of the relative velocity and has a magnitude exactly one-half of that which would result if all collisions were head-on. Further, it may be easily shown that the number rate of collisions that drops from Group A experience with drops from Group B per unit volume is

$$(12) N_A N_B \pi/4 (D_A + D_B)^2 |\vec{w} - \vec{v}|$$

where  $N_A$  and  $N_B$  are the drop number concentrations of Group A and B, respectively. Thus, the expected force per unit volume on Group A due to Group B can be written as

$$\vec{F}_A^B = \frac{12}{8c} N_A N_B \frac{\pi}{4} (D_A + D_B)^2 \frac{\mu_A \mu_B}{\mu_A + \mu_B} |\vec{w} - \vec{v}| (\vec{w} - \vec{v})$$

Finally, the force on an arbitrary group  $j$  due to collisions in general can be found by summing the individual forces:

$$\vec{F}_j = \sum_{k \neq j} \vec{F}_j^k \quad (68)$$

These force terms were added to the original droplet momentum equations.

The effect of the droplet collisions upon downstream mixture ratio can be significant in cases which provide an initial spray mixture ratio bias. For example, in the 72-element, like-doublet-pair injector ICC1, which was built and tested under the previous contract (Ref. 1), an initial mixture ratio bias is provided by an outboard ring of fuel elements. A blocking of the hot, high mixture-ratio combustion gases from the wall by the outer fuel spray has been demonstrated experimentally (Ref. 1); however, this blocking was not predicted by the previous 3D-COMBUST program. As a checkout case for the droplet collision model, a prediction of gas and spray mixture ratio after 1.0 inch of marching calculations by the 3D-COMBUST program was made with and without collisions between fuel and oxidizer drop. The results are shown in Fig. 48 and 49. There is only a small reduction in calculated gas mixture ratio; however, there is a marked reduction in calculated spray mixture ratio at the wall. Because the axial location represented by Fig. 48 and 49 corresponds to a point at which spray combustion is only about 35 percent complete, the spray mixture ratio distribution is the most relevant to the eventual downstream wall mixture ratio. The circumferential differences in spray mixture ratio shown in Fig. 49 represent differences of up to 480 R in predicted adiabatic wall temperature for the propellant combination  $N_2O_4/50\%N_2H_4-50\%$  UDMH. The difference between the two calculation schemes is, therefore, significant, and based upon experimental values of measured adiabatic wall temperature and wall charring, the calculation with droplet collision is more accurate.

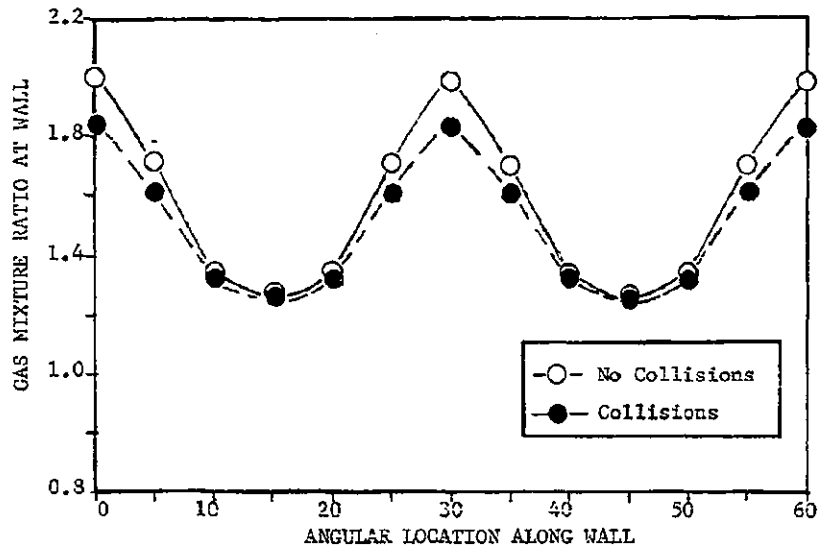


Figure 48 Effect of Droplet Collisions on Gas Mixture Ratio at Chamber Wall of Like Doublet Injector

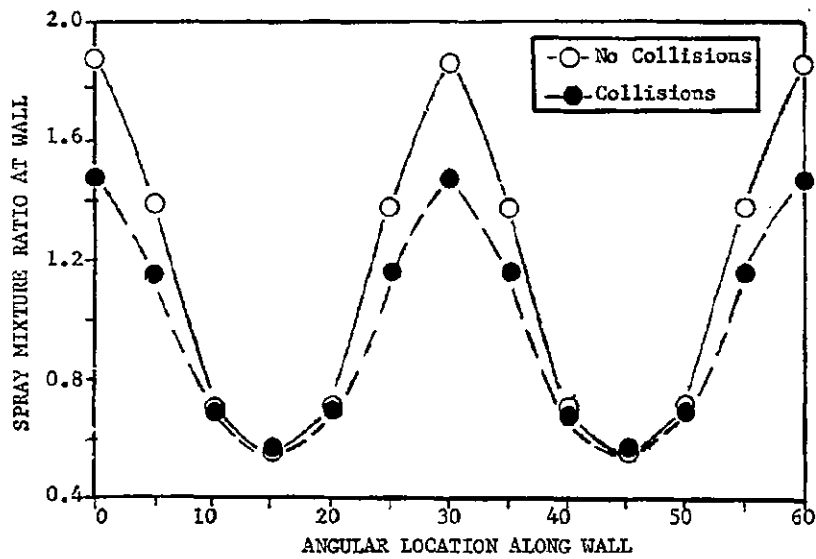


Figure 49 Effect of Droplet Collisions on Spray Mixture Ratio at Chamber Wall of Like Doublet Injector

## VARIABLE AXIAL GAS VELOCITY

During original development of the 3D-COMBUST analytical model, an attempt was made to determine the four gas-phase variables  $u_z$ ,  $u_r$ ,  $u_\theta$ , and  $p$  as functions of  $r, \theta, z$  from solution of the gas-phase continuity equation and the  $z$ -,  $r$ -, and  $\theta$ -gas phase momentum equations. Because of the partially elliptic character of the four partial differential equations, the system was unstable and the numerical solution by a marching technique was unsuccessful. Therefore, the initial formulation was made solvable by requiring the axial gas velocity to be uniform (constant) at any cross section, but also to satisfy the global continuity requirement

$$\frac{\partial \bar{u}_z(z)}{\partial z} = - \frac{\iint \dot{m}(r, \theta, z) r dr d\theta}{\iint \rho(r, \theta, z) r dr d\theta}$$

This one-dimensional definition of axial gas velocity was rationalized on the basis that the flow in a rocket engine combustion chamber resembled the flow in a closed duct for which the pressure and axial pressure gradient should be essentially uniform across the duct. A uniform axial pressure gradient was then assumed to imply that the axial velocity gradient was also uniform across the chamber cross section. The latter assumption, however, proved to be inconsistent with the downstream calculations of the STRMTB multiple stream tube analysis which predicted significantly nonuniform axial gas velocities with a uniform axial pressure gradient. Differences in axial gas velocities are calculated primarily because of the nonuniform axial drag forces in a nonuniformly distributed spray and also because of the variation in gas density and specific heat ratio due to the nonuniform mixture ratio. During the present investigation, the assumption of a uniform axial pressure gradient was retained, but the axial gas velocity together with this pressure gradient were calculated. This was done by simultaneous solution of the  $z$  momentum equation for the gas at all the  $r$ - $\theta$  mesh points in a given  $z$  plane and the global continuity relation

$$\iint \frac{\partial}{\partial z} (\rho u_z) r dr d\theta = \iint \dot{m} r dr d\theta$$

with  $\rho$ ,  $u_z$ , and  $\dot{m}$  being functions of  $(r, \theta, z)$ .

In finite difference form, the axial gas momentum equation is

$$\begin{aligned}
 & \frac{(rou_z^2)_{i,j,2} - (rou_z^2)_{i,j,1}}{\Delta z} + \frac{(rou_{rz})_{i+1,j,2} - (rou_{rz})_{i-1,j,2}}{2\Delta r} + \\
 & \frac{(ou_{\theta z})_{i,j+1,2} - (ou_{\theta z})_{i,j-1,2}}{\Delta \theta} + r_i \frac{g_c}{12} \left( \frac{\partial p}{\partial z} \right)_2 \\
 & = \frac{r_i}{12} \sum_n (\dot{m}_{n_z})_{i,j,2} + \frac{r_i g_c}{12} \sum_n (\ddot{b}_z)_{i,j,2} \\
 & + F_{n,n_2,i,j,2} + \tau_{r,i,j,2} + \tau_{\theta,i,j,2}
 \end{aligned}$$

where droplet collision force  $F_{n,n_2,i,j,2}$  is given by Eq. 68, and the viscous shear stresses are given by

$$\begin{aligned}
 \tau_{r,i,j,2} &= \frac{1}{144\Delta r^2} \left[ (\mu r_z)_{i+1,j,2} - 2(\mu r_z)_{i,j,2} + (\mu r_z)_{i-1,j,2} \right] \\
 \tau_{\theta,i,j,2} &= \frac{1}{144\Delta \theta^2 r_{i,j,2}} \left[ (\mu u_z)_{i,j+1,2} - 2(\mu u_z)_{i,j,2} + (\mu u_z)_{i,j-1,2} \right]
 \end{aligned}$$

Here,  $i$  represents a radial mesh point,  $j$  represents an angular mesh point, and 2,1 refers to  $z$  planes 1 and 2 of the marching calculation. (See Fig. 5). Note that subscripts  $i$  and  $j$  have been deleted from the  $\partial p / \partial z$  term in line with the requirement that this term be a function of  $z$  only. This equation can be written for  $i = 1, \dots, I$  and  $j = 1, \dots, J$  with appropriate modifications at the boundaries. In each equation, the axial velocity at the new level (corresponding to the subscript 2) and the pressure gradient  $(\partial p / \partial z)_2$  are treated as unknowns. Replacing all other variables with either their known (old)  $z$  level values or with their predicted values yields a system of  $I \times J$  equations, which is uncoupled from the other differential equations. There are  $I \times J + 1$  unknowns in this system, namely  $u_{z,i,j,2}$  for  $i = 1, \dots, I$  and  $j = 1, \dots, J$  and  $(\partial p / \partial z)_2$ . The problem is closed when the global continuity equation, written in finite difference form, is adjoined to the system. It is



~~These values of  $k'$  are then calculated at each  $r, \theta$  mesh and from the definition of gas temperature by interpolation within the grid and etc.~~

To determine whether significant differences in local mixture ratios are predicted by the variable  $k'$  model as opposed to the simpler definition of a single average  $k'$  as used in the previous 3D-COMBUST program, comparative calculations were made with the old and new versions of 3D-COMBUST. Different results were obtained with the two models, examples of which are shown in Fig. 50 (a specific injector). In a given problem, the differences in local predictions of mixture ratio apparently due to the differences in  $k'$  definition are also influenced by the particular characteristics of the injector geometry and propellant combination; therefore, no general conclusions should be drawn about the significance of the results shown in Fig. 50 for other injectors. The use of the variable  $k'$  calculation does always represent a clear improvement, however, from one standpoint. Together with the variable axial velocity assumption, it makes the 3D-COMBUST program consistent with the STIRTS stream tube program in its combustion and axial momentum mechanisms and therefore makes the overall performance calculation less sensitive to the length of the chamber over which calculations are performed with the respective computer programs.

#### INITIALIZATION OF GAS FLOW FIELD

The LISP computer program ordinarily supplies a definition of a uniform axial gas velocity and mixture ratio to the 3D-COMBUST program at its starting plane  $z$ . These definitions are based upon global continuity for that fraction of the injected propellants calculated to be gasified between the injector and plane  $z_0$ . However, LISP can supply no definition of radial or tangential velocities; consequently, they are defined to be zero. In the usual situation in which the LISP definition of axial gas velocity is greater than the spray axial velocity, the 3D-COMBUST marching calculation is started with no problems provided that short (approximately .005 - .02 inch) increments are employed during the first few steps in the  $z$  direction. The marching calculation quickly develops a non-uniform axial velocity and the required transverse velocities to satisfy continuity and axial momentum.

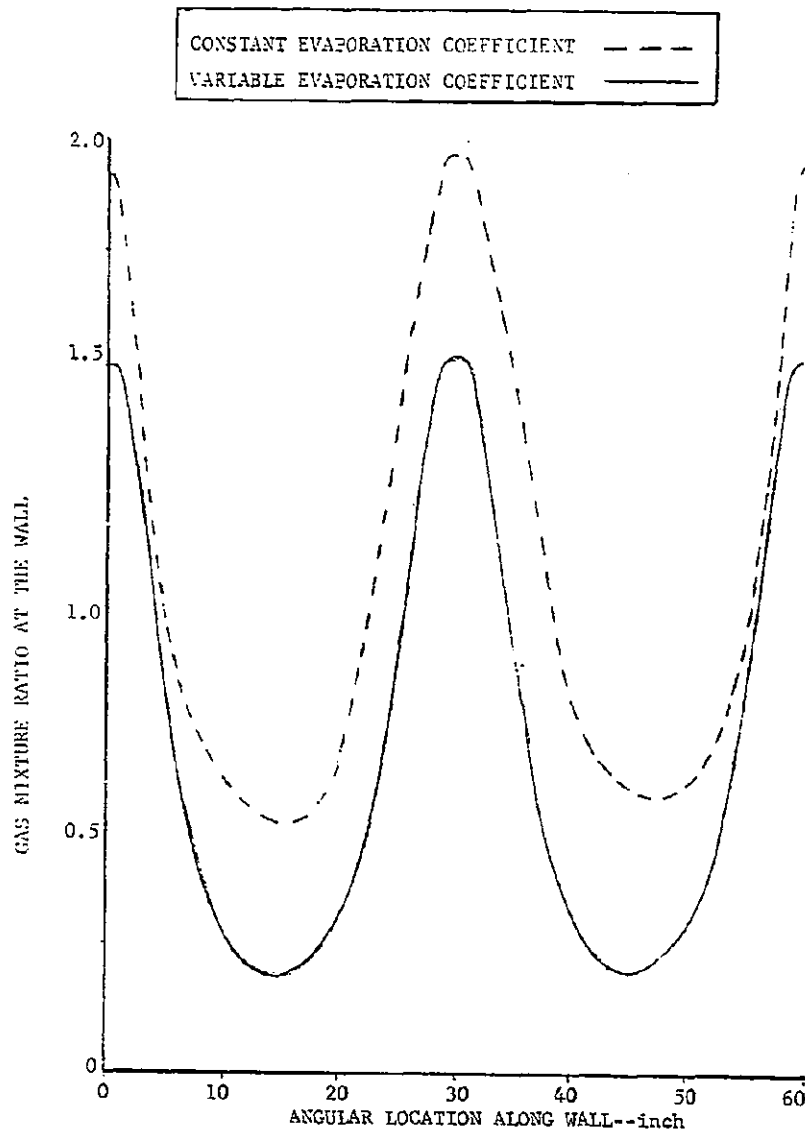


Figure 50 The Effect of a Variable Evaporation Coefficient Upon Calculation of a Local Mixture Ratio for a Like Doublet Injector

If, however, the axial gas velocity defined by the LISP program is less than the axial spray velocities (also supplied by LISP), the usual boundary condition leads to numerical instabilities through the coupling of overpredicted values in the subsequent marching calculations of axial, radial, and tangential gas velocities within 3D-COMBUST. This instability arises in cases where drag forces between spray and drops accelerate rather than hold back the axial gas movement.

To overcome this difficulty, an alternate initialization procedure was adopted for cases where axial gas velocity is less than the axial velocity of the slowest moving spray drop group. The local axial acceleration of the gas  $\partial u / \partial z$  is defined as being equal to the local value of the spray vaporization rate  $\dot{m}$ ; therefore, no transverse gas velocities are initially required to satisfy mass continuity. The axial gas momentum equation is then rewritten to solve for an initial local gas velocity (at each mesh point) which satisfies the axial momentum relationship, Eq. 16, under conditions of no transverse gas velocity. This procedure has been incorporated into a subroutine UZSTRT which is employed only when the uniform axial gas velocity specified by LISP is everywhere less than the spray velocity. The subsequent definition of a non-uniform axial gas velocity supplied by UZSTRT permits the 3D-COMBUST marching calculation to proceed without numerical instabilities. Based upon examinations of 3D-COMBUST calculations, the definition of a local gas acceleration that is equal to the local vaporization rate is considered to be a fairly realistic simplifying assumption provided that the average axial gas velocity is in the range 0.6-0.8 of the spray axial velocities. If, however, the gas velocity is less than approximately 0.6 of the spray velocity, numerical instabilities still result (presumably because  $\partial u / \partial z$  is substantially greater than  $\dot{m}$ ). In the case where the average axial gas velocity lies in the range 0.8-1.0 of the spray velocity, the non-uniform axial gas velocity defined by UZSTRT appears to be unrealistic from a physical standpoint, because axial gas velocities higher than the spray velocities are predicted in regions of low spray concentration. The LISP calculational plane and hence the start of the 3D-COMBUST program should be selected such that

the starting plane for the combustion calculation lies within the regions

$$0.6 u_{d_z} < u_z < 0.8 u_{d_z}$$

$$u_{d_z} < u_z$$

#### RESUME OF THE 3D-COMBUST PROGRAM

The 3D-COMBUST program performs a marching calculation from an initial plane Z1 to a terminal plane ZSTOP in increments DZ between successive planes Z1 and Z2\*. A logical map of the calculation path is shown in Fig. 51. The overall calculational network consists of a MAIN or calling program together with five groups of subprograms. The functions of the five subprogram sets are described in the paragraphs below. The interaction of the separate subprograms and subprogram groups may be followed by reference to Fig. 51.

The first group of subprograms (INITIAL, CHANGE, CONCHK, KPRIME, and UZSTRT) together with the MAIN program reads in the input punch card data, defines the areas associated with the mesh point geometry, calculates a table of k' evaporation coefficients to be used throughout the calculation, redefines (when  $u_z$  less than  $u_d$ ) the axial gas velocity in the starting plane Z1, and updates the definitions of all parameters at each subsequent pair of calculational planes Z1 and Z2.

The second group of subprograms (PN, SPRAY, PRØD, PUDZ, PUDT, ZMØM, CØNTIN, and PMIX) constitute a predictor cycle in which spray and gas densities, velocities, mixture ratios, and coupling terms in plane Z2 are calculated upon the basis of controlling parameters defined in the associated plane Z1. In all subprograms which begin with the letter P, variables along any radial mesh line J are calculated simultaneously with the calculations sweeping in the angular direction from the right to the left boundaries of the slice defined in Fig. 5.

---

\*The actual Fortran nomenclature for key variables and routines is used where applicable in this section.

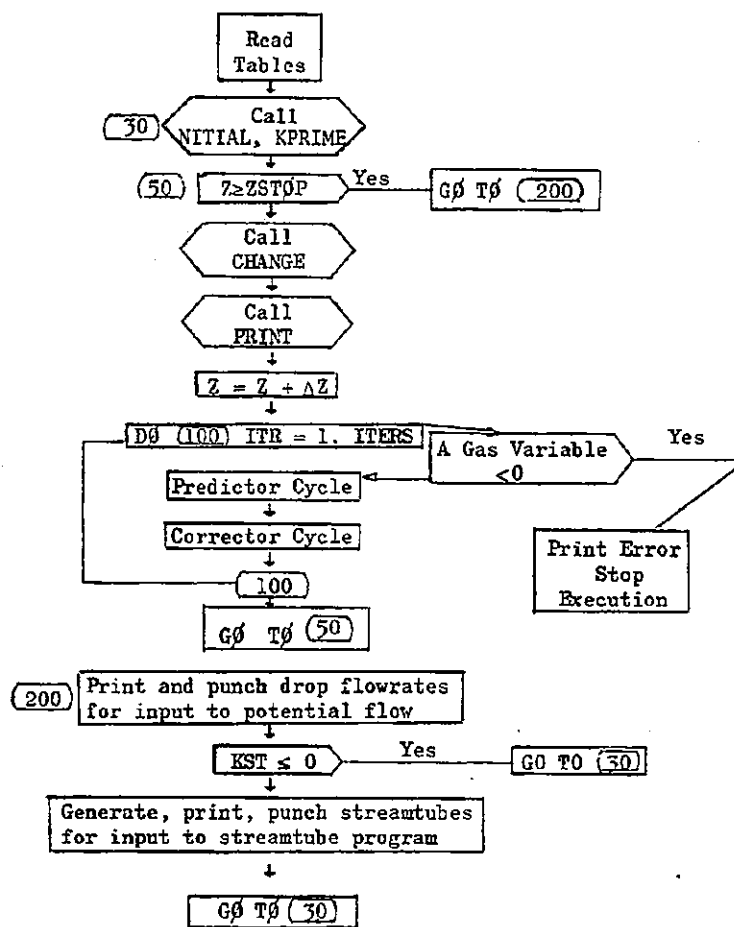


Figure 51 Logic Map of 3D-COMBUST Computer Program

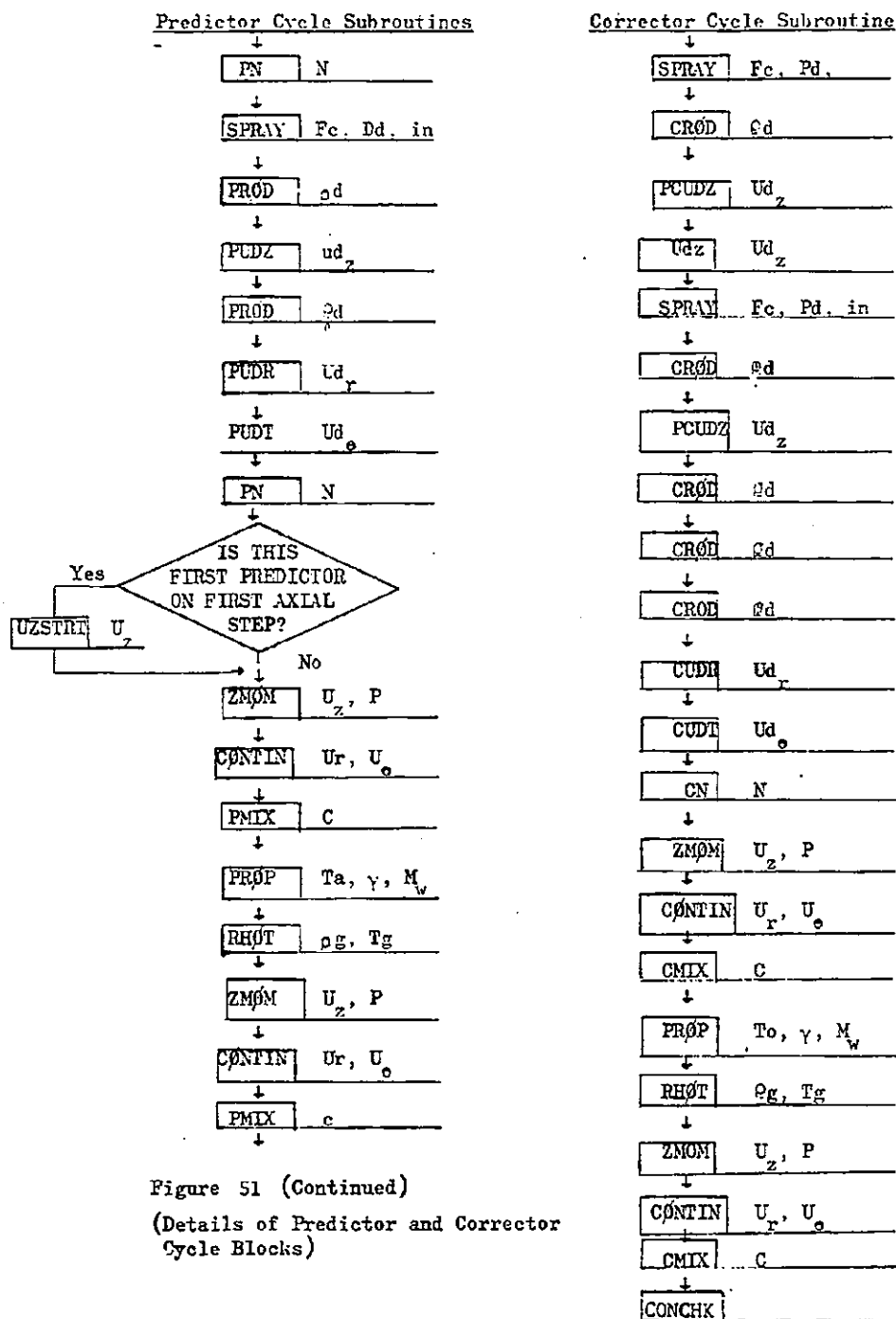


Figure 51 (Continued)  
 (Details of Predictor and Corrector  
 Cycle Blocks)

The third group of subprograms (SPRAY, CRØD, CUDZ, CUDR, CUDT, CN, ZMØM, CØNTIN, and CMIX) constitute a corrector cycle which recalculates the values of spray and gas variables in plane Z2 based upon the preliminary estimates of the controlling parameters in plane Z2 made in the predictor cycle. In the subprograms which begin with the letter C, variables along any circumferential mesh line I are calculated simultaneously with the calculations sweeping in the radial direction from the midpoint of the chamber to the chamber wall in the slice shown in Fig. 5 . It may be noted that the SPRAY (calculates coupling terms), ZMØM (calculates axial gas velocity), and CØNTIN (calculates transverse gas velocities) are used in both the predictor and corrector cycles.

The fourth group of subprograms (PRINT, BLMP, and CPUNI) together with the MAIN program prints out the calculated spray and gas variables (see Output Data) in each Z2 plane and punches out input data to be used in the STRMTB and BLEAT programs.

The fifth set of subprograms (PRØP, RHØT, TRPLIN, TRIDI, BAND, ABAND, XITRP, LØCATE, and YØF) are a service group which look up data stored in tables and perform the mechanical operations of the matrix solutions to the various conservation equations.

#### Input Data

The required input data for 3D-CØMBUST consists of:

- (1) Two punch cards which give a general description of the problem being analyzed (alphanumeric format)
- (2) Seven punch cards which provide the general data necessary to control printout of calculated data, and to define the calculational mesh point system, the initial and terminal z planes of the calculation, number of drop groups to be employed in the calculation, liquid propellant properties, and the axial gas velocity, mixture ratio, temperature, density, and pressure, if these parameters are to be assumed uniform in the initial z plane. Definition of uniform gas parameters are ordinary supplied by the LISP computer program.

- (3) Tables defining the gas viscosity, stagnation temperature, molecular weight, and specific heat ratio, as functions of gas mixture ratio. These tables are usually available on punch cards from the LISP program.
- (4) Tables of  $k'$  evaporation parameters for each propellant.
- (5) The values of the diameters, of the axial, radial, and circumferential velocities, and of the mass flux ( $\text{lbm/in}^2 \text{ sec}$ ) for each propellant drop group at each mesh point in the initial  $z$  plane. The punch cards supplying these data are ordinarily available as a deck of LISP punch card output.
- (6) The values of the axial, radial, and circumferential gas velocities, together with the gas mixture ratio, temperature, density, and pressure if these parameters are not to be considered uniform in the initial  $z$  plane.
- (7) Instructions for the lumping of mesh points in the terminal  $z$  plane into stream tubes such that gas and spray data can be supplied as punch card input to the STRMTB program. ;
- (8) Instructions defining the  $z$  planes at which gas and spray data at the wall mesh points will be supplied as punch card input to the BLEAT program.

#### Output Data

The input data used by the 3D-COMBUST program is written out on tape (for subsequent printout) immediately after being read in to the computer such that input errors can be conveniently located. This output is followed by a listing of the  $k'$  tables and the initial plane gas and spray conditions as calculated by the subprograms NITIAL, CHANGE, and KPRIME.

In the initial plane and in each succeeding  $z$  plane, four separate tables are prepared which list respectively:

- (1) The density, mixture ratio, axial, radial and circumferential velocities, temperature, and pressure of the gas at each  $r, \theta$  mesh point.



- (2) The droplet diameter, spray density, evaporation rate, droplet number concentration, axial, radial and circumferential droplet velocities, and the axial mass fluxes for each drop group at each  $r, \theta$  mesh point.
- (3) The interphase drag forces at each  $r, \theta$  mesh point.
- (4) The droplet collision forces at each mesh point.

In addition, a listing is made of the mass balance of propellants at each plane and the required correction which is imposed to preserve mass continuity at each marching step.

The printout of the preceding data listings can be controlled in a flexible manner to give a tabulation at both predictor and corrector cycles in each  $z$  plane, at only the corrector cycle, or at only a limited number of  $z$  planes through the marching calculation.

Finally, a printing is made of the punch card output provided for the STRMTB and BLEAT programs.

# CHANGES IN THE BLEAT PROGRAM

The revisions to the BLEAT computer program included: (1) Incorporation of more detail into calculation of heat transfer coefficients in the downstream portion of the thrust chamber where the combustion gas stream is defined by the STRMTB program, (2) elimination of the direct use of radial gas velocity and spray impingement for calculation of heat transfer in the 3D-COMBUST portion of the chamber with the substitution of a model based upon injection Reynolds number, and (3) inclusion of heat flux and integrated heat load calculations for regenerative cooling applications.

## STRMTB REGION HEAT TRANSFER

Calculation of heat transfer coefficients in the boundary layer surrounding the STRMTB zone of Fig. 1 is based upon the Elliot-Bartz-Silver method of calculating the local energy thickness of the thermal boundary layer and then using the energy thickness as the characteristic length in defining the Stanton number. From Ref. 7, the buildup of the energy thickness\* is given by

$$\frac{d\delta_T}{dz} = St \left( \frac{T_{AW} - T_W}{T_o - T_W} \right) \left[ 1 + \left( \frac{dr_W}{dz} \right)^2 \right]^{1/2} \quad (69)$$

$$- \delta_T \left[ \frac{1 - M^2}{M(1 + \frac{\gamma-1}{2} M^2)} \frac{dM}{dz} + \frac{1}{r_W} \frac{dr_W}{dz} - \frac{1}{T_o - T_W} \frac{dT_W}{dz} \right]$$

Integration of Eq. 69 from the boundary layer attachment point  $z_o$  to axial coordinate  $z$  defines the energy thickness at  $z$  under conditions in which the flow undergoes both acceleration and cooling. If both  $T_o$  and  $T_W$  are assumed to be relatively constant, Eq. 69 can be reduced to

\* The energy thickness is defined as the thickness of a potential flow which contains the same decrement in energy from the free stream condition as the real boundary layer.

$$\frac{d\phi_T}{dz} = St \left( \frac{T_{AW} - T_W}{T_O - T_W} \right) \left[ 1 + \left( \frac{dr_W}{dz} \right)^2 \right]^{1/2} \quad (70)$$

$$- \phi_T \left[ \frac{1 - M^2}{1 + \frac{\gamma - 1}{2} M^2} \frac{d \ln M}{dz} + \frac{d \ln r_W}{dz} \right]$$

A numerical integration of Eq. 70 from the start of the STRMTB region to the z-plane of interest has been substituted for Eq. 28 as the means of calculating the energy thickness. The integration is carried out separately for each wall stream tube. To start the integration, the energy thickness is defined at the first calculational plane in the STRMTB region by

$$\phi_T = \phi_M = .037 Re_z^{-.2} (z - z_O) \quad (71)$$

$$Re_z = \rho_g u_z (z - z_O) / \mu_g$$

Equation 71 is based upon the assumption that temperature and velocity profiles are similar for gas streams and that the boundary layer can be approximated by the corresponding flat plate flow system with sufficient accuracy to initiate the integral solution.

For highly cooled turbulent boundary layers ( $T_W \ll T_O$ ), the following definition for Stanton number can be defined based upon similarity between skin friction and heat transfer

$$St = .012 \left( \frac{T_O}{T_r} \right) \left( \frac{\rho_g}{\rho_r} \right)^{.25} \left( \frac{\mu_r}{\mu_g} \right)^{.25} Re_{\phi_T}^{-.25} Pr^{-.67} \quad (72)$$

The reference temperature,  $T_r$ , for evaluating mean gas properties is taken as the arithmetic mean between the temperatures of the main gas stream and the chamber wall, i.e.,

$$T_r = (T_g - T_w)/2 \quad (73)$$

Equations 70 and 72 have been programmed into the BLEAT program to permit a calculation of the heat transfer coefficient defined by

$$h_g = \rho_g u_z C_p St \quad (74)$$

under both the ablative wall condition and the highly cooled wall condition associated with regenerative cooling. A suitable value of  $T_w$  is supplied as input data by the BLEAT user; otherwise the program assumes an ablative chamber wall with a surface temperature equal to  $T_{AW}$  in Eq. 70.

For conditions of high acceleration when the dimensionless Launder parameter\* is greater than  $3.0 \times 10^{-6}$  and a subsequent laminarization of the boundary layer is expected to occur the definition of Stanton numbers is changed to

$$St = .008 \left( \frac{T_g}{T_r} \right) \left( \frac{\rho_g}{\rho_r} \right)^{.25} \left( \frac{\mu_r}{\mu_g} \right)^{.25} Re_T^{-.25} Pr^{-.67} \quad (75)$$

In the case of either laminar or turbulent boundary layers, the gas density and viscosity ratios are assumed to be given by

$$\frac{\rho_g}{\rho_r} = \frac{T_r}{T_g}$$

$$\frac{\mu_r}{\mu_g} = \left( \frac{T_r}{T_g} \right)^{.6}$$

\* Definition of the Launder parameter and a discussion of the effects of flow acceleration upon heat transfer are presented in the following section dealing with heat transfer in the 3D-COMBUST zone. The change from Eq. 72 to Eq. 75 for calculation of Stanton number is made when the Launder parameter is  $3.0 \times 10^{-6}$  rather than the usual  $2.0 \times 10^{-6}$  so as to provide for conservative heat transfer calculations. The coefficient 0.008 in Eq. 75 was also chosen to give a conservative estimation of reduction in heat transfer coefficient even when laminarization is calculated.

The definition of effective combustion gas temperature previously employed for the STRMTB region (Ref. 1) has been retained. The equilibrium combustion gas temperature defined by the local gas mixture ratio is multiplied by the local percent completion of combustion.

### 3D-COMBUST REGION HEAT TRANSFER

The heat transfer model set up in Ref. 1 for the 3D-COMBUST zone of Fig. 1 included two mechanisms, spray impingement and radial velocity, whose effects could not be calculated with any degree of confidence because experimental data in equivalent systems were not available at that time. Accordingly, a critical review of recent literature was made to determine whether the initial model was realistic. This survey, results of which are presented in the following paragraphs, indicated that the model was incorrect with respect to radial velocity effects and also indicated that substantially more experimental effort was required before spray impingement heat transfer could be predicted with a useful degree of confidence.

### Literature Survey

From continuity requirements, the presence of a transverse velocity in a flow passage is always associated with an acceleration or deceleration of the axial flow in the passage. In two-dimensional cartesian coordinates, this relationship is represented for incompressible flow by

$$\frac{\partial u}{\partial y} = - \frac{\partial u}{\partial x}$$

Although negligible experimental data are available in the literature directly concerning the effects of a normal flow into the wall superimposed upon the main flow parallel to the wall, a great deal of work has been done recently concerning the effects of a varying axial flow. Back and co-workers (Ref. 19, 20, and 21) have investigated the velocity and temperature distributions in nozzles

of varying convergence angle. Kays and Moretti (Ref. 22 ) and Junkhan and Serovy (Ref. 23 ) have investigated the effects of flow acceleration on boundary layer velocity profiles and/or heat transfer upon flat plate surfaces. In all these investigations, if the acceleration of the axial flow exceeded a critical value, heat transfer was reduced and the velocity profiles approached a shape equivalent to that calculated for a laminar boundary layer. The effect of acceleration has been correlated to the dimensionless Launder parameter,  $K_L$ , defined by

$$K_L = \frac{\mu_g}{\rho_g u_z} \frac{du_z}{dz} \quad (76)$$

If this parameter exceeds a critical value of approximately  $2.0 \times 10^{-6}$ , turbulent boundary layers apparently undergo a re-transition to laminar flow, and the associated reduction in the eddy diffusivity for heat dominates the increase in heat transfer due to the accompanying flow into the wall. The theoretical analysis of radial velocity effects in the original BLEAT program was based upon the assumption that turbulent velocity profiles and eddy diffusivities under accelerating flow were similar to those under developed flow conditions (see page 35 ). Based upon the experimental investigations described immediately above, this assumption is no longer considered to be correct and a search was made for an alternate method of explaining and correlating the high heat transfer coefficients measured near the injectors of rocket thrust chambers.

Whereas rapid acceleration of the axial flow reduces heat transfer, the opposite has been found to be true for the case where an abrupt enlargement produces a rapid deceleration. Zemanick and Dougall (Ref. 24 ) measured the heat transfer to air, and Krall and Sparrow measured the heat transfer to water downstream of stepwise expansions in circular ducts. Seban (Ref. 26 ) and Filetti and Kays (Ref. 27 ) measured heat transfer coefficients downstream of step changes in rectangular cross-sectioned ducts. In these investigations, the ratio of the heat transfer coefficient at the attachment point to the fully developed

coefficient farther downstream was as high as 5.0. The increased heat transfer coefficients fell off gradually over a considerable distance downstream in the neutral acceleration region downstream of the attachment point. The interesting feature of the circular duct data of Refs. 24 and 25 was that the attachment point heat transfer for both water and air could be correlated by

$$Nu = .24 Re_S^{.67} Pr^{.4} \quad (77)$$

where the Nusselt number has its usual definition in terms of the local diameter

$$Nu = \frac{h D}{k}$$

but the Reynolds number is based upon the diameter of the passage just before the sudden enlargement

$$Re_S = \frac{D_S W_S}{A_S \mu_S}$$

Although attachment point heat transfer data for the rectangular cross-sectioned ducts were not correlated to this correlation in Refs. 26 and 27, an examination of graphically presented results indicates that a correlation would have been obtained on a similar basis. The implication of this common agreement for such differing fluids as water and air and for differing geometries is that a Reynolds number based upon injection conditions might provide the basis for calculating heat transfer at the attachment point in thrust chambers. Such a concept is applied in the following section.

Limited data were found in the literature survey describing impinging spray heat transfer, and only the studies by Rowley (Ref. 8, 9, and 10) were directly concerned with a bi-propellant burning spray fan. Rowley made a limited determination of the net heat transfer to a surface normal to the resultant momentum line of a single unlike doublet with the weakly hypergolic methanol/nitric acid propellant combination. Other less-directly-related data included the results of Nurick (Ref. 28), who determined the heat transfer from a heated surface to impinging sodium droplets, and that of Holman

and McGinnis (Ref. 29 ) who measured the cooling of a surface by single droplets of water, alcohol, and acetone. The data of Rowley and Nurick both indicate that spray heat transfer is proportional to approximately the normal spray mass flux raised to the .4-.5 power. These heat transfer results are correlated to a temperature driving potential (i.e., as a heat transfer coefficient); however their reported data do not cover the situation where the surface temperature is substantially above the saturation temperature of the liquid droplets. For a superheated surface, the data of Holman and McGinnis indicates that cooling peaks out at a superheat of approximately 300 F and then falls off very rapidly. This observed high temperature tailoff in heat transfer coefficient, which is probably related to the Liedenfrost phenomenon, makes the calculation of thrust chamber wall cooling by impinging spray very uncertain if based upon low wall temperature data.

This fact, together with the inconclusive experimental spray heat transfer data obtained in this project\* has resulted in the removal of the explicit spray cooling mechanism from the BLEAT theoretical model and its replacement with a simpler definition of adiabatic wall temperature and net film coefficient in the 3D-COMBUST zone of the thrust chamber.

#### Heat Transfer Model

In the 3D-COMBUST zone, the model assumes that the re-circulation region of Fig. 1 is followed by a wall attachment point where the local heat transfer coefficient is controlled by an injection Reynolds number according to Eq. 77 . The attachment point,  $z_A$ , is assumed to occur when the average axial gas velocity exceeds the average axial spray velocity. Because of the drag forces appearing in the z-momentum relation for the gas (Eq. 16 ), gas is drawn into the dense portions of the spray field upstream of  $z_A$ . However, downstream of  $z_A$ , the gas generated in the regions of high spray density must spread rapidly over the entire chamber cross section for the chamber pressure field to be one-dimensional as assumed in the 3D-COMBUST model. The attachment point must also be the

\* See pages 197-202.



axial location at which an adverse pressure gradient becomes a favorable pressure gradient. The acceleration of the average axial gas velocity due to the high rate of vaporization in the 3D-COMBUST zone is assumed to establish the boundary layer quickly. Accordingly, the high heat transfer coefficient at the attachment point is reduced over the 3D-COMBUST region (usually only 1-2 inch) to the film coefficient calculated by means of the Elliot-Bartz-Silver analysis for the STRMTB downstream region of Fig. 1. Film coefficients in the 3D-COMBUST region are therefore calculated by a linear interpolation between the value of  $h_g$  at the attachment point and the value of  $h_g$  at the start of the STRMTB region where the attachment enhancement to heat transfer is assumed to have disappeared.

For application in the BLEAT program, the Nusselt number representation of the heat transfer coefficient given by Eq. 77 is modified to a Stanton number correlation to eliminate the need to evaluate combustion gas thermal conductivity. By definition

$$St = \frac{Nu_D}{Re_D Pr}$$

therefore, Eq. 77 can be replaced by

$$St = \frac{Nu_D}{Re_D Pr} = C_A \frac{Re_S^{.67}}{Re_D} Pr^{-.6} \quad (78)$$

Heat transfer coefficients at the attachment point are calculated from Eq. 78 and Eq. 74. The injection Reynolds number employed in Eq. 77 is obtained from the general definition for a pipe flow system.

$$Re = \frac{4A}{P} \frac{W}{A} = \frac{4W}{\mu P}$$

For an injector with weight flow rates,  $W_1$  and  $W_2$ , of fuel and oxidizer, respectively, the injection Reynolds number becomes

$$Re_S = \frac{4(W_1 + W_2)}{u_g(P_1 + P_2)} \quad (79)$$

In Eq. 79,  $P_1$  is the perimeter of all the fuel orifices,  $P_2$  is the perimeter of all the oxidizer orifices, and  $u_g$  is the combustion gas viscosity. For lack of sufficient attachment point heat transfer data in thrust chambers, the coefficient  $C_A$  is defined as 0.24, the value which fits the data of Ref. 24 and 25. For liquid injection into a combustion gas environment, this is obviously an oversimplification and an appropriate empirical value must eventually be defined.

The adiabatic wall temperature is defined by the relation

$$T_{AW} = \frac{\rho_{d_1} T_{SAT,1} + \rho_{d_2} T_{SAT,2} + \rho_g T_g}{\rho_{d_1} + \rho_{d_2} + \rho_g} \quad (80)$$

Equation 80 amounts to the assumption that the local effective temperature for calculation of heat transfer is equal to the temperature of a gas flow whose enthalpy potential is equal to the mean enthalpy of the two-phase gas mixture\*.

In the present formulation of BLEAT, the effects of radial gas velocity and spray cooling are now contained only implicitly. The attachment of a flow stream downstream of a step change in cross-sectional area is necessarily accompanied by a radial velocity component; however, it is the turbulence carried by the radial velocity rather than the radial velocity, itself, that determines the heat transfer. Similarly, although spray cooling film coefficients are no longer explicitly calculated, the calculated heat transfer is affected by the reduction in the definition of adiabatic wall temperature due to the presence of an evaporated spray.

---

\*The heats of vaporization of the liquid propellants are ignored.

## HEAT FLUX

Local heat flux to the chamber walls is calculated by the standard definition

$$q/A = h_g (T_{AW} - T_{W,REF})$$

for an assumed gas-side wall temperature,  $T_{W,REF}$ , which is supplied by the BLEAT user as input data. (If no value of  $T_{W,REF}$  is assigned, by the user, the program assigns the value of  $T_{AW}$  to it and then calculates the zero heat flux condition which is approximately true for ablative systems). The overall heat load to the chamber walls is then calculated by

$$Q_{TOT} = \frac{2}{\Delta\theta} \int_0^{z^*} \int_0^\theta (q/A)_{z,\theta} A_{z,\theta} dz d\theta$$

The integration is made numerically by summation of local heat fluxes and local areas defined by

$$A_{z,\theta} = r_{Wz} \Delta\theta \Delta z$$

over all the wall mesh points.

## COMPUTER PROGRAM

A flow chart of the BLEAT computer program logic is shown in Fig. 52. The program structure consists of MAIN, the calling program, the major subroutines DTIN and DTOUT that, respectively, read the input data and write out the calculated results, the function YOF and subroutine ITRP2 which look up the physical properties of the propellants and combustion gas as functions of pressure, mixture ratio, and Mach number; the sub-routine LOCATE and function XITRP used within ITRP2 and finally the sub-routine TIME, which records the machine time required for the various steps of the BLEAT program. BLEAT is dimensioned to define local heat transfer parameters at a total of 120 wall mesh points. Ninety of these mesh points can incorporate the effects of transverse gas velocities and spray cooling.

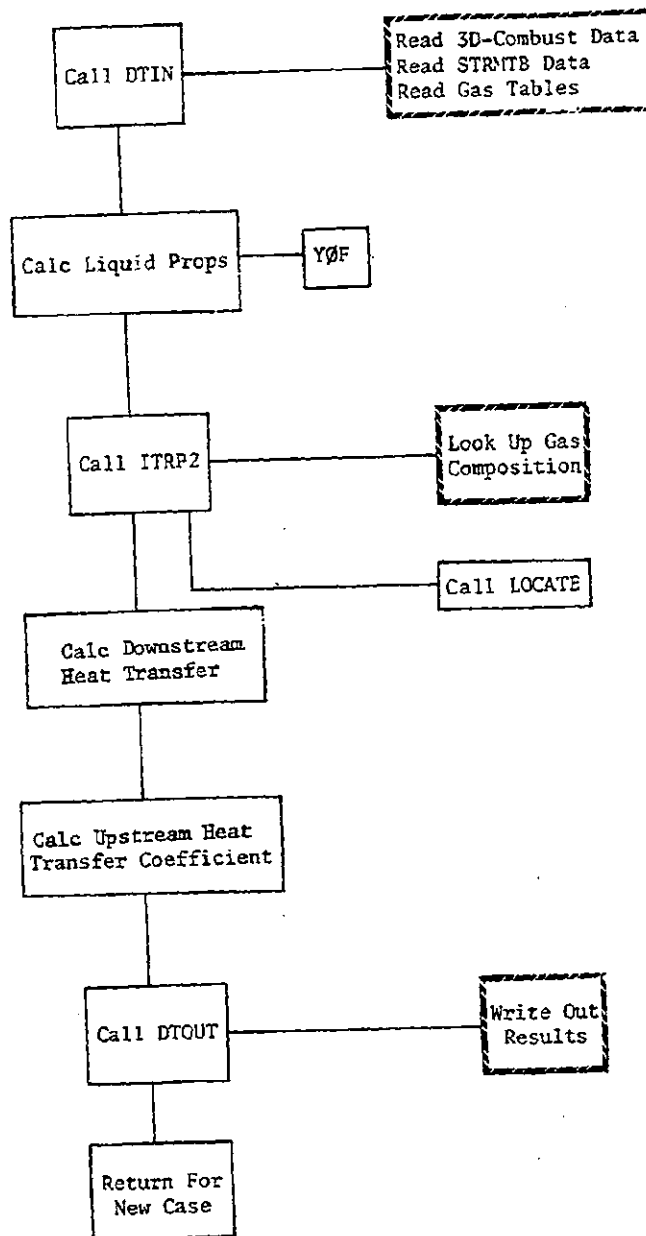


Figure 52 Logic Diagram for BLEAT Computer Program

### Input Data

Input data to the boundary layer program consists of:

1. The definition of the wall mesh point system, including the total number of wall mesh points, the number of wall mesh points that will receive input from the 3D-COMBUST program and the number of wall mesh points at each axial station.
2. Gas temperature, mixture ratio, and density; spray evaporation rates and the three gas and droplet velocity components at each wall mesh point
3. Tables of saturation temperature, heat of vaporization, and vapor specific heat for the propellants as functions of pressure
4. Tables of specific heat ratio, viscosity, and specific heat of the combustion gas as functions of mixture ratio
5. Tables of the mole fractions of  $H_2O$ ,  $CO_2$ , and  $H_2$  in the combustion gas as functions of the combustion gas mixture ratio and Mach numbers
6. Assigned values for  $C_A$ ,  $T_{W,REF}$ ,  $z_A$ ,  $w_1$ ,  $w_2$ ,  $P_1$ , and  $P_2$

Most of the input data to BLEAT are supplied directly as decks of punch card output supplied directly from the 3D-COMBUST and STRMTB programs.

### Computer Calculations

Based on the input data and the subprograms, the program first calculates required gas and liquid properties as a function of mixture ratio and pressure. Calculated properties include the mole fractions of  $H_2O$ ,  $CO_2$ , and  $H_2$ . The hot-gas heat transfer coefficient and the adiabatic wall temperatures are calculated in the upstream and downstream regions. Finally, local heat fluxes and the integrated chamber heat load are calculated.

### BLEAT Output

The printed output from BLEAT consists of four tabular arrays, the first of which contains a listing of all the input data. The second table gives the attachment plane heat transfer data. The third table of calculated data contains the local adiabatic wall temperatures, combustion gas heat transfer coefficients and local heat fluxes, together with the coordinates ( $r$ ,  $\theta$ ,  $z$ ) of each of the wall mesh points. The last table gives local values of pressure, gas temperature, mixture ratio, axial gas velocity, gas specific heat, and the mole fractions of  $H_2O$ ,  $CO_2$  and  $H_2$  in the gas at each mesh point.

## EXPERIMENTAL STUDIES

### INTRODUCTION AND SUMMARY

The objectives of the experimental program were threefold. One objective was to obtain data necessary to extend the range of empirical coefficients for relations already incorporated into the various computer programs of the Injector/Chamber Compatibility analysis, particularly the LISP program. The second objective was to explore certain mechanisms such as recirculatory flows and impinging spray heat transfer, the effects of which have been incorporated into the various analytical models, although these mechanisms are as yet only poorly understood. The third objective was to support in a general way the development of the IHTM injector face heat transfer analysis, providing both empirical heat transfer data and a general verification of assumed relations between heat transfer and such parameters as chamber pressure, injection velocity, etc. Because of the wide range of the objectives, they could necessarily be pursued in only limited depth within the scope of the overall investigation.

The experimental program can be subdivided into three phases. The first phase consisted of a series of cold-flow experiments with either single elements or complete injectors. The purpose of the single element tests was to obtain spray distribution data for the unlike doublet, the triplet, and the HIPERTHIN like doublet elements. The cold-flow tests with multielement injectors were performed to determine the extent to which liquid spray accumulates on chamber walls near the injector and to establish the occurrence of recirculatory gas flows between the spray fans of conventional liquid injector elements. The second phase consisted of a series of model motor firings whose purpose was to obtain injector face heat transfer data plus data describing the variation of chamber pressure with distance from the injector through the combustion chamber. The objective of the chamber pressure profile measurements was to establish the propellant vaporization rate through the chamber, particularly in the region close to the injector. The third phase consisted of a series of impinging spray heat transfer measurements performed in open air with an electrically heated strip and either water or the  $\text{N}_2\text{O}_4/50\% \text{N}_2\text{H}_4$  - 50% UDMH propellant combination. The purpose of these experiments was to determine the effectiveness of liquid spray impingement for chamber wall cooling.

## COLD FLOW EXPERIMENTS

### TEST FACILITY

Cold flow experiments to determine the spray distribution characteristics of both single injection elements and multi-element injectors were performed in a facility developed for this purpose at the Propulsion Research Area of the Rocketdyne Santa Susana field laboratory. In this facility, non reactive immiscible propellant simulants sprayed from the injector model are collected by a matrix of square-ended tubes. The spray collected by each tube flows on into individual glass tubes where the separation of the immiscible fluids into layers permits a direct volumetric measurement of spray mass and mixture ratio distributions.

A schematic representation of the flow system is shown in Fig. 53 . The propellant simulants, water and trichloroethylene, are pushed by high pressure nitrogen gas from their separate supply tanks through turbine flowmeters, filters, and shutoff valves to the model injector. High-speed shutters, which deflect the spray away from the collector until steady-flow conditions are obtained, are located between the injector and collector matrix to reduce the errors due to start and stop transients. The shutters are pneumatically operated and have an opening and closing travel time of 200 milliseconds. Two shutters are employed which move in opposite directions to reduce the error bias introduced by the shutter opening and closing.

The spray collector matrix is formed by 841 square-entrance stainless steel tubes in a 7-3/4-inch square array with 29 tubes on each side. Photographs of this spray distribution sampling system are shown in Fig. 54 . Each of the stainless steel tubes is connected to a separate glass tubular receptacle mounted in a collector rack at the base of the apparatus. Each of these glass tubes (receptacles) will hold 685 milliliters of liquid.



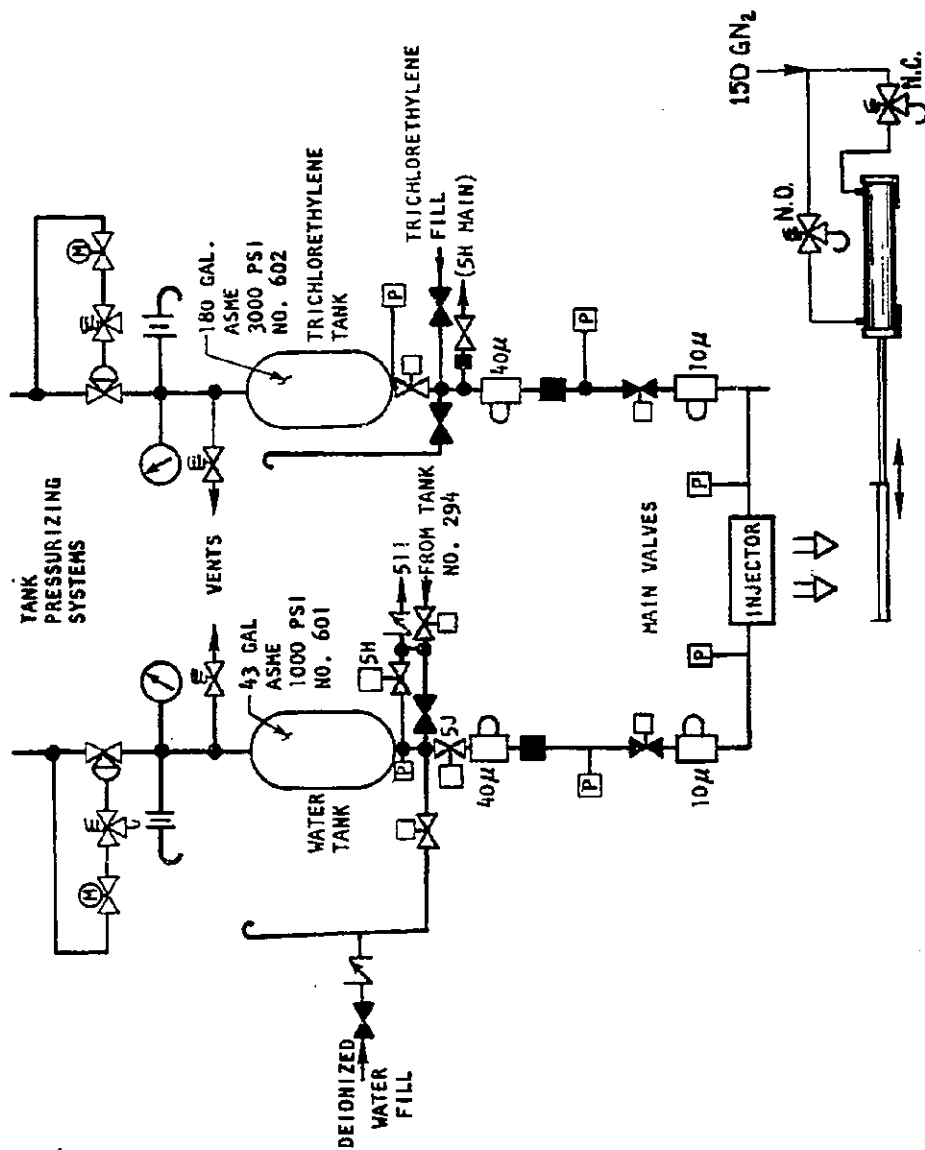
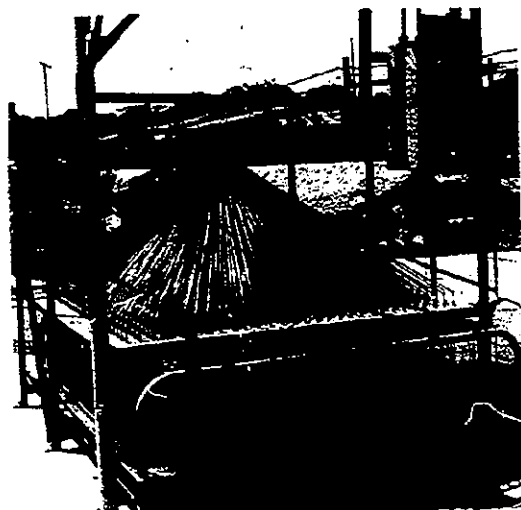
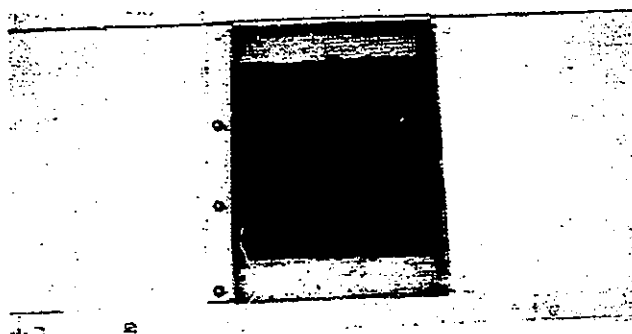


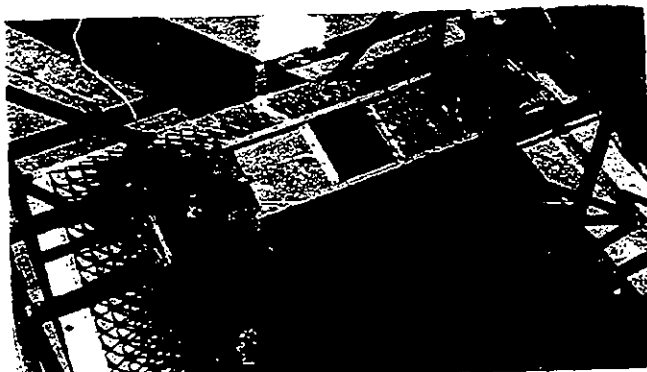
Figure 53 Cold Flow Test Facility (Flow System)



Overall View of Collector



Closeup View of Collection Grid



Shutter Arrangement

Figure 54 Cold Flow Mass Distribution Facility

The middle photograph in Fig. 54 shows the collection grid consisting of the 29 x 29 array of 1/4-inch-diameter x .020-inch-wall-thickness tubes which have been swaged to a .265-inch-square cross section. The lower photograph shows the pneumatically operated shutter arrangement over the collection grid.

The injector model to be tested is mounted above the face of a collector sampling grid, and is oriented so that its spray axis is vertical. The spray of simulated propellants from the injector is then intercepted at each individual sampling station and directed to individual collector tubes. The height of the injector above the collection plane is adjusted from 1 to 4 inches to get the maximum differentiation of the mass flux distribution while keeping the spray within the boundaries of the collector.

Because trichloroethylene and water are immiscible and have substantially different specific gravities, they quickly separate, and determination of the volume of each simulant can be easily made. To facilitate this determination, the trichloroethylene is dyed with duPont No. 885, a red dye which is soluble in oil but insoluble in water. The liquid collected in each tube is poured into graduated cylinders and the volume of trichloroethylene and total liquid volume are read and recorded.

The collector matrix as shown in the middle photograph of Fig. 54 was used for conventional planar sampling experiments, i.e., for determination of mass and mixture ratio distribution in a given plane some distance downstream of the injector face. For experiments performed to determine the radial spray flux which impinges upon chamber walls immediately downstream of given injector configurations, the collection system was modified to incorporate the spray sampling tray shown in Fig. 55 and 56. Flexible Tygon tubing was used to carry the spray, collected in nine 10-degree collector trays and three 90-degree collectors around the injector, to glass tubes in the rack shown in Fig. 57.

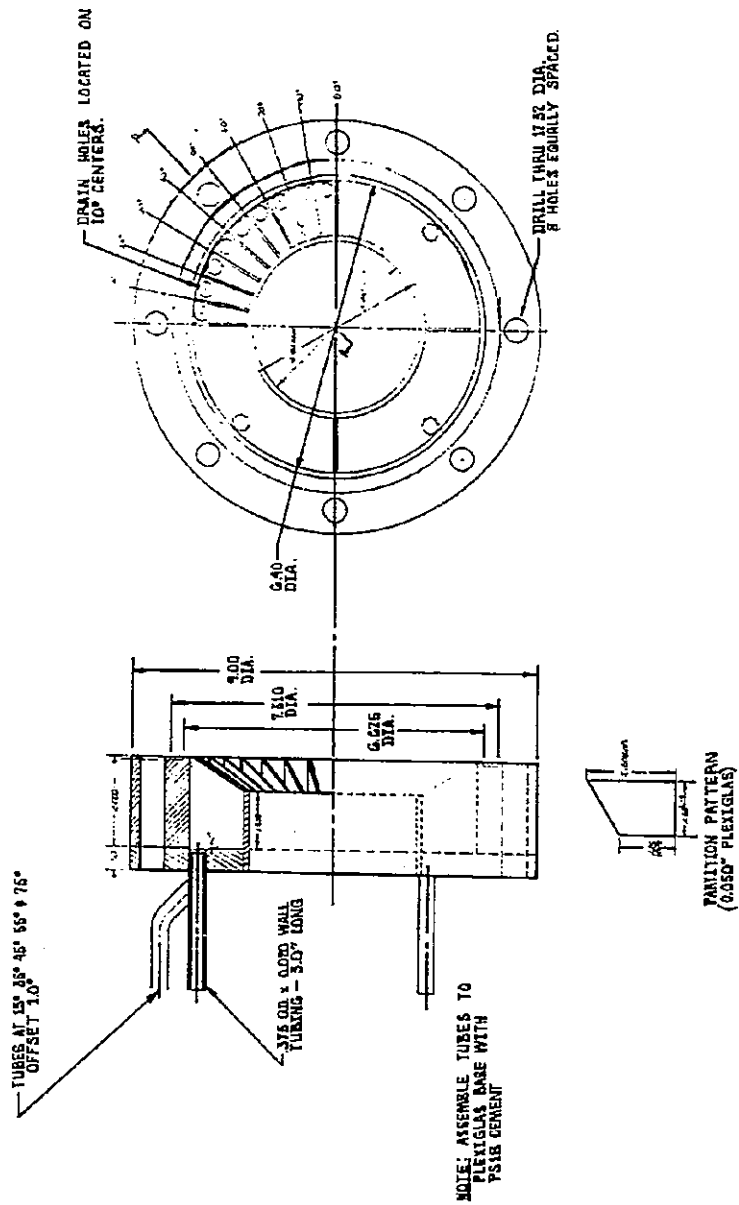


Figure 55 Radial Spray Flux Sampling Tray

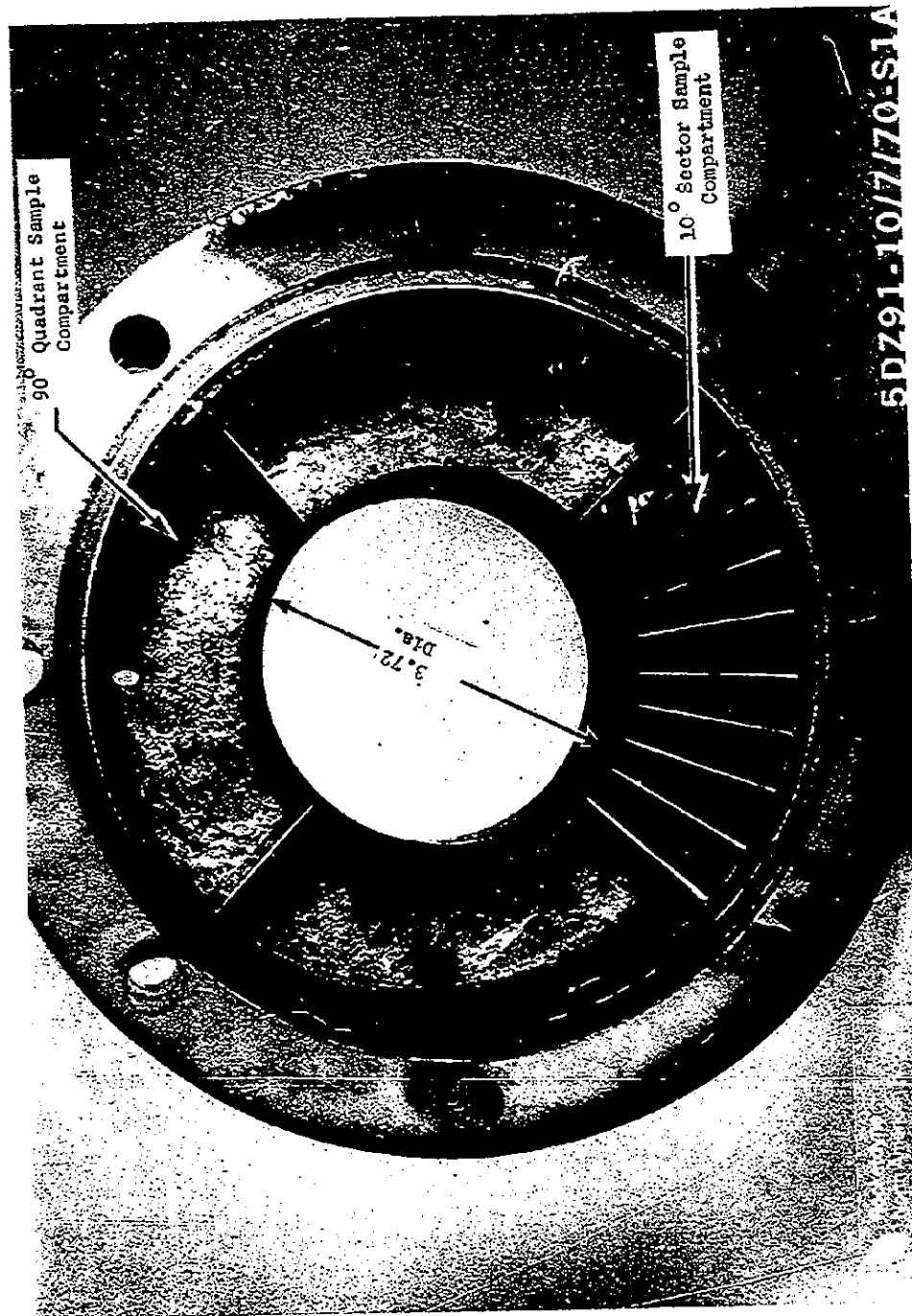


Figure 56 Radial Spray Collector Tray

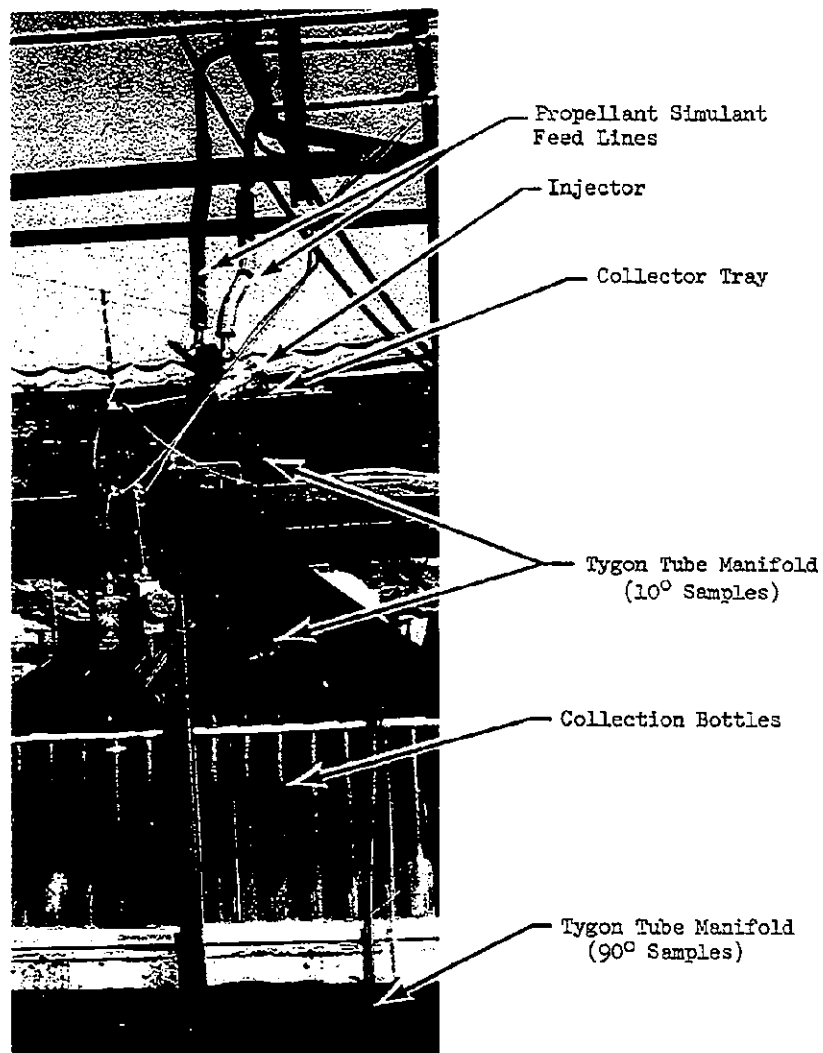


Figure 57 Cold Flow Test Stand Modified for Radial  
Spray Sampling Experiment

For cold flow experiments performed to demonstrate that gas recirculation between injector spray fins could be driven by the aspirating effects of dense spray jets, the test injectors were mounted in the system of Fig. 53 and 54 . A Lucite shroud with a diameter of 3.75-inch and a length of 2.0-inch was bolted to the injector face to insure that gas aspirated into the spray jets were supplied by recirculation between the jets rather than a base bleed across the injector face.

#### COLD FLOW HARDWARE

Cold flow tests were performed with both single element injection models for determination of LISP equation spray coefficients and with the multi-element injectors used in the model motor firing experiments of both the previous Injector/Chamber Compatibility project (Ref. 1) and the current program. The latter multi-element experiments were performed either to determine radial spray fluxes or spray-driven gas recirculation.

#### Single Element Models

Four single element injector models were employed in the cold flow experiments including one unlike doublet, one triplet, and two HIPERTHIN like doublet configurations. The unlike doublet and triplet models were fabricated from lengths of stainless steel tubing and standard AN flared tube fittings clamped into the adjustable workhorse jig assembly shown schematically in Fig. 58. Pertinent dimensions of the elements are listed below:

	<u>Doublet</u>	<u>Triplet</u>
Water Orifice(s) diameter (inch)	0.085	0.085
Trichlor orifice diameter (inch)	0.132	0.132
Diameter ratio	1.55	1.55
Orifice L/D (water)	20	20
Orifice L/D (Trichlor)	13	13
Impingement angle (deg.)	60	60

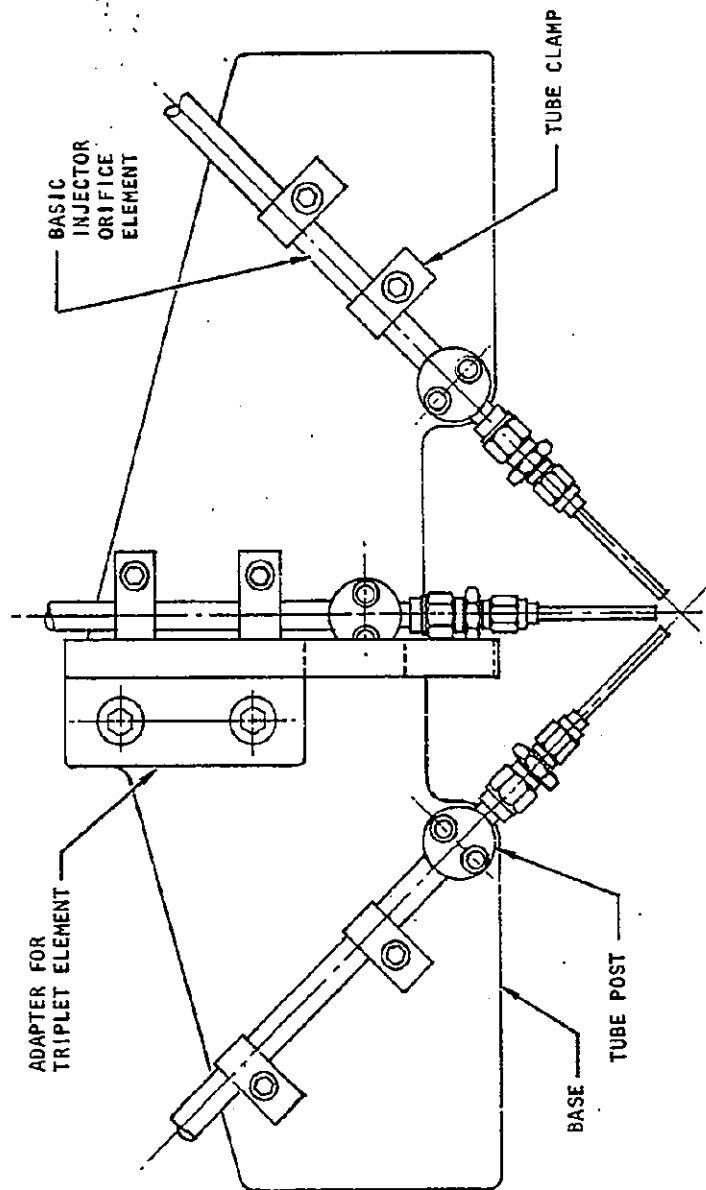


Figure 58 Workhorse Single Element Cold Flow Injector Arranged as a Triplet



A photograph of a cold flow with the triplet hardware is shown in Fig. 59 .

The two HIPERTHIN like doublet models were fabricated from mating steel blocks in accordance with the specifications presented in Fig. 60 . Each element basically consisted of two rectangular orifices (either .004-inch x .0185-inch or .008-inch x .0185-inch) edge-impinging at 60 degrees along a plane parallel to the long sides of the orifices.

#### Multi-Element Injectors

Four multi-element injectors were employed in the cold flow experiments performed to determine radial spray fluxes. They included:

ICC1, a 72-element like doublet injector designed to provide mixture ratio bias, and whose detailed configuration is presented in Fig. 67 and 84 of Ref. 1.

ICC2, an 8-element unlike doublet injector with essentially the same specifications as injector ICC2A described in Fig. 64 of this report.

ICC3, an 18-element triplet injector whose specifications are presented in Fig. 69 and 86 of Ref. 1.

ICC4, a 16-element like-doublet pair injector whose specifications are presented in Fig. 71 and 81 of Ref. 1. Injector ICC4 was cold flowed both with and without a three-bladed baffle.

The two injectors, ICC2A and ICC6, which were cold flowed to investigate gaseous recirculation are described in the model motor firing hardware section of this report.



Figure 59 Single Element Workhorse Injector  
During Triplet Cold Flow Experiment



## TEST PROGRAM AND RESULTS

### Single Element

Initially, three cold flow mass distribution tests were performed with each of the single element unlike doublet and single element triplet models described above. Test conditions and results are summarized as Runs 501-506 of Table 7. The purpose of these experiments was to generate data for determining LISP spray coefficients; therefore the tests spanned a much wider range of momentum ratio than would ordinarily be employed for mixing optimization. As a consequence, the Rupe mixing indices shown in Table 7 for most of the experiments are low. However, examination of the collected spray histograms indicated that not only was poor mixing being obtained, but the sprays were not symmetric as assumed in the LISP correlation. Part of the observed symmetry was traced to inadequately controlled impingement with the fans being particularly sensitive to very slight misalignments at the non-optimum momentum ratios. Because new reliable mass distribution data were particularly needed for the triplet, five additional cold-flow tests (Runs 521-525 of Table 7) were performed in which the extreme momentum ratios were avoided and extra care was taken to provide the best possible impingement. Fan symmetry was considerably improved.

The spray mass distribution results were incorporated with other available data to correlate LISP spray coefficients as described in the Analytical Developments section of this report.

### Radial Spray Flux

The cold flow experiments were performed to determine the spray which impinges upon chamber walls in the first 0.75-inch downstream of the injector face for the four multi-element injectors employed in the previous Injector/Chamber Compatibility project. These cold flows were performed at flow rates and simulant mixture ratios equivalent to the operation of the injectors at a chamber pressure of 200 psia and nominal overall mixture ratios of 1.2 and 1.6 for the  $N_2O_4/50\%$  UDMH

TABLE 7 SUMMARY OF SINGLE ELEMENT COLD FLOW EXPERIMENTS  
PERFORMED TO DETERMINE MASS DISTRIBUTION CHARACTERISTICS

RUN NUMBER	ELEMENT TYPE	WATER FLOW RATE	TRICHLOROETHYLENE FLOW RATE	MOMENTUM RATIO	RUPE MIXING INDEX
501	Unlike Doublet*	.268 lb <sub>m</sub> /sec	.442 lb <sub>m</sub> /sec	.78	46.1
502	"	.268	.531	1.18	55.7
503	"	.268	.785	2.51	78.2
504	Triplet**	.544	.443	.38	38.1
505	"	.540	.698	.96	48.7
506	"	.543	1.025	2.04	66.6
521	"	.485	.525	.68	52.9
522	"	.489	.638	.97	66.7
523	"	.487	.640	.99	69.3
524	"	.474	.485	.60	48.5
525	"	.490	.695	1.15	68.4

\* For doublet,  $D_{TRIC} = .132$ ,  $D_{H_2O} = .085$

\*\* For triplet,  $D_{TRIC} = .132$ ,  $D_{H_2O} = .085$

propellant combination. The cold flow conditions therefore modeled the conditions at which most of the motor firings of the previous project had been performed.

The purpose of the experiments was to determine whether a sufficient amount of spray was impinging upon the chamber walls close to the faces of the injectors tested to account for the low upstream adiabatic wall temperatures measured in the motor firings described in Ref. 1. Based upon mass balances during cold flow tests and upon visual observations of multi-element injector cold flows, estimates of spray back wash in excess of 5 percent of the main propellant flow have been made. The results of the current cold flow tests were, therefore, very surprising in that they indicated that negligible amounts of spray were impinging upon the near-injector walls of the chamber.

The results of the radial spray experiments are summarized in Table. 8 . The experiments show that the radially directed spray near the injector was never greater than 0.6 percent of the total propellant flow and was ordinarily less than 0.1 percent of the total flow. The higher amounts of radial spray were associated with the baffled injector ICC4 and with the 72-element like doublet injector ICC1 which contained an outer ring of 24 fuel elements close to the chamber wall. As shown by a comparison of the data in the last two columns of Table 8 , the radial spray flux varied substantially around the circumference of the collector spray; however the collected radial mass was always a negligible part of the overall flow. These experimental results agree with the predictions of the LISP program for the same region.

From the results of the radial spray cold flow experiments, it was concluded that the amount of spray impinging directly upon chamber walls very close to the injector<sup>\*</sup> was negligible relative to the main flow. Therefore, even if this small amount of spray is an important factor in the adiabatic wall temperature distribution, the uncertainty in defining the density and mixture ratio of this small fraction of the total spray by means of the LISP computer program precludes use of near-injector spray impingement as the basis of a wall temperature calculation.

---

\* Unless the thrust chamber is designed specifically for liquid spray cooling.

TABLE 8 RESULTS OF RADIAL SPRAY SAMPLING EXPERIMENTS  
WITH MULTI-ELEMENT INJECTORS

RUN	INJECTOR	TOTAL PROPELLANT FLOW RATE lb <sub>m</sub> /sec	TOTAL PROPELLANT COLLECTION RATE lb <sub>m</sub> /sec	MIXTURE RATIO OF COLLECTED PROPELLANT	MAXIMUM RADIAL SPRAY FLUX lb <sub>m</sub> /in <sup>2</sup> sec	AVERAGE RADIAL SPRAY FLUX lb <sub>m</sub> /in <sup>2</sup> sec
511	ICC4(Baffle)	5.28	.004	13.6	.006	.0005
511A	"	5.12	.029	1.0	.015	.0033
512	"	5.11	.029	2.2	.006	.0033
513	ICC(No Baffle)	5.43	0.0	--	0.0	0.0
514	ICC2	5.05	.002	1.6	.0005	.0002
515	"	5.07	.003	0.6	.0005	.0003
516	ICC3	5.11	0.0	--	0.0	0.0
517	ICC3	5.14	0.0	--	0.0	0.0
518	ICC1	5.10	.007	0.0	.0012	.0008
519	ICC1	5.16	.007	0.0	.0013	.0008

#### HIPERTHIN-LIKE DOUBLET

Three sets of cold flow experiments were performed with the HIPERTHIN element shown in Fig. 60. Six spray mass distribution experiments were performed over an injection velocity range of 34 to 72 ft/sec with the spray sampled at a distance of either 1.0- or 2.0-inch downstream of the element impingement point. The results of these experiments and their correlation to the LISP distribution formula (Eq. 5b) are discussed in the Analytical Developments Section (pp. 60-63).

Because the liquid fans formed by the HIPERTHIN element were so narrow, essentially all mass was collected in a single row of spray sampling matrix. The definition of the corresponding LISP spray coefficient  $b$  was essentially impossible under these circumstances; therefore, an additional set of experiments was made to further clarify the thickness of the liquid film. In these experiments, a No. 61 drill (0.039-inch diameter) was placed beside the fan as a reference and photographs were taken. A special sampling device consisting of a small inclined chute was also improvised and three mass distribution samples were taken with the upper end of the chute being moved in and out of the fan and spray being collected at the lower end of the chute. When the sampling rig was 3/32 (.094-inch) from the center of the fan, the collected mass fell to a single drop over a 70-second collection period. This result was compared to the photographs of the fan and adjacent drill. Within the resolution of the two techniques, the total thickness of the HIPERTHIN spray fan was determined to be less than 0.15-inch.

#### Gas Re-Circulation

An exploratory set of cold flow experiments was performed to verify that spray jets do induce re-circulation as assumed in the injector face heat transfer model. In these experiments, a lucite plastic shroud was attached to unlike doublet injector ICC2A (Fig. 64) and triplet injector ICC6 (Fig. 66), and the injectors were then water flowed. The plastic shroud, which was 2.0-inch long, insured that the air aspirated into the injector element spray jets must be replaced by re-circulation rather than a base flow across the injector face. Total pressure probes or pitot tubes were mounted at eight locations on the injector face together with two



additional probes adjacent to the shroud walls at distances of 0.50 and 1.00-inch downstream of the injector. The total pressure probes were positioned with their ram sensing ports open to reverse flows and were referenced to flush mounted pressure taps in the shroud walls. Pressure differences were measured with an inclined manometer.

Tests were run at injection velocities of 108 to 200 ft/sec with the doublet injector ICC2A. Depending on the locations, both positive and negative momentum pressure drops were measured. A positive pressure drop was interpreted as a reverse flow. A negative pressure drop was interpreted as the base pressure behind a trailing surface, i.e., as the indication of flow away from the injector.

Reverse flows were measured at three locations on the injector face and at the probes next to the shroud walls. The momentum pressure drops on the injector face were weak; however, near the shroud, a re-circulation air velocity of -35 ft/sec was measured at a water injection velocity of 108 ft/sec and an air velocity of -65 ft/sec was measured at an injection velocity of 165 ft/sec. A satisfactory calibration of the base pressure response of the probes to positive gas velocities was not obtained; therefore the magnitude of the positive air velocities was not established.

Although the experiments were limited in scope and did not attempt to systematically map the re-circulation region, they indicated the existence of the significant reverse flows required if the injector heat transfer model is to be physically correct.

## MOTOR FIRING EXPERIMENTS

### FACILITY

The motor firing experiments made to determine injector face heat transfer and axial chamber pressure profiles were performed on Pad 3B of the Rocketdyne Combustion and Heat Transfer Laboratory. A schematic of the overall facility is shown in Fig. 61. The general appearance of the test stand as set up for a motor firing together with a general view of the high pressure propellant tank system are presented in Fig. 62 and 63. Nitrogen gas was employed both as the tank pressurant and as a purge for the injector and thrust chamber. High pressure water was used to cool the basic 2.15:1 contraction ratio nozzle and to flush the fuel manifold and chamber after each firing.

Experiments were controlled from a concrete blockhouse adjacent to the test stand. Propellant flow rates during a firing were established by regulation of the supply tank pressure and the setting of adjustable cavitating venturis. Data from the various pressure, temperature, and flow transducers were automatically recorded through a multi-channel Beckman digital voltmeter system.

### INJECTORS

Two injectors, ICC2A with eight unlike doublet elements and ICC6 with twelve triplet elements, were used during the motor firing experiments. A single element unlike doublet injector was also fabricated but was never fired due to a revision in the test program.

Figure 64 is a detailed drawing of the ICC2A configuration. This injector is essentially a re-work of the ICC2 hardware employed in the previous Injector/Chamber Compatibility project (Ref. 1) to permit installation of heat transfer instrumentation in the injector face. This was accomplished by replacement of the conventional fuel dome with a single 0.625-inch diameter tubular downcomer. The downcomer terminated in a small cross-shaped manifold milled in the back of the injector and sealed by a similarly-shaped welded cover plate. This manifold fed fuel to the required eight injector orifices but opened the original dome

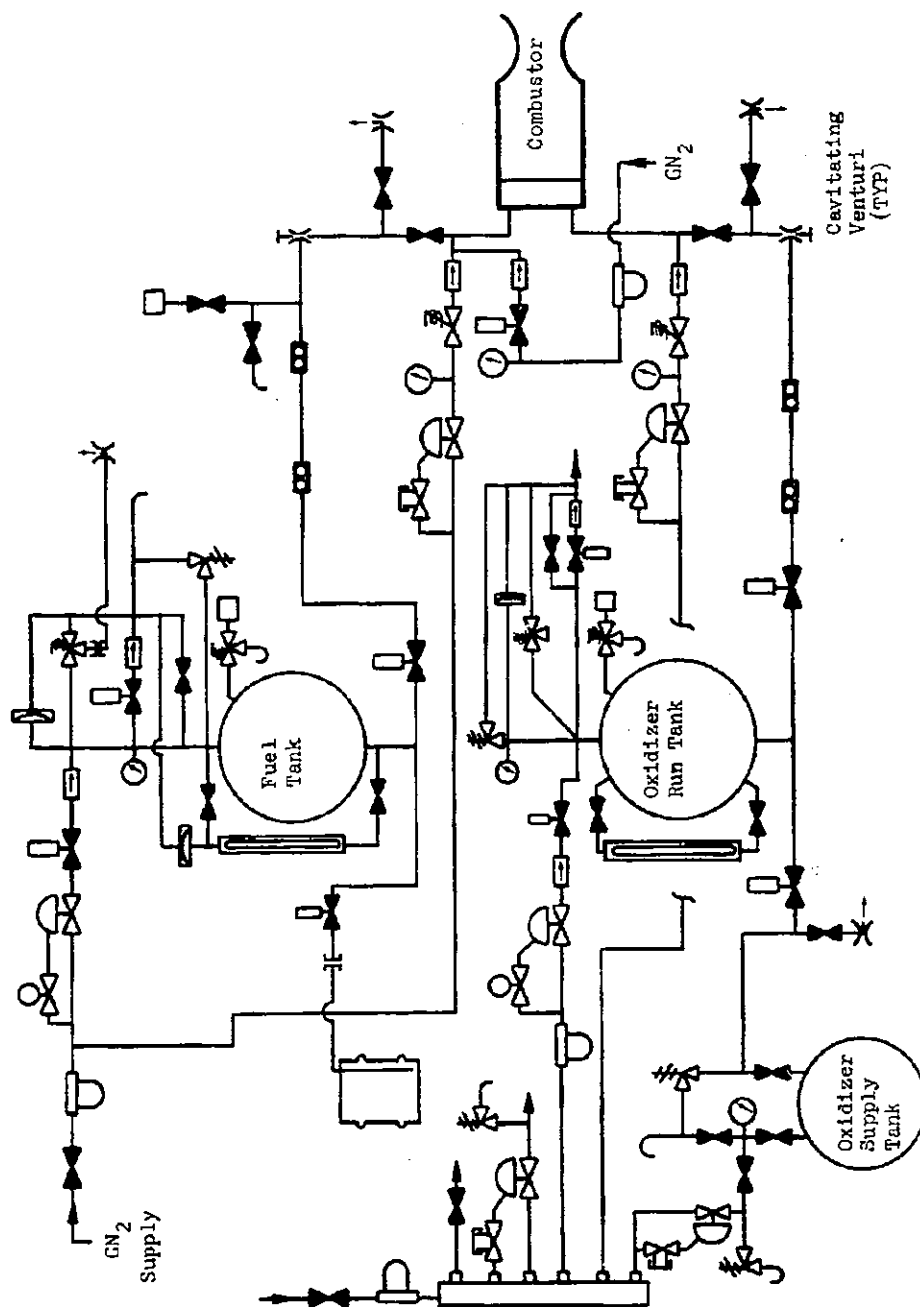


Figure 61 Pad 3B Test Stand for Storable Propellant Motor Firing Experiments

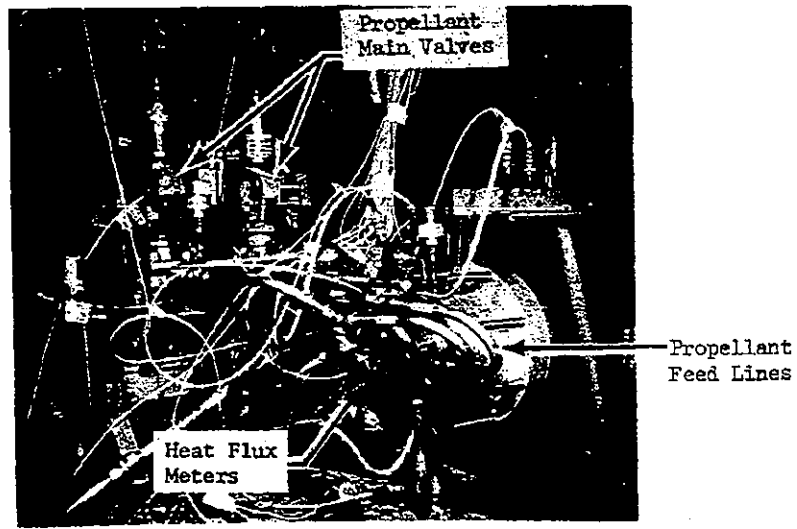


Figure 62 Test Stand and Hardware



Figure 63 High Pressure Propellant Tanks at Pad 3B

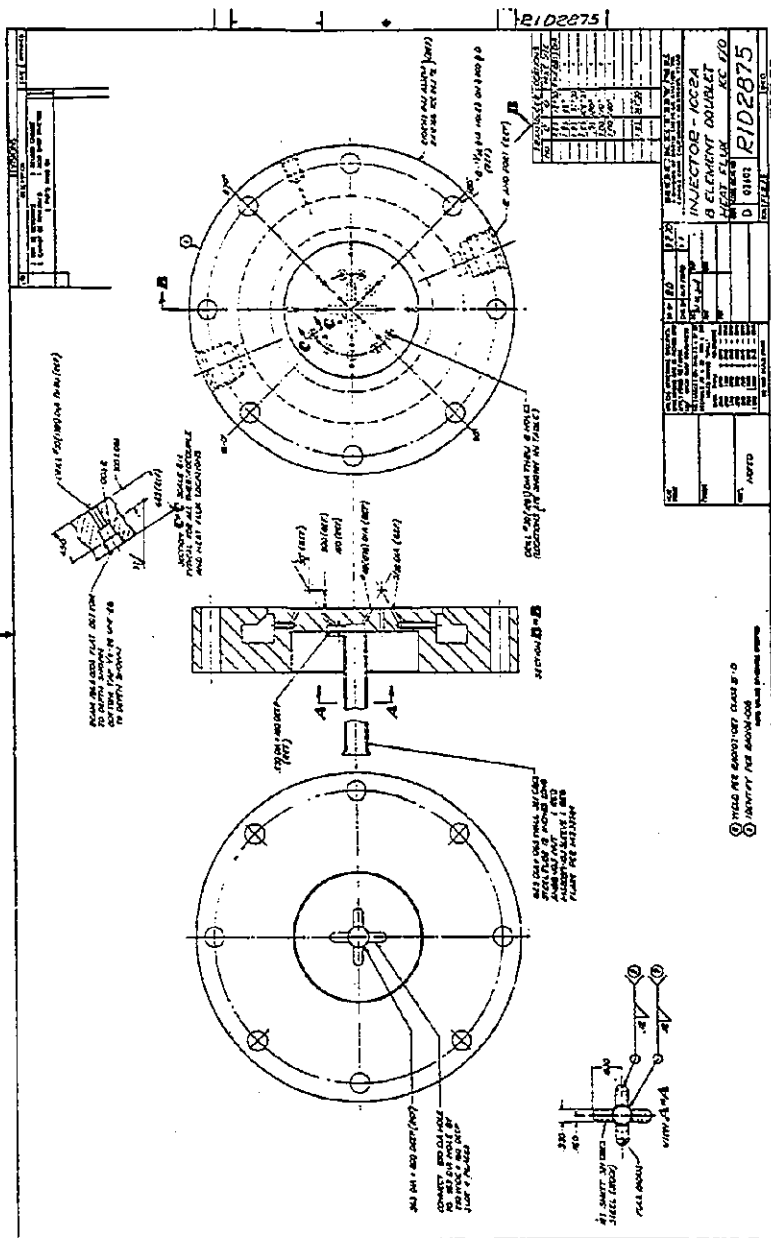


Figure 64 Night Element Unlike Doublet Injector ICC 2A

space to the installation of eight probes for measurement of either heat flux or gas temperature at the radial and angular locations tabulated in Fig. 64. The arrangement of the heat transfer instrumentation in the dome space at the back face of injector ICC2A is shown in Fig. 65.

The 12-element triplet injector ICC6 configuration is shown in Fig. 66. Because of the unusual space requirements imposed by the need to bring heat transfer instrumentation from the back side of the injector through to the injector face, an offset ring manifold, from which twelve separate tubular feed passages led to the oxidizer orifices, was incorporated into the design. A photograph of this novel manifolding arrangement together with the heat transfer instrumentation which it permitted is shown in Fig. 67.

The design of ICC6 was unusual in that it intentionally utilized very high oxidizer injection velocities, i.e., velocities of 100-200 ft/sec and higher. This was done to produce an exaggerated spray/gas drag and hence (according to the analytical model) high recirculation and injector face heat transfer for evaluation of empirical coefficients. Although the desired high heat transfer response was obtained, the extreme injection velocities were probably also partly responsible for the unusual chamber pressure profiles obtained with the injector.

#### THRUST CHAMBER HARDWARE

Motor firings were made in the workhorse combustor assembly utilized in the previous Injector/Chamber Compatibility project (Ref. 1). The chamber consisted of either one or two 3.72-inch ID by 8.0-inch long copper heat sink liners. Tests were made at three contraction ratios. A 2.15:1 contraction ratio nozzle segment was the same water-cooled section used in the previous Injector/Chamber Compatibility project. The configurations of two uncooled copper heat sink nozzle segments with contraction ratios of 1.045:1 and 4.3:1 are shown in Fig. 68 and Fig. 69, respectively.

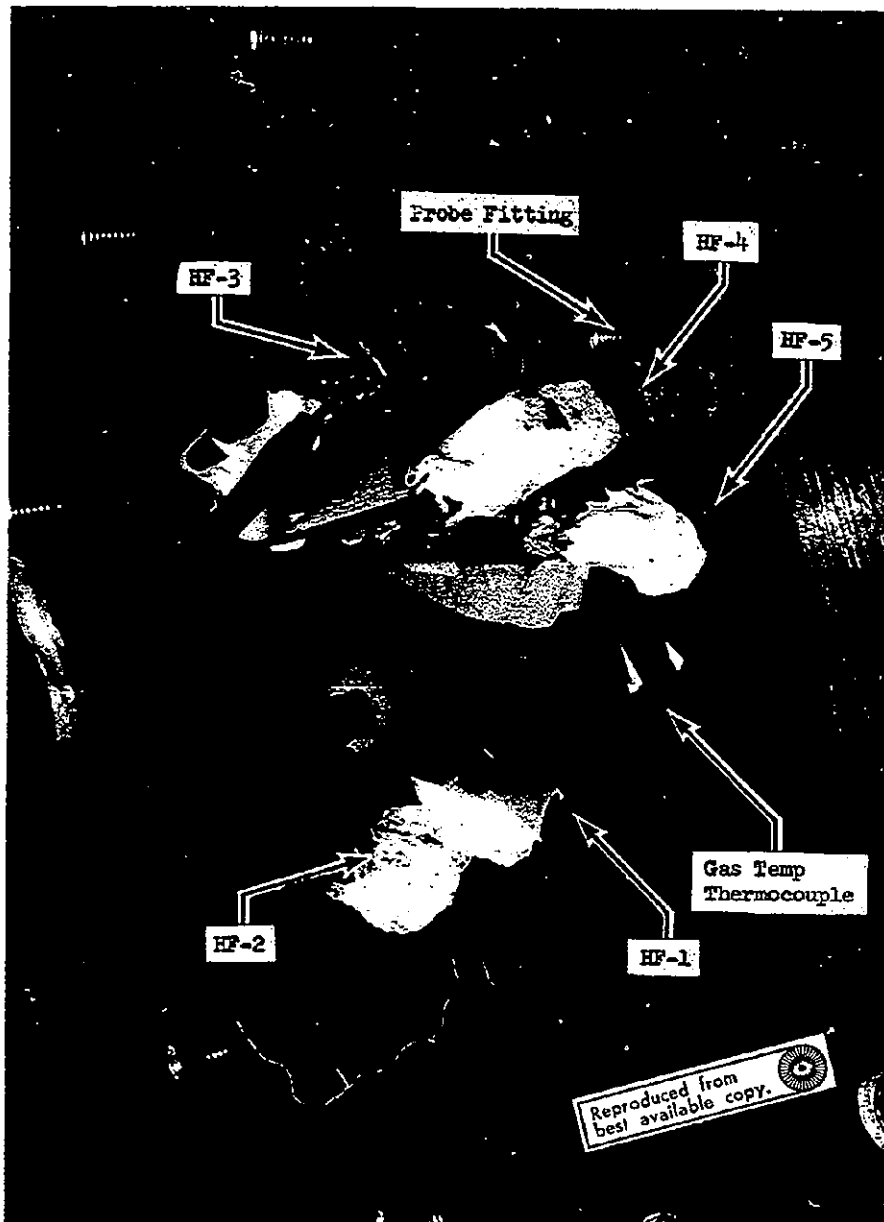
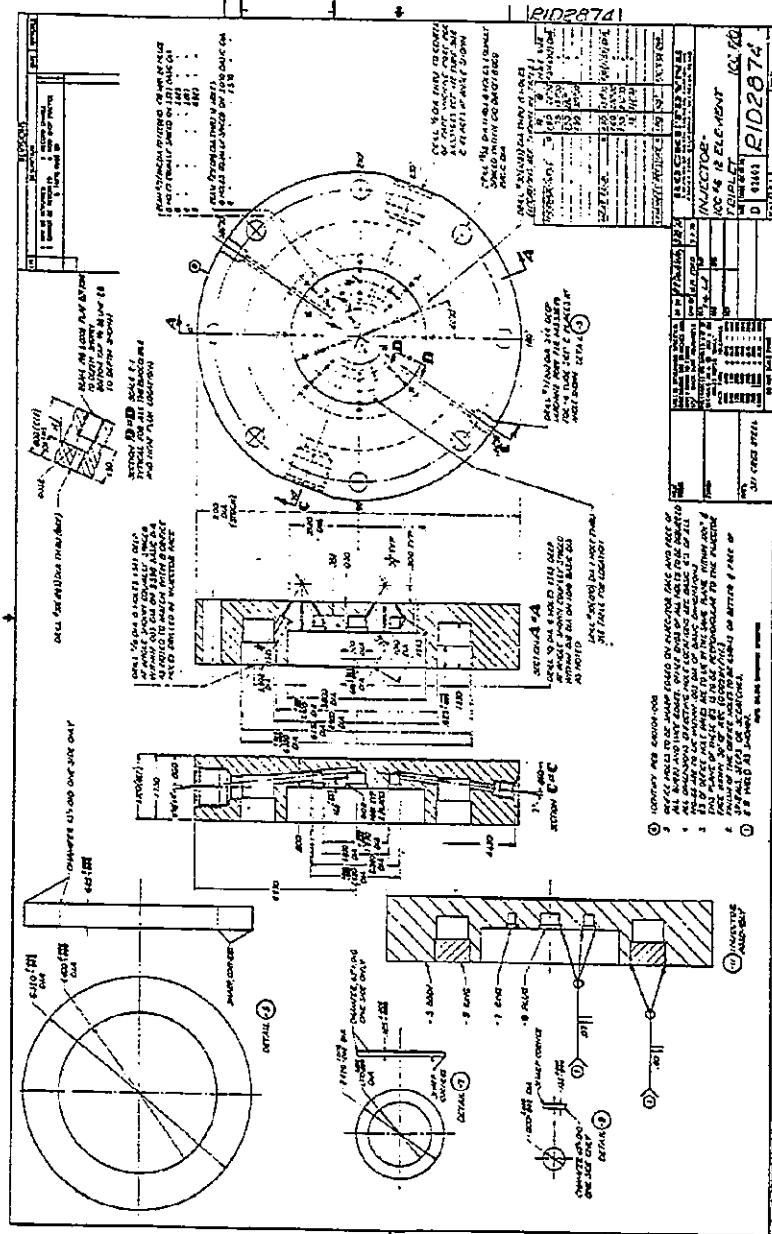


Figure 65 Backwall View of Injector ICC2A with Heat Transfer Instrumentation





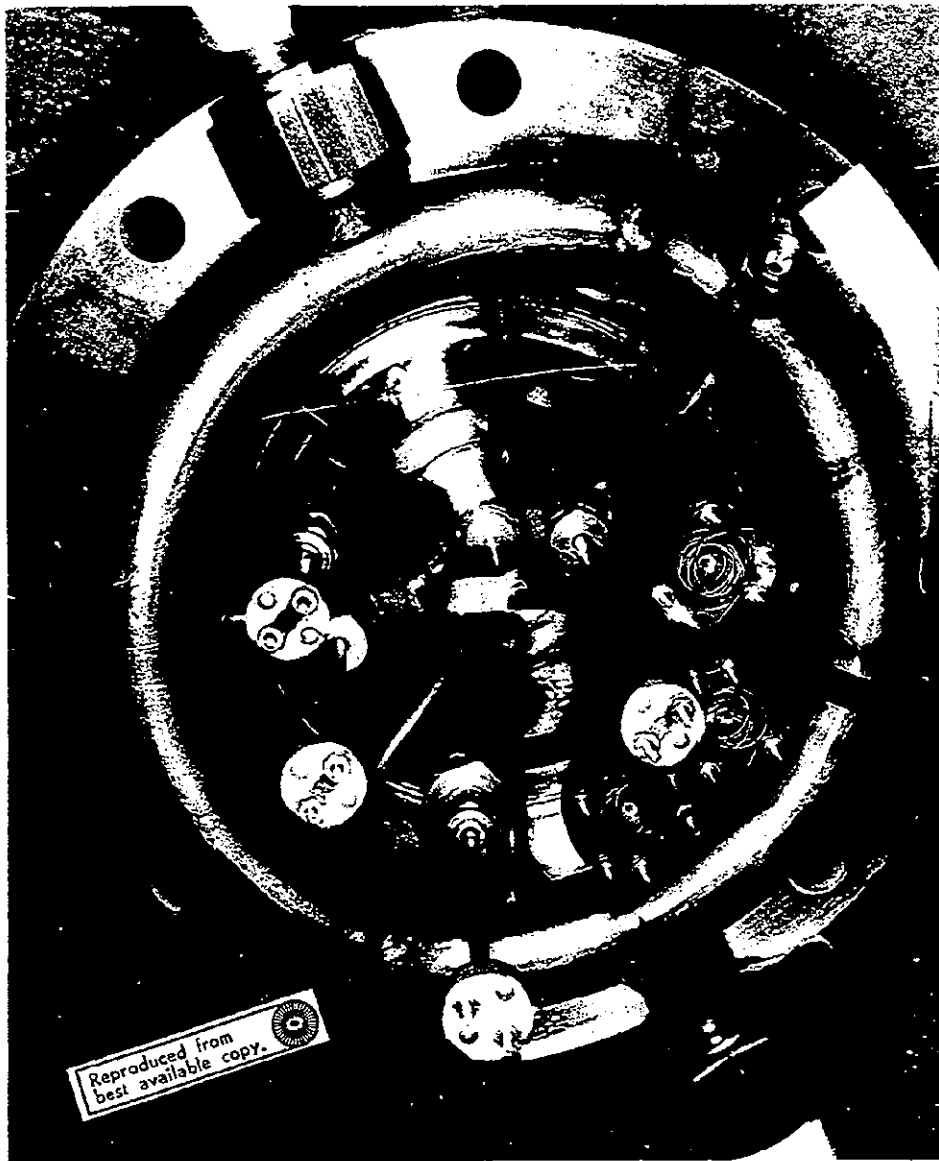
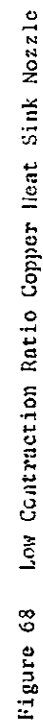


Figure 67 Backwall View of Triplet Injector ICC6



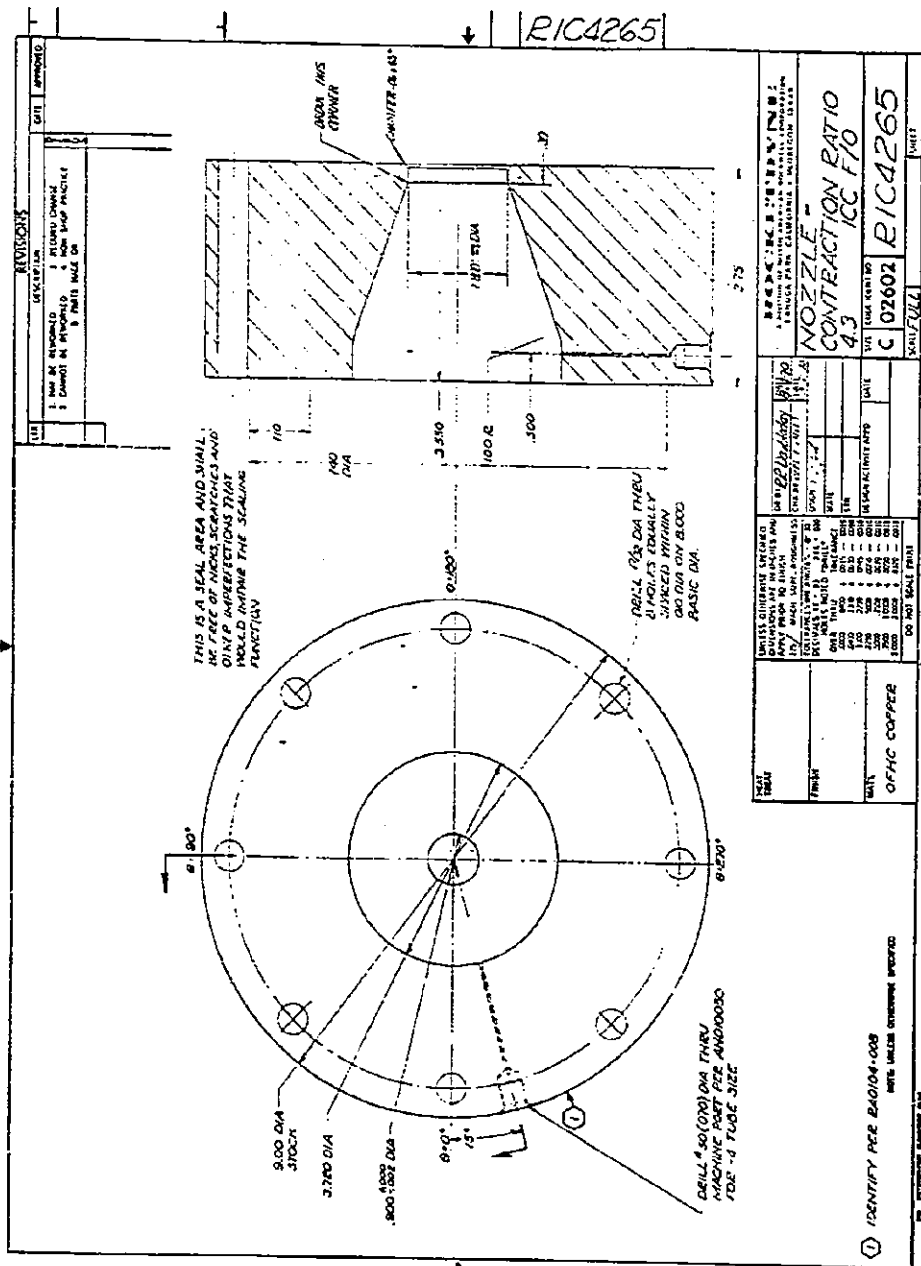


Figure 69 High Contraction Ratio Copper Heat Sink Nozzle

## INSTRUMENTATION

### Heat Flux Transducers

Economical measurement of local injector face heat fluxes in short duration model motor firings required the development and manufacture of a small fast response heat flux transducer. The difference thermocouple probe illustrated schematically in Fig. 70, which was manufactured by press fitting two sheathed constantan leads inside a slender copper plug and had been used successfully for measuring chamber wall heat flux in the previous Injector/Chamber Compatibility project (Ref. 1, pp 203-208), provided the basis for a transducer design. However, because the previous design did not lend itself to an economical volume production and because external instrument lead attachment had been a problem, development of a new design based upon electroforming OFHC copper to the bared ends of a pair of sheathed constantan leads was attempted. Two designs were utilized.

The first design is shown in Fig. 71. A braided pair of sheathed 4.-mil constantan leads are threaded through a drilled copper body. The bared leads are spaced approximately .10-inch apart. An excess deposit of OFHC copper is slowly plated around the ends of the leads and adjacent copper body and then machined back to the dimensions shown in Fig. 71. At the back surface of the copper transducer body, the small diameter, high resistance constantan leads are spot welded to heavier constantan leads and potted within an epoxy jacket for strength. Finally an additional copper lead is spot welded to the back surface of the probe body.

The second probe design, which is illustrated in Fig. 72 and 73, was similar to the first except that thermocouple leads are carried from the rear of the copper transducer body to a plastic terminal block in a rigid tubular conduit. The result was a more rugged instrument with a reduced problem of external lead breakage during installation and motor firings.

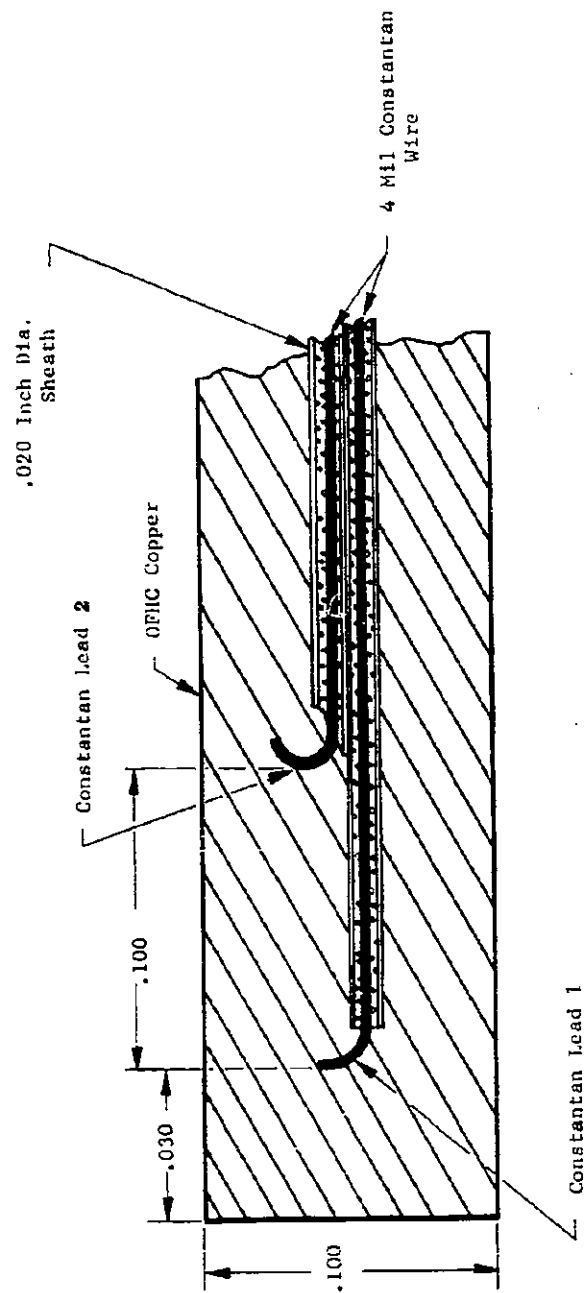
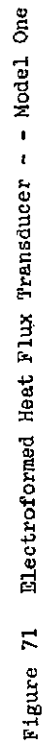
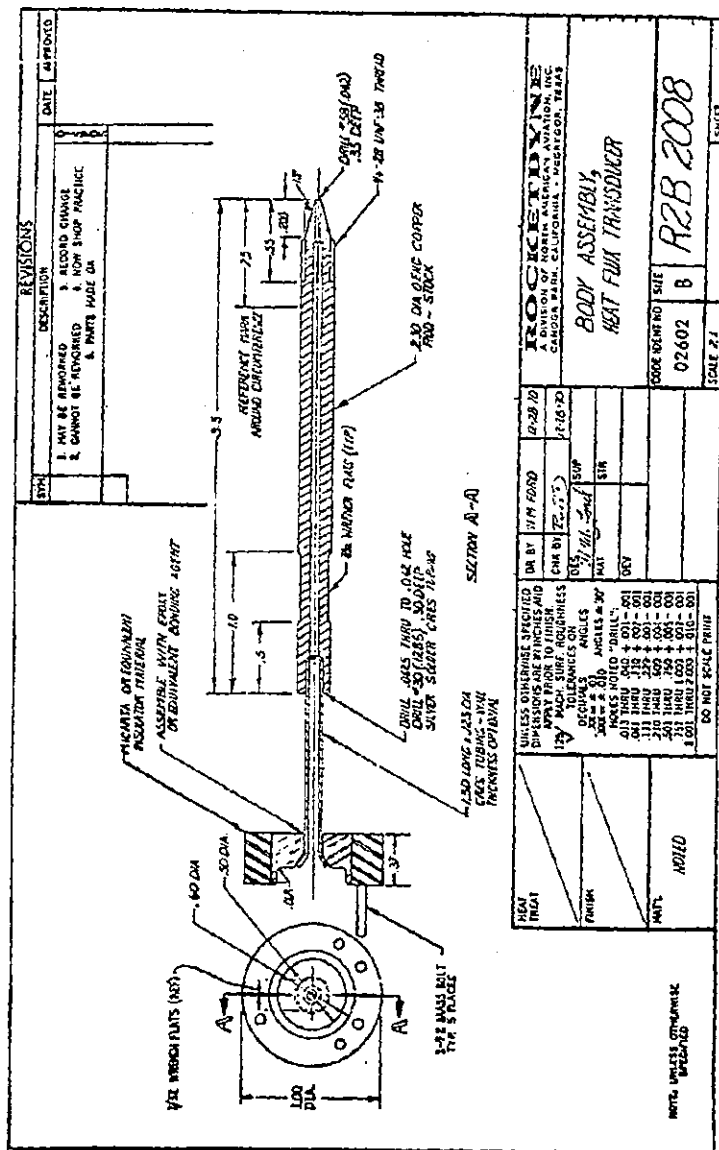


Figure 70 Difference Thermocouple Heat Flux Probe





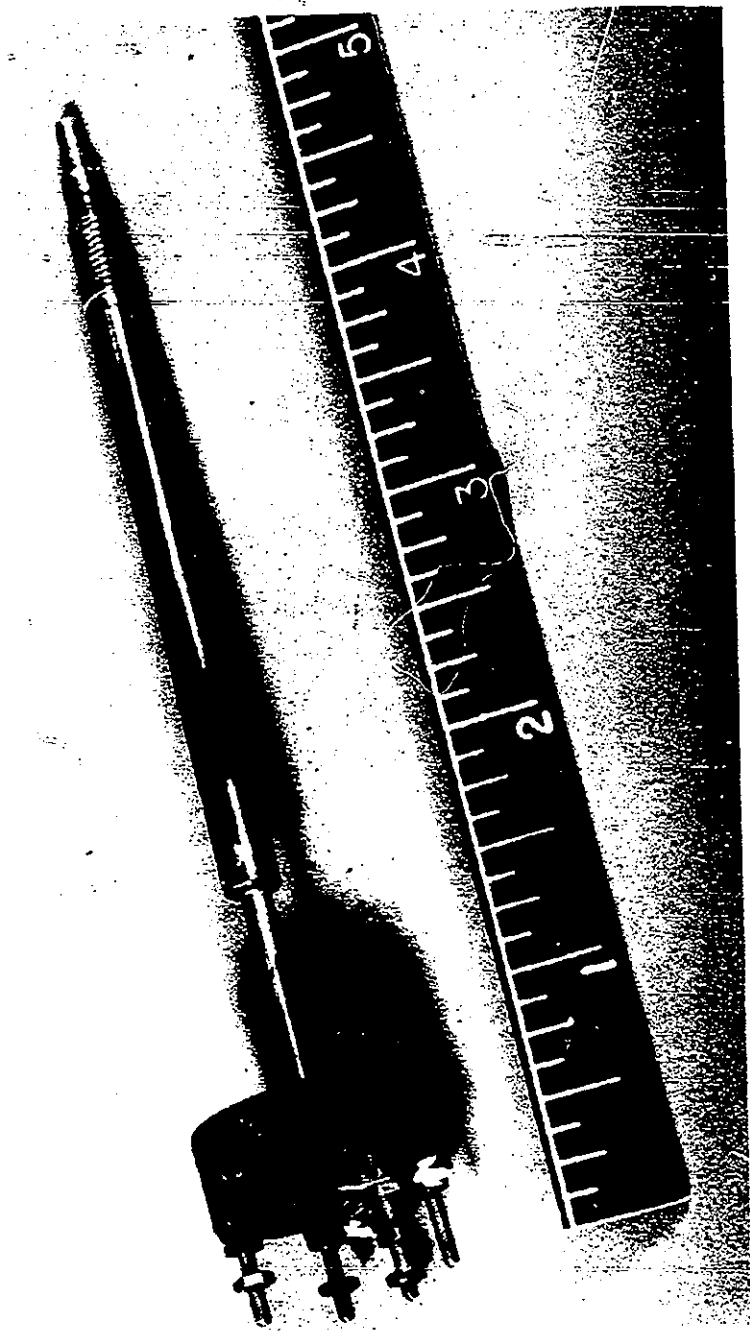


Figure 73 Heat Flux Transducer Ready for Installation



With the probe inserted through a wall and flush mounted at the heated face, measurement of heat flux by the transducer is based upon the difference in EMF between the spaced ends of the two constantan leads. Together with the intervening copper, they act as a difference thermocouple to sense the thermal gradient introduced by a heat flux passing along the probe. Under steady state conditions, heat flux is defined by

$$q/A = -k \frac{\partial T}{\partial X} = -k \frac{\Delta T}{\Delta X} \quad (81)$$

The thermal EMF response of a transducer is related to Eq. 81 by calibration against a thermal transfer standard plug. The calibration setup (Fig. 74) consisted of a heat source, the heat flux transducer, a thermal transfer standard and a heat sink connected in series. The interface connections were made with soft solder via copper area adaptors and the space surrounding the transducer insulated by radiation shields. The steady-state heat flux calibration of the first four transducers used is shown in Fig. 75. The accuracy of this calibration technique depends upon transfer standard calibration, maintaining steady-state conditions, and minimum system heat loss. The calibration system precision is estimated to be 6-8 percent for a calibration standard accuracy of 1-2 percent. The copper wire attached to the back wall of the sensor provides direct temperature measurement at the copper constantan junctions. The instantaneous  $\Delta T$  between the constantan leads and the transient temperature response of the individual junctions together with the analytic expression obtained by expansion of the conduction equation

$$k \frac{\partial^2 T}{\partial x^2} = \rho C_p \frac{\partial T}{\partial t}$$

into a truncated Taylor series

$$\Delta T_{1-2} = \left. \frac{\partial T}{\partial x} \right|_1 \Delta x + \left. \frac{\partial^2 T}{\partial x^2} \right|_1 \frac{\Delta x^2}{2} + \left. \frac{\partial^3 T}{\partial x^3} \right|_1 \frac{\Delta x^3}{6}$$

and the steady-state relation

$$q/A|_1 = -k \left. \frac{\partial T}{\partial x} \right|_1$$

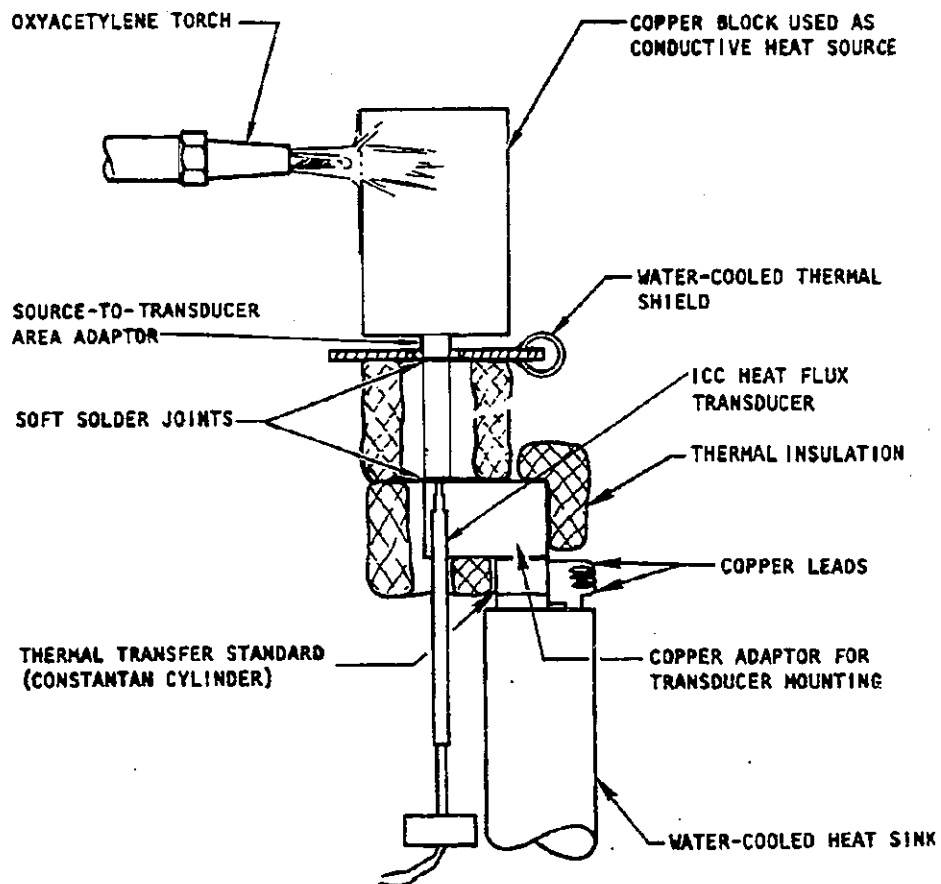


Figure 74. Schematic of Heat Flux Transducer Calibration Apparatus

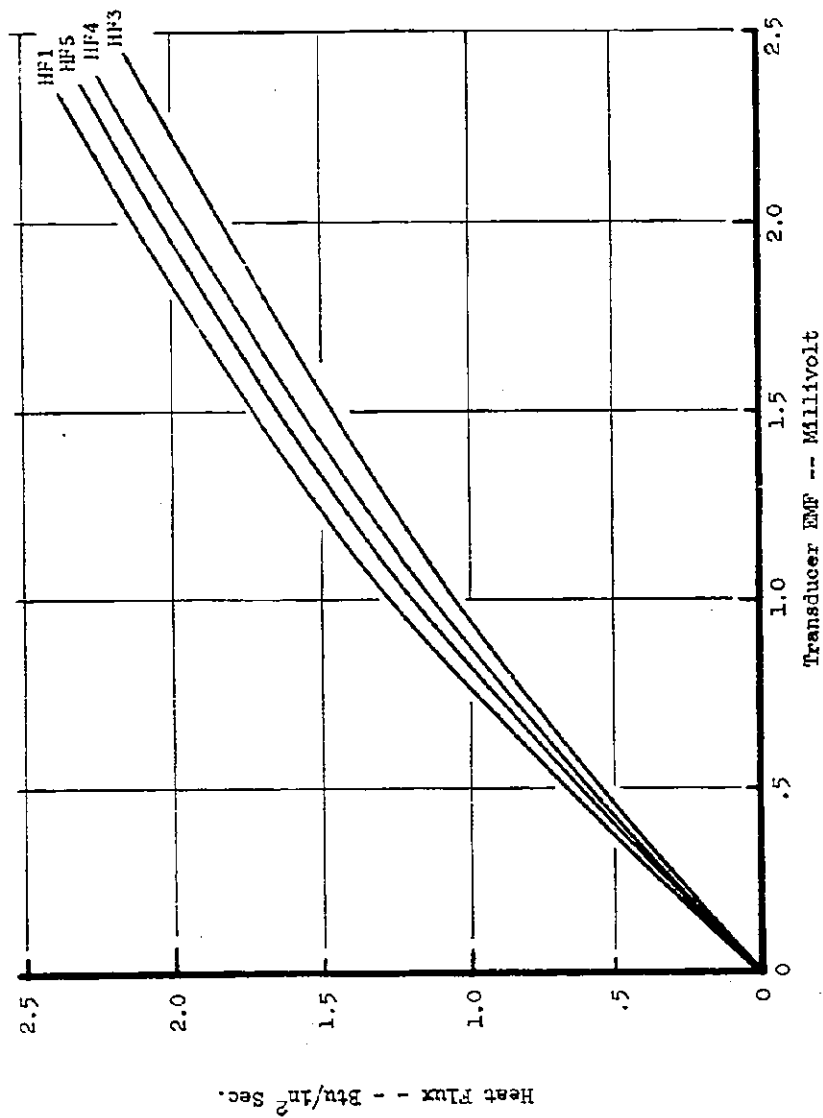


Figure 75 Calibration Curves for Heat Flux Transducers

permit a calculation of the transient heat flux at the constantan junction (lead 1) nearest the hot gas surface. The effective distance between lead 1 and lead 2 ( $\Delta x$ ) is defined by (1) the sensor dimensions, (2) the thermal conductivity of copper, (3) the EMF versus temperature relation for copper constantan, and (4) the EMF versus steady-state heat flux calibration of the transducer. Because of the close proximity of lead 1 to the heated surface of the probe, it is possible to employ the heat flux at lead 1 defined by Eq. 81 as the surface heat flux, even under transient conditions.

Although the operation of the calibrated heat flux transducers during actual model motor firings was satisfactory, the rejection rate during manufacture was unexpectedly high, primarily due to cracks which developed in the electrodeposited copper during machining and breakage of the constantan leads within the probe during either the electroforming or machining processes. As a consequence, a sufficient number of transducers were not available during the model motor firing program to thoroughly map the injector face heat flux profile.

#### Gas Temperature Measurements

In addition to measurements of injector face heat flux, a limited number of combustion gas temperature measurements were made by tungsten-5% rhenium/tungsten-26% rhenium thermocouple probes inserted through the injector. Measurements were first attempted with the bare junction tips a nominal 0.2-inch from the injector face. The thermocouples failed after one or two firings, recording almost instantaneous temperature rises to 3900-4000 R. To extend the thermocouple life, the probes were recessed into the injector such that their bared junctions were nominally flush with the injector face. In this configuration, the thermocouple lifetime was extended, but the lower maximum temperatures recorded during the short duration firings together with a rather sluggish rate of recorded temperature rise indicated that the thermocouples were probably within the laminar sublayer on the injector face. The junction locations were therefore returned to a distance of 0.2 inch from the face and a limited thermocouple lifetime (and consequently a limited number of gas temperature measurements) was accepted. Repair of burned out thermocouple junctions proved impractical.

### Performance Measurements

Measurements of chamber pressure were made with Tabor strain gage pressure transducers connected to pressure ports in the chamber walls. The locations of the chamber pressure probes during the motor firing experiments with unlike doublet injectors ICC2A and triplet injector ICC6 are listed in Table 9 .

The volumetric propellant flow rates were measured with turbine flowmeters located in the feed lines as shown in the facility schematic drawing Fig. 61 . Because of problems encountered with flowmeter response with the corrosive propellant combination, duplicate flowmeters were installed in each line to increase measurement reliability. Even with this arrangement, erratic readings were encountered, usually during the first one or two tests of a motor firing sequence. Propellant temperatures (to define liquid density) were measured with thermocouple probes immediately upstream of the flowmeters.

Chamber pressure was also recorded on a CEC oscillograph to determine the occurrence, frequency, and approximate amplitude of any undesirable chugging forms of combustion instability.

TABLE 9 CHAMBER PRESSURE MEASUREMENT LOCATIONS

RUN NUMBER	INJECTOR	CHAMBER LENGTH (Inch)	CONTRACTION RATIO	DISTANCE FROM INJECTOR					
				PC-1	PC-2	PC-3	PC-4	PC-5	PC-6
6-14	ICC2A	8.0	1.045	--	1.03	2.03	3.42	4.78	6.15
16-24	"	8.0	4.3	8.5	1.03	2.03	3.43	4.78	6.15
25-32	"	8.0	2.15	--	1.03	2.03	3.43	4.78	6.15
34-41	ICC6	16.0	2.15	0.0	0.38	6.53	9.00	11.45	14.15
42-50	"	16.0	4.3	0.0	0.38	6.53	9.00	11.45	16.50
51-56	"	16.0	1.045	0.0	0.38	6.53	9.00	11.45	14.15
57-68	"	8.0	1.045	0.0	1.03	2.03	3.43	4.78	6.15
69-78	"	8.0	4.3	0.0	1.03	2.03	3.43	4.78	8.50
79-86	"	8.0	2.15	0.0	1.03	2.03	3.43	4.78	6.15

## TEST PROGRAM AND RESULTS

A total of 86 model motor firings was made with the  $N_2O_4/50\%N_2H_4-50\%UDMH$  propellant combination and the two injectors, ICC2A and ICC6. Test conditions covered a range of stagnation chamber pressures from 46.6 to 472 psia and of mixture ratios from 0.91 to 1.84, contraction ratios of 1.045, 2.15, and 4.3, and combustion chamber lengths of 8.0 and 16.0 inches. The first five firings with injector ICC2A were made for system checkout purposes and the data were not analyzed. Local injector face heat transfer was successfully measured at three locations at each injector, and chamber pressure was measured at either five or six axial stations along the combustion chamber. At the lowest propellant injection rates, the unlike doublet injector, ICC2A, was unstable and several sets of data were discarded. As might be expected, the overall combustion efficiency  $\eta_c^*$  during the motor firings showed a wide variation with propellant flowrate and mixture ratio. The poorest performance was obtained with ICC6 at either low chamber pressures or high mixture ratios possibly because of an unusually high oxidizer injection velocity which had been incorporated into the design for the injector heat transfer studies.

### Injector Face Heat Transfer

The local heat fluxes measured during the motor firing program at three locations on the face of unlike doublet injector ICC2A are listed in Table 10.\* The locations of the transducers, HF-1, HF-3, and HF-5, are also listed in

\* Data obtained with two other transducers were discarded because of instrumentation problems.

TABLE 10. SUMMARY OF INJECTOR FACE HEAT FLUXES MEASURED WITH  
UNLIKE DOUBLET INJECTOR ICC2A

Run	Propellant Flow Rate (lbm/sec)	Mixture Ratio	Chamber * Pressure (psia)	Contraction Ratio	Injector Face Heat Flux (Btu/in <sup>2</sup> sec)		
					HF-1 ** 75/180°	HF-3 1.25/12.5°	HF-5 1.25/102.5°
6-8	-	-	Unstable	1.045	-	-	-
9	6.03	1.35	95.2	↓	2.09	1.80	1.78
10	6.51	1.51	100.9		2.40	2.14	1.86
11	6.72	1.59	103.4		2.25	2.30	1.98
12	8.63	1.36	138.7		3.27	2.85	2.74
13	9.30	1.54	148.2		3.36	4.12	3.48
14	9.54	1.62	153.0		3.35	4.49	3.71
16-18	-	-	Unstable	4.3	-	-	-
19	4.43	1.42	284.2	↓	2.87	2.78	2.28
20	4.76	1.61	306.6		3.05	5.11	3.47
21	4.89	1.44	317.8		2.92	5.43	3.48
22	6.28	1.40	416.1		5.16	4.95	4.19
23	6.74	1.63	455.0	↓	3.87	7.67	5.21
24	6.93	1.71	472.0		4.28	7.71	4.76
25-27	-	-	Unstable	2.15	-	-	-
28	5.97	1.39	178.0	↓	2.04	2.99	2.18
29	6.40	1.56	193.4		2.69	4.08	3.97
30	6.63	1.65	202.0		2.94	4.66	3.40
31	8.91	1.37	281.0		5.44	6.06	5.68
32	9.73	1.60	310.0	↓	5.81	6.85	5.56

\* Estimated stagnation pressure at the throat

\*\* Location of transducers is presented as radius/angular coordinate, (Ref. Fig. 64)



Table 10 in the coordinate system of Fig.64 . A photograph illustrating the placement of the transducers relative to the injector face pattern is shown in Fig.76 .

The local heat fluxes measured at three locations on the face of triplet injector ICC6 are listed in Table 11 along with location of these elements in the coordinate system of Fig.66 . The locations of the instruments are further illustrated relative to the injector face pattern in Fig.77 .

The measured local heat fluxes ranged from 1.78 to 7.71 Btu/in<sup>2</sup>sec with injector ICC2A and ranged from 0.70 to 3.77 Btu/in<sup>2</sup>sec with injector ICC6. At fixed contraction ratio, the heat flux with both injectors varied with  $P_c$ , the chamber pressure, raised to approximately the 0.8 - 0.9 power. This variation agrees with the analytical model presented earlier in the report, which predicts that heat flux should vary approximately as  $(P_c^2/\epsilon_c)^{0.5}$ ; and it also agrees with the observed effects of chamber pressure upon heat transfer at downstream locations for developed turbulent pipe flow.

Heat flux trends shown in runs 19-21 and 28-30 with injector ICC2A together with the trends particularly shown in runs 34-36, 48-50, and 73-75 with injector ICC6 indicate a very significant effect of mixture ratio upon the injector face heat flux. However, the mechanism for this apparent effect is certainly not clear, primarily for two reasons. First, the mixture ratio variation was not made independently of chamber pressure. Secondly, with a fixed injector face geometry and orifice size, the changes in mixture ratio represent corresponding changes in the impinging stream momenta of the injected propellants, drop sizes, and drop mixture ratio distribution, all of which



Fig. 76. Location of Heat Transfer Instrumentation on  
Injector ICG2A

TABLE 11 . SUMMARY OF INJECTOR FACE HEAT FLUXES MEASURED  
WITH TRIPLET INJECTOR ICC6 (RUNS 34-86)

Run	Propellant Flow Rate (lbm/sec)	Mixture Ratio	Chamber Pressure (psia)	Contraction Ratio	Chamber Length (inch)	Injector Face Heat Flux***		
						HF-11 1.60/202	HF-12 1.50/236	HF-15 1.50/157
34	3.09	1.36	99.7	2.15	16.0	2.41	1.63	2.8
35	3.37	1.55	107.2			2.39	2.15	2.72
36	3.48	1.62	110.7			3.04	2.55	2.95
37	5.64	1.25	181.6			2.71	4.26	3.38
38	6.29	1.51	192.8			2.44	4.57	3.01
39	6.48	1.58	195.6			2.75	4.21	3.37
40	7.39	.95	232.9			3.71	6.26	4.34
41	8.03	1.12	251.7			4.19	5.71	5.57
42	2.22	1.47	93.5	4.3	16.0	-	.97	1.78
43	2.39	1.66	128.8			.70	1.07	1.31
44	-	-	-			-	1.29	1.35
45	4.42	1.45	300.7			3.14	1.74	3.88
46	4.73	1.63	319.6			3.25	3.06	4.66
47	4.87	1.71	327.2			3.85	3.45	2.91
48	5.83	1.20	397.6			5.61	3.44	7.18
49	6.31	1.38	426.2			3.75	5.28	4.04
50	6.49	1.45	436.5			3.31	5.77	4.43
51	6.98	.91	111.3	1.045	16.0	3.72	3.86	5.20
52	7.42	1.03	121.2			3.19	3.78	4.21
53	7.60	1.08	125.0			3.47	3.75	3.30
54	5.80	1.25	93.9			1.33	2.70	2.50

TABLE 11. (CONTINUED)

Run	Propellant Flow Rate (lbm/sec)	Mixture Ratio	Chamber Pressure (psia)	Contraction Ratio	Chamber Length (inch)	Injector Face Heat Flux ***		
						HF-11	HF-12	HF-15
						1.50/202	1.50/236	1.50/157
55	6.21	1.40	100.8	1.045	16.0	1.80	2.55	1.95
56	6.41	1.46	103.6			2.83	2.57	2.06
57	3.05	1.48	47.4			1.09	1.45	1.55
58	3.31	1.65	50.8			1.10	1.49	1.10
59	3.41	1.73	52.1			.60	1.58	.85
60	3.08	1.48	49.7			1.02	.98	1.51
61	3.31	1.67	48.9			1.15	.81	1.42
62	3.40	1.74	46.6			1.04	.75	1.25
63	5.72	1.27	-			1.78	1.81	2.49
64	6.22	1.45	98.4			1.43	1.36	2.16
65	6.43	1.53	95.0	4.3	8.0	1.37	1.17	2.08
66	6.97	1.84	125.8			2.57	2.66	4.06
67	7.41	1.03	-			2.39	2.72	3.86
68	7.60	1.08	-			2.41	2.56	3.30
69	2.27	1.41	142.3			2.05	1.01	2.06
70	2.44	1.60	145.0			1.82	.86	1.81
71	2.44	1.60	151.6			2.14	1.25	2.23
72	2.50	1.66	154.2			1.89	1.26	2.42
73	4.46	1.41	288.1			3.19	2.43	4.60
74	4.79	1.59	305.1			2.94	3.38	4.10
75	4.92	1.66	314.2	4.3		3.41	3.65	3.56
76	5.89	1.20	385.2			4.03	3.29	5.40
77	6.36	1.37	416.3			4.31	5.30	4.75
78	5.88	1.20	385.2			4.04	3.29	5.40

TABLE 11. (CONTINUED)

Run	Propellant Flow Rate (lbm/sec)	Mixture Ratio	Chamber Pressure (psia)	Contraction Ratio	Chamber Length (inch)	Injector Face Heat Flux***		
						HF-11 1.60/202	HF-12 1.50/236	HF-15 1.50/157
79	3.17	1.46	96.7	2.15	8.0	1.89	2.12	2.28
80	3.40	1.64	101.6			1.80	2.39	2.58
81	3.53	1.74	103.5			1.82	2.24	2.67
82	5.76	1.30	174.1			3.18	4.54	4.38
83	6.17	1.46	180.8			2.79	4.66	4.19
84	6.38	1.54	182.0			2.40	4.38	3.67
85	7.34	.93	228.5			4.42	5.84	5.29
86	7.94	1.09	242.5			3.82	5.23	5.28

\* Estimated stagnation pressure at the throat

\*\* Location of transducers is presented as radius/angular coordinate, Ref. Fig. 66

\*\*\* (Btu/in<sup>2</sup> sec)

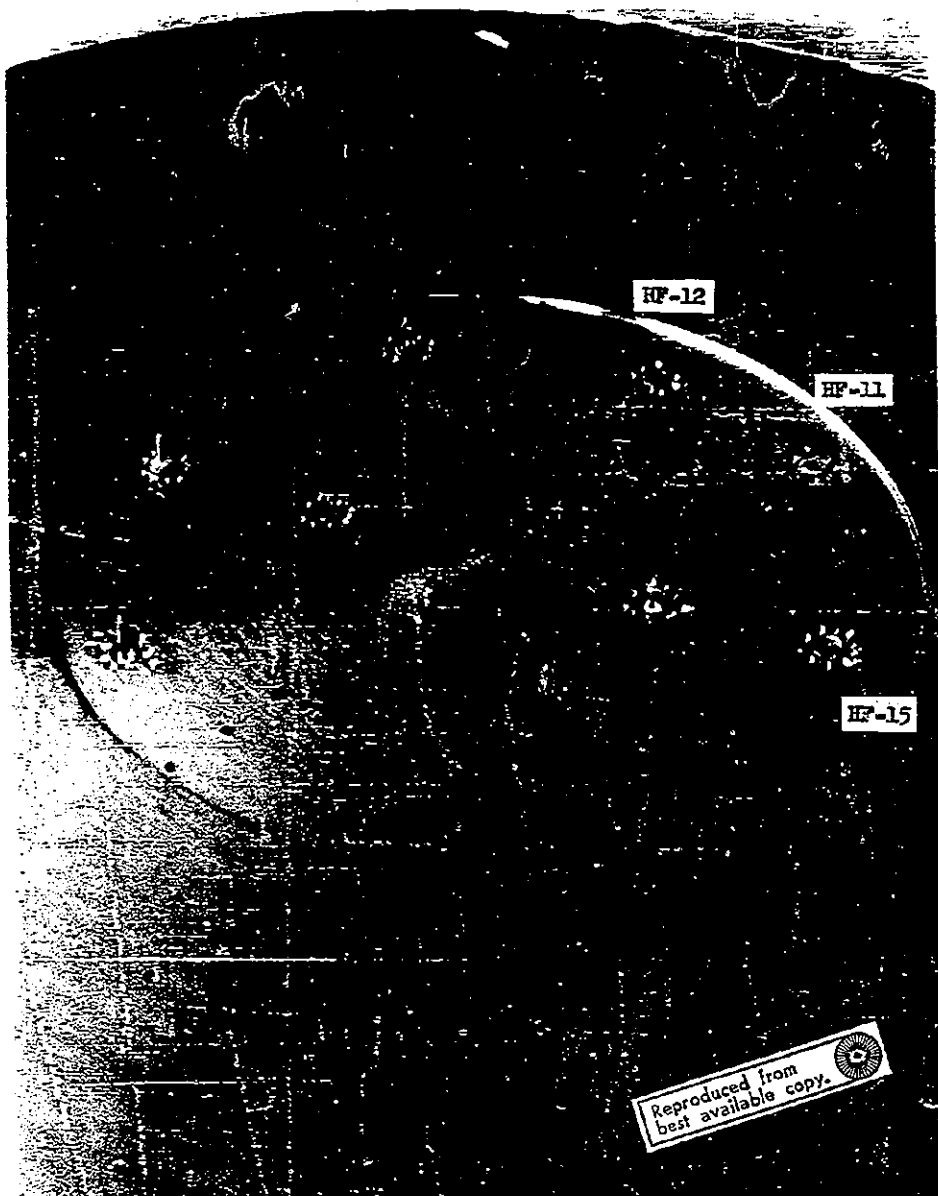


Figure 77 . Location of Heat Transfer Instrumentation on Injector ICC6

changes should affect the near injector combustion and therefore the heat transfer to the injector face.

It may be noted the limited heat flux results shown in Tables 10 and 11 do not indicate a particularly wide spatial variation in heat transfer. In particular, the variation in measured heat flux during a particular motor firing between transducers HF-3 and HF-5 which occupy similar locations on the ICC2A face pattern indicate that the spatial variation in heat flux may not be much greater than the probable  $\pm 20$  percent apparent scatter in results indicated by the variance between the two transducers. However, the limited number of locations at which heat transfer data were obtained are not sufficient to either establish or disprove the wide variation in local heat transfer which is predicted by the analytical model. As shown in the correlated results for injector heat transfer in the Analytical Development Section, the empirical coefficients in the model provide a reasonable fit of experiment to calculation for a limited number of points without demonstrating the overall applicability.

Similarly, the agreement between the data and the analytical model concerning the combined effects of chamber pressure and contraction ratio upon heat transfer does not prove that the analytical model based upon a recirculatory convection driven by droplet drag is better than a prediction based purely upon injection mass density (which is also dependent upon chamber pressure and contraction ratio). However, the analytical model predicts that the recirculation is proportional to the propellant injection velocity. This is directly proportional to injection mass density only for a fixed orifice size; therefore,

a key set of experiments to establish the model validity would involve repeating the motor firings with the element orifices enlarged to give reduced injection velocities at similar injection densities.

The actual correlation of the injector face heat transfer results to the analytical model is discussed in the Analytical Developments Section of this report (pp 99-108).

#### Chamber Pressure Profile

The chamber pressure profiles measured with injector ICC2A are listed in Table 12. The desired exaggerated profile was achieved during the firings made at a contraction ratio of 1.045 (runs 9-14), and the resultant axial pressure gradient was therefore used as described in the Analytical Developments Section (pp. 81 -85 ) to define the axial variation of spray vaporization and, by extrapolation, the initial degree of vaporization to be assigned by LISP. Analysis of the pressure profiles obtained with the 2.15 and 4.3 contraction ratios indicated that they could not be utilized with sufficient confidence to define a contraction ratio effect on initial vaporization for use in the LISP program.

An anomolous variation in  $\eta_{c*}$  was noted with contraction ratio with injector ICC2A. As shown in Tables 10 and 12, combustion efficiency was highest at the highest contraction ratio; i.e., the highest  $L^*$ , but the combustion efficiency was also better at the lowest contraction ratio, 1.045, than at the intermediate contraction ratio of 2.15. According to the data, the enhanced secondary breakup at the low contraction ratios must outweigh the effect of low  $L^*$  and provide improved performance.



The axial pressure profiles measured with injector ICC6 are listed in Table 13 together with the overall performance results. The flowrates shown in Table 13 during the low contraction ratio tests in the 8.0-inch combustion chamber were uncertain. The oxidizer turbine flowmeters gave erratic readings and flowrates were recalculated based upon the calibration of the cavitating venturi and the oxidizer injection pressure drop. However, the resultant errors in overall combustion efficiency (note calculated  $\eta_{c*}$  greater than 100 percent in runs 66-68) made the interpretation of the chamber pressure profiles impossible for injector ICC6.

Examination of the overall combustion efficiency results shown in Table 13 also indicates that performance was higher at both the 4.3 and 1.045 contraction ratios than at the intermediate 2.15 contraction ratio.

TABLE 12 SUMMARY OF LOCAL STATIC PRESSURE DISTRIBUTIONS MEASURED  
WITH UNLIKE DOUBLET INJECTOR ICC2A

RUN	PROPELLANT FLOW RATE (lbm/sec)	MIXTURE RATIO	STAGNATION PRESSURE (psia)	$\eta_{c^*}$ %	LOCAL STATIC CHAMBER PRESSURE, PSIA						
					PC-1 8.5*	PC-2 1.03	PC-3 2.03	PC-4 3.43	PC-5 4.78	PC-6 6.15	
6-8	- -	- -	Unstable	--	DNA**	--	--	--	--	--	
9	6.03	1.35	95.2	89.6	- -	95.2	87.5	80.0	70.7	--	
10	6.51	1.51	100.9	89.3	- -	102.0	92.6	84.6	74.8	67.0	
11	6.72	1.59	103.4	89.4	- -	105.3	95.4	87.0	76.9	71.5	
12	8.63	1.36	138.7	92.3	- -	138.7	128.4	116.8	104.7	73.7	
13	9.30	1.54	148.2	92.1	- -	150.5	137.0	124.2	110.7	97.7	
14	9.54	1.62	153.0	92.7	- -	155.4	140.9	127.0	123.2	105.2	
16-18	- -	- -	Unstable	--	- -	- -	- -	- -	- -	- -	
19	4.43	1.42	284.2	90.2	280.5	285.6	284.6	282.6	281.5	281.8	
20	4.76	1.61	306.6	90.6	303.2	308.3	306.8	304.9	303.6	303.8	
21	4.89	1.44	317.8	91.2	314.6	319.7	318.2	316.1	315.1	314.9	
22	6.28	1.46	416.1	93.1	412.5	418.2	416.6	414.6	412.3	413.2	
23	6.74	1.63	455.0	94.4	450.9	457.1	455.0	452.5	450.9	451.0	
24	6.93	1.71	472.0	95.5	466.9	473.7	471.7	468.9	467.4	467.3	
25-27	- -	- -	Unstable	--	DNA**	- -	- -	- -	- -	- -	
28	5.97	1.39	178.0	85.6	- -	180.9	177.0	173.0	170.0	169.6	
29	6.40	1.56	193.4	86.3	- -	197.2	191.7	187.9	184.7	184.3	
30	6.63	1.65	202.0	87.4	- -	205.9	200.5	196.2	192.8	192.6	
31	8.91	1.37	281.0	89.9	- -	285.2	279.2	273.3	267.4	267.7	
32	9.73	1.60	310.0	90.6	- -	314.9	307.5	301.9	294.7	295.4	

\* Distance from injector

\*\* Not taken, Runs 6-14 and Runs 25-32

TABLE 13. SUMMARY OF LOCAL STATIC PRESSURE DISTRIBUTIONS  
MEASURED WITH TRIPLET INJECTOR ICC6 (RUNS 34-86)

Run	Propellant Flow Rate (lbm/sec)	Mixture Ratio	Stagnation Pressure (psia)	$\eta_c^*$ %	Local Static Chamber Pressure, psia					
					PC-1	PC-2	PC-3	PC-4	PC-5	PC-6
					0.00*	.38	6.53	9.0	11.45	14.15
34	3.09	1.36	99.7	92.4	103.6	103.4	98.3	96.1	95.6	94.9
35	3.37	1.55	107.2	91.0	110.9	110.5	106.0	103.7	102.8	102.0
36	3.48	1.62	110.7	91.0	114.3	113.9	109.3	107.1	106.1	105.3
37	5.64	1.25	181.6	92.0	186.1	185.8	177.0	174.9	173.6	172.6
38	6.29	1.51	192.8	87.4	196.4	196.1	188.8	185.9	184.6	183.2
39	6.48	1.58	195.6	86.0	198.9	198.7	191.8	188.3	187.7	186.0
40	7.39	.95	232.9	90.5	238.8	238.4	225.7	221.7	221.9	221.2
41	8.03	1.12	251.7	91.8	256.8	256.5	244.9	240.5	240.3	239.2
42	2.22	1.47	93.5	59.3	94.8	94.6	93.6	92.2	92.7	92.6
43	2.39	1.66	128.8	76.5	130.4	130.1	129.5	127.2	128.2	127.5
44	-	-	-	-	-	-	-	-	-	-
45	4.42	1.45	300.7	96.5	301.9	301.2	299.2	297.0	297.7	297.7
46	4.73	1.63	319.7	95.5	320.3	319.8	318.2	315.7	316.3	316.4
47	4.87	1.71	327.2	95.0	328.2	327.7	326.5	323.6	324.1	324.0
48	5.83	1.20	397.6	97.4	398.7	398.0	395.4	393.1	393.4	393.6
49	6.31	1.38	426.2	96.4	426.7	426.0	424.8	421.6	421.9	422.0
50	6.49	1.45	436.5	95.2	436.9	436.1	435.0	432.0	432.2	432.2
51	6.98	.91	111.3	98.2	128.6	127.4	79.8	84.5	80.9	77.7
52	7.42	1.03	121.2	98.5	137.6	136.6	92.3	94.5	89.5	84.8
53	7.60	1.08	125.2	98.6	139.8	140.0	97.9	98.8	93.1	87.7
54	5.80	1.25	93.9	95.6	107.1	106.7	71.0	65.6	49.7	55.1
55	6.21	1.40	100.8	95.0	111.5	111.1	78.8	74.5	57.0	60.1

TABLE 13. (CONTINUED)

Run	Propellant Flow Rate (lbm/sec)	Mixture Ratio	Stagnation Pressure (psia)	$\eta_o^*$	Local Static Chamber Pressure psia					
					PC-1 0.00	PC-2 1.03	PC-3 2.03	PC-4 3.43	PC-5 4.78	PC-6 6.15
56	6.41	1.46	103.6	94.4	112.9	112.4	81.4	77.7	60.1	62.3
57	3.05	1.48	47.4	90.8	34.5	41.5	20.8	28.6	-	22.7
58	3.31	1.65	50.8	90.2	37.5	43.5	32.0	32.7	-	25.2
59	3.41	1.73	52.1	89.2	38.5	45.4	33.9	33.7	-	26.1
60	3.08	1.48	49.7	94.3	34.4	33.9	31.2	20.9	25.3	24.2
61	3.31	1.74	48.9	80.6	32.3	32.2	30.0	28.2	24.6	23.8
62	3.40	1.27	46.6	80.0	30.0	27.0	28.0	26.4	23.0	22.2
63	5.77				-					
64	6.22	1.47	98.4	92.2	140.2	104.4	69.8	87.0	61.2	58.6
65	6.43	1.53	95.0	85.9	136.7	101.2	67.0	64.5	58.8	56.4
66	6.97	1.84	125.8	106.0	176.2	136.5	141.4	108.3	142.4	89.8
67	7.41	1.03	136.5	109.0	181.1	142.9	150.7	118.1	152.6	97.4
68	7.60	1.08	129.0	102.5	128.2	125.3	113.5	107.6	96.3	92.1
69	2.27	1.41	142.3	89.4	143.2	142.8	143.1	142.2	141.4	140.9
70	2.44	1.60	148.0	86.1	148.9	148.7	149.2	148.3	147.8	146.6
71	2.44	1.60	151.6	88.0	152.4	152.2	152.6	151.7	150.9	150.1
72	2.50	1.66	154.2	87.4	154.8	154.7	155.1	154.3	153.5	152.7
73	4.46	1.41	288.2	91.8	289.0	288.0	288.2	287.2	285.5	285.2
74	4.79	1.69	305.1	90.1	305.6	304.8	305.2	304.1	302.9	302.1
75	4.92	1.66	314.2	90.2	314.3	314.0	314.5	313.1	312.0	311.1
76	5.88	1.20	385.2	94.4	385.8	384.6	384.2	383.2	381.7	381.4
77	6.36	1.37	416.3	92.9	415.8	415.3	415.3	414.3	412.8	412.2
78	5.88	1.20	385.2	94.4	385.8	384.6	384.2	383.2	381.7	381.4

TABLE 13. (CONTINUED)

Run	Propellant Flow Rate (lbm/sec)	Mixture Ratio	Stagnation Pressure (psia)	$\eta_c^*$ %	Local Static Chamber Pressure, (psia)					
					PC-1	PC-2	PC-3	PC-4	PC-5	PC-6
79	3.17	1.46	96.7	87.4	0.00	.38	6.53	9.0	11.45	14.15
80	3.40	1.64	101.6	85.6	97.9	96.6	95.7	94.3	90.5	92.1
81	3.53	1.74	103.5	84.5	102.4	101.4	100.8	99.6	95.4	96.8
82	5.76	1.30	174.1	86.9	104.5	103.5	103.0	101.9	98.5	98.7
83	6.17	1.46	180.8	83.8	175.3	174.1	172.8	170.3	165.5	166.0
84	6.38	1.54	182.0	81.5	181.4	180.3	179.4	177.8	172.7	172.3
85	7.34	.93	228.5	93.6	181.8	180.8	180.2	178.5	174.2	173.4
86	7.94	1.09	242.8	90.0	232.0	230.0	226.0	221.4	215.4	217.8
					244.1	243.2	240.2	235.9	230.4	231.3

\* Distance from Injector

\*\* 16.5 in Runs 42-50 and 8.50 in Runs 69-78

## SPRAY HEAT TRANSFER EXPERIMENTS

A brief experimental program was conducted to determine whether propellant spray impingement upon chamber walls contributes significant cooling and also determine whether this cooling could be correlated sufficiently well to be incorporated into the BLEAT heat transfer program. Either water or burning  $N_2O_4/50\%N_2H_4-50\%$  UDMH propellant spray from a single doublet element was directed against a stainless steel strip which could be electrically heated. Heat transfer rates were determined either from the electrical power generation within the strip or from the transient response of thermocouples spot welded to the back surface of the strip. The experiments were carried out in open air to minimize ordinary convective heat transfer from combustion gas. A limited correlation was made of the experimental results obtained with water. The data obtained with burning propellant spray indicated that any liquid spray cooling was counteracted so strongly by heat transfer from entrained combustion gas that a simple but reliable heat transfer correlation will be obtained only after comprehensive experimental investigation.

### EXPERIMENTAL APPARATUS

The test section consisted of a vertical stainless steel strip 5.0-inch long x 1.0-inch wide x .032-inch thick. The strip was silver soldered between two copper bus bars so that the strip could be electrically heated. The back wall (the side of the strip away from the impinging spray) was instrumented with either six or ten spot welded chromel/alumel thermocouples to measure the wall temperature. Spray impinged upon the front surface of the strip from a single unlike doublet element positioned 1.0-inch upstream from upper end of the heated strip. The stream impingement point was 0.68-inch away from the strip in the direction normal to the strip surface. Injector orifice diameters were 0.043-inch. The impinging streams of the doublet element formed a fan whose impingement was "edge-on" to the centerline of the test section. The heated strip was mounted on a large vertical plate to prevent water or recirculating gas from reaching the back surface of the strip.

Electrical heating was provided by a pair of d-c welding generators with a rated output of 30 kw. The current through the test section, together with the voltage drop between the copper bus bars, defined the resistive heating in the test section during the experiments with water. All the electrical power dissipation, except for a small correction provided for natural convection and for conduction through the bus bars, was assumed to be absorbed by the water.

The millivolt outputs of the strip thermocouples were recorded on a multi-channel digital voltmeter. Electrical current, voltage, flowrates of water and propellants, and the necessary liquid supply tank pressures for controlling flowrates were all recorded on Brown recording potentiometers.

#### EXPERIMENTAL PROCEDURE AND RESULTS

The actual heat transfer experiments were preceded by cold flows in which water spray from the doublet was collected at positions equivalent to the test section axis. These experiments established the weight flux of liquid spray impinging upon the test section required for correlation of heat transfer data.

The experiments with water were performed by establishing a desired water flow rate, bringing the electrical current slowly to a desired level and then, after allowing approximately one minute for steady state conditions to be established, recording the back surface temperatures of the thermocouples. Electrical power levels were progressively increased until the test section burned out or showed signs of thermal distortion. The experiments with the burning propellant spray were performed by procedures equivalent to a model rocket motor firing. Duration of the burning propellant spray experiments was ordinarily 3-5 seconds.

The heat transfer experiments with water were performed at injection velocities of 70 to 92 ft/sec. These velocities resulted in local spray mass fluxes to the test section which ranged from  $0.006 \text{ lb}_m/\text{in}^2\text{sec}$  to  $0.038 \text{ lb}_m/\text{in}^2\text{sec}$  depending upon both injection flow rate and location on the strip. Heat fluxes ranged from  $.065 \text{ Btu}/\text{in}^2\text{sec}$  to  $1.43 \text{ Btu}/\text{in}^2\text{sec}$  in the experiments. The wall temperatures ranged from the injection temperature of the water (50-58 F) to 860 F depending upon both location and heat flux.

Fifteen experiments were performed with the  $N_2O_4/50\%N_2H_4$ -50% UDMH propellant combination. All the tests were performed at a single nominal mixture ratio, 1.25, in order to balance the momenta of the impinging streams and therefore keep a proper fan impingement on the test section. Most of the experiments were performed with an initially cold strip; however, in several of the experiments, the strip was preheated to approximately 300-400 F by electrical heating at a low power level. The cooling produced by liquid impingement in these experiments was apparently less than the convection from the entrained combustion gases in the spray jet because back wall temperatures of the strip rose to temperatures as high as 1700 F after 5 seconds. When a transient conduction analysis was applied equivalent to that described in the sections dealing with the model motor firings (see p. 182), net heat fluxes ranging from 0.04 Btu/in<sup>2</sup>sec to 0.39 Btu/in<sup>2</sup>sec were calculated.

#### DISCUSSION OF EXPERIMENTAL RESULTS

Correlation of the spray heat transfer data consisted of the evaluation of an accommodation coefficient (or Stanton number) relating the heat absorbed by the impinging spray to the possible heat absorption. In this context, the definition for Stanton number becomes

$$St = \frac{h}{C_p \dot{w}_R} = \frac{q/A}{C_p \dot{w}_R (T_W - T_\ell)}$$

where  $\dot{w}_R$  is the local spray mass flux (lbm/in<sup>2</sup>sec) normal to the wall and the specific heat defined by

$$C_p = \frac{H(T_W) - H(T_\ell)}{T_W - T_\ell}$$

includes latent heat effects. Based upon the previous spray heat transfer work of Holman and McGinnis (Ref. 29) and Nurick (Ref. 28) the following general non-dimensional relation was chosen

$$St Pr^{-6} = C_1 We^a Co^b$$



where the dimensionless Weber number and concentration number groupings are defined by

$$We = \frac{\rho_l V_R^2 D}{\sigma g_c}$$

$$Co = \frac{w_R}{\rho_l V_R}$$

A least-squares fit of the spray heat transfer data obtained from water with an electrically heated strip during the current program resulted in the following relation for  $T_W < T_{SAT}$

$$St Pr^{.6} = 2.1 We^{-.23} Co^{-.07}$$

When the surface temperature in the experiments exceeded 212 F (the saturation temperature of water), it was necessary to develop a second correlation

$$St Pr^{.6} = .0155 e^{.58 \left( \frac{T_W - T_l}{T_{SAT}} \right)} We^{-.233} Co^{-.07} \quad (82)$$

The preceding relationship was substantially more effective in correlating the experimental data for wall temperatures up to approximately 800 F. However, it should be noted that a correlation of data at wall temperatures between 212 F and 800 F does not necessarily imply the successful prediction of spray heat transfer at the ablative chamber wall temperatures (1000 F to 2500 F) encountered in regions of maximum spray impingement. Developing a reliable method required that equivalent results be obtained with water and reactive propellants.

Figure 78 shows the temperature response of the strip thermocouples during a typical reactive spray heat transfer experiment. Of particular interest is the fact that the local temperatures have not begun to level off at temperatures as high as 1600 F. If the cooling effect of liquid spray impingement is calculated by means of Eq. 82, then the overall positive heat transfer rate shown in the temperature histories of Fig. 78 indicates that the heat

transfer by convection from entrained combustion gas had not been minimized by running the experiment in open air as was crucial in the concept of the experiment. Under these circumstances, the direct cooling effects of liquid propellant spray impingement cannot be compared in a simple fashion to the spray heat transfer data with water; the comparison is entirely a function of the assumed direct heat transfer from the gas. A useful correlation of burning propellant spray impingement heat transfer will therefore only be obtained after a more comprehensive investigation. Such an investigation must include a wider range of surface temperatures (longer heating times) and should also include a range of mixture ratios. It can be concluded from the experiments, however, that spray cooling is not particularly effective when the mixture ratio of the impinging liquid spray is such that high flame temperatures are produced.

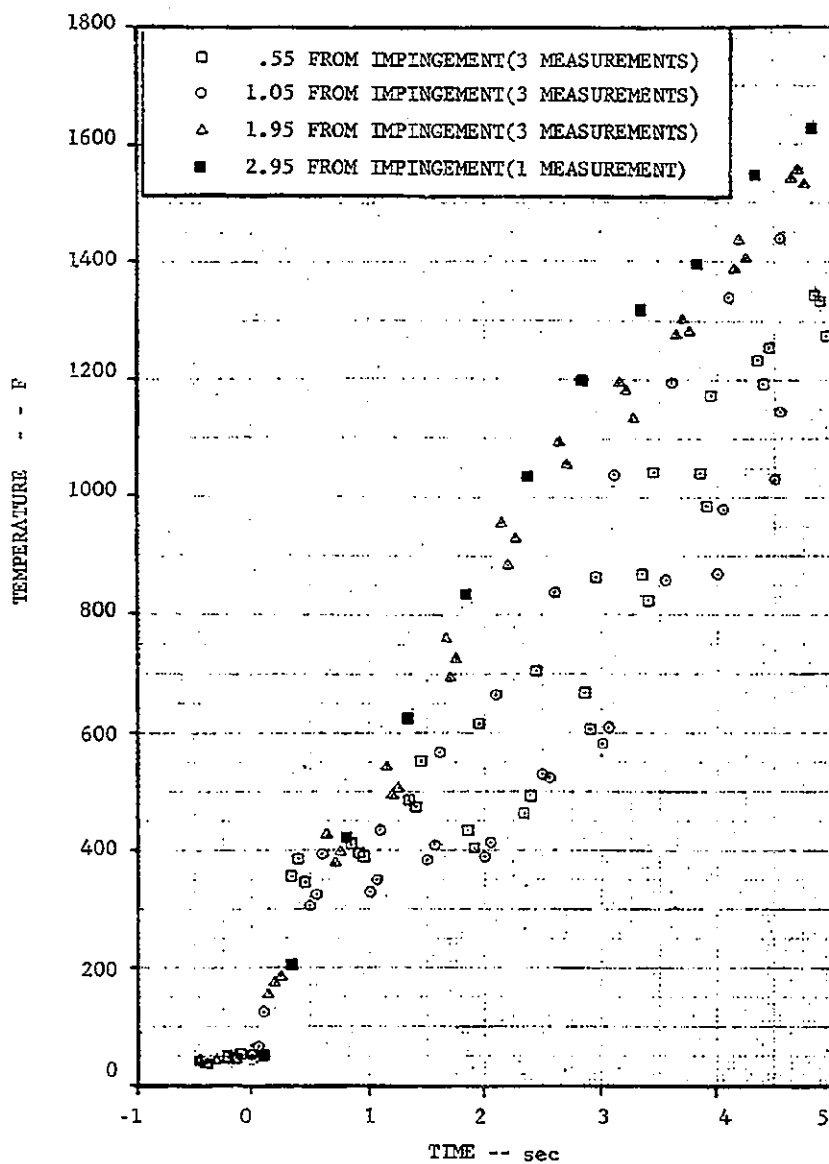


Figure 78. Transient Temperature Response of the Backwall of Heat Strip Exposed to Burning  $N_2O_4$ /50% $N_2H_4$ -50%UDMH

DEMONSTRATION ANALYSES OF  
MOTOR FIRING EXPERIMENTS

INTRODUCTION AND SUMMARY

Four analyses were made (or attempted) of motor firing experiments to evaluate the usefulness of the Injector/Chamber Compatibility Model in real design and development problems. These problems included:

1. Case TCC-1, the analysis of injector face heat transfer for an AFRPL motor firing performed at the Edwards facility to evaluate the IHTM program.
2. Case TCC-2, the analysis of the chamber wall heat flux and performance in a motor firing performed at Rocketdyne under conditions equivalent to a regeneratively cooled engine. (The purpose of this case was to evaluate the capabilities of the overall system, and particularly of the new BLEAT program, for regeneratively cooled systems).
3. Case TCC-3, the analysis of ablative wall response in an AFRPL motor firing performed at Edwards with a triplet element injector and the IRFNA/HYDYNE propellant combination. (The objective of this analysis was to demonstrate the overall system for ablative wall applications.)
4. Case TCC-4, analysis of an AFRPL motor firing made with a multi-element coaxial injector and the  $\text{GH}_2/\text{LO}_2$  propellant combination. (The objective of this case was to determine whether the changes in the LISP program would permit analysis of gas/liquid injectors).

The first three cases were processed through the required computer programs and the resultant predictions were compared to the corresponding experimental results. The analysis of case TCC-4 was not completed after a partial processing of the problem through the LISP, 3D-COMBUST, and STRMTB programs indicated that the LISP modifications made during the project were not sufficient by themselves to permit analysis of gas/liquid systems.

The comparison between experimental data and analytical predictions in the first three cases results in mixed conclusions about the effectiveness of the overall system of computer programs; both capabilities and limitations were demonstrated for the programs. After selection of a realistic definition of limiting face temperature, the IHTM program predicted several compatibility problem areas on the injector where erosion was actually encountered. However, the analysis did not make predictions about manifold effects and reactive stream blowpart effects which seemed to be very important for the actual injector. Local heat flux was correctly predicted in Case TCC-2 over those portions of the chamber where ordinary turbulent forced convection was occurring. However, an unusual reduction in throat region heat flux measured in the actual experiment did not follow ordinary forced convection theory or other rocket nozzle corrections; this unusual behavior was also not predicted by the BLEAT program. In Case TCC-3, the location of streaking patterns produced in the experiment by the injector configuration was correctly predicted by the combination of the LISP, 3D-COMBUST, and STRMTB computer programs. However, when a calculation of ablative wall response to the predicted gas-side boundary conditions was attempted on the AFRPL computer using the 2D-ABLATE computer program, unexplained numerical instabilities were encountered in the calculation which led to obviously incorrect erosion prediction.

The general conclusion drawn from the demonstration cases was that effective design calculations can be made from the Injector/Chamber Compatibility system of computer programs, but that a number of limitations still exist which must be appreciated by the user before application of the system is made to specific problems.

## ANALYSIS OF DEMONSTRATION CASE TCC-1

The objective of Demonstration Case TCC-1 was to evaluate the capabilities of the injector face heat transfer model in analyzing a real injector. The motor firing experiment analyzed for this purpose was performed at the Air Force Rocket Propulsion Laboratory with an injector designated as Flintstone No. 31, and with the CTF/M-20\* propellant combination. Motor firings were made at nominal chamber pressures of 300 and 500 psia. Test conditions during the motor firings are summarized below.

### Test Conditions During Demonstration Case TCC-1

<u>Parameter</u>	<u>500 psia Case</u>	<u>300 psia Case</u>
Chamber Pressure, psia	500	300
Mixture Ratio	3.02	3.15
Fuel Flowrate, lbm/sec	2.95	3.5
Oxidizer Flowrate, lbm/sec	9.0	11.1
Burn Duration, seconds	120	20
Throat Diameter, inches	2.29	3.31
Chamber Diameter, inches	6.0	6.0

The injector contained 169 fuel and 169 oxidizer like-doublat elements in six concentric rings. Orifice diameters for the fuel elements were 0.020 inch; for the oxidizer elements, the orifice diameters were 0.025 inch. Impingement angles for all elements were 60 degrees. A high degree of radial mixture ratio bias was provided by:

- (1) Enlarging the outer orifice of the outboard oxidizer elements to turn the fans from these elements away from the chamber wall

\* CTF is the designation for chlorine trifluoride oxidizer. M-20 is the designation for 80% hydrazine-20% monomethylhydrazine fuel blend.

- (2) An outward radial displacement of 0.20 inch of the outboard ring of 36 fuel elements relative to the outboard ring of 36 oxidizer doublets
- (3) Canting the outboard oxidizer elements 12 degrees radially inward while keeping the outboard fuel elements aligned with the chamber axis.

#### Setup of Analysis

Because of the size of the injector it was necessary to split the analysis into several regions. A pie-shaped slice of the injector end bounded by planes of symmetry (15 degrees wide), was selected for the analysis of the inner element rows; a pie-shaped slice of 5 degrees width was selected for the analysis of the outer element rows. The distribution of injector elements in and around these slices are shown in Fig. 79. Keeping within the IHTM limitation of 20 basic orifices and 50 dummy orifices required that the inner and outer row slices be further sub-divided into smaller pie-shape slices. Shown in Fig. 80 are the final slices selected for the outer element rows. Figs. 81 and 82 show the final slices selected for the inner element rows. Figs. 80 through 82 also distinguish between the orifices that were considered in the analysis to be basic orifices and those which were considered to be dummy orifices.

Evaluation of the IHTM program was made in terms of its ability to predict the regions of injector face erosion encountered during the motor firing experiment. For this purpose, it was necessary to establish a definition of the conditions under which injector face erosion is expected. On the assumption that the nickel surface of the injector was reasonably compatible with the combustion gas at all mixture ratios, erosion was defined as occurring only when the injector face temperature approached the melting point of nickel (3110R). A reference wall temperature of 3000R was therefore selected for use with the IHTM analysis. Erosion was considered likely only at the locations where the gas temperature adjacent to the injector face was above 3000R such that a positive heat flux was calculated. However, because a regenerative cooling of the face is supplied by the fuel flowing through the radial feed passages

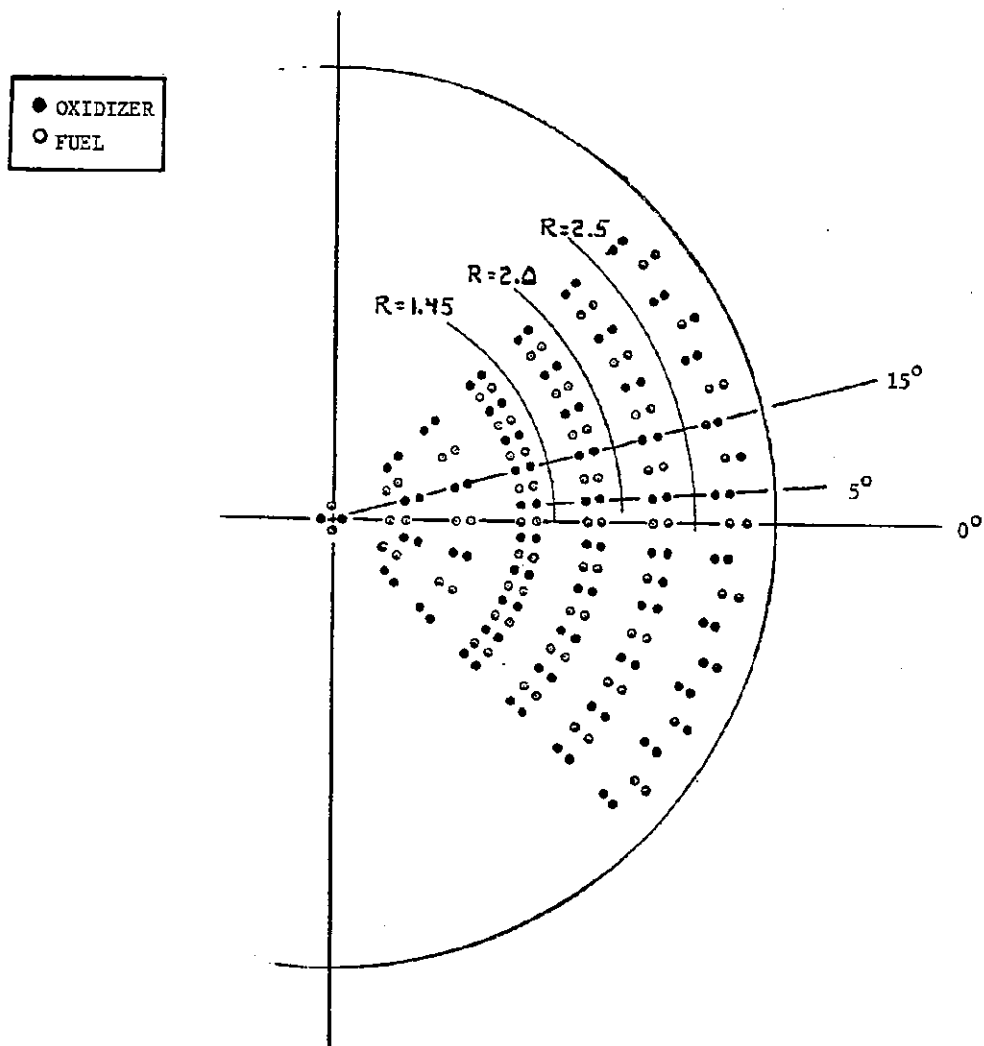


Figure 79 Face Pattern of Flintstone Injector Analyzed to Evaluate Injector Heat Transfer Model



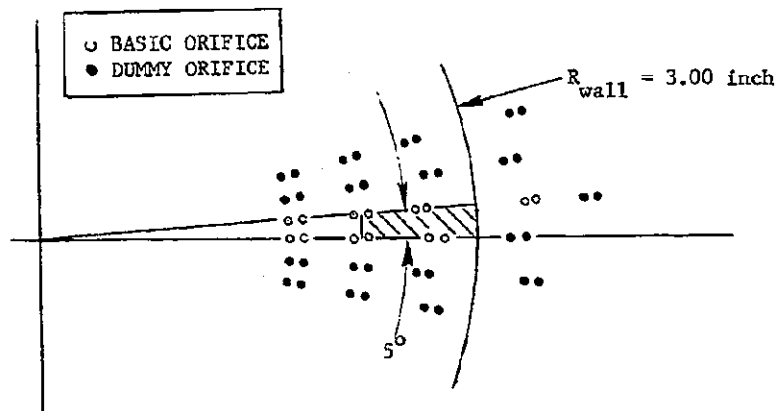


Figure 80a Layout of Injector Elements In and Around Flintstone  
Injector Segment Extending From  $R = 2.19$  Inch to  
 $R = 3.00$  Inch (shaded area)

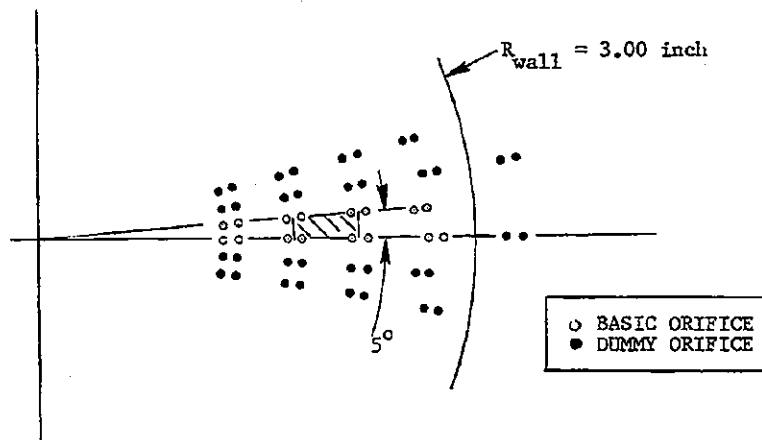


Figure 80b Layout of Injector Elements In and Around Flintstone  
Injector Segment Extending From  $R = 1.75$  Inch to  
 $R = 2.19$  Inch (shaded area)

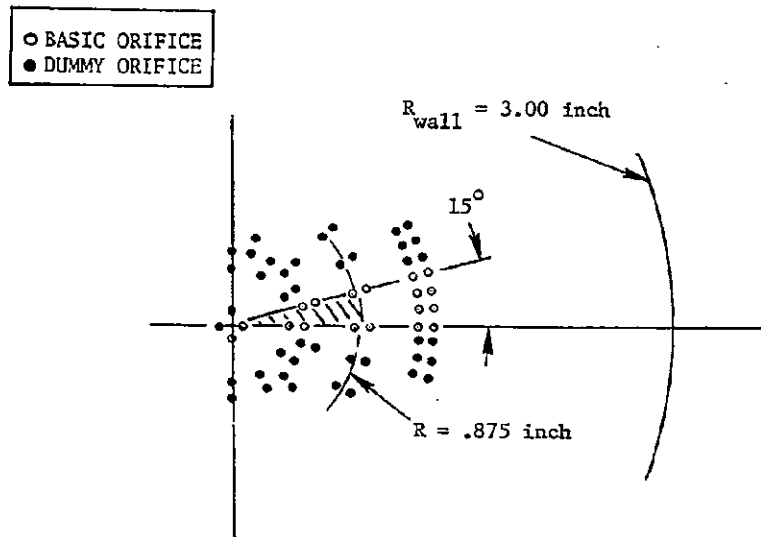


Figure 81 Layout of Injector Elements In and Around Innermost Slice of Flintstone Injector Analyzed for Heat Transfer

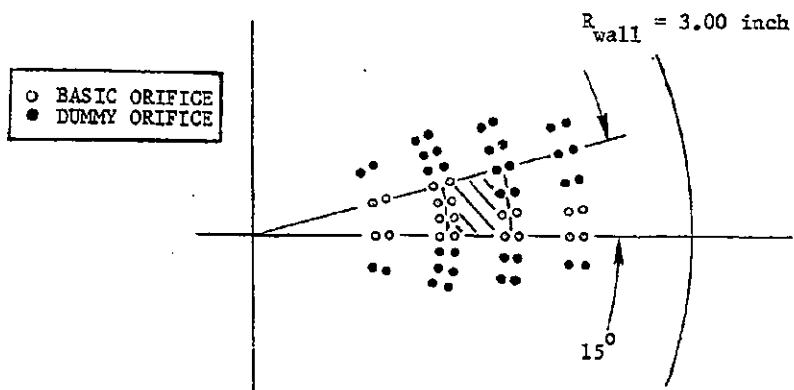


Figure 82a Layout of Injector Elements In and Around Flintstone Injector Segment Extending From  $R = 1.312 \text{ Inch}$  to  $R = 1.75 \text{ Inch}$  (shaded area)

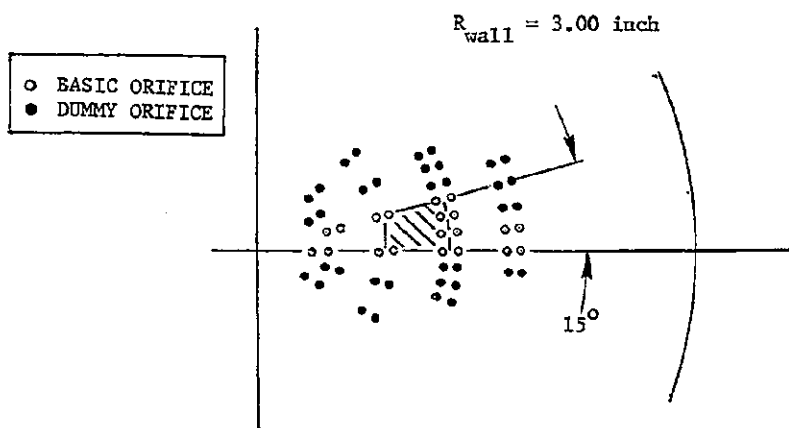


Figure 82b Layout of Injector Elements In and Around Flintstone Injector Segment Extending From  $R = .875 \text{ Inch}$  to  $R = 1.312 \text{ Inch}$  (shaded area)

shown in Fig. 83, a second calculation of heat transfer was required in the potential erosion areas indicated by the IHTM program to determine whether the regenerative cooling capability of the fuel was sufficient to lower the face temperature while absorbing the incoming heat flux. The regenerative cooling capability of the fuel was defined by two criteria:

- (1) The gas side heat flux must be less than the peak nucleate boiling heat flux of the M-20 fuel blend.
- (2) The conduction temperature drop between the injector face and the coolant passage required to transmit the face heat flux to the coolant must be less than  $(3000R - T_{SAT})$  where  $T_{SAT}$  is the saturation temperature of the fuel at the chamber pressure of the experiment.

No directly applicable nucleate boiling heat transfer data were available for the M-20 fuel blend, or for the separate fuel constituents at the low velocity but highly subcooled conditions of the flow passages. However, an extrapolation of available hydrazine, monomethylhydrazine, and 50%  $N_2H_4$ -50% UDMH data at higher velocities and lower subcooling indicated that a nominal value of 5.0 Btu/in<sup>2</sup> sec could be assigned as the maximum allowable heat flux.

Similarly, an analysis of the second criterion indicated that the conduction requirement could be stated as

$$q/A|_{MAX} \leq \frac{1.4}{\Delta z_{MIN}} \text{ (inch)}$$

where  $\Delta z_{MIN}$  is the shortest distance from a given location on the injector face to the nearest fuel passage and  $q/A|_{MAX}$  is the allowable injector face heat flux calculated from conduction limitations by assuming a nickel conductivity of 0.0007 Btu/inch sec R and a (3000R-950R) available  $\Delta T$ .

#### Results of the IHTM Analysis

Each of the five slices of the injector shown in Fig. 80 through Fig. 82 were processed through the IHTM computer program. A face temperature of 3000 R was assumed in each of the heat transfer calculations. The computer analysis was made only for the lower chamber pressure of 300 psia. The face heat fluxes

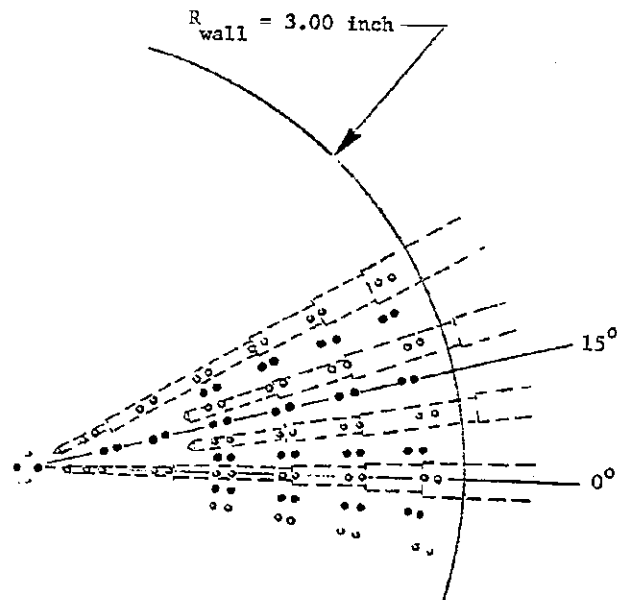
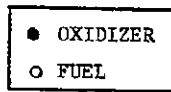


Figure 83 Layout of Fuel Orifice Feed Passages Supplying  
 Regenerative Cooling to Flintstone Injector Face

calculated at 300 psia were scaled up by a factor of 1.14, which corresponds to the ratio of the parameter  $(\rho_g U_{inj})^{0.4}$  evaluated at a chamber pressure of 500 psia to the same parameter evaluated at 300 psia. This scaling method was done according to the discussion on p. 108. With the assumed high face temperature, negative heat fluxes (heat flowing from the injector face into the combustion gas) were calculated at many locations on the injector. These calculations have no real physical meaning, of course, because the real face temperature would assume a lower value at these locations; however, the negative local fluxes conveniently indicate the areas where no face erosion problem is expected.

The heat fluxes calculated along rays at the 0.0 and 5.0 degree locations of Fig. 79 are shown in Fig. 84 and Fig. 85, respectively. When heat fluxes were calculated as negative, they have been set equal to zero. Both the directly calculated results at a 300 psia chamber pressure and the scaled results at 500 psia are shown. Also shown in Fig. 84 and 85 are the predicted allowable heat fluxes based upon the two regenerative cooling criteria listed above. From the graphical results shown in the two figures, two conclusions may be drawn. First of all, it appears that no face erosion problem was expected at the lower chamber pressure. At the higher chamber pressure, no erosion was predicted near the center of the injector. At chamber radii from approximately 2.0 inch out to the chamber wall, a number of marginal locations are predicted along the 5.0-degree ray. The locations of maximum predicted heat flux shown in the graphs correspond to the computer program mesh points adjacent to oxidizer orifices in the outer two rings of oxidizer elements. In general, the maximum predicted face heat flux was predicted to encircle the oxidizer orifices in the outer rings. These locations also correspond to the locations of minimum allowable heat flux from regenerative cooling criteria. Face erosion was therefore considered most likely near the outer oxidizer orifices.

The analysis predicted a marginal rather than a failure condition at the regions of highest heat flux. However, the assumption made in the analysis that the nickel surface can approach to within 100R of its melting temperature without chemical attack was certainly optimistic. A lower allowable surface temperature based upon chemical corrosion considerations must both increase the predicted face heat flux and reduce the regenerative cooling capability. Under the circumstances, erosion near the oxidizer orifices was considered likely to occur at the higher chamber pressure.

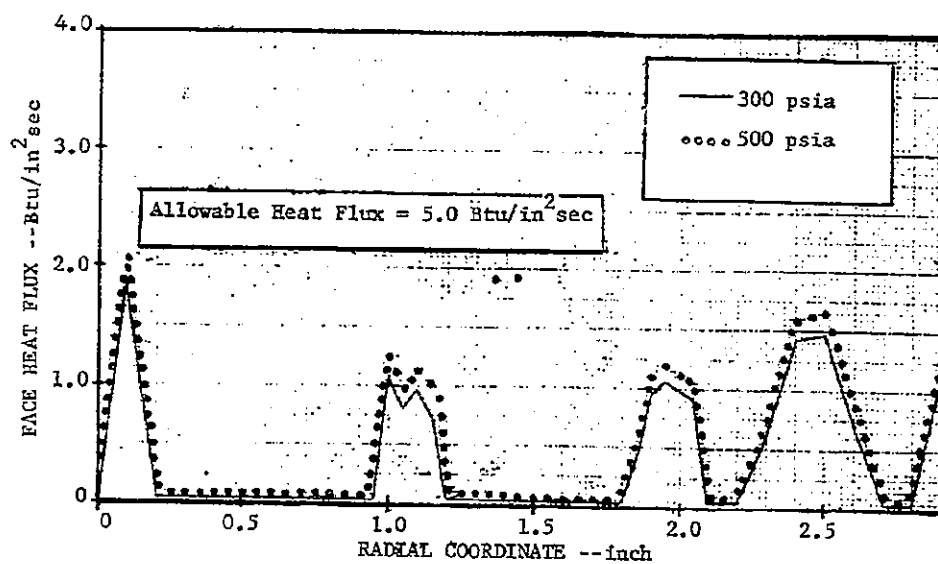


Figure 84 Face Heat Flux For a Surface Temperature of 3000 R Along 0-Degree Ray Corresponding to Fuel Orifices

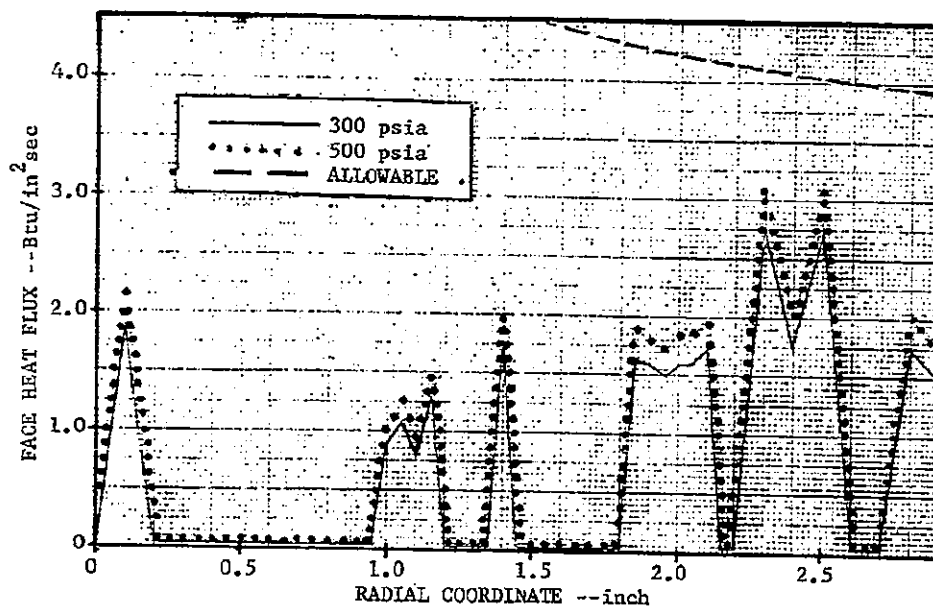


Figure 85 Face Heat Flux For a Surface Temperature of 3000 R Along 5-Degree Ray Corresponding to Oxidizer Orifices

The appearance of the Flintstone injector after the 500 psia motor firing is shown in Fig. 86. Whereas the analysis had predicted a marginal compatibility situation rather than an obvious failure condition (with damage most likely near the outer orifices), the real motor firing produced very severe face burning. Damage was heaviest at the center of the injector where the face had eroded back into the radial fuel feed passages shown in Fig. 83; however, substantial erosion also occurred at chamber radii from 2.0 to 2.70-inch, corresponding approximately to the radial location of the two outboard rings of oxidizer elements. The damage near the center of the injector was so severe that it was impossible to trace the sequence of events by which gross failure had occurred; however, consideration of the relative erosion depths suggested that an initial burnout probably occurred at the quadlet element in the very center of the injector and that the subsequent maldistribution of propellant flow propagated the failure to the nearby elements.

Because the injector compatibility was substantially different from the analytical prediction, a review was made of both the general assumptions made in the analysis and of the particular configuration of the Flintstone injector. Based upon this review, four factors which were not considered in setting up the analysis appear to have possibly contributed in various degrees to the differences between the real and the predicted behavior. These factors are:

1. The reactivity of fluorine oxidizers with metals can cause the melting point of the injector face to become a completely unrealistic standard reference point for defining a limiting wall temperature. As discussed on p. 212, a limiting surface temperature 100R below the melting point of nickel was selected as the basis for heat transfer calculations with a nominally compatible material, chiefly because the melting point is a well defined parameter, while corrosion and strength limits are much harder to establish in a simple consistent manner. However, a brief review of the literature indicates that the real limiting temperature is substantially lower. Godwin and Lorenzo (Ref. 30) reported that nickel wires ignited in fluorine-containing atmospheres at surface temperatures of 1096 to 1219C (2460 to 2690R). In an earlier reference, Simons (Ref. 31) prescribes a limiting temperature of only 750C (1840R) for nickel in contact with





Figure 86 Erosion of Flintstone Injector After Motor Firing at  
Chamber Pressure of 500 psia

fluorine. If the more optimistic compatibility data of Godwin and Lorenzo are used to define a surface temperature of 2500R as the point at which surface burning is very likely to occur, and this temperature is employed as the reference temperature for heat transfer calculations, the original predictions shown in Fig. 84 and 85 are changed to the revised predictions shown in Fig. 87 and 88. The changes represent an increase in expected gas-side heat transfer due to an increased  $\Delta T$  between combustion gas and the lower surface temperature, and a very substantial decrease in allowable heat flux due to the decrease in available  $\Delta T$  within the injector walls. As shown in Fig. 88, erosion is predicted to be very likely in the region corresponding to the outboard oxidizer orifices (where erosion was noted), and a possible compatibility problem is predicted near the center of the chamber.

2. The burnout heat flux of the M-20 fuel coolant flowing in radial passages behind the injector face was estimated to be  $5.0 \text{ Btu/in}^2\text{sec}$ . Although this value is probably realistic for the portions of the passages where a positive cross-flow is maintained, it may not be correct for the end of passages where the flow stagnates (Fig. 85). However, these stagnation locations are just the region where the heat flux from the center of the injector (i.e., the point of most severe erosion) had to be absorbed. A breakdown in fuel cooling is therefore a possible mechanism for the injector failure. Unfortunately, although stagnation in hydrazine coolant passages has been blamed for failures in a number of previous rocket engine programs, no quantitative data exist to directly substantiate this mechanism and it can only be considered a possibility.
3. The heat transfer analysis assumed good distribution of propellants in their respective manifolds and, therefore, uniform propellant injection velocities across the injector face\*. However, an inspection of the actual hardware indicates that a serious maldistribution of oxidizer may have resulted from introduction to its dome manifold from a single centrally located downcomer passage. The likely effect of the oxidizer manifolding

\*Drawings of the propellant manifolds were not available for the original analysis.

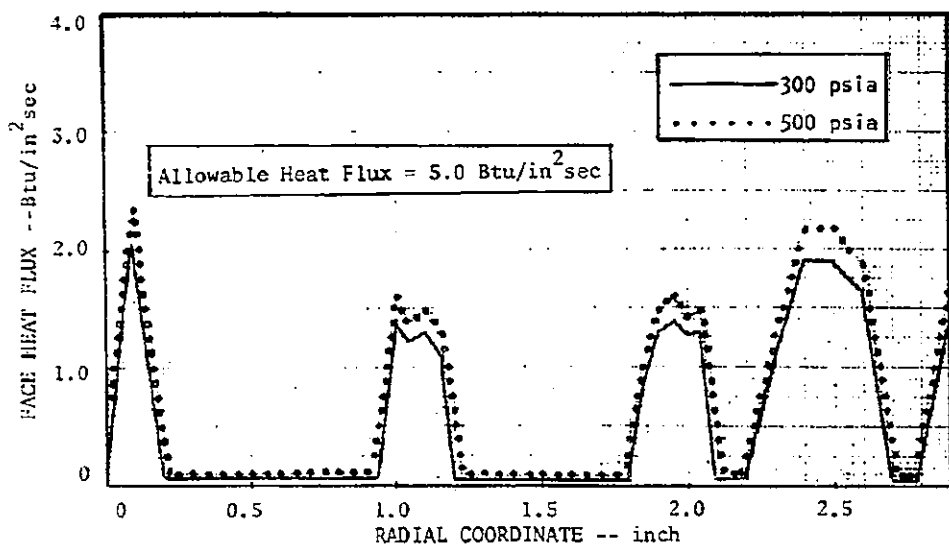


Figure 87 Face Heat Flux (Along 0° Ray) For a Revised Surface Temperature of 2500R

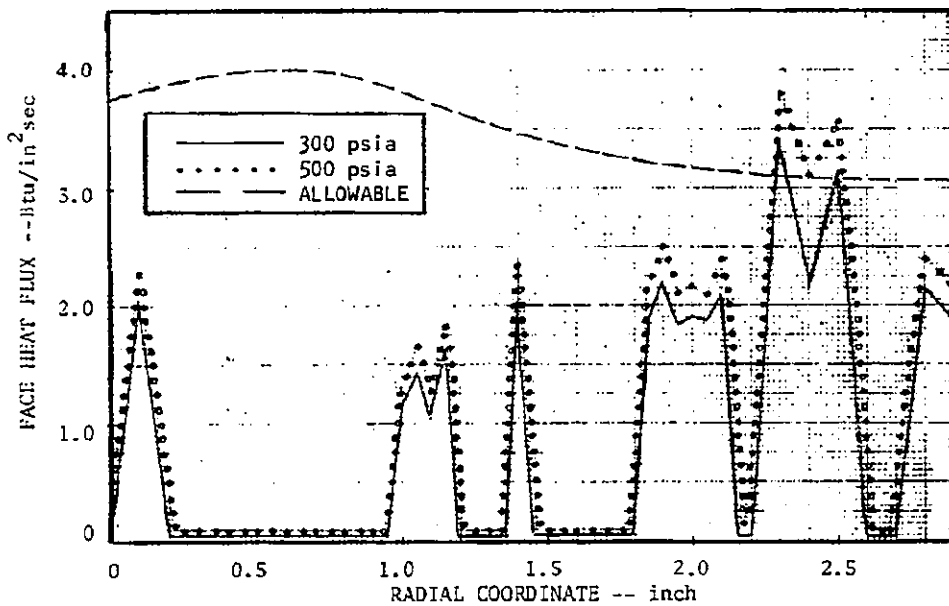


Figure 88 Face Heat Flux (Along 5° Ray) For a Revised Surface Temperature of 2500R

arrangement would be to produce a higher injection velocity at the center of the injector and, therefore, a higher heat flux in that region and a lower heat flux near the outboard elements. Although the possible increase in heat flux at the center of the injector is not considered to be sufficient by itself to produce a failure condition at that location, the interaction of all of the first three factors provides a possible explanation for the pattern by which the injector burned out.

4. The analysis made of the Flintstone injector assumed that no combustion gas was generated close to the injector face and out through the element impingement points; all of the near-injector gas flows are considered to be recirculation driven by gas-droplet drag forces. This assumption is considered to be particularly appropriate for like doublet injectors similar to the Flintstone, and the assumption probably introduced no difficulties in the analysis except at the very center of the injector. As shown in Fig. 79, the center of the Flintstone injector is occupied by a quadlet (symmetrical two-on-two) element whose mean impingement point was only 0.11-inch from the injector face. Based upon the reactive stream blow-apart studies of Nurick and Cordill with  $\text{ClF}_3/\text{N}_2\text{H}_4$  (Ref. 32), a powerful reaction and net combustion gas generation would exist at the impingement point of the quadlet. Because the four converging liquid streams form a sort of "umbrella" over the generated gas, a powerful recirculation pattern would then be expected behind the impingement point, with a subsequent high local heat flux to the injector face in and around the four quadlet orifices. Because no accepted correlation exists for impingement point gas evolution, no capability for analyzing such a situation was programmed into the IHTM model and no special consideration was given to the quadlet area in the Flintstone analysis.

The four considerations discussed above provide explanations for the differences between analytical predictions and experimental results with the Flintstone injector and indicate several areas in which the program must be judiciously employed. In particular, it appears that the limiting surface temperature must be carefully

selected, that possible effect of manifolding upon the injection velocities from individual elements should be considered, and finally the limitations of the present analysis for bipropellant elements and very reactive propellant combinations should be appreciated. Alternatively, at least a simplified theoretical model for the recirculation behind an element under "blowapart" conditions should be developed and incorporated into the IHTM model.

## ANALYSIS OF CASE TCC-2

Demonstration case TCC-2 consisted of the analysis of a motor firing experiment made at Rocketdyne with the FLOX/LPG propellant combination under NASA Contract NAS3-11199 (Ref. 5). Its purpose was to evaluate the ability of the overall injector/chamber compatibility model to predict heat transfer and performance with the highly cooled chamber walls typical of regeneratively cooled thrust chambers. The conditions during the motor firing (designated as Test No. 8 in Ref. 5) are summarized below.

### Test Conditions During Motor Firing TCC-2

Chamber Pressure, psia	103.8
Mixture Ratio	3.75
Fuel Flowrate, lbm/sec	2.72
Oxidizer Flowrate, lbm/sec	10.22
Throat Diameter, inch	5.70
Chamber Diameter, inch	8.06
Chamber Length (injector-to-throat), inch	15.77
Chamber Length (injector-to-start of convergence), inch	12.19
Contraction Ratio	2.0

The FLOX oxidizer was a blend of 70% fluorine and 30% oxygen. The LPG fuel was the 55% ethane-45% methane eutectic blend.

The injector, designated as LD-1 in Ref. 5 contained 112 like-doublet pair elements in six concentric rings. Fuel orifice diameters were 0.020 inch, oxidizer orifice diameters were 0.029-inch, and stream impingement angles were 60 degree. Other pertinent data for the individual elements (see Fig. 9 for nomenclature) were:

Fan cant angle, $\gamma_F$	0.0 degree
Element spacing, X	0.20-inch
Fan spacing, Y	0.0-inch

The 32 elements in the outer ring were canted 15 degree toward the chamber axis for chamber wall compatibility.

The uncooled copper chamber walls were instrumented with thermocouples attached to the back wall at a number of axial and circumferential locations. The transient temperature response of these thermocouples defined local heat flux during short duration motor firings. The heat fluxes measured during the test analyzed in demonstration case TCC-2 are listed in Table 14 .

Although, heat fluxes shown in Table 14 were measured at three circumferential locations, these locations were not referenced to the injector face pattern; therefore the circumferential measurements serve only as an indication of local deviation from the average heat flux at a given axial station.

Table 14 Chamber Wall Heat Flux (Btu/in<sup>2</sup> sec)  
Obtained with Injector LD-1

Axial Station (Inch)	Heat Flux $\theta_1$	Heat Flux $\theta_2$	Heat Flux $\theta_3$	Heat Flux Average
2.50	2.63	2.78	2.80	2.74
3.75	3.07	NT *	3.29	3.18
5.00	3.37	3.38	3.35	3.37
10.69	2.71	2.99	2.98	2.89
13.57	NT *	3.35	3.00	3.17
14.07	2.65	NT	NT	2.65
14.57	NT	3.40	2.72	3.06
15.46	2.47	NT	NT	2.47
15.77	NT	2.78	2.35	2.57
16.34	2.14	NT	NT	2.14
16.84	NT	2.16	1.80	1.98

\*Not taken

The axial variation of the heat fluxes listed in Table 14 shows an unusual characteristic. The average heat flux at a given axial station does not maximize at or immediately upstream of the nozzle throat as ordinarily expected in thrust chamber heat transfer. This anomalous behavior was exhibited to some extent in all the heat transfer results reported in Ref. 5 for 125 motor firings made with a variety of injector configurations, chamber lengths, contraction ratios, chamber pressures, and mixture ratios. The heat flux generally maximized approximately 2-inches upstream of the geometric throat (approximately halfway through the convergence section) and then decreased rather sharply despite the fact that the axial velocity and axial mass flux were increasing. The anomalous heat transfer behavior was particularly true of the earlier motor firings, including test No. 8, where the heat fluxes maximized in the combustion chamber and then decreased monotonically in the nozzle. Because the unusual axial heat transfer profile represented the consistent results of 20 local measurements along the wall, it cannot logically be attributed to a faulty thermocouple or to other instrumentation problems. The authors of Ref. 5 had no explanation for the experimental heat transfer anomaly in the nozzle throat region which seemed to violate all conventional heat transfer theory.



### Setup of the Analysis

Analysis was made of a pie-shaped slice of the chamber 22.5 degrees wide. The distribution of the like-doublet-pair elements within and around this repeating segment of the chamber cross section is shown in Fig. 89. The standard spray coefficient correlations contained in the LISP subroutine library for the like-doublet-pair element were employed in the analysis. Mean droplet diameters of 0.003-inch were defined for both propellants. Performance parameters and combustion gas properties were calculated by means of the Rocketdyne N-element performance program (Ref. 35).

### Results of the Analysis

The initial spray distribution was calculated by the LISP program in a plane 1.00-inch downstream of the injector. At this plane, the Rupe mixing index,  $E_M$ , was 79.5 and the mixing-limited characteristic exhaust efficiency,  $\eta_{Mix}$  was 94.2 percent. After the analysis was processed through the 3D-COMBUST and STRMTB programs, the final calculation of overall characteristic exhaust efficiency,  $\eta_{c*}$ , was 98.8 percent. This performance prediction reflected the calculated mixing in the 3D-COMBUST zone. The experimental value of  $\eta_{c*}$ , as reported in Ref. 5, was 97.1 percent.

The 3D-COMBUST program was employed to a point 2.22-inch downstream of the injector, at which location approximately 64.5 percent of the injected propellants were calculated to have burned. Because no experimental measurements of wall heat flux less than 2.50-inch downstream of the injector are reported in Ref. 5 (see Table 14), no calculations of 3D-COMBUST-region heat transfer were made in the BLEAT analysis.

In the throat region, the calculated mixture ratio at the chamber wall ranged from 3.40 to 6.41 with a corresponding variation in  $T_{AW}$  from 6730R to 7437R.\* In the combustion chamber at a distance of 3.05-inch downstream of the injector, the calculated wall mixture ratio ranged from 3.67 to 6.09 with a corresponding variation in calculated  $T_{AW}$  from 5520R to 5907R. The lower values of calculated  $T_{AW}$  in the combustion chamber result from the lower percent vaporization of the

\*circumferential variation

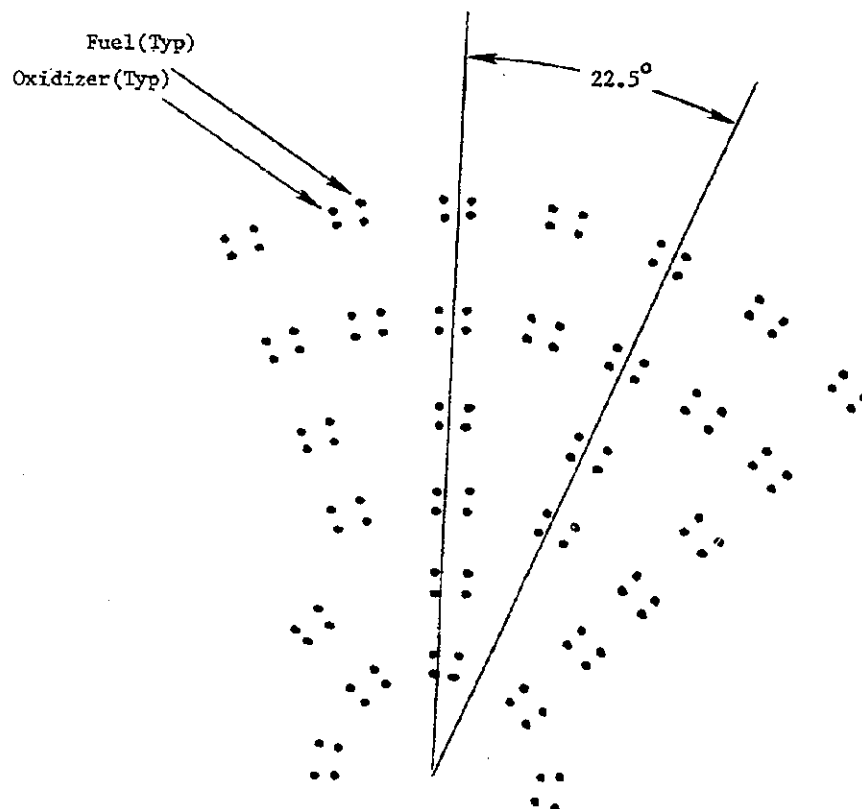


Figure 89 Face Pattern of Like-Doublet-Pair Injector LD-1 Showing Elements In and Around 22.5 Degree Chamber slice Used in Analysis of FLOX/LPG Motor Firing Test No. 8.

propellants. Because the motor firing experiment was of short duration in a copper chamber, the reference wall temperature for heat transfer,  $T_{W,REF}$ , was selected as 600R which corresponds approximately to the mean wall temperature measured during the experiment. Under these circumstances, the range of the circumferential variation in  $T_{AW}$  listed above is seen to produce a negligible percentage variation in gas-to-wall  $\Delta T$ .

The calculated average heat flux at given axial stations is compared to the experimental average heat flux in Fig. 90. The agreement between the calculated and the experimental heat fluxes is good in the combustion chamber but is poor in converging portion of the nozzle. A possible explanation for this discrepancy may be the laminarization of the boundary layer due to the high acceleration of the combustion gas in this region. The axial variation of the Launder acceleration parameter (see p. 137) is shown in Fig. 91. The experimental heat fluxes fall below the calculated heat fluxes at the location where the laminarization is usually considered to occur but less than the conservative critical value of  $3.0 \times 10^{-6}$  which is assigned in the BLEAT computer program as the lower limit for calculation of reduced heat flux by Eq. 75. The lack of agreement may, therefore, reflect the conservative definition of the effects of relaminarization deliberately built into the BLEAT analytical model (because relaminarization phenomena are not as yet considered to be fully understood) rather than a breakdown of the model itself in the converging region of the nozzle.

Fig. 92 compares the experimental heat fluxes with the values calculated when the critical Launder parameter is defined as  $2.0 \times 10^{-6}$ . The agreement is substantially improved in the converging portion of the nozzle. It would be substantially better if the constant coefficient 0.008 in Eq. 75 were made an increasing function of the total acceleration work performed on the gas (the integral of the acceleration with axial distance) as suggested in Ref. 22. However, such refinement is not presently considered warranted for conservative rocket nozzle calculations because most of the available data concerning acceleration effects have not been performed at the high heat flux conditions of interest. For reference, the heat flux profile calculated by the widely used simplified Bartz correlation is also presented in Fig. 92. It is seen that the unusual decrease in nozzle heat transfer exhibited in the Test 8 data are also not predicted by other conventional rocket heat transfer correlations.

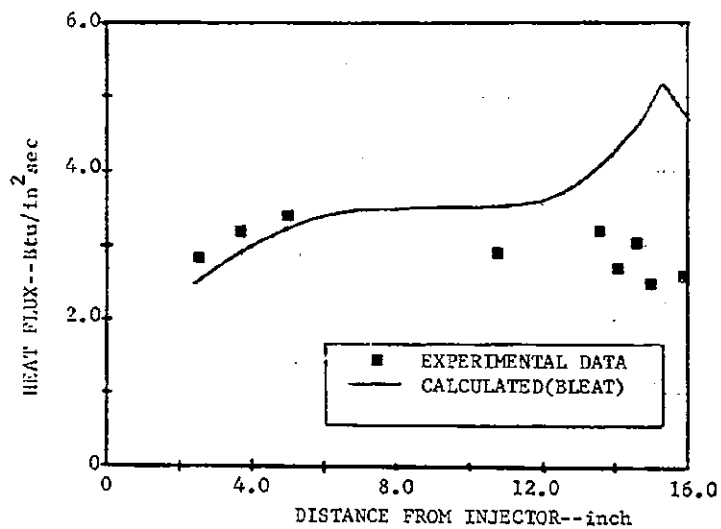


Figure 90 Comparison of Calculated Axial Heat Flux Profile for FLOX/LPG Motor Firing Test No. 8 With Circumferentially Averaged Experimental Results

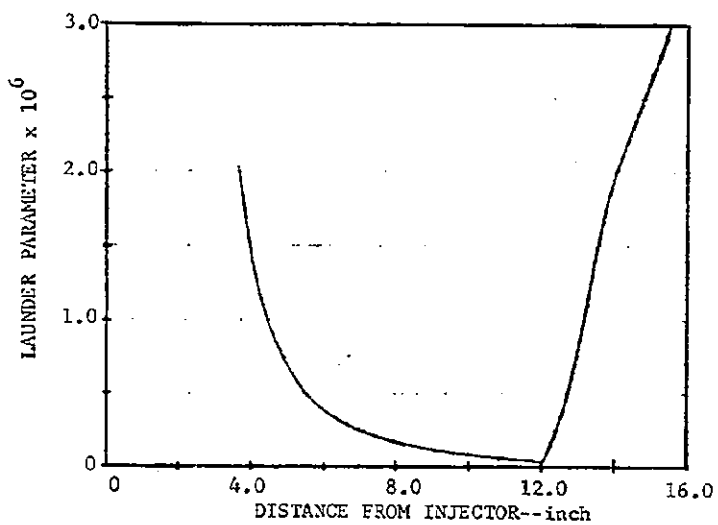


Figure 91 Variation of Launder Acceleration Parameter With Distance From Injector During FLOX/LPG Test No. 8

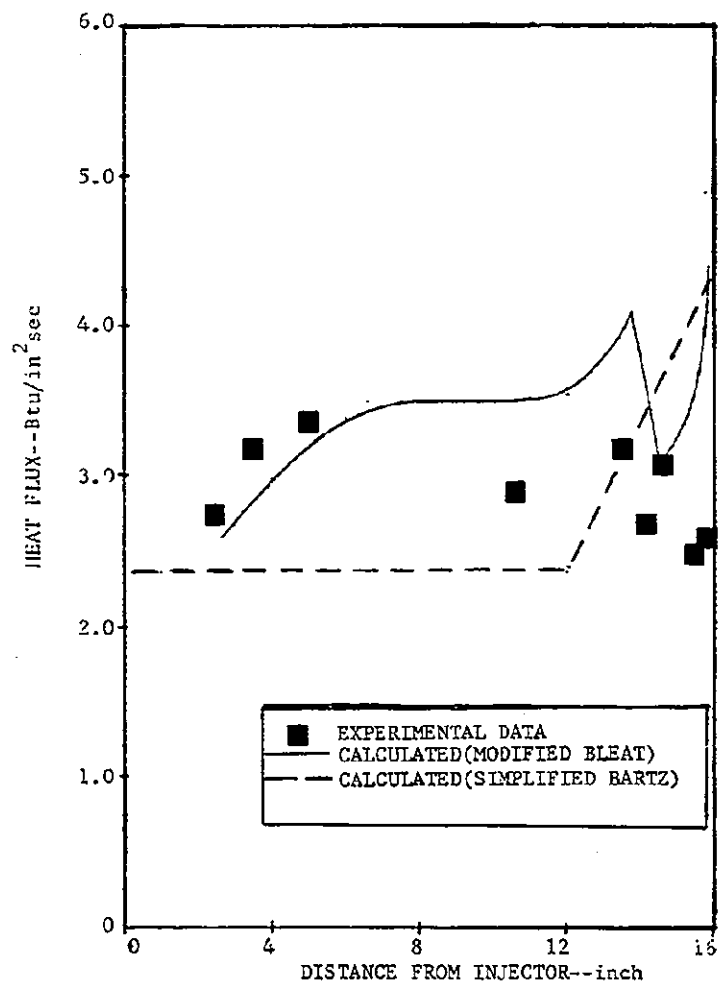


Figure 92 Comparison of Experimental Heat Flux Profile for FLOX/LPG Motor Firing Test No. 8 With Calculated Axial Profile Using Additional Allowance for Acceleration and With Simplified Bartz Correlation

### ANALYSIS OF CASE TCC-3

Demonstration case TCC-3 consisted of the analysis of a motor firing experiment made with the IRFNA/HYDYNE propellant combination at the Air Force Rocket Propulsion Laboratory. The objective of the analysis was to evaluate the ability of the new computer programs to predict ablative wall compatibility. The chamber pressure and the propellant flowrates during the experiment are classified information. Other nominal conditions pertinent to the experiment are summarized below.

#### Test Conditions During Motor Firing TCC-3

Mixture Ratio (nominal)	3.0
Throat Diameter, inch	1.16
Chamber Diameter (at injector), inch	2.64
Chamber Length (injector-to-throat), inch	7.63

The injector consisted of eighteen triplet elements located on circles of two basic diameters and a single quadlet element located at the center of the injector. The triplet element utilized a pair of oxidizer jets impinging on a single fuel stream at a distance of .025-inch from the injector face.

For the triplet elements, oxidizer orifice diameters were 0.032-inch. For the twelve triplet elements located on the outer basic diameter of 2.00-inch, the fuel orifice diameters were 0.026-inch; for the six elements on the inner basic diameter of 1.25-inch, the fuel orifice diameters were 0.028-inch. The quadlet orifice diameters were 0.028-inch and 0.0469-inch for fuel and oxidizer, respectively. The injector face pattern is shown in Fig. 93. It should be noted that the triplet fans are oriented along chamber radii rather than parallel to the chamber wall.

The thrust chamber employed a unique design consisting of a regeneratively cooled outer jacket surrounding a phenolic reffrasil chamber liner and a JTA graphite throat insert. A Hastelloy-X skirt is provided downstream of the nozzle insert. A schematic representation of the chamber wall configuration is shown in Fig 94. The real contours of the interface between the ablative liner and the throat insert and of the Hastelloy-X skirt are slightly simplified in Fig. 94 for inclusion in the 3D-ABLATE wall response program.

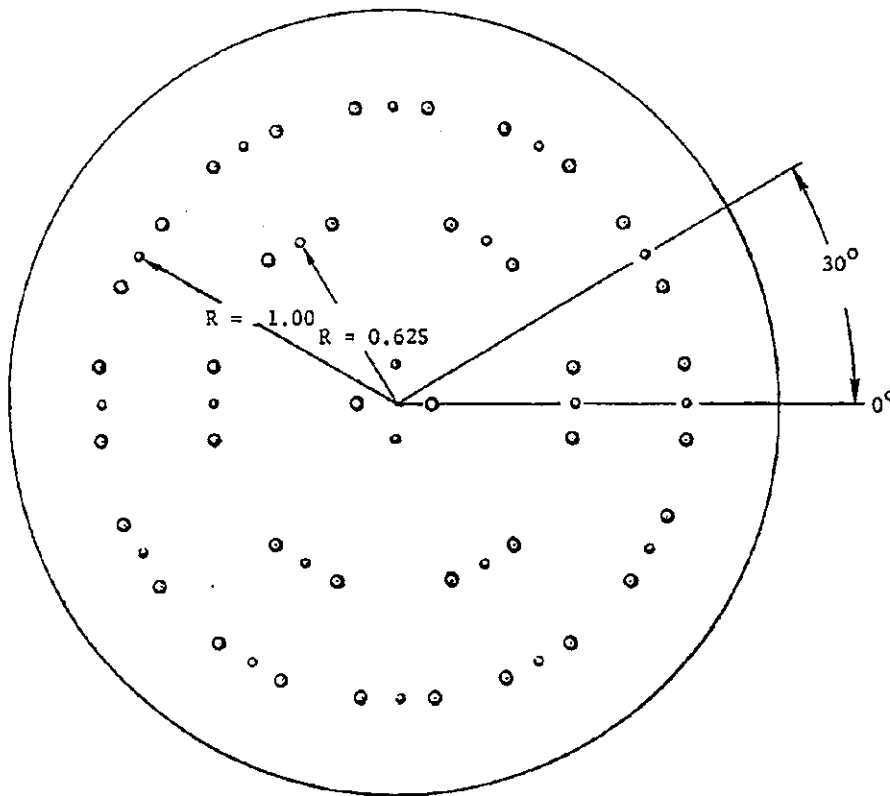


Figure 93 Face Pattern of Nineteen Element Triplet/Quadlet Injector  
Showing 30 Degree Slice Used to Analyze IRFNA/HYDYNE Motor  
Firing in an Ablative and Refractory Lined Regeneratively  
Cooled Thrust Chamber

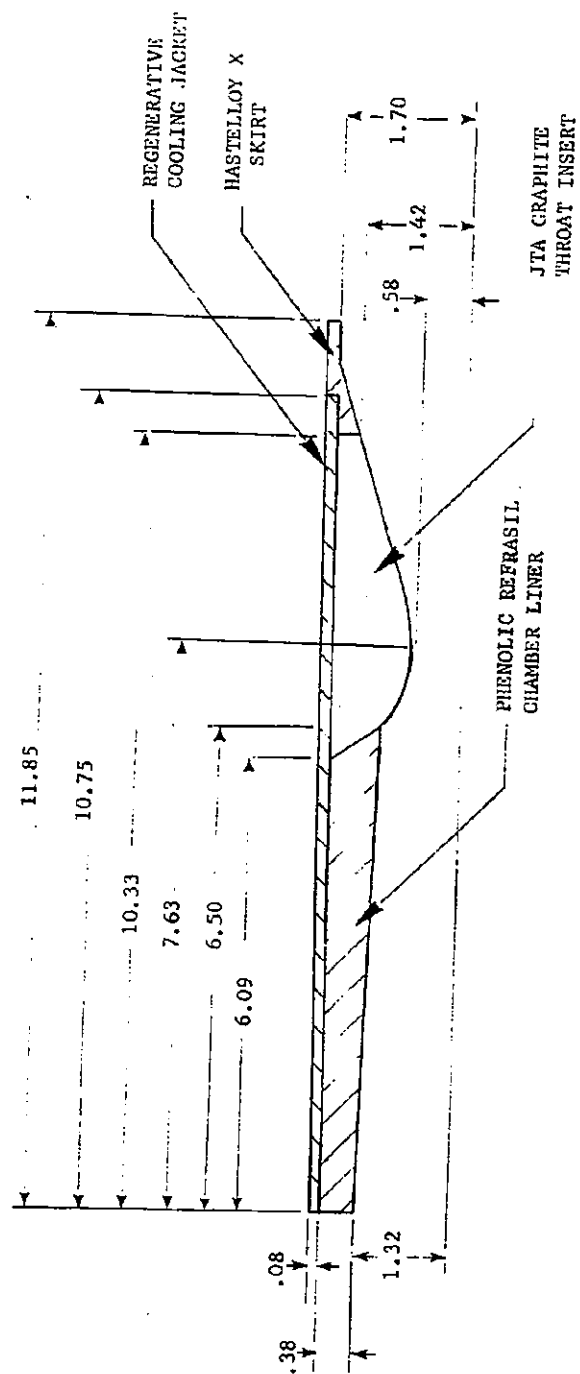


Figure 94 Thrust Chamber Wall Geometry for IRFNA/HYDYNE Motor Firing with Triplet/Quadlet Injector (Simplified for 2D-ABLATE Analysis)



### Setup of the Analysis

The pie-shaped slice of the chamber cross section shown in Fig. 93 was selected for analysis. This 30 degree slice represents a repeating segment of the injector face pattern and therefore should be representative of the entire chamber cross section. Eleven injector elements were considered in the LISP analysis, including all six inboard triplet elements, the four outboard triplets at the 0, 30, 60 and 330 degree locations of Fig. 93 and 1/12 of the center quadlet element.

Although the diameter ratio of the triplet elements was outside the range over which the empirical spray coefficients of Fig. 15 through 19 were correlated, lack of alternate data made it necessary to employ the standard triplet spray coefficients. The quadlet element at the center was described as a Type 8 element (see page 18). The a and b coefficients were assigned values of 10.0 for all four propellant orifices; the other spray coefficients for the quadlet were assigned zero values.

Although the real thrust chamber converged uniformly from a diameter of 2.64-inch at the injector face to a 2.08-inch diameter at a distance 6.50-inch downstream as shown in Fig. 94, it was necessary to assign a constant mean chamber diameter of 2.50-inch for the first 1.90 inch of the chamber to permit use of 3D-COMBUST program which is restricted to a constant chamber area. The usual 15 x 7 system of radial and circumferential mesh lines was utilized in both the LISP and 3D-COMBUST analyses. Twenty seven stream tubes were used in the STRMTB program.

Performance parameters and combustion gas properties were calculated by means of the Rocketdyne N-element performance program (Ref. 33). Liquid properties for the IRENA (inhibited red fuming nitric acid) and HYDYNE (60% UDMH-40% diethylenetriamine) propellants were obtained from the Aerojet General Corporation propellant handbook. (Ref. 34).

### Results of the Analysis

The initial spray distribution was calculated by the LISP program in a plane 1.20-inch downstream of the injector. At this plane, the Rupe mixing index,  $E_M$ , was calculated to be 77.8 and the mixing-limited characteristic exhaust efficiency,  $\eta_{Mix}$ , was 92.2 percent. The attachment point for the wall boundary layer (the point where the gas and spray velocities are equal) was also calculated to occur at this same plane, 1.20-inch from the injector face.

After the analysis was further processed through the 3D-COMBUST, STRMTB and BLEAT programs, the calculated overall characteristic exhaust efficiency rose to 93.9 percent, including a vaporization efficiency of 97.7 percent and a mixing-limited efficiency of 96.0 percent.

At the nozzle throat, the calculated mixture ratio at the wall ranged from 1.40 to 4.12. The adiabatic wall temperature as calculated by the BLEAT program ranged from 3125R to 5475R. The circumferential variations of mixture ratio and  $T_{AW}$  are shown in Fig. 95. Comparison of Fig. 95 with the injector face pattern shown in Fig. 93 shows that points of lower mixture ratio correspond approximately to the location of the outboard triplet elements with the highest mixture ratio occurring approximately midway between the outboard elements. Because the maximum stagnation temperature corresponds to a mixture ratio of 3.0 for the IRFNA/HYDYNE propellant combination, the predicted points of maximum  $T_{AW}$  shown in Fig. 95 are displaced to either side of the midway point between outboard elements.

The calculated circumferential variations in mixture ratio and  $T_{AW}$  at a distance of 3.96-inch from the injector face are shown in Fig. 96. The shape of the curves is essentially the same as at the throat, although the adiabatic wall temperatures at all circumferential locations are approximately 10 percent lower than the corresponding throat values.

Comparison of the  $T_{AW}$  distributions in both Fig. 95 and 96 to the injector face pattern in Fig. 93 indicated that a streaking pattern should occur along most of the length of the chamber which should be periodic with the outboard

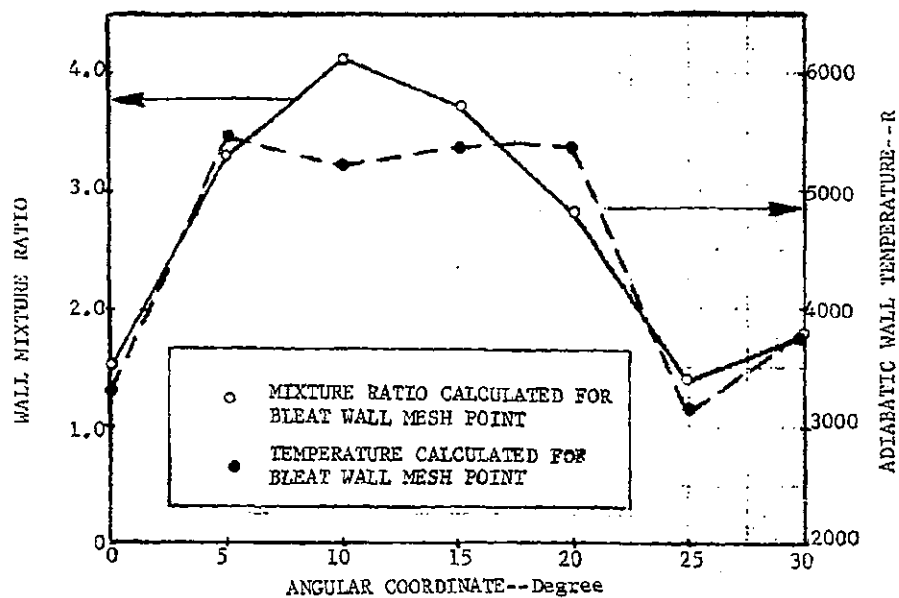


Figure 95 Variation of Wall Mixture Ratio and Adiabatic Wall Temperature With Angular Coordinate as Defined in Fig. 93 at the Nozzle Throat

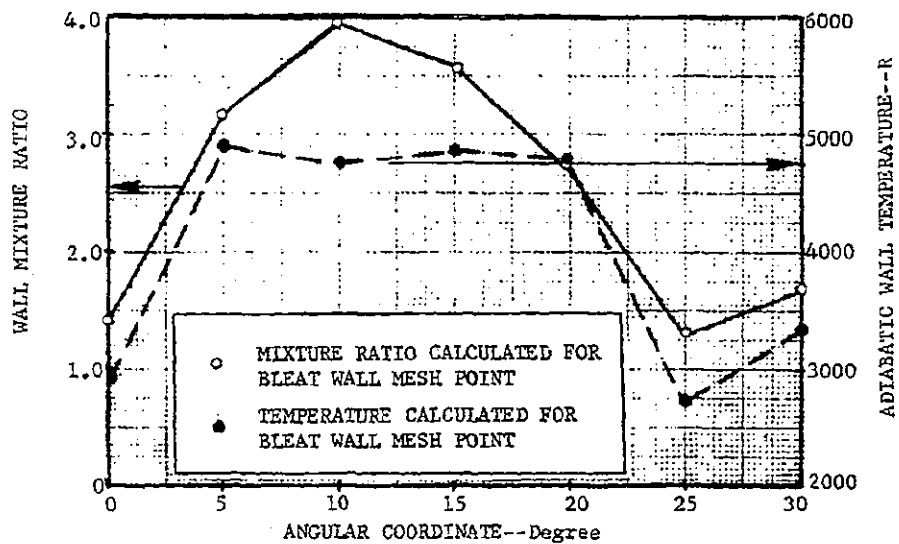


Figure 96 Variation of Wall Mixture Ratio and Adiabatic Wall Temperature With Angular Coordinate 3.96-inch From Injector

triplet elements. The cooler wall region should be aligned approximately with each outboard element with a broad hot streak occupying most of the intervening space. As shown in the graphs, a slight displacement in the circumferential locations of the calculated maximum  $T_{AW}$  is apparently associated with the unsymmetrical location of the inboard triplet elements relative to the 30-degree slice of the chamber employed in the analysis.

Conversion of the axial and circumferential distribution of wall mixture ratio,  $T_{AW}$  and  $h_g$  as calculated the BLEAT program into predictions of the char and erosion rates required use of an ablation/conduction wall response analysis. Initially, the 2D-ABLATE program was used to make this calculation upon the IBM7040 computer at Edwards AFB. This program, which was developed for the Air Force by Rocketdyne under Contract AF04(611)-11415 (Ref. 35), calculates char rate and surface recession in multi-material thrust chamber walls for an assumed axisymmetric (r,z) geometry. Because the 2D-ABLATE program does not consider either circumferential variations in boundary conditions or the effect of circumferential conduction in the chamber walls and requires, in addition, a constant value of  $T_{AW}$  for erosion calculations, the calculation of wall response to the "streaky" situation shown in Fig. 95 and 96 could not be calculated rigorously. Instead, separate calculations were set up for approximately the two extremes in  $T_{AW}$  shown in Fig. 95, namely 5300R and 3125R.

The lower  $T_{AW}$  case was processed through the 2D-ABLATE computer program and resulted in a prediction of no erosion in either the throat insert or in the combustion liner regions of the wall structure shown in Fig. 94. The char penetration in the phenolic refrasil chamber liner was calculated to range from 0.20-inch to 0.30-inch for the nominal burn time. However, when the high  $T_{AW}$  (5300R) case was processed through the computer, numerical instabilities encountered in the machine calculation prevented its successful completion. Examination of the computer printout suggests that the combination of a regeneratively cooled liner together with the high conductivity throat insert and low conductivity phenolic refrasil may have constituted an unacceptable set of wall regions for the computer program. An alternate calculation of charring and erosion for the high temperature condition was then made at Rocketdyne using the THAB computer program, a one-

dimensional analysis in a cylindrical (r) coordinate system. The THAB program is essentially a one-dimensional version of 2D-ABLATE with essentially the same mechanisms for charring and for erosion by melting and/or chemical attack. In the throat region, no erosion was predicted for the JTA graphite throat insert.\* In the combustion chamber, the liner was calculated to erode (by surface melting) at a steady rate of 0.00056 inch/sec after a heat up period of 42 sec. This resulted in the prediction of a total recession of 0.060-inch for its nominal burn period. The char depth was predicted as 0.16-inch. The calculation was very sensitive to the value assigned to  $T_{AW}$ . When the THAB calculation was repeated with a value of 4900R assigned to  $T_{AW}$  (corresponding to the maximum temperature at the combustion chamber location shown in Fig. 96), only negligible erosion was predicted. The calculation is similarly sensitive to the local value of  $h_g$  employed in the calculation.

The wall response in the actual motor firing experiment was qualitatively similar to that predicted in the analysis. There was no significant throat erosion and a streaking erosion pattern was obtained in the combustion chamber which correlated with the injector face pattern. The erosion pattern in the combustion chamber is shown in Fig. 97. The eroded streaks at the downstream end of the combustion chamber liner are seen to lie approximately halfway between the spots of virgin material at the upstream end of the liner which are presumed to correspond to the locations of maximum spray impingement, i.e., to be in line with fans of the outboard triplet injector elements (Fig. 93). When Fig. 93, 96, and 97 are correlated it is seen that the streaks of maximum erosion are in line with the regions of high  $T_{AW}$  shown in Fig. 96. The depth of the eroded grooves was not completely uniform around the chamber periphery; gouging of the refrasil was most extensive over approximately 120 degrees of the periphery. At a distance of 4.0-inch from the injector face (corresponding to the conditions in Fig. 96), the depth of grooves ranged from only 0.05-inch to a maximum of approximately 0.17-inch. The average depth in the most severely eroded portion was approximately 0.12-inch.

\*The mechanism for erosion of JTA graphite was assumed to be the same as that for silicon carbide, namely decomposition of the silica protective layer; however, the thermal conductivity of ATJ graphite was employed in the calculation.

MAXIMUM EROSION STREAKS APPROXIMATELY 10  
DEGREES FROM MAXIMUM LIQUID IMPINGEMENT



MAXIMUM LIQUID IMPINGEMENT IN LINE  
WITH OUTBOARD TRIPLET ELEMENTS

Figure 97 Erosion of Phenolic Refrasil Combustion Chamber  
Liner During Motor Firing With IRFNA/HYDYNE  
Propellant Combination and Triplet Injector

Reproduced from  
best available copy.

Char depths in the refrasil liner at the 4.0-inch distance from the injector ranged from approximately 0.20 to 0.25-inch at the eroded portions of the chamber to 0.30 to 0.35-inch in the noneroded portions. Apparently, there was a smearing of the char front advance by circumferential conduction.

The qualitative agreement between the experimental results and the analytical predictions is, therefore, seen to be very good. The occurrence or nonoccurrence of erosion was predicted at the proper locations. The quantitative agreement is not as good; the degree to which melting erosion occurs was generally underpredicted by a factor of 2 to 3. This lack of agreement is probably due more to uncertainty in the details of the melting erosion process itself within a given chamber once the surface temperature reaches high levels (it is certainly a function of the purity of the refrasil reinforcement and probably of the fiber size and orientation, as well); therefore, the overall correlation of the thrust chamber compatibility model predictions to the experimental results of case TCC-3 is considered to be very good.

#### ANALYSIS OF CASE TCC-4

Demonstration case TCC-4 was analyzed to evaluate the capabilities and limitations of the overall analytical model with coaxial element gas/liquid injectors. It provided the first test of whether an analysis based upon bipropellant liquid injection could be adapted to gas/liquid systems simply by providing a description of the two-phase mass distribution patterns in the LISP computer program. The case considered for this purpose was a motor firing experiment made at the AFRL facility at Edwards, California, with the gaseous hydrogen/liquid oxygen ( $\text{GH}_2/\text{LO}_2$ ) propellant combination in a water-cooled thrust chamber. The nominal conditions are summarized immediately below.

##### Test Conditions During Motor Firing TCC-4

Chamber pressure, psia	500
Mixture Ratio	6.0
Fuel Flowrate, lbm/sec	0.74
Oxidizer Flowrate, lbm/sec	4.44
Throat Diameter, inch	1.75
Chamber Diameter (injector end), inch	3.50
Chamber Length (injector-to-throat), inch	5.00
Contraction Ratio	4.00

The injector employed in the experiment is shown in Fig. 98. It contained 40 gas/liquid coaxial elements in a Rigimesh transpiration cooled face. Pertinent dimensions of the coaxial elements were:

Liquid Oxidizer Orifice Diameter, inch	0.057
Oxidizer Post Diameter, inch	0.075
Cup and Annular Orifice Exit Diameter, inch	0.161
Post Recess in Cup, inch	0.080

Design of the injector provided for a transpiration coolant flow rate through the Rigimesh injector face equal to 8 percent of the total  $\text{GH}_2$  flow or 0.059 lbm/sec. For the individual coaxial elements, design flow rates were 0.017 lbm/sec for the  $\text{GH}_2$  fuel and 0.111 lbm/sec for the liquid oxygen. The water-cooled copper chamber converged gradually over the entire chamber length from



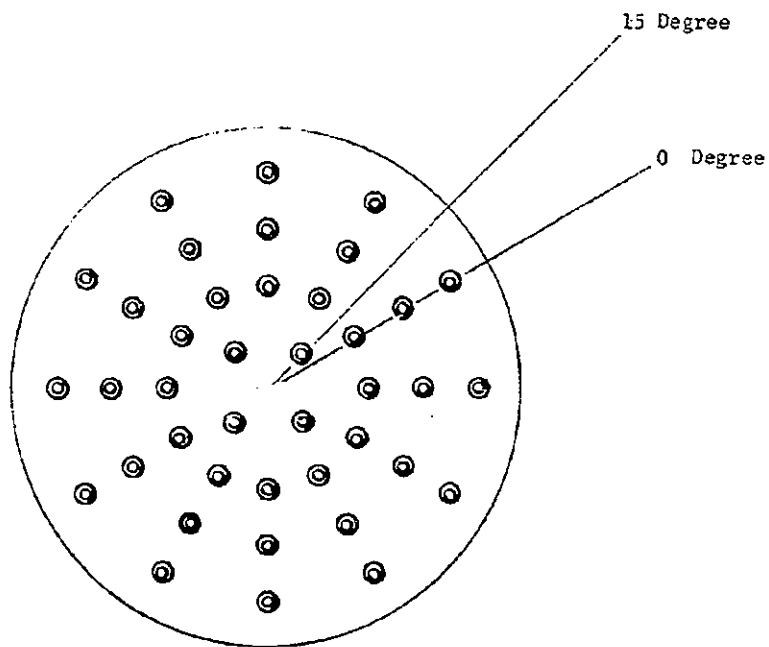


Figure 98 Face Pattern of Gas/Liquid Coaxial Element Injector Showing  
15 Degree Slice Analyzed in  $\text{GH}_2/\text{LO}_2$  Motor Firing

the injector end diameter of 3.50-inch to the throat diameter of 1.75-inch. Near the injector, however, the convergence was sufficiently slow to permit analysis on the basis of a constant chamber diameter as required by the 3D-COMBUST analysis.

#### Setup of the Analysis

The setup of the analysis was dictated by a desire to differentiate the extreme circumferential mass and mixture ratio gradients anticipated because of the narrow spray patterns associated with the gas/liquid element while staying within the limit of seven radial mesh lines allowed by the 3D-COMBUST program. The narrow 15 degree slice of the chamber shown in Fig. 98 was, therefore, selected for analysis rather than the actual 45 degree slice which comprises the repeating interval of the injector face pattern. This choice of narrow slice required that the four innermost elements be divided into twelve equivalent elements at the same distance from the center of the chamber in order to produce a pie-shaped slice whose flow could be considered typical of any 15 degree portion of the chamber cross section. Six of the regular coaxial elements in and around the 15 degree slice were considered in the analysis, with gas and spray mass distributions defined by the Type 6 element correlations in the LISP program. The transpiration coolant flow was defined as being a Type 9 element distributed over the pie-shaped slice.

#### Results and Discussion of the Analysis

The analysis of Case TCC-4 was made in the usual fashion (successive application of the LISP, 3D-COMBUST, and STRMTB computer programs). The principal conclusion reached after examination of the calculated results is that the additions made to the LISP program were not, by themselves, sufficient to adapt the overall model to gas/liquid coaxial injectors. It appears that a number of modifications to the 3D-COMBUST computer program will be required before the gas flow field can be calculated on a three-dimensional basis. The calculated results, which are discussed in the following paragraphs, also seem to indicate the analytical problems are due to the combination of (1) the unusually narrow liquid spray fan as compared to doublet or triplet elements and (2) the rapid evaporation rate of oxygen as compared to storable propellants.

The propellant distribution was calculated by the LISP computer program at a distance 1.0-inch downstream of the injector. At this plane, the liquid oxygen

was calculated to be 48.6 percent vaporized and the gas velocity profiles from the individual elements overlapped to an extent that the uniform gas velocity option in LISP (see p. 79 ) was applied. With this option, the RUPE mixing index,  $E_{M1}$ , was calculated to be only 59.4 percent and the mixing limited character exhaust efficiency,  $\eta_{Mix}$ , was only 89.5 percent.

Whereas the gas velocity (or mass flux) profiles could be considered to be completely overlapped, the extreme opposite was true in the case of the spray distribution. Fig. 99 shows the mass flux distribution of the unevaporated oxidizer as calculated by the LISP program along the two boundaries of the 15 degree slice of the chamber which was analyzed (see Fig. 98 ). The distribution is shown in terms of the local mesh point values and straight-line-segment gradients in which calculations are performed in the LISP and 3D-COMBUST programs. Comparison of Fig. 99 and 98 shows that the spray is concentrated at the elements with negligible spray in the intervening space. The calculated order-of-magnitude differences in oxidizer spray flux between adjacent mesh points are in agreement with photographic studies of combustors using gas/liquid coaxial element injectors. These studies indicate that the spray remains concentrated in slender jets until evaporation is essentially complete.

These extreme differences in oxidizer spray concentration proved to be incompatible with the numerical procedures employed by the 3D-COMBUST program to solve the conservation relations for droplet mass and momentum (Eq. 19 through 21). The solution of this non-linear system of partial differential equations involves alternate direction sweeps in the r- and  $\theta$ - directions, a procedure which is economical in computer time and core storage requirements relative to a simultaneous solution at all mesh points. However, this technique is numerically unstable if extreme gradients exist in both directions. Because of the numerical instabilities encountered, the 3D-COMBUST computer program could not be employed in a marching calculation over the region in which non-uniformly generated combustion gas must be distributed by transverse velocities. The possibility of transferring the calculation directly from the LISP program to the STRMIB program was investigated to see whether a useful calculation could be made. This procedure proved impractical because the calculated results were dependent upon the number of stream tubes employed in the analysis.

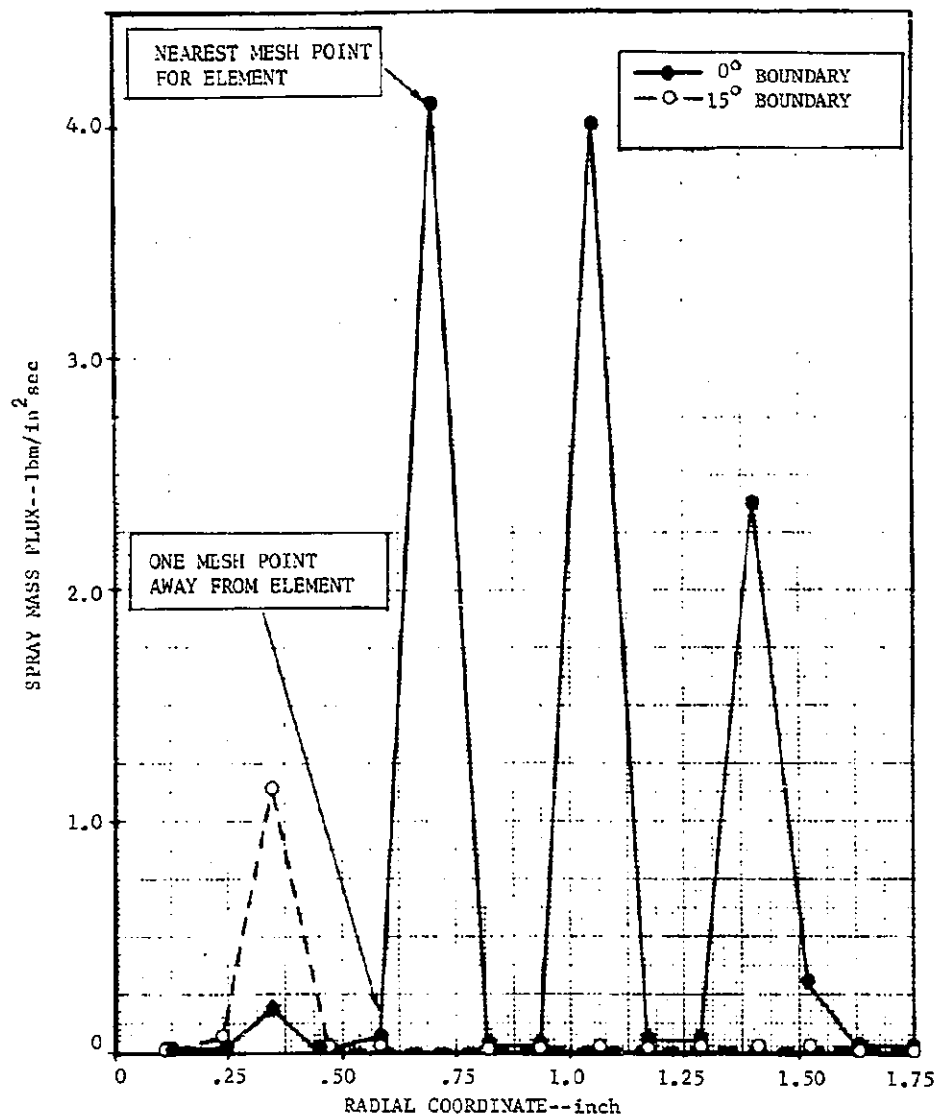


Figure 99 Spray Mass Distribution Along the Boundary Rays of the 15 Degree Slice of Fig. 98 Used to Analyze Gas/Liquid Coaxial Injector

Although the calculational problems encountered with Case TCC-4 proved that the addition of gas/liquid mass flux correlations to the LISP program were not sufficient to permit the analysis of gas/liquid coaxial injector systems on a three-dimensional basis, the attempted analysis suggested a number of straightforward modifications to the 3D-COMBUST program which should eventually introduce the capability\*. Because both cold flow and motor firing experiments indicate that the spray from a coaxial element shows little transverse dispersion, it may be possible to remove the non-linear transverse spray momentum equations from the 3D-COMBUST program. This simplification amounts to the assumption that the spray will act only as line sources of combustion gases along the mesh points in line with the coaxial elements. A more elegant (but still straightforward) procedure is to employ the cold flow spray distributions calculated by the LISP program at two distances from the injector to define a spreading coefficient. This coefficient would be used together with the spray concentration profile to calculate the lateral dispersion of the spray by a Poisson diffusion equation. The latter procedure does not ignore lateral diffusion but replaces the non-linear momentum relations with a stable linear relation. It should be noted, however, that the proposed methods of analyzing coaxial elements would require a particular version of the 3D-COMBUST program which is not meant for use with liquid/liquid injection systems.

---

\*Although the suggested modifications are straightforward, they were beyond the scope of the present project.

## CONCLUSIONS AND RECOMMENDATIONS

### CONCLUSIONS

Improvements have been incorporated into the LISP, 3D-COMBUST, and BLEAT computer programs which will allow the overall Injector/Chamber Compatibility Model to make better predictions of performance and chamber wall compatibility for both ablative and regeneratively-cooled thrust chambers with liquid/liquid injectors.

A model for predicting the mass distribution downstream of multi-element gas/liquid coaxial element injectors has been added to the LISP program. Additional modifications to the 3D-COMBUST program are required before the complete combustion chamber flowfield can be predicted for this type of injector.

An injector face heat transfer computer program (IHTM) has been developed for liquid/liquid injectors. Based upon the limited effectiveness of IHTM in analyzing a motor firing conducted by the Air Force at Edwards, California, the program can be employed where the near-injector flowfield is not dominated by manifold effects or reactive stream blowapart.

Additional experimental investigations of burning spray heat transfer are required before wall heat transfer can be confidently predicted by the BLEAT computer program in the regions of heavy spray impingement.

The 2D-ABLATE computer program which is used to analyze the charring and erosion response of multi-material ablative walls is subject to numerical instabilities for certain combinations of wall geometry and physical properties. These instabilities should be eliminated from the program, or an alternate computer program should be incorporated into the injector/chamber compatibility system of programs.

Effective use of the Injector/Chamber Compatibility Model requires an experienced analytical engineer sufficiently familiar with both the computer programs and with rocket combustion and heat transfer to properly set up the problem and interpret the calculated results.

## RECOMMENDATIONS

A number of straightforward minor modifications to the system of computer programs are suggested which will widen their range of application and are expected to improve their accuracy.

The model employed in LISP for the multi-element gas/liquid coaxial injector should be modified such that mass and momentum continuity relations for all elements are solved simultaneously, rather than for individual elements.

The spray subroutines in 3D-COMBUST should be modified to handle the extremely narrow spray fans of the gas/liquid coaxial element, so that this type of injector can be analyzed by the overall Injector/Chamber Compatibility Model.

A simple model for reactive stream blowpart and manifold effects should be incorporated into the IHTM program, so that face heat transfer can be analyzed for a wider range of injectors.

In addition to the modifications described above, the data from a wider range of experimental motor firings should be analyzed to provide a more thorough evaluation of the overall system of computer programs. The conclusions from these analyses shall be incorporated into a designer's guide for use with the computer programs.

#### REFERENCES

1. AFRPL-TR-70-12, Development of Injector Chamber Compatibility Analysis, Final Report, Contract F04611-6S-C-0043, Edwards AFB, California, March 1970.
2. Contract AF49(638)-1705, "Research on Pressure Wave Growth in a Homogeneous Monodisperse Spray/Gas Mixture," Air Force Office of Scientific Research with Rocketdyne, 1967-1970. Also, the Ph.D. Thesis of R. D. Sutton, University of California, Berkeley, California (To Be Awarded 1972).
3. Rupe, J. H. and Jaivin, G. H., Technical Report No. 32-648, Jet Propulsion Laboratory, Pasadena, California, 1 October 1964.
4. AFRPL-TR-68-147, Correlation of Spray Injector Parameters with Rocket Engine Performance, Edwards AFB, California, June 1968.
5. Falk, A. Y., et. al., Space Storable Propellant Performance Study, Final Report, NASA CR-72487, Contract NAS3-11199, Rocketdyne, a Division of North American Rockwell Corporation, Canoga Park, California, 24 November 1968.
6. Combs, L. P., et. al., Liquid Rocket Performance Computer Model with Distributed Energy Release, R-8298, Contract NAS7-746, Rocketdyne, a Division of North American Rockwell Corporation, Canoga Park, California, September 1970.
7. Elliott, D. G., et. al., Technical Report No. 32-587, Jet Propulsion Laboratory, Pasadena, California, 15 February 1963.
8. Rowley, R. W., "Gas-Side Boundary Phenomena," in JPL Space Programs Summary 37-42, Vol. IV, Jet Propulsion Laboratory, Pasadena, California, 31 December 1966.
9. Rowley, R. W., "Gas-Side Boundary Phenomena," in JPL Space Programs Summary 37-32, Vol. IV, Jet Propulsion Laboratory, Pasadena, California, 30 April 1965.
10. Rowley, R. W., "Gas-Side Boundary Phenomena," in JPL Space Programs Summary 37-38, Vol. IV, Jet Propulsion Laboratory, Pasadena, California, 30 April 1966.



21. Back, L. H., et. al., "Laminarization of a Turbulent Boundary Layer in Nozzle Flow-Boundary Layer and Heat Transfer Measurements with Wall Cooling," J. of Heat Transfer, Trans. ASME, 333, August 1970.
22. Moretti, P. M., and Kays, W. M., "Heat Transfer to a Turbulent Boundary Layer with Varying Free-Stream Velocity and Varying Surface Temperature - an Experimental Study," Int. J. of Heat and Mass Transfer, 8, 1187, 1965.
23. Junkham, G. H., and Serovy, G. K., "Effects of Free Stream Turbulence and Pressure Gradient on Flat Plate Boundary Layer Velocity Profiles and Heat Transfer," J. of Heat Transfer, Trans. ASME, 169, May 1967.
24. Zemanick, P. P. and Dougall, R. S., "Local Heat Transfer Downstream of Abrupt Circular Expansion," J. of Heat Transfer, Trans. ASME, 53, February 1970.
25. Kroll, K. M. and Sparrow, E. M., "Turbulent Heat Transfer in the Separated, Reattached, and Redevelopment Regions of a Circular Tube," J. of Heat Transfer, Trans. ASME, 131, February 1966.
26. Seban, R. A., "Heat Transfer to the Turbulent Separated Flow of Air Downstream of a Step in the Surface of a Plate," J. of Heat Transfer, Trans. ASME, 259, May 1964.
27. Filetti, E. G. and Kays, W. M., "Heat Transfer in Separated, Reattached, and Redevelopment Regions Behind a Double Step at the Entrance to a Flat Duct," J. of Heat Transfer, Trans. ASME, 163, May 1967.
28. Nurick, W. H., et. al., "Transient Heat Transfer from a Liquid Metal Spray Impinging on a Vertical Surface," Chem. Eng. Progress Symposium Series, 59, 61, 127, 1964.
29. McGinnis, F. K. and Holman, J. P., "Individual Droplet Heat Transfer Rates for Splattering on Hot Surfaces," Int. J. of Heat and Mass Transfer, 12, 9, 1969.
30. Godwin, T. W. and Lorenzo, C. F.: Ignition of Several Metals in Fluorine, ARS paper No. 740-58 (1958).
31. Simons, J. H., Fluorine Chemistry, Volume I, Academic Press, 1950.

32. Nurick, W. H., and Cordill, J. D.: Reactive Stream Separation Photography, Final Report, Contract NAS7-720, (R8490), Rocketdyne, a Division of North American Rockwell Corporation, Canoga Park, California, October 1971.
33. Thompson, R. J., Jr., The Chemistry of Propellants, pp. 25-120, Pergamon Press, New York, 1960.
34. Aerojet General Corporation, Properties of Liquid Propellants, Sacramento, California.
35. AFRPL-TR-67-159, Designer's Guide and Computer Program for Ablative Materials in Liquid Rocket Thrust Chambers, Final report contract AF04(611)-11415, Edwards AFB, California, June 1967.

UNCLASSIFIED

Security Classification

## DOCUMENT CONTROL DATA - R &amp; D

(Security classification of title, body of abstract and indexing annotation must be entered when the overall report is classified)

1. ORIGINATING ACTIVITY (Corporate author) ROCKETDYNE a division of North American Rockwell Corporation 6633 Canoga Avenue, Canoga Park, California 91304		2a. REPORT SECURITY CLASSIFICATION UNCLASSIFIED	
3. REPORT TITLE EXTENSION OF A THRUST CHAMBER COMPATIBILITY MODEL		2b. GROUP	
4. DESCRIPTIVE NOTES (Type of report and inclusive dates) Final Report; June 1970 to June 1971			
5. AUTHOR(S) (First name, middle initial, last name) W. S. Hines, M. D. Schuman, W. M. Ford, and K. D. Fertig			
6. REPORT DATE March 1972	7a. TOTAL NO. OF PAGES	7b. NO. OF REFS 32	
8a. CONTRACT OR GRANT NO. F04611-70-C-0056	9a. ORIGINATOR'S REPORT NUMBER(S) R-8745		
d. PROJECT NO.	9b. OTHER REPORT NO(S) (Any other numbers that may be assigned this report) AFRPL-TR-72-19		
10. DISTRIBUTION STATEMENT Distribution limited to U.S. Government agencies only; test and evaluation; March 1972; All other requests for this document must be referred to AFRPL (STINFO/DOZ) Edwards, CA93523.			
11. SUPPLEMENTARY NOTES		12. SPONSORING MILITARY ACTIVITY AFRPL, Director of Laboratories, AFSC, U.S. AF, Edwards, California	
13. ABSTRACT <p>This report describes a combined analytical and experimental program which extended and improved a system of computer programs which calculates the effects of injector configuration on performance and upon thrust chamber wall compatibility. Improved correlations for the spray mass distribution patterns for liquid/liquid injector elements and the capability of predicting the mass distribution downstream of gas/liquid coaxial elements were incorporated into the LISP computer program. Calculation of the effects of droplet collisions, nonuniform axial gas velocity and variable droplet evaporation rates were added to the 3D-COMBUST program which predicts the gas flow field in thrust chambers. An improved forced convection model was added to the BLEAT boundary layer program to permit heat transfer calculations under regenerative cooling conditions. Finally an injector face heat transfer program, IHTM, was added to the system.</p> <p>An experimental program consisting of model motor firings with the <math>N_2O_4/50\%N_2H_4</math>-50%UDMH propellant combination, cold flow tests, and spray heat transfer experiments supported the program. The overall system of computer programs were evaluated by comparison of analytical predictions to experimental results obtained in motor firings at the Air Force Rocket Propulsion Laboratory and Rocketdyne.</p>			

DD FORM 1473

UNCLASSIFIED  
Security Classification

UNCLASSIFIED  
Security Classification

14	KEY WORDS	LINK A		LINK B		LINK C	
		ROLE	WT	ROLE	WT	ROLE	WT

UNCLASSIFIED  
Security Classification